THE STATE-OF-ART TECHNIQUES OF SEISMIC IMAGING FOR THE DEEP AND ULTRA-DEEP HYDROCARBON RESERVOIRS

EDITED BY: Jianping Huang, George Mcmechan, Jidong Yang, Hua-Wei Zhou, Keyu Liu, Yong Zheng and Wei Zhang

PUBLISHED IN: Frontiers in Earth Science

frontiers Research Topics

frontiers

ISSN 1664-8714
ISBN 978-2-83250-501-4
DOI 10.3389/978-2-83250-501-4

About Frontiers

Frontiers is more than just an open-access publisher of scholarly articles: it is a pioneering approach to the world of academia, radically improving the way scholarly research is managed. The grand vision of Frontiers is a world where all people have an equal opportunity to seek, share and generate knowledge. Frontiers provides immediate and permanent online open access to all its publications, but this alone is not enough to realize our grand goals.

Frontiers Journal Series

The Frontiers Journal Series is a multi-tier and interdisciplinary set of open-access, online journals, promising a paradigm shift from the current review, selection and dissemination processes in academic publishing. All Frontiers journals are driven by researchers for researchers; therefore, they constitute a service to the scholarly community. At the same time, the Frontiers Journal Series operates on a revolutionary invention, the tiered publishing system, initially addressing specific communities of scholars, and gradually climbing up to broader public understanding, thus serving the interests of the lay society, too.

Dedication to Quality

Each Frontiers article is a landmark of the highest quality, thanks to genuinely collaborative interactions between authors and review editors, who include some of the world's best academicians. Research must be certified by peers before entering a stream of knowledge that may eventually reach the public - and shape society; therefore, Frontiers only applies the most rigorous and unbiased reviews.
Frontiers revolutionizes research publishing by freely delivering the most outstanding research, evaluated with no bias from both the academic and social point of view. By applying the most advanced information technologies, Frontiers is catapulting scholarly publishing into a new generation.

What are Frontiers Research Topics?

Frontiers Research Topics are very popular trademarks of the Frontiers Journals Series: they are collections of at least ten articles, all centered on a particular subject. With their unique mix of varied contributions from Original Research to Review Articles, Frontiers Research Topics unify the most influential researchers, the latest key findings and historical advances in a hot research area! Find out more on how to host your own Frontiers Research Topic or contribute to one as an author by contacting the Frontiers Editorial Office: frontiersin.org/about/contact

THE STATE-OF-ART TECHNIQUES OF SEISMIC IMAGING FOR THE DEEP AND ULTRA-DEEP HYDROCARBON RESERVOIRS

Topic Editors:
Jianping Huang, China University of Petroleum, Huadong, China
George Mcmechan, The University of Texas at Dallas, United States
Jidong Yang, China University of Petroleum, Huadong, China
Hua-Wei Zhou, University of Houston, United States
Keyu Liu, Commonwealth Scientific and Industrial Research Organisation (CSIRO), Australia
Yong Zheng, China University of Geosciences Wuhan, China
Wei Zhang, Southern University of Science and Technology, China

Citation: Huang, J., Mcmechan, G., Yang, J., Zhou, H.-W., Liu, K., Zheng, Y., Zhang, W., eds. (2022). The State-of-Art Techniques of Seismic Imaging for the Deep and Ultra-Deep Hydrocarbon Reservoirs. Lausanne: Frontiers Media SA. doi: 10.3389/978-2-83250-501-4

Table of Contents

frontiers | Frontiers in Earth Science

TYPE Editorial
PUBLISHED 30 September 2022
DOI 10.3389/feart.2022.1043314

OPEN ACCESS

EDITED AND REVIEWED BY
Alexander Kokhanovsky,
Max Planck Institute for Chemistry, Germany

*CORRESPONDENCE
Jidong Yang,
jidong.yang@upc.edu.cn
Jianping Huang,
jphuang@upc.edu.cn

SPECIALTY SECTION
This article was submitted to Environmental Informatics and Remote Sensing, a section of the journal Frontiers in Earth Science

RECEIVED 13 September 2022
ACCEPTED 14 September 2022
PUBLISHED 30 September 2022

CITATION
Yang J and Huang J (2022), Editorial: The state-of-art techniques of seismic imaging for the deep and ultra-deep hydrocarbon reservoirs.
Front. Earth Sci. 10:1043314.
doi: 10.3389/feart.2022.1043314

Editorial: The state-of-art techniques of seismic imaging for the deep and ultra-deep hydrocarbon reservoirs

Jidong Yang* and Jianping Huang*

Geophysics Department, China University of Petroleum (East China), Qingdao, China

KEYWORDS

seismic modeling, seismic imaging, seismic interpretation, seismic inversion, seismic acquisition

Editorial on the Research Topic
The state-of- art techniques of seismic imaging for the deep and ultra-deep hydrocarbon reservoirs

At present, oil and gas resources that are relatively simple to explore have been extensively developed. Deep and ultra-deep hydrocarbon becomes one of the most important exploration targets. Under high-temperature and high-pressure conditions, deep oil and gas reservoirs have different hydrocarbon sources, accumulation mechanisms, geophysical and geochemical characteristics from conventional shallow-to-intermediate reservoirs. Seismic data from deep and ultra-deep strata have weak amplitudes, low signal-to-noise ratio, and bad resolution. These issues make it difficult for geophysicists to build accurate subsurface velocity models and produce high-quality images.

The Research Topic "*The State-of-Art Techniques of Seismic Imaging for the Deep and Ultra-deep Hydrocarbon Reservoirs*" aims to receive the Frontier research and application for deep and ultra-deep oil/gas exploration using seismic techniques, toward a better understanding of deep and ultra-deep petroleum systems. Twelve manuscripts have been accepted so far, covering seismic acquisition, modeling, imaging, inversion, and interpretation. For example, optimized acquisition systems have been proposed to improve the quality of full-waveform inversion and reverse-time migration for deep reservoirs. Accurate numerical modeling methods combined with high-performance computation have been developed to simulate seismic propagations in land exploration areas. Advanced migration approaches, including least-squares migration, attenuation compensation, scattering imaging and Gaussian beam migration for VSP surveys, have been presented to improve image quality for deep targets. Robust hydrocarbon prediction algorithms have been proposed to improve the accuracy of reservoir

characterization for land low-signal-to-noise data. These developments provide new ideas for deep and ultra-deep seismic exploration.

Author contributions

JY and JH collaborate to write this editorial.

Conflict of interest

The authors declare that the research was conducted in the absence of any commercial or financial relationships that could be construed as a potential conflict of interest.

Publisher's note

frontiers in Earth Science

METHODS
published: 10 January 2022
doi: 10.3389/feart.2021.800312

Simultaneous Inversion of Layered Velocity and Density Profiles Using Direct Waveform Inversion (DWI): 1D Case

Zhonghan Liu, Yingcai Zheng and Hua-Wei Zhou*

Department of Earth and Atmospheric Sciences, The University of Houston, Houston, TX, United States

To better interpret the subsurface structures and characterize the reservoir, a depth model quantifying P-wave velocity together with additional rock's physical parameters such as density, the S-wave velocity, and anisotropy is always preferred by geologists and engineers. Tradeoffs among different parameters can bring extra challenges to the seismic inversion process. In this study, we propose and test the Direct Waveform Inversion (DWI) scheme to simultaneously invert for 1D layered velocity and density profiles, using reflection seismic waveforms recorded on the surface. The recorded data includes primary reflections and interbed multiples. DWI is implemented in the time-space domain then followed by a wavefield extrapolation to downward continue the source and receiver. By explicitly enforcing the wavefield time-space causality, DWI can recursively determine the subsurface seismic structure in a local layer-by-layer fashion for both sharp interfaces and the properties of the layers, from shallow to deep depths. DWI is different from the layer stripping methods in the frequency domain. By not requiring a global initial model, DWI also avoids many nonlinear optimization problems, such as the local minima or the need for an accurate initial model in most waveform inversion schemes. Two numerical tests show the validity of this DWI scheme serving as a new strategy for multi-parameter seismic inversion.

Keywords: full waveform inversion (FWI), velocity model building, density inversion, waveform inversion, multi-parameter inversion, modeling

OPEN ACCESS

Edited by:
Christine Thomas,
University of Münster, Germany

Reviewed by:
Jie Zhang,
University of Science and Technology of China, China
Ya-juan Xue,
Chengdu University of Information Technology, China

****Correspondence:***
Zhonghan Liu
lyuuu@hotmail.com

Specialty section:
This article was submitted to Solid Earth Geophysics, a section of the journal Frontiers in Earth Science

Received: *22 October 2021*
Accepted: *03 December 2021*
Published: *10 January 2022*

Citation:
Liu Z, Zheng Y and Zhou H-W (2022) Simultaneous Inversion of Layered Velocity and Density Profiles Using Direct Waveform Inversion (DWI): 1D Case. Front. Earth Sci. 9:800312. doi: 10.3389/feart.2021.800312

INTRODUCTION

Seismic full waveform inversion (FWI), formulated originally by (Lailly, 1983; Tarantola, 1984), is a powerful process in subsurface velocity model building. The goal of FWI is to find a model such that the model-predicted waveforms fit the observed waveforms. Since FWI is an iterative gradient-based method, its success depends on how much the initial model differs from the true model (Virieux and Operto, 2009). The limitation of the iterative FWI scheme was recognized early on by many authors (Gauthier et al., 1986; Tarantola, 1986; Mora, 1987; Bourgeois et al., 1989). Tarantola (2005, p.128) pointed out that the local Fréchet gradient used in FWI was equivalent to the single scattering Born approximation. Therefore the performance of FWI relies on an accurate and long-wavelength initial velocity model in which case the Born approximation is more accurate. As the correspondence between low-frequency seismic data and low-wavenumber/large-scale structures is linear in the Born single scattering (Wu and Zheng, 2014), due to the lack of low-frequency content (<5 Hz) in most

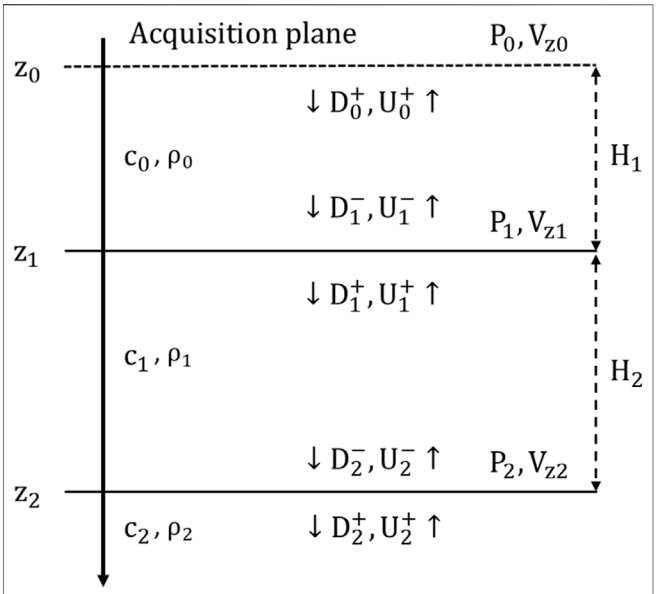

FIGURE 1 | Wavefields in a 1D layered model. c_0, c_1, ... are layer velocities. ρ_0, ρ_1, ρ_2 are densities in layers. H_1, H_2 are the layer thicknesses. P_i, v_{zi} are pressure and vertical component of the particle velocity at the depth z_i, respectively. U_i, D_i are the up-going and down-going pressure fields respectively at depth z_i, where "-" indicates the wavefields on the top side of z_i, "+" indicates the wavefields on the bottom side of z_i. Figure modified from Zheng and Liu (2020).

reflection seismic data, most developments in FWI have been focusing on how to recover large-scale structural information when low-frequency data are not available. These developments include, for example, the Laplace FWI (Shin and Cha, 2008; Shin and Ha, 2008; Kim et al., 2013), envelope inversion (Wu et al., 2014; Luo and Wu, 2015; Chen et al., 2018), intensity inversion (Liu et al., 2018; Liu et al., 2020), and the FWI using deep learning techniques (Richardson, 2018).

To circumvent the challenges in FWI, we proposed an alternative waveform inversion scheme (Liu and Zheng, 2015; 2017), called the direct waveform inversion (DWI), to invert for subsurface models without the need for a global initial model. DWI combines seismic imaging and velocity model building into one single process. In order to use DWI, it is necessary for the input seismic data to include both free-surface and inter-bed multiples. Using surface recorded reflection seismic data, DWI is able to deliver accurate P-wave velocity inversion results without using a global initial model, for both 1D and 2D layered scalar (i.e., no density variation) models (Zheng and Liu, 2020). Without using a global model, DWI inverts the model from shallow to deep depths. In this regard, DWI is similar to the layer-stripping methods (Claerbout, 1976) and the approach by Goupillaud (1961). However, there are important differences in the methods, in particular the explicit use of the time-space causality in DWI and local inversion in both space and time.

In the current industry, simultaneous inversion of multiple rock physical parameters is one of the state-of-art workflows that can much directly benefit the subsurface reservoir characterization and improve production (Brossier et al., 2009), using surface seismic data. To address the demand of multi-parameter inversion, many FWI methods are developed to invert for parameters like the P-wave velocity, S-wave velocity, density, and seismic anisotropy (Sears et al., 2008; Brossier et al., 2009; Jeong et al., 2012; Warner et al., 2013; Alkhalifah and Plessix, 2014). However, for these multi-parameter inversion methods based on FWI, the increased number of the model

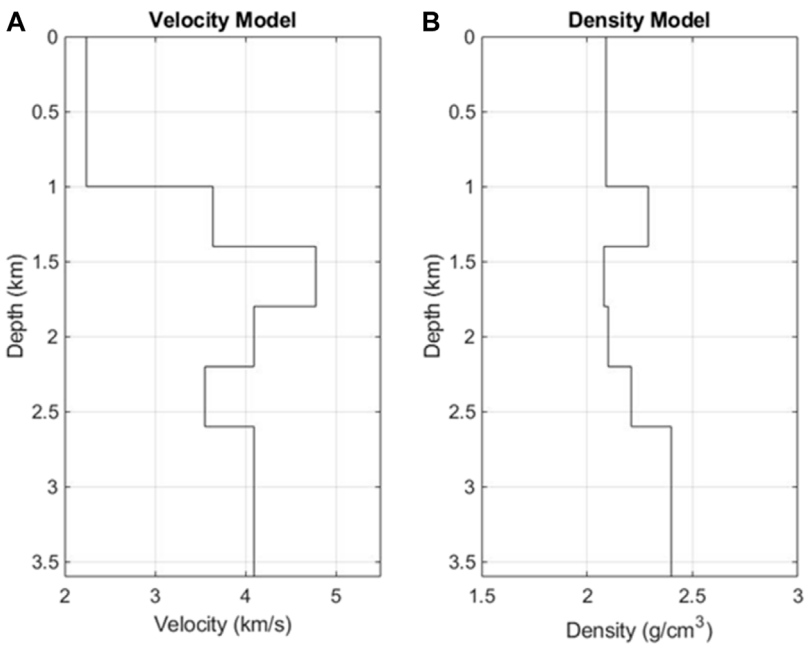

FIGURE 2 | Velocity **(A)** and density **(B)** profiles of the true model.

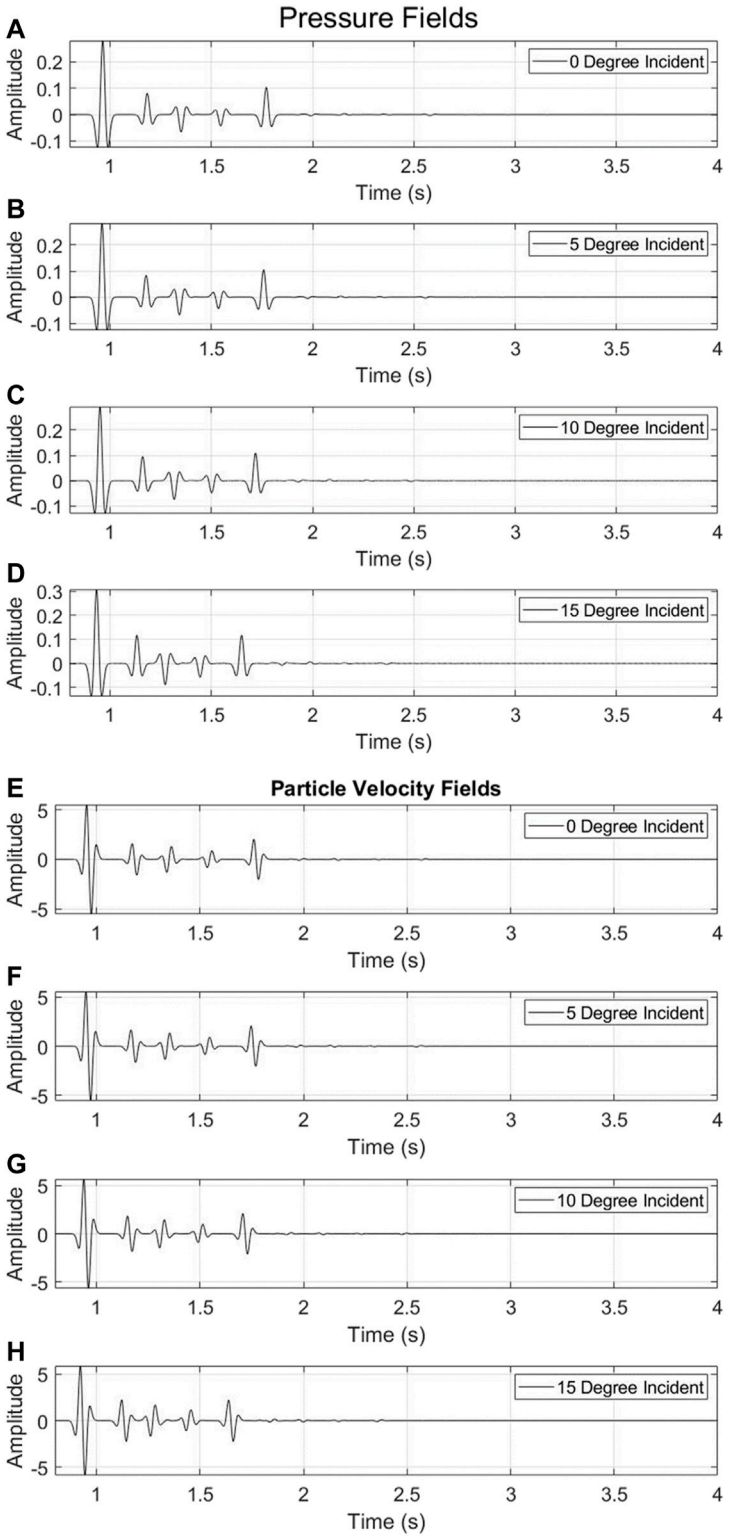

FIGURE 3 | Recorded waveforms of pressure **(A–D)** and vertical component of particle velocity **(E–H)** in response to four different plane waves.

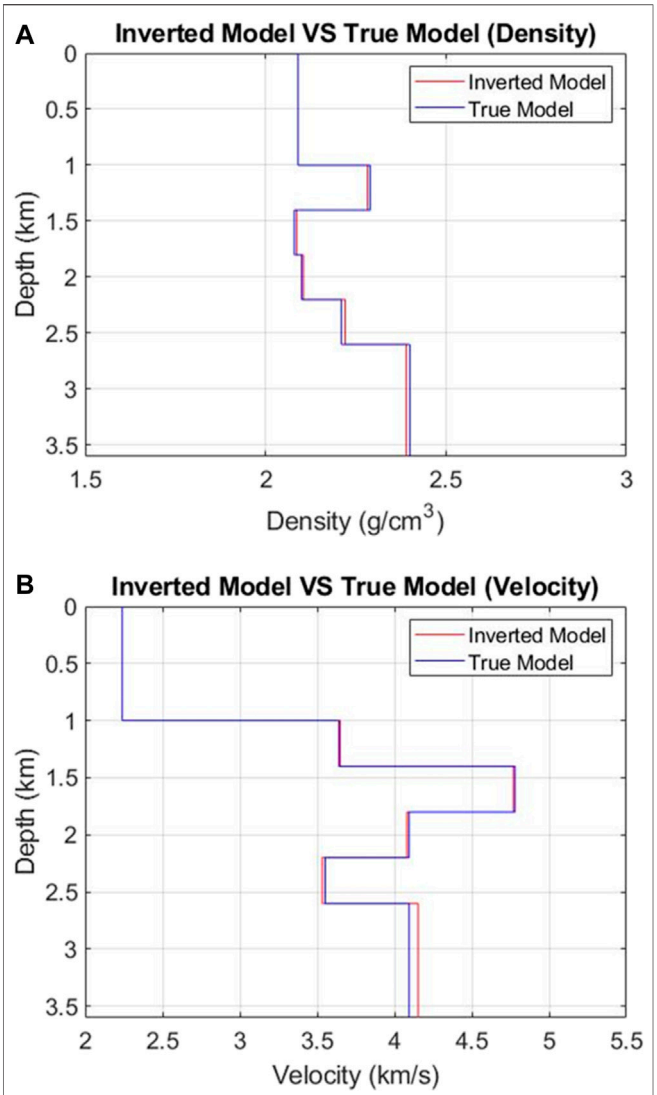

FIGURE 4 | Comparisons between DWI inversion result and true model for both velocity **(A)** and density **(B)** structure.

TABLE 1 | The misfit of velocities and densities between the inverted model and true model (the velocity and density information of the first layer are known).

	Misfit of velocity	Misfit of density
Layer 2	0.28(%)	0.32(%)
Layer 3	0.26(%)	0.29(%)
Layer 4	0.34(%)	0.23(%)
Layer 5	0.54(%)	0.47(%)
Layer 6	1.33(%)	0.44(%)

parameters means higher computational cost, and increased ill-posedness of the inverse problem (Virieux and Operto, 2009). In contrast, benefited from the localized inversion and explicit use of the time-space causality, our DWI method can be implemented for multi-parameter inversion without increasing much computational cost and numerical instability.

In this paper, we start from a 1D acoustic layered medium to demonstrate the ability of DWI in the simultaneous inversion of multiple parameters. Such 1D layered examples can fundamentally validate the feasibility of this state-of-art DWI method. The numerical examples demonstrate that the DWI method could play an important role in the multi-parameter seismic inversion.

1D Scalar DWI With Constant Density Throughout the Model

In this section, we briefly summarize the scalar DWI procedure for inverting the sound wave velocity in a horizontally stratified layered medium that has a constant density throughout the model (**Figure 1**), i.e., $\rho_i = \rho_0$. In the next section, we will consider the case where densities may be different in different layers.

DWI explicitly uses the time-space causality property of the wavefield in the inversion. Starting from the source-receiver layer near the surface, we recursively (not iteratively) build the model downward by fitting the earliest parts of the waveforms of pairs of source-receivers of short (or zero) offsets. We then extrapolate the sources and receivers downward to the bottom of the inverted region, and repeat the process.

To illustrate the DWI process, we assume that both the pressure waveform, P, and particle velocity, V_z, are recorded on the surface (z_0). The incident plane wave is vertical or at zero incident angle. We further assume that c_0, the velocity of the first layer, is known. We decompose the wavefields (P and V_z) into up-going, U, and down-going, D, pressure wavefields, respectively (Liu and Zheng, 2015) as follows

$$D + U = P \tag{1}$$

$$D - U = \rho c V_z \tag{2}$$

where ρ and c are density and wave velocity, respectively. Conversely, if we know U and D, we can compose P and V_z. In this section, we assume a constant density profile ρ.

DWI consists of four steps:

- Step 1. At the acquisition plane depth z_0, we use the recorded waveforms, $P_0(t)$ and $V_{z0}(t)$, and the first layer's velocity c_0 (assumed to be known), to calculate the up-going and down-going pressure fields at depth z_0^+, denoted as U_0^+ and D_0^+, respectively, using **Eq. 1**. From the point of view of the input/output system, we can view the medium below z_0 as a linear system. D_0^+ is the incident wave (or input), and U_0^+ is the reflection response (or output) of the system. Following the time-space causality of the wavefield, the earliest up-going impulse in U_0^+ must be generated from the first (earliest) down-going impulse in D_0^+, reflected by the reflector at depth z_1 to be determined. A causal time-domain deconvolution between D_0^+ and U_0^+ can generate a response consisting of a series of impulses. The time of the first impulse gives a time difference, 2τ. Hence the depth of the reflector z_1, or the thickness of the first layer H_1, can be calculated by multiplying c_0 with the one-way traveltime τ.

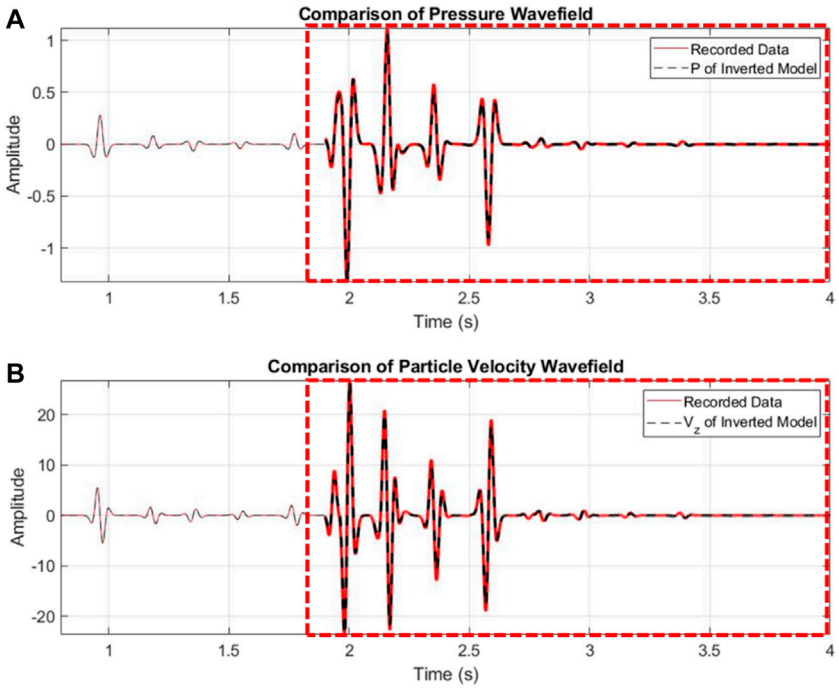

FIGURE 5 | Comparisons of the recorded data (red) and synthetics (black) modeled using the DWI inverted model. **(A)** pressure waveforms; **(B)** particle velocity waveforms at the 0-degree incidence. Note the waveform amplitudes of the multiples in the red dashed box are amplified by 300 times.

- Step 2. We then extrapolate fields U_0^+ and D_0^+ to the bottom of the first layer (depth z_1^-) in the frequency (ω) domain

$$U_1^- = U_0^+ exp(-i\omega\tau) \tag{3}$$

$$D_1^- = D_0^+ exp(+i\omega\tau) \tag{4}$$

  This wavefield extrapolation can be done by many different methods. In 1d, we choose the phase shift approach shown here because it is easy to implement.

- Step 3. After extrapolation, the first impulse in U_0^- and the first impulse in D_0^- should be time-shifted to the same time as if the incidence and reflection occur right above z_1. We use their amplitude ratio, R_0, which is the reflectivity in a constant-density medium

$$R_0 = \frac{c_1 - c_0}{c_1 + c_0} \tag{5}$$

  To determine the velocity, c_1, of the next (or the second) layer since c_0 is known.

- Step 4. Finally, we can use c_1, U_1^-, and D_1^-, to obtain the pressure and particle velocity fields, P_1 and v_{z1}, respectively at depth z_1^-, using **Eqs 1**, **2**. Because the pressure and the particle velocity fields should be continuous across a boundary, we can get their values at z_1^+ in layer 2. At this point, we also know c_1, so our situation is the same as in Step 1.

The aforementioned process, using the recorded fields, P_0 and V_{z0}, and c_0, to obtain the other parameters of the second layer (z_1, P_1, V_{z1}, and c_1), can be recursively repeated downward layer by layer. As the inversion process goes deeper, there will be fewer and fewer remaining seismic events in both the up-going data. Eventually, DWI stops when there are no seismic events in the extrapolated upgoing fields due to finite recording time of the seismic traces. At this point, all the layers have been inverted or the inverted model has expanded downward to its maximum extent and converged to the final model. In this sense, DWI always converges, unconditionally.

Simultaneous DWI for Both Velocity and Density

In the previous 1D DWI scheme, we assume the density is constant throughout the model. For the 1D inversion on models of depth dependent density profiles, there were some relevant work by Coen in 1980s (Coen, 1981a; Coen, 1981b; Coen, 1981c). In Coen's work, the density and velocity are inverted separately using a dataset from oblique incident plane waves based on the Gel'fand-Levitan-Marchenko (GLM) theory (Agranovich and Marchenko, 1963; Berryman and Greene, 1980). In our study, instead of applying the GLM theory, we directly use the incident angle (θ)-dependence of the reflectivity, $R(\theta)$, to invert for both velocities and densities of a layered model. To achieve simultaneous inversion of velocities and densities, we show how to modify the steps in the previous section respectively.

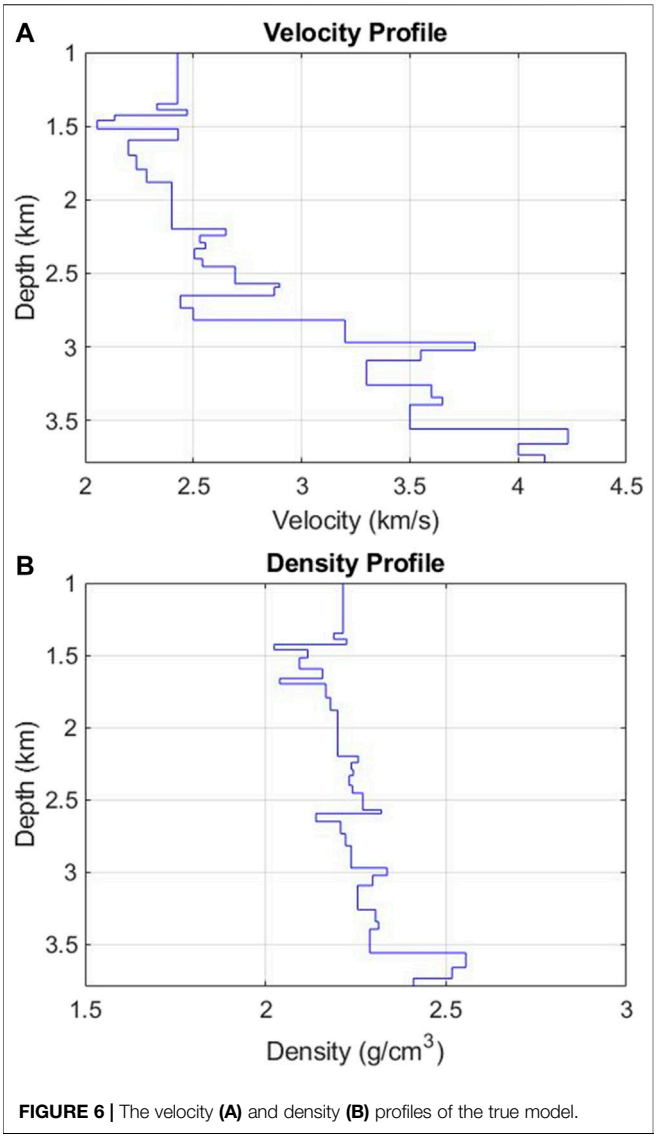

FIGURE 6 | The velocity **(A)** and density **(B)** profiles of the true model.

Assuming the wave is incident from medium-1 (ρ_1, c_1) at an angle θ to medium-2 (ρ_2, c_2), we have the angle-dependent reflectivity

$$R(\theta) = \frac{\rho_2 c_2 cos\theta - \rho_1 \sqrt{c_1^2 - c_2^2 sin^2\theta}}{\rho_2 c_2 cos\theta + \rho_1 \sqrt{c_1^2 - c_2^2 sin^2\theta}} \tag{6}$$

If we have two plane waves of two different incident angles θ_1 and θ_2 and two measured amplitudes, $R_1 = R(\theta_1)$ and $R_2 = R(\theta_2)$, we can in principle determine c_2, and ρ_2, simultaneously.

To increase robustness of the inversion, we can make use of waves of multiple incident angles ($n \geq 2$), and minimize the objective function

$$J[c_2, \rho_2] = \sum_{i=1}^{n} \left| R(\theta_i; \rho_2, c_2) - r_i \right|^2 \tag{7}$$

In **Eq. 7**, for a plane wave at the incident angle θ_i, $R(\theta_i)$ is theoretically modeled reflectivity using **Eq. 6**, and r_i is the measured reflectivity. As we only have two unknowns (c_2 and ρ_2), using a grid search method can quickly get the results.

Assuming the incident wave angle is θ and in order to invert for the density profile, the steps of the scalar DWI need to be modified as follows:

In Step 1, **Eq. 2**, the relationship between the pressure and vertical component of the particle velocity, should be changed to

$$D - U = \rho c V_z / cos\theta \tag{8}$$

In Step 2, the extrapolation of up-going and down-going pressure fields should be modified as

$$U_2^- = U_1^+ exp(-i\omega\tau cos\theta) \tag{9}$$

$$D_2^- = D_1^+ exp(+i\omega\tau cos\theta) \tag{10}$$

In Step 3, using the amplitude ratio $R(\theta_i)$ and the measured data, r_i, from multiple incident angles, θ_i, we can obtain c_2 and ρ_2 by either solving **Eq. 6** directly or fitting **Eq. 7**.

In Step 4, we need to use **Eqs 1**, **8** to compose P and V_z from the up-going and the down-going fields.

Numerical Examples

In this section, we will present two synthetic examples to demonstrate the effectiveness of our proposed method: a simple layered model with six layers, and a more complex layered model with thirty-one layers. Both models are horizontally stratified. Within each layer, the velocity and density are constant. However, different layers have different properties. Both the top and bottom boundaries of the model are set up as half-space boundary conditions.

The synthetic data (pressure and particle velocity) in both examples are generated by a propagator matrix method (e.g., Eftekhar et al., 2018). The plane wave is injected at a depth of 0 m and propagated downward into the model. The receivers are placed at the same depth. Both the pressure and particle velocity wavefields are recorded at a time sampling interval of 1 ms.

Example 1.

In the first example, there are six layers (**Figure 2**) and the velocity contrast is up to 200%. Here we use a 15 Hz Ricker wavelet as the incident plane wave for the model (**Figure 2**). We conduct the modeling for four plane wave sources at different incident angles: 0, 5, 10, and 15°. The waveform records of the pressure and the vertical component of particle velocity are shown in **Figure 3**. In **Figure 3**, the recorded waveforms contain full information of the wavefields, including the primary reflections and multiples.

Using the recorded data shown in **Figure 3** and following the DWI steps in the previous section, we inverted for both the velocity and density profiles, shown in **Figure 4**. We also calculated the misfits in velocities and densities between the DWI results and the true models shown in **Table 1**, where most of them are less than 1%, except the velocity in the last layer (layer 6).

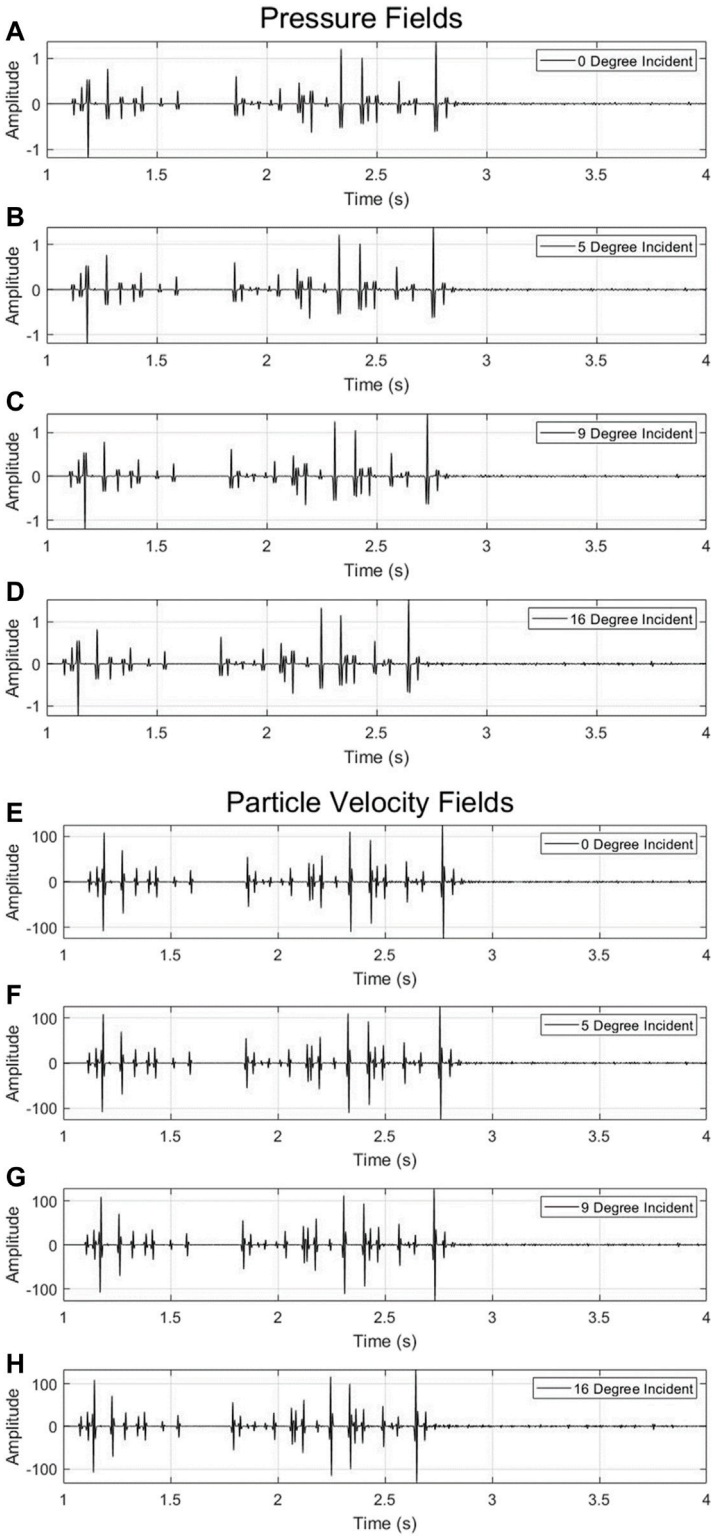

FIGURE 7 | Recorded waveforms of pressure **(A–D)** and vertical component of particle velocity **(E–H)** in response to four different plane waves.

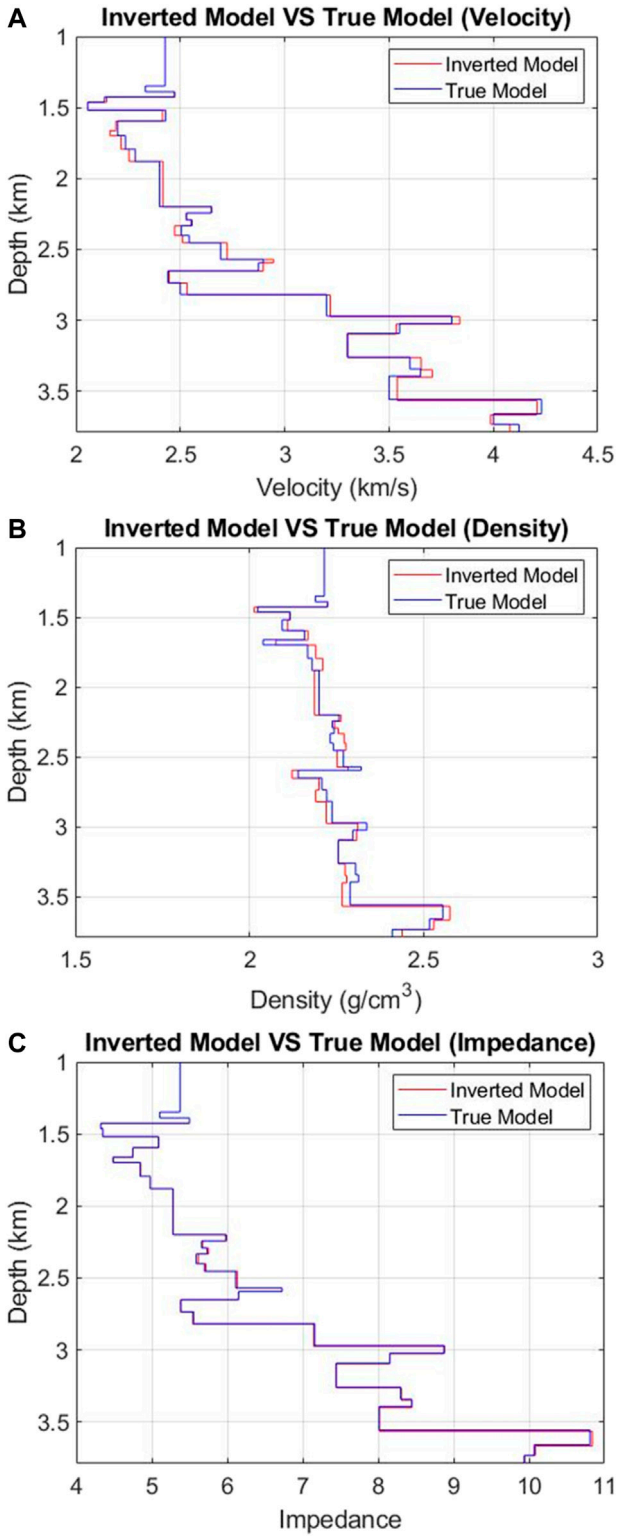

FIGURE 8 | Comparisons between DWI inversion result and true model on velocity **(A)**, density **(B)**, and impedance **(C)** models.

To check the validity of the inverted model in the data space, we conduct a forward synthetic modeling using the DWI inverted model (**Figure 4**). The modeled waveforms fit the data very well (**Figure 5**). Both the primary reflections and the internal multiples can be reproduced by the DWI inverted model.

Example 2.
In the second example, we build a model with 31 velocity and density layers (**Figure 6**). An 80 Hz Ricker wavelet was used as the incident plane wave source wavelet and we modeled the data for four plane waves at angles: 0, 5, 9, and 16°. The recorded waveform data of the pressure and the vertical particle velocity are shown in **Figure 7**.

Compared with the recorded waveforms in the first example (**Figure 3**), both the primary reflections and the internal multiples (**Figure 7**) are much more complicated. Using these recorded data, we applied our DWI scheme and obtained the inversion results of velocity, density, and impedance models shown in **Figure 8**.

From **Figure 8** we can see that the DWI scheme almost exactly recovers the impedance model. For the velocity and density models, although there are some small misfits (less than 2%), the inverted models still agree well with the true model. To further examine the influences of these modeled misfits, here we also conduct a forward synthetic modeling based on the inverted model (**Figure 8**). The results are shown in **Figure 9**. The modeled waveforms using the DWI model fit the data very well including not only the primary reflections but also the internal multiples.

DISCUSSION

We remark on limitations of DWI. DWI depends on reflection events in data to invert for the subsurface model. If the true model is smooth and does not have many reflectors, DWI may fail to find the true model. If the incident angle is too large and the total reflection occurs, DWI is not able to invert for model parameters below the total reflection depth.

The performance of the recursive DWI scheme may suffer from the accumulation of errors as the inversion process goes from shallow to deep depths. Data redundancy can help. In order to resolve reflectivities into P-wave velocity contrast and density contrast, respectively, we need to use several distinct incident angles. If the range of incident angles is narrow, DWI may not be able to resolve Vp and density correctly.

It is also worthwhile to provide some general remarks on the differences between DWI and FWI. Based on the single-scattering approximation (Tarantola, 2005), FWI linearizes the global non-linear seismic inversion problem by iteratively minimizing the misfit between the recorded data and the model predicted data. For FWI, if the intial model is far from the true model, the FWI convergence can be a problem (Sirgue and Pratt, 2004). Different

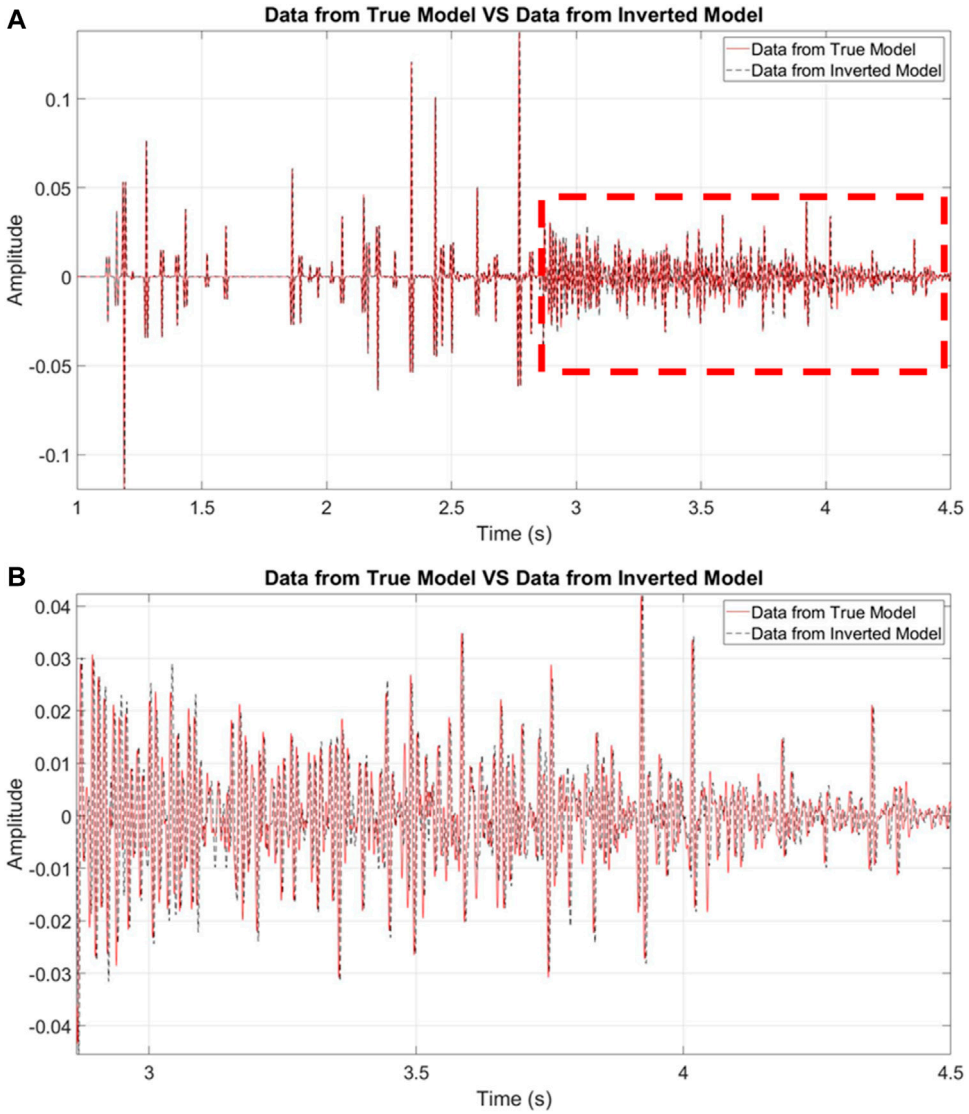

FIGURE 9 | Comparisons of data (red) and synthetics (black) modeled using the DWI inverted model for pressure at the 0-degree incidence **(A)**, the events in the red dashed box are amplified by 10 times. A zoom-in view of the events in the red dashed box in **(A)** is shown in **(B)**.

from FWI, DWI does not rely on an initial global model to start the waveform inversion process. It only needs the local velocity around the surface receivers. The DWI scheme converts the FWI global optimization problem into many localized reflectivity inversions by explicitly invoking the causality principle. Hence it reduces the nonlinearity significantly which is a strength over the FWI method. Another advantage for DWI is that it does not need low-frequency data as seen in our example 2. On the other hand, if the true model is smooth and data have only a few reflection events, FWI may perform better. In cases where DWI can be applicable, DWI can be significantly faster numerically to obtain a model.

There are also marked differences between DWI and the 1D inversion using the GLM theory. Most developments of the GLM theory are aiming at imaging and redatuming methods (e.g., Broggini et al., 2014; Wapenaar et al., 2014; van der Neut et al., 2015; Nowack and Kiraz, 2018). Recently, Wu and He (2020) used the GLM theory to invert for 1D impedance profile. For 1D GLM problem, a time to depth conversion is needed and is usually carried out by the Liouville transform. But for 2D and 3D spatial problems, a macro-velocity model need to be used and should be obtained *a prior*. However, for DWI, the inversion is localized in a shallow to deep fashion and the inverted model is automatically obtained in the depth domain and there is no need to use a global velocity model. In future we will show 2D inversion results in which the wavefield extrapolation is much more involved using integral equations.

CONCLUSION

We extend the scalar DWI scheme to invert for the subsurface density and velocity simultaneously, using multiple plane waves. Using recorded seismic data on the surface, our method inverts for the model parameters locally by explicitly employing time-space causality principle of the wavefield and recursively from shallow to deep depths. The new DWI scheme makes use of the angle dependent property of the reflectivity to solve for density and velocity simultaneously. The input seismic data to DWI must include all types of data including multiples. Numerical examples demonstrate the feasibility of the DWI approach to invert for both velocity and density using four plane wave sources. We find that the acoustic impedance profile is better resolved than the P-wave velocity or density owing to slight tradeoff (<1%) between the two parameters.

DATA AVAILABILITY STATEMENT

The raw data supporting the conclusion of this article will be made available by the authors, without undue reservation.

AUTHOR CONTRIBUTIONS

YZ, H-WZ, and ZL contributed to idea and design of the study. ZL realized the idea and generated numerical examples for testing. ZL wrote the first draft of the manuscript. All authors contributed to manuscript revision, read, and approved the submitted version.

REFERENCES

Agranovich, Z., and Marchenko, V. A. (1963). *The Inverse Problem of Scattering Theory*.

Alkhalifah, T., and Plessix, R.-É. (2014). A Recipe for Practical Full-Waveform Inversion in Anisotropic media: An Analytical Parameter Resolution Study. *Geophysics* 79 (3), R91–R101. doi:10.1190/geo2013-0366.1

Berryman, J. G., and Greene, R. R. (1980). Discrete Inverse Methods for Elastic Waves in Layered media. *Geophysics* 45 (2), 213–233. doi:10.1190/1.1441078

Bourgeois, A., Jiang, B. F., and Lailly, P. (1989). Linearized Inversion: a Significant Step beyond Pre-stack Migration. *Geophys. J. Int.* 99 (2), 435–445. doi:10.1111/j.1365-246x.1989.tb01700.x

Broggini, F., Snieder, R., and Wapenaar, K. (2014). Data-driven Wavefield Focusing and Imaging with Multidimensional Deconvolution: Numerical Examples for Reflection Data with Internal Multiples. *Geophysics* 79 (3), WA107–WA115. doi:10.1190/geo2013-0307.1

Brossier, R., Operto, S., and Virieux, J. (2009). Seismic Imaging of Complex Onshore Structures by 2D Elastic Frequency-Domain Full-Waveform Inversion. *Geophysics* 74 (6), WCC105–WCC118. doi:10.1190/1.3215771

Chen, G.-X., Wu, R.-S., and Chen, S.-C. (2018). Reflection Multi-Scale Envelope Inversion. *Geophys. Prospecting* 66 (7), 1258–1271. doi:10.1111/1365-2478.12624

Claerbout, J. F. (1976). *Fundamentals of Geophysical Data Processing*. Citeseer.

Coen, S. (1981a). Density and Compressibility Profiles of a Layered Acoustic Medium from Precritical Incidence Data. *Geophysics* 46 (9), 1244–1246. doi:10.1190/1.1441262

Coen, S. (1981c). On the Elastic Profiles of a Layered Medium from Reflection Data. Part II: Impulsive point Source. *The J. Acoust. Soc. America* 70 (5), 1473–1479. doi:10.1121/1.387104

Coen, S. (1981b). On the Elastic Profiles of a Layered Medium from Reflection Data. Part I. Plane-wave Sources. *J. Acoust. Soc. America* 70 (1), 172–175. doi:10.1121/1.386669

Eftekhar, R., Hu, H., and Zheng, Y. (2018). Convergence Acceleration in Scattering Series and Seismic Waveform Inversion Using Nonlinear Shanks Transformation. *Geophys. J. Int.* 214 (3), 1732–1743. doi:10.1093/gji/ggy228

Gauthier, O., Virieux, J., and Tarantola, A. (1986). Two-dimensional Nonlinear Inversion of Seismic Waveforms: Numerical Results. *Geophysics* 51 (7), 1387–1403. doi:10.1190/1.1442188

Goupillaud, P. L. (1961). An Approach to Inverse Filtering of Near-surface Layer Effects from Seismic Records. *Geophysics* 26 (6), 754–760. doi:10.1190/1.1438951

Jeong, W., Lee, H.-Y., and Min, D.-J. (2012). Full Waveform Inversion Strategy for Density in the Frequency Domain. *Geophys. J. Int.* 188 (3), 1221–1242. doi:10.1111/j.1365-246x.2011.05314.x

Kim, Y., Shin, C., Calandra, H., and Min, D.-J. (2013). An Algorithm for 3D Acoustic Time-Laplace-Fourier-Domain Hybrid Full Waveform Inversion. *Geophysics* 78 (4), R151–R166. doi:10.1190/geo2012-0155.1

Lailly, P. (1983). "The Seismic Inverse Problem as a Sequence of Before-Stack Migrations," in Conference on Inverse Scattering: Theory and Applications (Philadelphia, PA: SIAM), 206–220.

Liu, Y., He, B., Lu, H., Zhang, Z., Xie, X., and Zheng, Y. (2018). Full Intensity Waveform Inversion. *Geophysics* 86 (6), R649–R658.

Liu, Y., He, B., Zhang, Z., Zheng, Y., and Li, P. (2020). Reflection Intensity Waveform Inversion. *Geophysics*. doi:10.1190/geo2019-0590.1191

Liu, Z., and Zheng, Y. (2017). "Applications of the Direct-Waveform Inversion on 2D Models," in *87th Annual International Meeting, SEG, Expanded Abstracts* (Houston, TX: Series editor Society of Exploration Geophysicists), 1687–1691. doi:10.1190/segam2017-17791763.1

Liu, Z., and Zheng, Y. (2015). "Direct Waveform Inversion," in *85th Annual International Meeting, SEG, Expanded Abstracts* (New Orleans, LA: Series editor Society of Exploration Geophysicists), 1268–1273. doi:10.1190/segam2015-5923910.1

Luo, J., and Wu, R.-S. (2015). Seismic Envelope Inversion: Reduction of Local Minima and Noise Resistance. *Geophys. Prospecting* 63 (3), 597–614. doi:10.1111/1365-2478.12208

Mora, P. (1987). Nonlinear Two-dimensional Elastic Inversion of Multioffset Seismic Data. *Geophysics* 52 (9), 1211–1228. doi:10.1190/1.1442384

Nowack, R. L., and Kiraz, M. S. R. (2018). Virtual Green's Functions Using Seismic Interferometry and Marchenko Redatuming. *Seismological Res. Lett.* 89 (2A), 613–619. doi:10.1785/0220170211

Richardson, A. (2018). *Seismic Full-Waveform Inversion Using Deep Learning Tools and Techniques*.

Sears, T. J., Singh, S. C., and Barton, P. J. (2008). Elastic Full Waveform Inversion of Multi-Component OBC Seismic Data. *Geophys. Prospecting* 56 (6), 843–862. doi:10.1111/j.1365-2478.2008.00692.x

Shin, C., and Cha, Y. H. (2008). Waveform Inversion in the Laplace Domain. *Geophys. J. Int.* 173 (3), 922–931. doi:10.1111/j.1365-246x.2008.03768.x

Shin, C., and Ha, W. (2008). A Comparison between the Behavior of Objective Functions for Waveform Inversion in the Frequency and Laplace Domains. *Geophysics* 73 (5), VE119–VE133. doi:10.1190/1.2953978

Sirgue, L., and Pratt, R. G. (2004). Efficient Waveform Inversion and Imaging: A Strategy for Selecting Temporal Frequencies. *Geophysics* 69 (1), 231–248. doi:10.1190/1.1649391

Tarantola, A. (1986). A Strategy for Nonlinear Elastic Inversion of Seismic Reflection Data. *Geophysics* 51 (10), 1893–1903. doi:10.1190/1.1442046

Tarantola, A. (2005). *Inverse Problem Theory and Methods for Model Parameter Estimation*. Philadelphia, PA: SIAM.

Tarantola, A. (1984). Inversion of Seismic Reflection Data in the Acoustic Approximation. *Geophysics* 49 (8), 1259–1266. doi:10.1190/1.1441754

van der Neut, J., Wapenaar, K., Thorbecke, J., and Slob, E. (2015). Practical Challenges in Adaptive Marchenko Imaging. *77th EAGE Conf. Exhibition 2015* 2015, 1–5. doi:10.1190/segam2015-5791035.1

Virieux, J., and Operto, S. (2009). An Overview of Full-Waveform Inversion in Exploration Geophysics. *Geophysics* 74 (6), WCC1–WCC26. doi:10.1190/1.3238367

Wapenaar, K., Thorbecke, J., Van Der Neut, J., Broggini, F., Slob, E., and Snieder, R. (2014). Marchenko Imaging. *Geophysics* 79 (3), WA39–WA57. doi:10.1190/geo2013-0302.1

Warner, M., Ratcliffe, A., Nangoo, T., Morgan, J., Umpleby, A., Shah, N., et al. (2013). Anisotropic 3D Full-Waveform Inversion. *Geophysics* 78 (2), R59–R80. doi:10.1190/geo2012-0338.1

Wu, R.-S., Luo, J., and Wu, B. (2014). Seismic Envelope Inversion and Modulation Signal Model. *Geophysics* 79 (3), WA13–WA24. doi:10.1190/geo2013-0294.1

Wu, R.-S., and Zheng, Y. (2014). Non-linear Partial Derivative and its De Wolf Approximation for Non-linear Seismic Inversion. *Geophys. J. Int.* 196 (3), 1827–1843. doi:10.1093/gji/ggt496

Wu, R., and He, H. (2020). "Inverse Scattering for Schrödinger Impedance Equation and Simultaneous ρ-v Inversion in Layered Media," in 82nd EAGE Annual Conference & Exhibition, 2020, 1–5

Zheng, Y., and Liu, Z. (2020). Concepts in the Direct Waveform Inversion (DWI) Using Explicit Time-Space Causality. *Commun. Comput. Phys.* 28 (1), 342–355.

Conflict of Interest: The authors declare that the research was conducted in the absence of any commercial or financial relationships that could be construed as a potential conflict of interest.

frontiers in Earth Science

ORIGINAL RESEARCH
published: 11 January 2022
doi: 10.3389/feart.2021.777200

Trapezoid-Grid Finite-Difference Time-Domain Method for 3D Seismic Wavefield Modeling Using CPML Absorbing Boundary Condition

Bangyu Wu[1,2], *Wenzhuo Tan*[1,2], *Wenhao Xu*[3]* and *Bo Li*[2]

[1]School of Mathematics and Statistics, Xi'an Jiaotong University, Xi'an, China, [2]Sinopec Geophysical Research Institute , Nanjing, China, [3]School of Information and Communications Engineering, Xi'an Jiaotong University, Xi'an, China

The large computational memory requirement is an important issue in 3D large-scale wave modeling, especially for GPU calculation. Based on the observation that wave propagation velocity tends to gradually increase with depth, we propose a 3D trapezoid-grid finite-difference time-domain (FDTD) method to achieve the reduction of memory usage without a significant increase of computational time or a decrease of modeling accuracy. It adopts the size-increasing trapezoid-grid mesh to fit the increasing trend of seismic wave velocity in depth, which can significantly reduce the oversampling in the high-velocity region. The trapezoid coordinate transformation is used to alleviate the difficulty of processing ununiform grids. We derive the 3D acoustic equation in the new trapezoid coordinate system and adopt the corresponding trapezoid-grid convolutional perfectly matched layer (CPML) absorbing boundary condition to eliminate the artificial boundary reflection. Stability analysis is given to generate stable modeling results. Numerical tests on the 3D homogenous model verify the effectiveness of our method and the trapezoid-grid CPML absorbing boundary condition, while numerical tests on the SEG/EAGE overthrust model indicate that for comparable computational time and accuracy, our method can achieve about 50% reduction on memory usage compared with those on the uniform-grid FDTD method.

Keywords: finite difference, trapezoid-grid method, seismic wave simulation, 3D, time-domain method

OPEN ACCESS

Edited by:
Yong Zheng,
China University of Geosciences Wuhan, China

Reviewed by:
Wen-Yan Yin,
Zhejiang University, China
Xiaofeng Jia,
University of Science and Technology of China, China

***Correspondence:**
Wenhao Xu
doumifeiniao@163.com

Specialty section:
This article was submitted to Solid Earth Geophysics, a section of the journal Frontiers in Earth Science

Received: *15 September 2021*
Accepted: *03 December 2021*
Published: *11 January 2022*

Citation:
Wu B, Tan W, Xu W and Li B (2022) Trapezoid-Grid Finite-Difference Time-Domain Method for 3D Seismic Wavefield Modeling Using CPML Absorbing Boundary Condition. Front. Earth Sci. 9:777200. doi: 10.3389/feart.2021.777200

1 INTRODUCTION

Reverse time migration (RTM) (Baysal et al., 1983; Xuan et al., 2014; Qu et al., 2015; Xu et al., 2021a; Du et al., 2021) and full-waveform inversion (FWI) (Tarantola, 1984; Virieux and Operto, 2009; Cai and Zhang, 2015; Xia et al., 2017; Jia et al., 2019) play a fundamental role in geophysical exploration. Since forward modeling of the wave equation consumes most computational time in the RTM and FWI processes (Jing et al., 2019; Xu et al., 2021b; Liu et al., 2021), how to achieve the improvement of efficiency and the reduction of memory usage without a significant decrease of accuracy for 3D large-scale modeling is a key problem of seismic modeling. The finite-difference (FD) method has been regarded as one of the most popular wave modeling methods for its easy implementation and high-computational efficiency (Antunes et al., 2014; Abreu et al., 2015; Xu and Gao, 2018; Robertsson and Blanch, 2020). However, the numerical dispersion of the traditional FD method leads to the use of fine grids or high-order operators (Dablain, 1986; Liu and Sen, 2011b), which inevitably affects the efficiency of simulation.

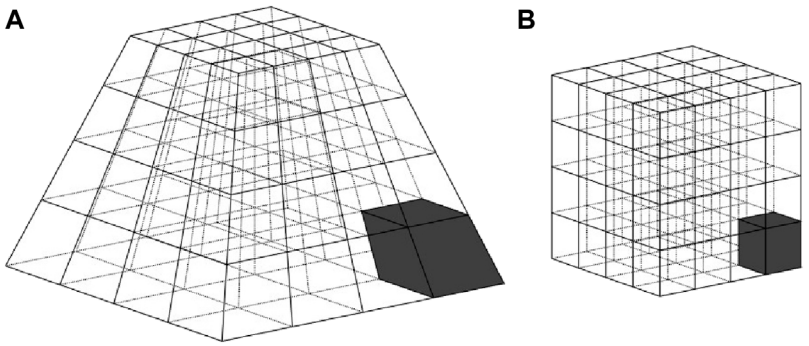

FIGURE 1 | Schematic of the 3D trapezoid coordinate transformation: **(A)** the trapezoid-grid mesh in the Cartesian coordinate system; **(B)** the uniform grid mesh in the transformed trapezoid coordinate system. The two gray regions in A and B represent the same physical region.

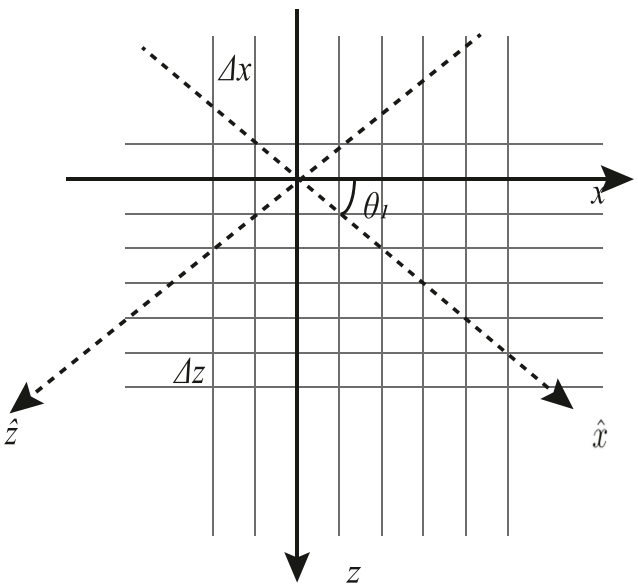

FIGURE 2 | Schematic of the rotation transformation in the trapezoid coordinate system for transforming mixed spatial derivatives into non-mixed spatial derivatives.

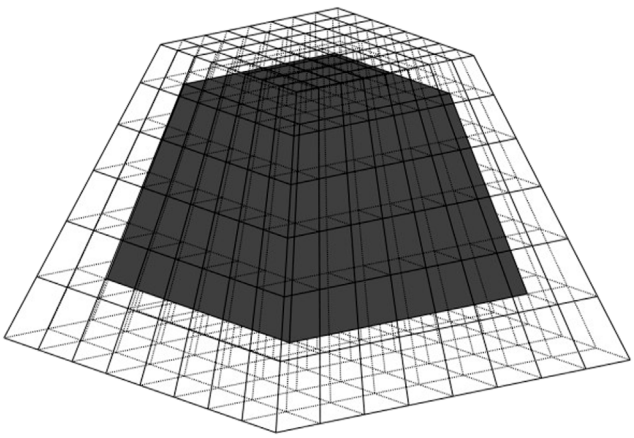

FIGURE 3 | Schematic of the grid discretization in the 3D trapezoid-grid CPML area.

The conventional FD method literally adopts a weighted summation of neighboring grid points' values to estimate the derivative for a designated grid point (Zhou et al., 2021), where the grid size (h) is fixed and the FD coefficients are calculated by Taylor expansion. In this way, the approximation error ϵ can be expressed as (Liu and Sen, 2011a; Wu et al., 2019b) follows:

$$\epsilon = O\left(\frac{hf}{v}\right)^{2M}, \tag{1}$$

where $2M$ is the length of the FD operator, h is the spatial interval, f is the frequency, and v is the seismic wave velocity. Considering that $\lambda = v/f$ is the wavelength and $G = \lambda/h$ is the number of grid points per wavelength (NPPW), we can rewrite **Eq. 1** as follows:

$$\epsilon = O\left(\frac{h}{\lambda}\right)^{2M} = O\left(\frac{1}{G}\right)^{2M}. \tag{2}$$

Eq. 2 indicates that the modeling accuracy of the conventional FD method is proportional to G and M. Because the seismic wave velocity is varying in different positions, the wavelength is short in low-velocity regions and long in high-velocity regions (Liu, 2020). Therefore, a part of computing resources is wasted in the high-velocity regions for the fixed spatial interval and FD order. With respect to this problem, there are two kinds of techniques corresponding to the different understanding of **Eq. 2**. The first one is the variable-operator FD method (Liu and Sen, 2011a), which adopts the long and short FD stencils in the low- and high-velocity region, respectively. For the scheme in Liu and Sen (2011a), the variable-length FD stencils are designed by approaching the dispersion relation in the time–space domain, and Liu (2020) subsequently optimizes their FD coefficients.

The second one is the variable-grid FD method, which adopts different gird sizes in different regions and can efficiently reduce the oversampling in the high-velocity region. The key problem of

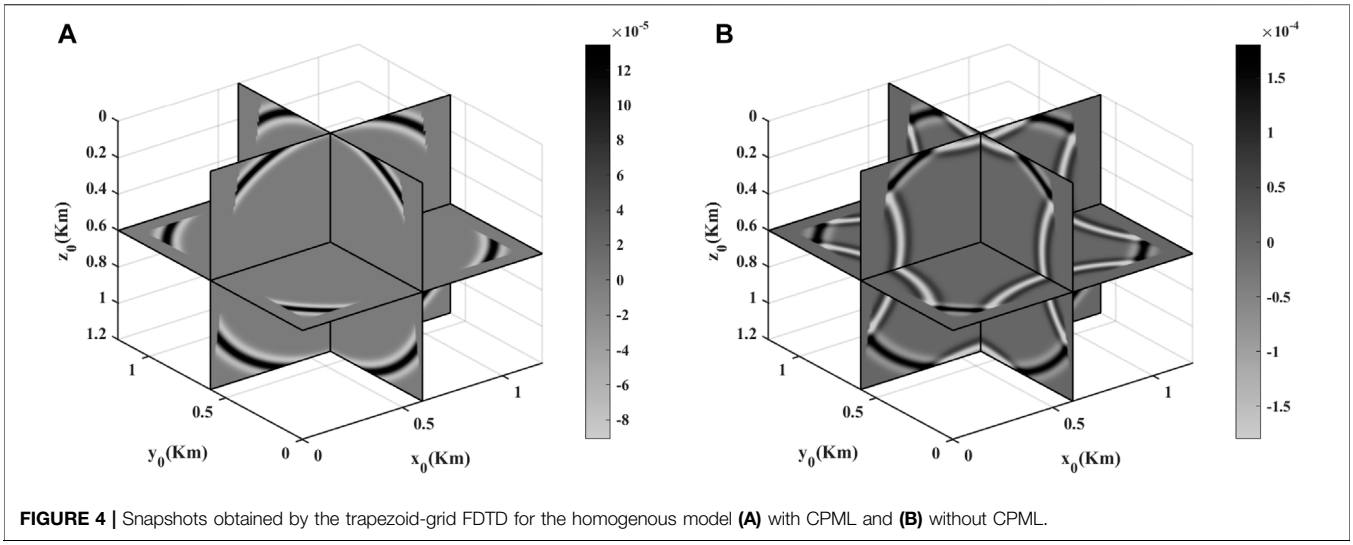

FIGURE 4 | Snapshots obtained by the trapezoid-grid FDTD for the homogenous model **(A)** with CPML and **(B)** without CPML.

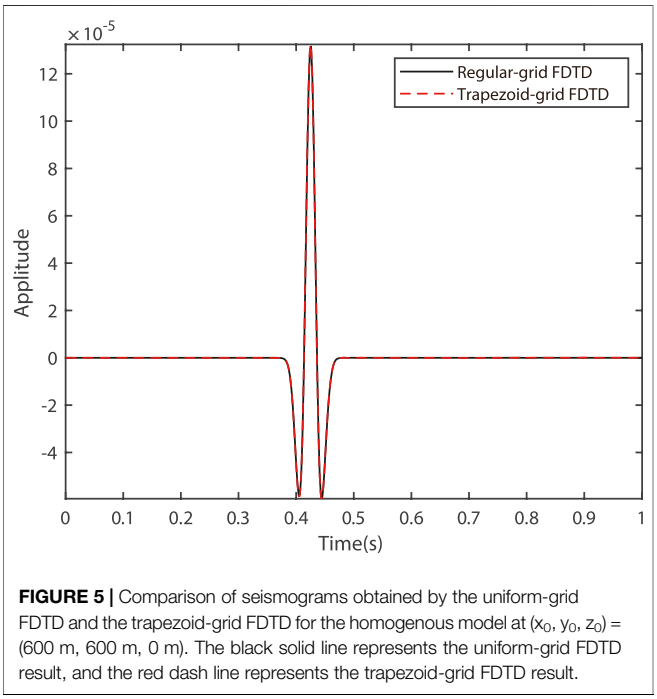

FIGURE 5 | Comparison of seismograms obtained by the uniform-grid FDTD and the trapezoid-grid FDTD for the homogenous model at (x_0, y_0, z_0) = (600 m, 600 m, 0 m). The black solid line represents the uniform-grid FDTD result, and the red dash line represents the trapezoid-grid FDTD result.

the variable-grid FD method is the processing of the transition area between the fine grids and the coarse grids. The variable-grid FD method based on interpolation (Hayashi and Burns, 2005; Pasalic and McGarry, 2010) is the easiest one, in which the lacking information in the transition area is completed by interpolation. However, the resulting artificial reflection in the transition area and the possible instability make it inefficient for high-accuracy seismic wave simulation. Another variable-grid FD method adopts irregular FD coefficients to process the transition region (Huang and Dong, 2009; Liu et al., 2014), which can significantly avoid the artificial reflection and improve the stability. The disadvantage of this type of variable-grid method is the additional computing cost brought by calculating irregular FD coefficients.

The trapezoid-grid FD method (Chen and Xu, 2012; Gao et al., 2018; Wu et al., 2018, Wu et al., 2019a, Wu et al., 2019b) is one of the practical variable-grid methods. It uses the trapezoid-grid mesh to fit the trend of velocity increasing with depth, which can effectively reduce the number of required grid points. Meanwhile, the use of trapezoid coordinate transformation can avoid the difficulty of processing ununiform grids in the physical Cartesian coordinate system. On the other hand, the significant reduction of memory requirement of trapezoid-grid FDTD can improve the easy implementation of GPU calculation (Fujii et al., 2013; Li et al., 2016). The existing research on trapezoid-grid FDTD methods mainly focuses on 2D wavefield modeling. Therefore, it is essential to expand trapezoid-grid FDTD from 2D to 3D for realistic seismic exploration research.

In this article, we propose a 3D trapezoid-grid FDTD method for acoustic wave modeling. First, we design the 3D trapezoid coordinate transformation and derive the 3D acoustic equation in the trapezoid coordinate system. Second, to reduce the artificial boundary reflection (Ma et al., 2018, Ma et al., 2019), we apply the corresponding trapezoid-grid convolutional perfectly matched layer (CPML) absorbing boundary condition. Third, stability analysis is given to generate stable modeling results. We then test our proposed method on the 3D homogenous model and the SEG/EAGE overthrust model and compare the efficiency and accuracy of the trapezoid-grid FDTD method with the uniform-grid FDTD method. Finally, conclusions are shown in the last section.

2 METHODS

2.1 3D Trapezoid Coordinate System

In this article, the 3D trapezoid coordinate transformation is defined as

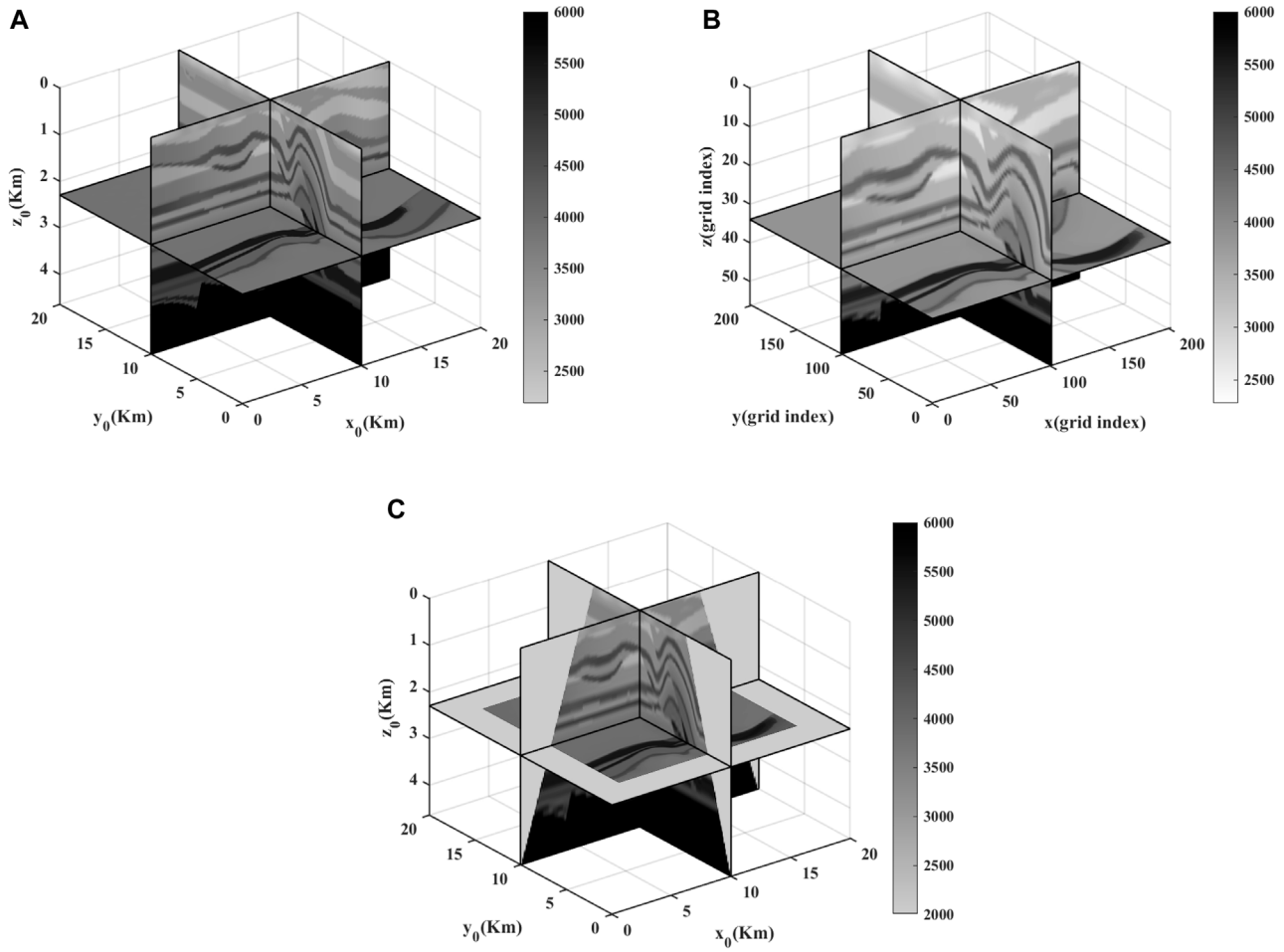

FIGURE 6 | (A) SEG/EAGE overthrust model; **(B)** SEG/EAGE overthrust model in the trapezoid coordinate system; **(C)** actual simulating area for the trapezoid-grid FDTD in the Cartesian coordinate system.

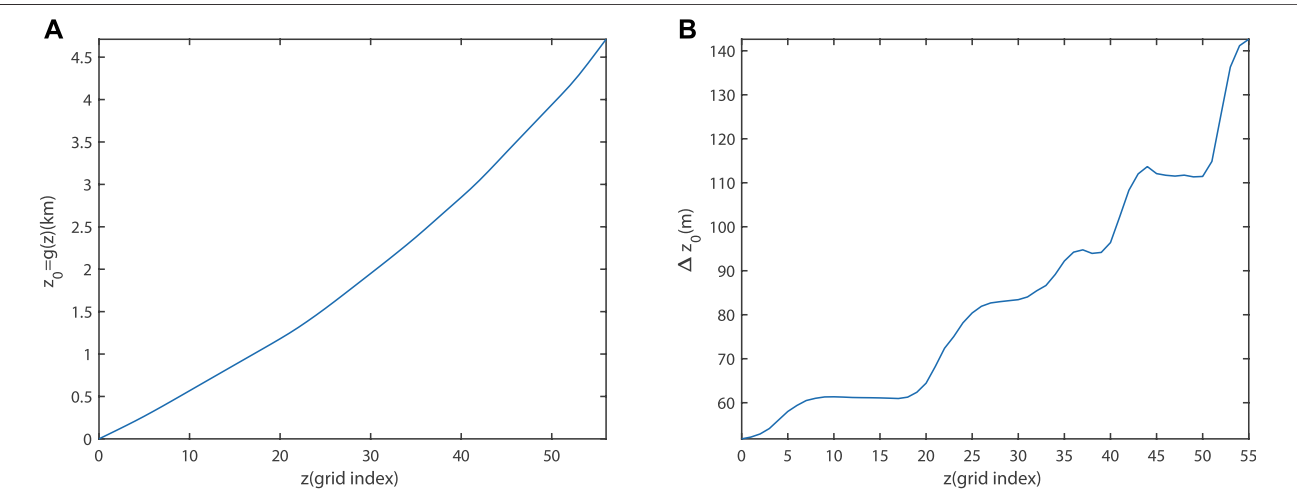

FIGURE 7 | (A) Vertical sampling function g(z); **(B)** variation of Δz_0 for the trapezoid-grid FDTD.

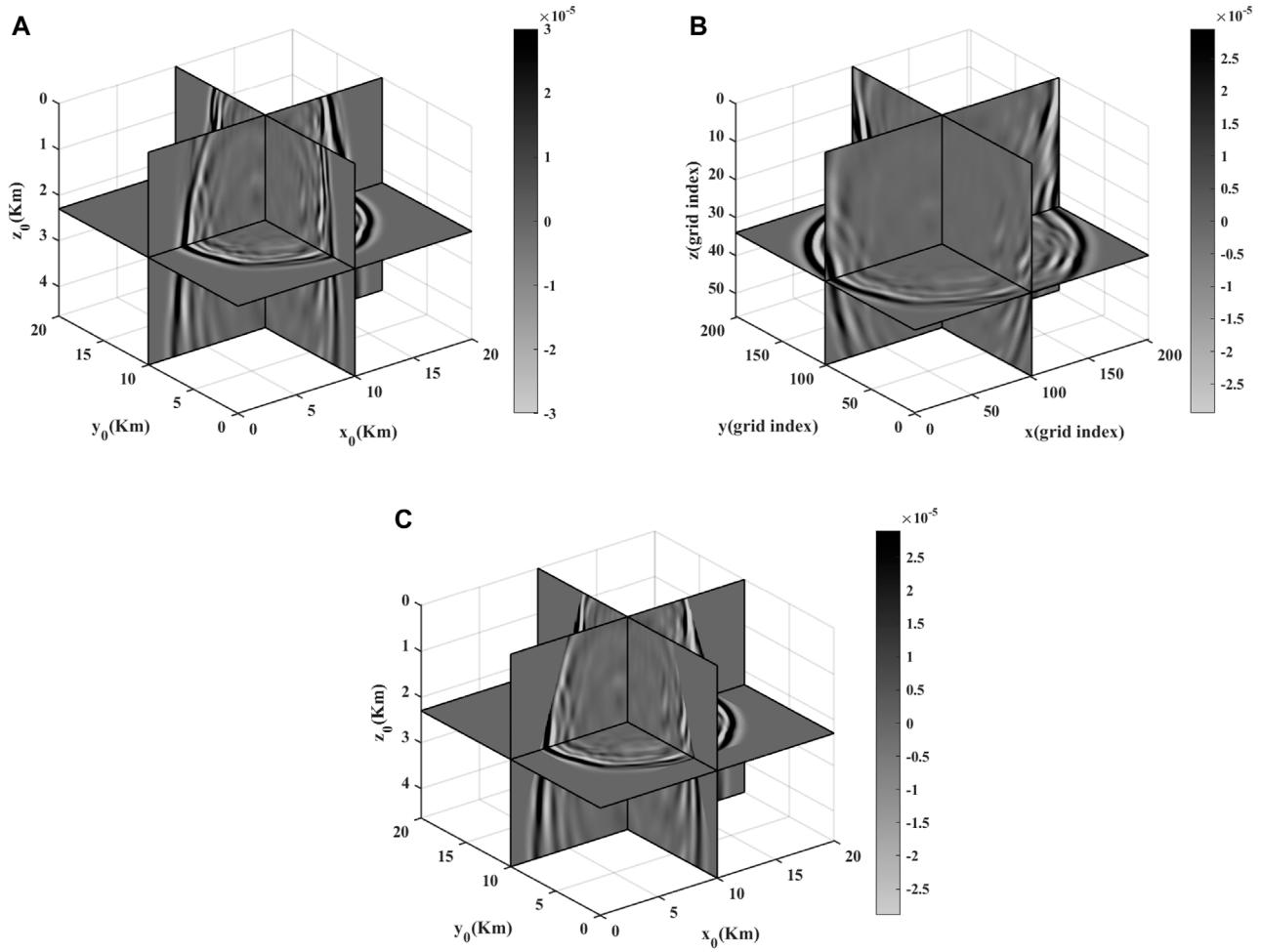

FIGURE 8 | Snapshots for the SEG/EAGE overthrust model at 2.5 s: **(A)** uniform-grid FDTD result; **(B)** trapezoid-grid FDTD result in the trapezoid coordinate system; **(C)** trapezoid-grid FDTD result in the Cartesian coordinate system.

$$x = \frac{x_0 - \alpha}{1 + \gamma z_0}; \tag{3a}$$

$$y = \frac{y_0 - \beta}{1 + \gamma z_0}; \tag{3b}$$

$$z_0 = g(z), \tag{3c}$$

where (x_0, y_0, z_0) is the Cartesian coordinate system, and (x, y, z) is the defined trapezoid coordinate system. In **Eq. 3**, α and β are central horizontal positions of the 3D trapezoid mesh, and γ is the scaling parameter for lateral coordinates. The velocity-related function $g(z)$ is the sampling function for z_0-axis, which should be first- and second-order continuous for deriving 3D wave equations in the trapezoid coordinate system. The discrete points of $g(z)$ are given by the following recursion:

$$g(0) = 0; \tag{4a}$$

$$g(z + \Delta z) = g(z) + \frac{v_{min}(g(z))}{f_0 N_0}, \tag{4b}$$

where f_0 is the dominant frequency of the source term, N_0 is the preferred NPPW and is related to the accuracy of the adopted FD scheme, and $v_{\min}(g(z))$ is the selected minimum velocity at depth $g(z)$ in the physical Cartesian coordinate system and is smoothed by solving a local polynomial fitting problem with the constraint that $v_{\min}(g(z))$ should not be greater than the model minimum velocity at depth $g(z)$. The central value of each local polynomial corresponds to a value of $v_{\min}(g(z))$. In particular, we usually set the order of the local polynomial as three. Such $v_{\min}(g(z))$ can lead to a smooth sampling function $g(z)$ for discontinuous velocity variation while satisfying the required number of points per wavelength in the z_0-direction.

If the grid sizes for the trapezoid-grid FDTD in the trapezoid coordinate system are defined as Δx, Δy, and Δz, then the corresponding grid sizes in the physical Cartesian system can be described as

$$\Delta x_0(z) = (1 + \gamma g(z))\Delta x; \tag{5a}$$

$$\Delta y_0(z) = (1 + \gamma g(z))\Delta y; \tag{5b}$$

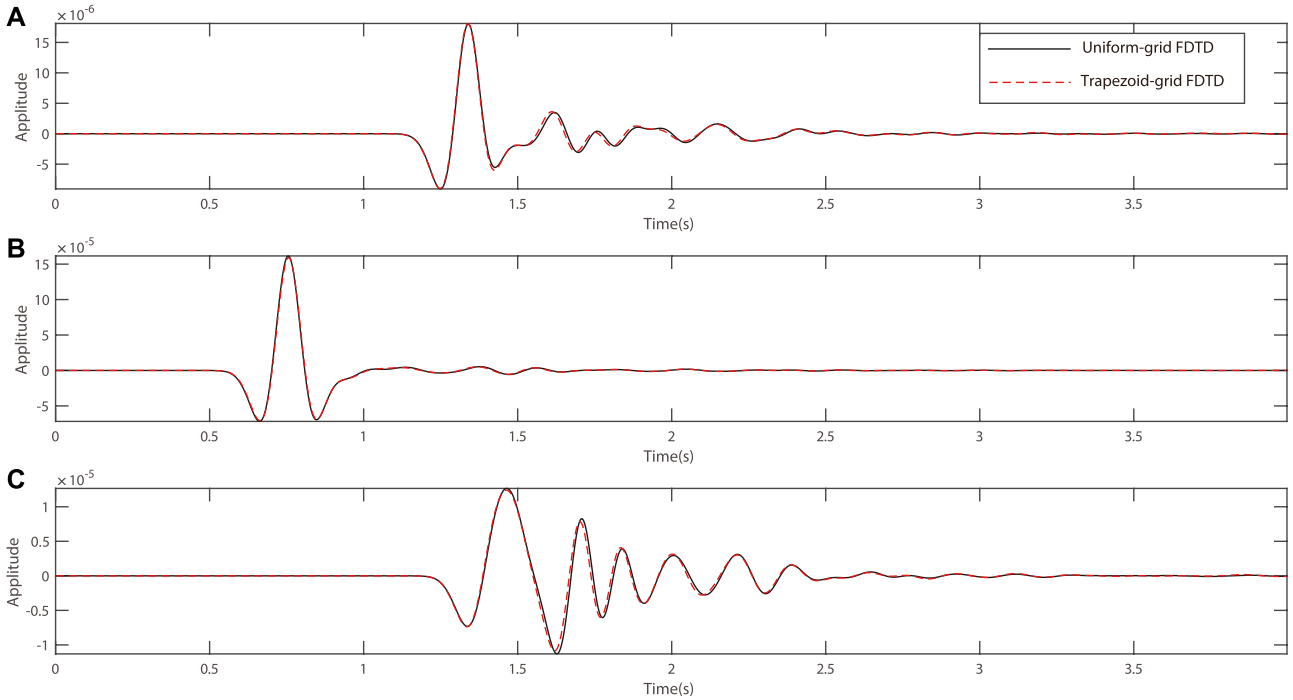

FIGURE 9 | Single-trace seismograms for the SEG/EAGE overthrust model at the receiver position of **(A)** (7.5, 10, 0 km); **(B)** (10, 10, 0 km); and **(C)** (12.5, 10, 0 km). The black solid lines represent the uniform-grid FDTD results, and the red dash lines represent the trapezoid-grid FDTD results.

$$\Delta z_0(z) = \frac{v_{min}(g(z))}{f_0 N_0}. \tag{5c}$$

In our work, γ and $g(z)$ are determined adaptively according to the model velocity. By selecting γ such that $\Delta x_0(z)$ and $\Delta y_0(z)$ are always smaller than or equal to $\Delta z_0(z)$, and a variable-grid mesh adaptive to the velocity model can be achieved in the physical Cartesian coordinate system. **Figure 1** shows the schematic of the 3D trapezoid coordinate transform. **Figure 1A** shows the trapezoid-grid mesh in the Cartesian coordinate system, while **Figure 1B** shows the corresponding uniform grid mesh in the transformed trapezoid coordinate system. In particular, the two gray regions in **Figure 1** represent the same physical region.

2.2 3D Acoustic Equation with CPML Absorbing Boundary Condition in the Trapezoid Coordinate System

According to the theory of Pasalic and McGarry (2010), the time-domain-discretization form of the 3D isotropic acoustic equation with the CPML absorbing boundary condition in the Cartesian coordinate system can be described as

$$\begin{aligned}&\frac{1}{v^2}\frac{u^{j+1}-2u^j+u^{j-1}}{\Delta t^2}-\frac{\partial^2 u^j}{\partial x_0^2}-\frac{\partial^2 u^j}{\partial y_0^2}-\frac{\partial^2 u^j}{\partial z_0^2}-\frac{\partial \psi_{x_0}^j}{\partial x_0}-\frac{\partial \psi_{y_0}^j}{\partial y_0}-\frac{\partial \psi_{z_0}^j}{\partial z_0}\\&-\zeta_{x_0}^j-\zeta_{y_0}^j-\zeta_{z_0}^j\\&=f\left(t_j\right)\delta(x_0-x_0^s)\delta(y_0-y_0^s)\delta(z_0-z_0^s);\end{aligned} \tag{6a}$$

$$\psi_{\tau_0}^{j+1} = a_{\tau_0}\psi_{\tau_0}^j + b_{\tau_0}\frac{\partial u^{j+1}}{\partial \tau_0}; \tag{6b}$$

$$\zeta_{\tau_0}^{j+1} = a_{\tau_0}\zeta_{\tau_0}^j + b_{\tau_0}\left(\frac{\partial^2 u^{j+1}}{\partial \tau_0^2}+\frac{\partial \psi_{\tau_0}^{j+1}}{\partial \tau_0}\right); \tag{6c}$$

$$a_{\tau_0} = e^{-\left(\sigma_{\tau_0}+\alpha_{\tau_0}\right)\Delta t}; \tag{6d}$$

$$b_{\tau_0} = \frac{\sigma_{\tau_0}}{\sigma_{\tau_0}+\alpha_{\tau_0}}\left(a_{\tau_0}-1\right), \tau_0 \in \{x_0, y_0, z_0\}, \tag{6e}$$

where $u^j = u(x_0, y_0, z_0, t_j)$ represents the scalar wavefield at the jth time step in the Cartesian coordinate system; v is the velocity; Δt is the time interval; $f(t)$ is the source term; (x_0^s, y_0^s, z_0^s) is the position of source; $\sigma_{\tau_0} = \frac{3v^{max}}{2L_{\tau_0}}\left(\frac{\bar{\tau}_0}{L_{\tau_0}}\right)^2 \ln\frac{1}{R}$, where R denotes the designated theoretical boundary reflection coefficient, $v^{\max}$ is the maximum velocity of the model, L_{τ_0} is the thickness of CPML absorbing boundary along the τ_0 direction, and $\bar{\tau}_0$ denotes the distance to the inner area in the τ_0 direction; $\alpha_{\tau_0} = \alpha^{max}\left(1-\frac{\bar{\tau}_0}{L_{\tau_0}}\right)$ and $\alpha^{\max} = \pi f_0$.

In order to derive the acoustic equation in the trapezoid coordinate system, we first need to transform the derivatives in the Cartesian coordinate system into the derivatives in the trapezoid coordinate system. Based on the definition of the trapezoid coordinate system in **Eq. 3** and the derivation rule of the composite function, the relationships of first- and second-order derivatives in the two coordinate systems can be given as

$$\frac{\partial}{\partial x_0} = \frac{1}{1+\gamma g(z)}\frac{\partial}{\partial x}; \tag{7a}$$

$$\frac{\partial}{\partial y_0} = \frac{1}{1+\gamma g(z)}\frac{\partial}{\partial y}; \tag{7b}$$

$$\frac{\partial}{\partial z_0} = -\frac{\gamma x}{1+\gamma g(z)}\frac{\partial}{\partial x} - \frac{\gamma y}{1+\gamma g(z)}\frac{\partial}{\partial y} + \frac{1}{g'(z)}\frac{\partial}{\partial z}; \tag{7c}$$

$$\frac{\partial^2}{\partial x_0^2} = \frac{1}{\left[1+\gamma g(z)\right]^2}\frac{\partial^2}{\partial x^2}; \tag{7d}$$

$$\frac{\partial^2}{\partial y_0^2} = \frac{1}{\left[1+\gamma g(z)\right]^2}\frac{\partial^2}{\partial y^2}; \tag{7e}$$

$$\begin{aligned}\frac{\partial^2}{\partial z_0^2} = {} & \frac{2\gamma^2 x}{\left[1+\gamma g(z)\right]^2}\frac{\partial}{\partial x} + \frac{\gamma^2 x^2}{\left[1+\gamma g(z)\right]^2}\frac{\partial^2}{\partial x^2} + \frac{2\gamma^{2xy}}{\left[1+\gamma g(z)\right]^2}\frac{\partial^2}{\partial x\partial y} \\ & - \frac{2\gamma x}{\left[1+\gamma g(z)\right]g'(z)}\frac{\partial^2}{\partial x\partial z} + \frac{2\gamma^2 y}{\left[1+\gamma g(z)\right]^2}\frac{\partial}{\partial y} \\ & + \frac{\gamma^2 y^2}{\left[1+\gamma g(z)\right]^2}\frac{\partial^2}{\partial y^2} - \frac{2\gamma y}{\left[1+\gamma g(z)\right]g'(z)}\frac{\partial^2}{\partial y\partial z} \\ & - \frac{g''(z)}{\left[g'(z)\right]^3}\frac{\partial}{\partial z} + \frac{1}{\left[g'(z)\right]^2}\frac{\partial^2}{\partial z^2}.\end{aligned} \tag{7f}$$

Since the mixed spatial derivatives in **Eq. 7f** are hard to discrete directly with the FD method, to transform the mixed spatial derivatives into non-mixed spatial derivatives, we define three rotation transformations in the trapezoid coordinate system as

$$\begin{bmatrix} x \\ z \end{bmatrix} = \begin{bmatrix} cos\theta_1 & -sin\theta_1 \\ sin\theta_1 & cos\theta_1 \end{bmatrix}\begin{bmatrix} \hat{x} \\ \hat{z} \end{bmatrix}; \tag{8a}$$

$$\begin{bmatrix} y \\ z \end{bmatrix} = \begin{bmatrix} cos\theta_2 & -sin\theta_2 \\ sin\theta_2 & cos\theta_2 \end{bmatrix}\begin{bmatrix} \tilde{y} \\ \tilde{z} \end{bmatrix}; \tag{8b}$$

$$\begin{bmatrix} x \\ y \end{bmatrix} = \begin{bmatrix} cos\theta_3 & -sin\theta_3 \\ sin\theta_3 & cos\theta_3 \end{bmatrix}\begin{bmatrix} \bar{x} \\ \bar{y} \end{bmatrix}, \tag{8c}$$

where $\hat{x}$ and $\hat{z}$ are axes along diagonals in the (x, z) planes, $\tilde{y}$ and $\tilde{z}$ are axes along diagonals in the (y, z) planes, and $\bar{x}$ and $\bar{y}$ are axes along diagonals in the (x, y) planes. θ_1 is the angle between x and $\hat{x}$ axes, θ_2 is the angle between y and $\tilde{y}$ axes, and θ_3 is the angle between x and $\bar{x}$ axes. A schematic of the coordinate transform in **Eq. 8a** is shown in **Figure 2**.

By using **Eqs. 8a–c**, the mixed spatial derivatives in **Eq. 7f** can be transformed as

$$\frac{\partial^2}{\partial x\partial z} = \frac{1}{2sin(2\theta_1)}\left(\frac{\partial^2}{\partial \hat{x}^2} - \frac{\partial^2}{\partial \hat{z}^2}\right); \tag{9a}$$

$$\frac{\partial^2}{\partial y\partial z} = \frac{1}{2sin(2\theta_2)}\left(\frac{\partial^2}{\partial \tilde{y}^2} - \frac{\partial^2}{\partial \tilde{z}^2}\right); \tag{9b}$$

$$\frac{\partial^2}{\partial x\partial y} = \frac{1}{2sin(2\theta_3)}\left(\frac{\partial^2}{\partial \bar{x}^2} - \frac{\partial^2}{\partial \bar{y}^2}\right). \tag{9c}$$

For simplicity, we usually use equal grid sizes in the trapezoid coordinate system ($\Delta x = \Delta y = \Delta z = \Delta$), which means $\theta_1 = \theta_2 = \theta_3 = \frac{\pi}{4}$. By substituting **Eq. 7** and **Eq. 9** into **Eq. 6**, we get the time-domain-discretization form of the 3D acoustic equation with the CPML absorbing boundary condition in the trapezoid coordinate system as

$$\begin{aligned}&\frac{1}{v^2}\frac{u^{j+1}-2u^j+u^{j-1}}{\Delta t^2} - \frac{\gamma^2x^2+1}{\left[1+\gamma g(z)\right]^2}\frac{\partial^2 u^j}{\partial x^2} - \frac{\gamma^2y^2+1}{\left[1+\gamma g(z)\right]^2}\frac{\partial^2 u^j}{\partial y^2} \\ &- \frac{2\gamma^2 x}{\left[1+\gamma g(z)\right]^2}\frac{\partial u^j}{\partial x} - \frac{2\gamma^2 y}{\left[1+\gamma g(z)\right]^2}\frac{\partial u^j}{\partial y} \\ &+ \frac{\gamma x}{\left[1+\gamma g(z)\right]g'(z)}\left(\frac{\partial^2 u^j}{\partial \hat{x}^2} - \frac{\partial^2 u^j}{\partial \hat{z}^2}\right) \\ &+ \frac{\gamma y}{\left[1+\gamma g(z)\right]g'(z)}\left(\frac{\partial^2 u^j}{\partial \tilde{y}^2} - \frac{\partial^2 u^j}{\partial \tilde{z}^2}\right) \\ &- \frac{\gamma^2 xy}{\left[1+\gamma g(z)\right]^2}\left(\frac{\partial^2 u^j}{\partial \bar{x}^2} - \frac{\partial^2 u^j}{\partial \bar{y}^2}\right) + \frac{g''(z)}{\left[g'(z)\right]^3}\frac{\partial u^j}{\partial z} - \frac{1}{\left[g'(z)\right]^2}\frac{\partial^2 u^j}{\partial z^2} \\ &- \frac{1}{1+\gamma g(z)}\frac{\partial \psi_x^j}{\partial x} - \frac{1}{1+\gamma g(z)}\frac{\partial \psi_y^j}{\partial y} + \frac{\gamma x}{1+\gamma g(z)}\frac{\partial \psi_z^j}{\partial z} \\ &+ \frac{\gamma y}{1+\gamma g(z)}\frac{\partial \psi_z^j}{\partial y} - \frac{1}{g'(z)}\frac{\partial \psi_z^j}{\partial z} - \zeta_x^j - \zeta_y^j - \zeta_z^j \\ &= f\left(t_j\right)(x-x^s)(y-y^s)(z-z^s);\end{aligned} \tag{10a}$$

$$\psi_x^{j+1} = a_x\psi_x^j + b_x\frac{1}{1+\gamma g(z)}\frac{\partial u^{j+1}}{\partial x}; \tag{10b}$$

$$\psi_y^{j+1} = a_y\psi_y^j + b_y\frac{1}{1+\gamma g(z)}\frac{\partial u^{j+1}}{\partial y}; \tag{10c}$$

$$\psi_z^{j+1} = a_z\psi_z^j + b_z\left(-\frac{\gamma x}{1+\gamma g(z)}\frac{\partial u^{j+1}}{\partial x} - \frac{\gamma y}{1+\gamma g(z)}\frac{\partial u^{j+1}}{\partial y} + \frac{1}{g'(z)}\frac{\partial u^{j+1}}{\partial z}\right); \tag{10d}$$

$$\zeta_x^{j+1} = a_x\zeta_x^j + b_x\left(\frac{1}{\left[1+\gamma g(z)\right]^2}\frac{\partial^2 u^{j+1}}{\partial x^2} + \frac{1}{1+\gamma g(z)}\frac{\partial \psi_x^{j+1}}{\partial x}\right); \tag{10e}$$

$$\zeta_y^{j+1} = a_y\zeta_y^j + b_y\left(\frac{1}{\left[1+\gamma g(z)\right]^2}\frac{\partial^2 u^{j+1}}{\partial y^2} + \frac{1}{1+\gamma g(z)}\frac{\partial \psi_y^{j+1}}{\partial y}\right); \tag{10f}$$

$$\begin{aligned}\zeta_z^{j+1} = {} & a_z\zeta_z^j + b_z\left[\frac{\gamma^2x^2}{\left[1+\gamma g(z)\right]^2}\frac{\partial^2 u^{j+1}}{\partial x^2} + \frac{\gamma^2y^2}{\left[1+\gamma g(z)\right]^2}\frac{\partial^2 u^{j+1}}{\partial y^2}\right. \\ & + \frac{2\gamma^2 x}{\left[1+\gamma g(z)\right]^2}\frac{\partial u^{j+1}}{\partial x} + \frac{2\gamma^2 y}{\left[1+\gamma g(z)\right]^2}\frac{\partial u^{j+1}}{\partial y} \\ & - \frac{\gamma x}{\left[1+\gamma g(z)\right]g'(z)}\left(\frac{\partial^2 u^{j+1}}{\partial \hat{x}^2} - \frac{\partial^2 u^{j+1}}{\partial \hat{z}^2}\right) \\ & - \frac{\gamma y}{\left[1+\gamma g(z)\right]g'(z)}\left(\frac{\partial^2 u^{j+1}}{\partial \tilde{y}^2} - \frac{\partial^2 u^{j+1}}{\partial \tilde{z}^2}\right) \\ & + \frac{\gamma^2 xy}{\left[1+\gamma g(z)\right]^2}\left(\frac{\partial^2 u^{j+1}}{\partial \bar{x}^2} - \frac{\partial^2 u^{j+1}}{\partial \bar{y}^2}\right) \\ & - \frac{g''(z)}{\left[g'(z)\right]^3}\frac{\partial u^{j+1}}{\partial z} + \frac{1}{\left[g'(z)\right]^2}\frac{\partial^2 u^{j+1}}{\partial z^2} - \frac{\gamma x}{1+\gamma g(z)}\frac{\partial \psi_z^{j+1}}{\partial x} \\ & \left. - \frac{\gamma y}{1+\gamma g(z)}\frac{\partial \psi_z^{j+1}}{\partial y} + \frac{1}{g'(z)}\frac{\partial \psi_z^{j+1}}{\partial z}\right],\end{aligned} \tag{10g}$$

where $u^j = u(x, y, z, t_j)$ represents the scalar wavefield at the jth time step in the trapezoid coordinate system; (x^s, y^s, z^s) is the position of the source in the trapezoid coordinate system; $\sigma_\tau = \frac{3v^{max}}{2L_\tau}(\frac{\bar{\tau}}{L_\tau})^2 \ln\frac{1}{R}$, where L_τ is the thickness of CPML absorbing boundary along the τ direction, $\bar{\tau}$ denotes the distance to the inner area in the τ direction; and $\alpha_\tau = \alpha^{max}(1 - \frac{\bar{\tau}}{L_\tau})$, $\tau \in \{x, y, z\}$.

A schematic of the grid discretization in the 3D trapezoid-grid CPML area is shown in **Figure 3**. In this work, 30 and 20 absorbing boundary layers are usually used for the trapezoid-grid CPML area in the horizontal and vertical directions, respectively.

2.3 Stability Analysis

Stability condition is usually required for the FD scheme to give a stable time step. From **Eq. 10a**, we use a local frozen coefficients technique in each discrete point and can get the full-discretization form of the 3D trapezoid coordinate system acoustic equation without the CPML boundary condition and source function:

$$\begin{aligned}
&\frac{1}{v^2}\frac{u^{j+1}_{m,n,l} - 2u^j_{m,n,l} + u^{j-1}_{m,n,l}}{\Delta t^2} - \frac{\gamma^2 x_m^2 + 1}{[1+\gamma g(z_l)]^2}\frac{1}{\Delta^2}\sum_{p=1}^{N_x}\eta_p^x\left(u^j_{m-p,n,l} - 2u^j_{m,n,l} + u^j_{m+p,n,l}\right)\\
&- \frac{\gamma^2 y_n^2 + 1}{[1+\gamma g(z_l)]^2}\frac{1}{\Delta^2}\sum_{p=1}^{N_y}\eta_p^y\left(u^j_{m,n-p,l} - 2u^j_{m,n,l} + u^j_{m,n+p,l}\right)\\
&- \frac{2\gamma^2 x_m}{[1+\gamma g(z_l)]^2}\frac{1}{\Delta}\sum_{p=1}^{N_x}c_p^x\left(u^j_{m+p,n,l} - u^j_{m-p,n,l}\right)\\
&- \frac{2\gamma^2 y_n}{[1+\gamma g(z_l)]^2}\frac{1}{\Delta}\sum_{p=1}^{N_y}c_p^y\left(u^j_{m,n+p,l} - u^j_{m,n-p,l}\right)\\
&+ \frac{\gamma x_m}{[1+\gamma g(z_l)]g'(z_l)}\frac{1}{2\Delta^2}\sum_{p=1}^{N_{xz}}\eta_p^{xz}\left(u^j_{m-p,n,l-p} + u^j_{m+p,n,l+p} - u^j_{m-p,n,l+p} - u^j_{m+p,n,l-p}\right)\\
&+ \frac{\gamma y_n}{[1+\gamma g(z_l)]g'(z_l)}\frac{1}{2\Delta^2}\sum_{p=1}^{N_{yz}}\eta_p^{yz}\left(u^j_{m,n-p,l-p} + u^j_{m,n+p,l+p} - u^j_{m,n-p,l+p} - u^j_{m,n+p,l-p}\right)\\
&- \frac{\gamma^2 x_m y_n}{[1+\gamma g(z_l)]^2}\frac{1}{2\Delta^2}\sum_{p=1}^{N_{xy}}\eta_p^{xy}\left(u^j_{m-p,n-p,l} + u^j_{m+p,n+p,l} - u^j_{m-p,n+p,l} - u^j_{m+p,n-p,l}\right)\\
&+ \frac{g''(z_l)}{[g'(z_l)]^3}\frac{1}{\Delta}\sum_{p=1}^{N_z}c_p^z\left(u^j_{m,n,l+p} - u^j_{m,n,l-p}\right)\\
&- \frac{1}{[g'(z_l)]^2}\frac{1}{\Delta^2}\sum_{p=1}^{N_z}\eta_p^z\left(u^j_{m,n,l-p} - 2u^j_{m,n,l} + u^j_{m,n,l+p}\right)\\
&= 0,
\end{aligned} \tag{11}$$

where $u^j_{m,n,l}$ is the wavefield at (x_m, y_n, z_l, t_j), $x_m = x^0 + (m-1)\Delta x$, $y_n = y^0 + (n-1)\Delta y$, $z_l = z^0 + (l-1)\Delta z$, $t_j = t^0 + (j-1)\Delta t$, N_x, N_y, N_z, N_{xy}, N_{xz}, N_{yz} are half-of-spatial FD orders, η^x, η^y, η^z, η^{xy}, η^{xz}, η^{yz} are corresponding FD coefficients of the second-order derivative, and c^x, c^y, c^z, c^{xy}, c^{xz}, c^{yz} are corresponding FD coefficients of the first-order derivative.

To derive the stability condition, we use the plane wave solution that is defined as

$$u(x, y, z, t) = u_0^* e^{i\omega t - ik_x x - ik_y y - ik_z z}, \tag{12}$$

where u_0^* is the amplitude of the plane wave, i is the imaginary unit, ω is the angular frequency, and k_x, k_y, k_z are wavenumbers in the x-, y- and z-directions, respectively. Similar to stability analysis of Kosloff and Baysal (1982), by substituting **Eq. 12** into **Eq. 11** and only considering the maximum wavenumber, the stability condition of the 3D acoustic equation in the trapezoid coordinate system can be expressed as

$$\begin{aligned}
\Delta t < \frac{\Delta}{v^{max}}\max_{m,n,l}\Bigg(&\frac{\gamma^2 x_m^2 + 1}{[1+\gamma g(z_l)]^2}\sum_{p=1}^{N_x}mod(p,2)\eta_p^x\\
&+\frac{\gamma^2 y_n^2 + 1}{[1+\gamma g(z_l)]^2}\sum_{p=1}^{N_y}mod(p,2)\eta_p^y + \frac{1}{[g'(z_l)]^2}\sum_{p=1}^{N_z}mod(p,2)\eta_p^z\Bigg)^{-\frac{1}{2}},
\end{aligned} \tag{13}$$

where *mod* is the function for the getting remainder, and $\max_{m,n,l}$ represents the maximum value of the objective function at those discrete points (x_m, y_n, z_l).

3 NUMERICAL RESULTS

In the following numerical examples, **Eq. 10** is discretized by the eighth-order FD in the space, and conventional Taylor-expansion–based high-order FD coefficients (Dablain, 1986) are adopted.

3.1 Homogenous Model

First, we use a 3D homogenous model with a constant velocity of 2000 m/s to verify the effectiveness of our trapezoid-grid FDTD method and corresponding CPML absorbing boundary condition. A Ricker wavelet with a dominant frequency of 20 Hz is located at the center of the model as the source. The FD time step is taken as 1.6 ms. The scaling parameter γ is set as 2.78×10^{-4}, the sampling function $g(z) = z$, and the lateral grid sizes in the Cartesian coordinate system increase from 7.5 to 10 from top to bottom. **Figure 4A** shows the snapshot obtained by the trapezoid-grid FDTD with CPML at 0.45 s, while **Figure 4B** shows the corresponding snapshot without CPML. **Figure 5** shows the comparison between the recorded seismograms computed by the uniform-grid FDTD and the trapezoid-grid FDTD at $(x_0, y_0, z_0) = (600, 600, 0$ m). The comparison between **Figures 4A,B** demonstrates that trapezoid-grid CPML can effectively reduce boundary reflections, while **Figure 5** demonstrates the accuracy of the trapezoid-grid FDTD method for the homogenous model.

3.2 Overthrust Model

Then, we apply our method to the SEG/EAGE overthrust model (**Figure 6A**), which is based on the real overthrusts of South America. **Figures 6B,C** show the modeling area of the SEG/EAGE overthrust model in the trapezoid coordinate system and the Cartesian coordinate system, respectively. A Ricker wavelet with the dominate frequency of 4.2 Hz is located at (10 km, 10 km, 0.5 km) as the source. The grid sizes for the uniform-grid FDTD are 50 m × 50 m × 50 m, which means the minimum NPPW in each direction is close to 10. We therefore set the minimum NPPW in x_0-, y_0-, and z_0-direction as 10 for the trapezoid-grid FDTD method, and get the scaling parameter as $\gamma = 2.07 \times 10^{-4}$.

Figure 7A shows the vertical sampling function $g(z)$ used for this model, and the vertical grid sizes in the Cartesian coordinate system increase from 51.8 m in the shallow region to a maximum value of 142.6 m in the deep region, as shown in **Figure 7B**. Based on the stability analysis, the time step for the trapezoid-grid FDTD and the uniform-grid FDTD are 3.697 and 3.585 ms, respectively. Receivers are located on the surface along y_0 = 10 km. **Figure 8A** shows the snapshot at 2.5 s computed by the uniform-grid FDTD, and **Figure 8B** is the snapshot at 2.5 s in the trapezoid coordinate system computed by our trapezoid-grid method. Using coordinate transformation and cubic spline interpolation, we can get the corresponding snapshot in the Cartesian coordinate system, as shown in **Figure 8C**. **Figures 8A,C** show good agreement. To give more detailed comparisons, single-trace seismograms at (7.5, 10, 0 km), (10, 10, 0 km), and (12.5, 10, 0 km) for both the uniform-grid (black solid line) and the trapezoid-grid (red dash line) FDTD are shown in **Figure 9**. **Figure 9** also shows good agreement between the uniform-gird FDTD and the trapezoid-grid FDTD. On our computing platform (Intel(R) Xeon(R) Sliver 4216 CPU @ 2.10GHz, 256GB of memory, and C++ codes), using 16-threads computation and similar code optimization techniques, the running time for the trapezoid-grid FDTD and the uniform-grid FDTD is calculated as 2203 s and 2925 s, respectively, which shows a calculation efficiency improvement of 24.7%. The memories for the trapezoid-grid FDTD and the uniform-grid FDTD are about 336 and 1213 MB, respectively, which shows a memory reduction of 72.3%. Considering that the simulation area of our trapezoid-grid method is almost 60% of that of the uniform-grid method, for the common simulation area, we can achieve about 50% reduction on memory usage.

4 CONCLUSION

In this article, we propose a 3D trapezoid-grid FDTD seismic wave modeling method based on the increasing trend of seismic wave velocity with depth. The trapezoid-grid mesh in the physical Cartesian system can effectively reduce the oversampling in the high-velocity region compared with the uniform-grid method, and the design of 3D trapezoid coordinate transform greatly avoids the difficulty of processing an irregular grid. We derive the 3D acoustic equation in the trapezoid coordinate system. The corresponding CPML boundary condition is also given to decrease artificial boundary reflection. To obtain a stable and efficient wave modeling result, we combine the plane wave theory and frozen coefficients technique and provide an effective stability condition for the 3D trapezoid-grid FDTD method. The discretization of the 3D acoustic equation in the trapezoid coordinate system is completed by the eighth order and second order finite-difference method in the space and time domain, respectively. The 3D homogenous model is given to verify the effectiveness of trapezoid-grid FDTD and the performance of the CPML boundary. Numerical tests on the SEG/EAGE overthrust model indicate the accuracy and the significant memory reduction of our method compared with uniform-grid FDTD. The key idea of our method is the combination of the trapezoid coordinate transformation and the FD stencils. Such idea can be generalized to many other wave equations such as elastic equation (Zhan et al., 2017) and Maxwell's equations (Zhan et al., 2021). Besides, our method is actually dealing with the regular grids in the trapezoid coordinate system, which means that we can combine other methods to treat the irregular surface (Li et al., 2020) or curved interfaces (Zhan et al., 2020).

DATA AVAILABILITY STATEMENT

The original contributions presented in the study are included in the article/Supplementary Material; further inquiries can be directed to the corresponding author.

AUTHOR CONTRIBUTIONS

BW contributed to the conception of the study. Writing, compiling, and debugging of the program were completed by WX. WT wrote the first draft of the manuscript, and all authors contributed to the revision.

FUNDING

We would like to thank the Natural Science Foundation of Shaanxi Province under Grant No. 2020JM-018 and National Natural Science Foundation (41974122) of China for funding this work.

REFERENCES

Abreu, R., Stich, D., and Morales, J. (2015). The Complex-Step-Finite-Difference Method. *Geophys. J. Int.* 202, 72–93. doi:10.1093/gji/ggv125

Antunes, A. J. M., Leal-Toledo, R. C. P., Filho, O. T. d. S., and Toledo, E. M. (2014). Finite Difference Method for Solving Acoustic Wave Equation Using Locally Adjustable Time-Steps. *Proced. Computer Sci.* 29, 627–636. doi:10.1016/j.procs.2014.05.056

Baysal, E., Kosloff, D. D., and Sherwood, J. W. C. (1983). Reverse Time Migration. *Geophysics* 48, 1514–1524. doi:10.1190/1.1441434

Cai, J., and Zhang, J. (2015). "Acoustic Full Waveform Inversion with Physical Model Data," in *2015 Workshop: Depth Model Building: Full-Waveform Inversion*. Beijing, China: Society of Exploration Geophysicists (SEG), 146–149. doi:10.1190/FWI2015-036

Chen, F., and Xu, S. (2012). "Pyramid-shaped Grid for Elastic Wave Propagation," in *SEG Technical Program Expanded Abstracts 2012* (Las Vegas: Society of Exploration Geophysicists (SEG)), 1–5. doi:10.1190/segam2012-0890.1

Dablain, M. A. (1986). The Application of High-order Differencing to the Scalar Wave Equation. *GEOPHYSICS* 51, 54–66. doi:10.1190/1.1442040

Du, Q., Zhang, X., Zhang, S., Zhang, F., and Fu, L.-Y. (2021). The Pseudo-laplace Filter for Vector-Based Elastic Reverse Time Migration. *Front. Earth Sci.* 9, 538. doi:10.3389/feart.2021.687835

Fujii, Y., Azumi, T., Nishio, N., Kato, S., and Edahiro, M. (2013). "Data Transfer Matters for Gpu Computing" in Proceeding of the 2013 International Conference on Parallel and Distributed Systems, Seoul, Korea (South), 15-18 Dec. 2013, (IEEE), 275–282. doi:10.1109/ICPADS.2013.47

Gao, J., Xu, W., Wu, B., Li, B., and Zhao, H. (2018). Trapezoid Grid Finite Difference Seismic Wavefield Simulation with Uniform Depth Sampling Interval. *Chin. J. Geophys.* 61, 3285–3296. doi:10.6038/cjg2018M0313

Hayashi, K., and Burns, D. R. (1999). "Variable Grid Finite-difference Modeling Including Surface Topography," in *SEG Technical Program Expanded Abstracts 1999* (Houston: Society of Exploration Geophysicists (SEG)), 528–531. doi:10.1190/1.1821071

Hong-Qiao, X., Xiao-Yi, W., Chen-Yuan, W., and Jiang-Jie, Z. (2021a). Sparse Constrained Least-Squares Reverse Time Migration Based on Kirchhoff Approximation. *Front. Earth Sci.* 9, 770. doi:10.3389/feart.2021.731697

Huang, C., and Dong, L.-G. (2009). Staggered-Grid High-Order Finite-Difference Method in Elastic Wave Simulation with Variable Grids and Local Time-Steps. *Chin. J. Geophys.* 52, 1324–1333. doi:10.1002/cjg2.1457

Jia, J., Wu, B., Peng, J., and Gao, J. (2019). Recursive Linearization Method for Inverse Medium Scattering Problems with Complex Mixture Gaussian Error Learning. *Inverse Probl.* 35, 075003. doi:10.1088/1361-6420/ab08f2

Jing, H., Yang, G., and Wang, J. (2019). An Optimized Time-Space-Domain Finite Difference Method with Piecewise Constant Interpolation Coefficients for Scalar Wave Propagation. *J. Geophys. Eng.* 16, 309–324. doi:10.1093/jge/gxz008

Kosloff, D. D., and Baysal, E. (1982). Forward Modeling by a Fourier Method. *GEOPHYSICS* 47, 1402–1412. doi:10.1190/1.1441288

Li, J., Tseng, H.-W., Lin, C., Papakonstantinou, Y., and Swanson, S. (2016). HippogriffDB. *Proc. VLDB Endow.* 9, 1647–1658. doi:10.14778/3007328.3007331

Li, X., Yao, G., Niu, F., and Wu, D. (2020). An Immersed Boundary Method with Iterative Symmetric Interpolation for Irregular Surface Topography in Seismic Wavefield Modelling. *J. Geophys. Eng.* 17, 643–660. doi:10.1093/jge/gxaa019

Liu, S., Yan, Z., Zhu, W., Han, B., Gu, H., and Hu, S. (2021). An Illumination-compensated Gaussian Beam Migration for Enhancing Subsalt Imaging. *Geophys. Prospecting* 69, 1433–1440. doi:10.1111/1365-2478.13117

Liu, X., Yin, X., and Wu, G. (2014). Finite-difference Modeling with Variable Grid-Size and Adaptive Time-step in Porous media. *Earthq Sci.* 27, 169–178. doi:10.1007/s11589-013-0055-7

Liu, Y. (2020). Acoustic and Elastic Finite-Difference Modeling by Optimal Variable-Length Spatial Operators. *GEOPHYSICS* 85, T57–T70. doi:10.1190/geo2019-0145.1

Liu, Y., and Sen, M. K. (2011a). Finite-difference Modeling with Adaptive Variable-Length Spatial Operators. *GEOPHYSICS* 76, T79–T89. doi:10.1190/1.3587223

Liu, Y., and Sen, M. K. (2011b). Scalar Wave Equation Modeling with Time-Space Domain Dispersion-Relation-Based Staggered-Grid Finite-Difference Schemes. *Bull. Seismological Soc. America* 101, 141–159. doi:10.1785/0120100041

Ma, X., Yang, D., He, X., Huang, X., and Song, J. (2019). Nonsplit Complex-Frequency-Shifted Perfectly Matched Layer Combined with Symplectic Methods for Solving Second-Order Seismic Wave Equations - Part 2: Wavefield Simulations. *GEOPHYSICS* 84, T167–T179. doi:10.1190/geo2018-0349.1

Ma, X., Yang, D., Huang, X., and Zhou, Y. (2018). Nonsplit Complex-Frequency Shifted Perfectly Matched Layer Combined with Symplectic Methods for Solving Second-Order Seismic Wave Equations - Part 1: Method. *GEOPHYSICS* 83, T301–T311. doi:10.1190/geo2017-0603.1

Pasalic, D., and McGarry, R. (2010). "A Discontinuous Mesh Finite Difference Scheme for Acoustic Wave Equations," in *SEG Technical Program Expanded Abstracts 2010* (Denver: Society of Exploration Geophysicists (SEG)), 2940–2944. doi:10.1190/1.3513457

Qu, Y., Li, Z., Huang, J., Deng, W., and Li, J. (2015). "The Least-Squares Reverse Time Migration for Viscoacoustic Medium Based on a Stable Reverse-Time Propagator," in *SEG Technical Program Expanded Abstracts 2015*(New Orleans: Society of Exploration Geophysicists (SEG)), 3977–3980. doi:10.1190/segam2015-5835196.1

Robertsson, J. O. A., and Blanch, J. O. (2020). "Numerical Methods, Finite Difference," in *Encyclopedia of Solid Earth Geophysics*. Editor H. K. Gupta (Cham: Springer International Publishing), 1–9. doi:10.1007/978-3-030-10475-7_135-1

Tarantola, A. (1984). Inversion of Seismic Reflection Data in the Acoustic Approximation. *Geophysics* 49, 1259–1266. doi:10.1190/1.1441754

Virieux, J., and Operto, S. (2009). An Overview of Full-Waveform Inversion in Exploration Geophysics. *Geophysics* 74, WCC1–WCC26. doi:10.1190/1.3238367

Wu, B., Li, B., Yang, H., and Jia, J. (2019a). "Trapezoid Grid Finite Difference for Acoustic Wave Modeling," in *SEG 2018 Workshop: SEG Seismic Imaging Workshop*. Beijing, China: Society of Exploration Geophysicists (SEG), 52–55. 12–14 November 2018. doi:10.1190/SEIM2018-13.1

Wu, B., Xu, W., Jia, J., Li, B., Yang, H., Zhao, H., et al. (2018). "Convolutional Perfect-Matched Layer Boundary for Trapezoid Grid Finite-Difference Seismic Modeling," in *SEG Technical Program Expanded Abstracts 2018* (Anaheim: Society of Exploration Geophysicists (SEG)), 3989–3993. doi:10.1190/segam2018-2995754.1

Wu, B., Xu, W., Li, B., and Jia, J. (2019b). Trapezoid Coordinate Finite Difference Modeling of Acoustic Wave Propagation Using the CPML Boundary Condition. *J. Appl. Geophys.* 168, 101–106. doi:10.1016/j.jappgeo.2019.06.006

Xia, D.-m., Xie, C., Song, P., Tan, J., Li, J.-s., and Zhao, B. (2017). "A Time Domain Full Waveform Inversion Method Based on Well-Constrained Regularization," in *SEG 2017 Workshop: Full-Waveform Inversion and beyond*. Beijing, China: Society of Exploration Geophysicists (SEG), 136–139. 20-22 November 2017. doi:10.1190/FWI2017-036

Xu, W., and Gao, J. (2018). Adaptive 9-point Frequency-Domain Finite Difference Scheme for Wavefield Modeling of 2D Acoustic Wave Equation. *J. Geophys. Eng.* 15, 1432–1445. doi:10.1088/1742-2140/aab015

Xu, W., Zhong, Y., Wu, B., Gao, J., and Liu, Q. H. (2021b). Adaptive Complex Frequency with V-Cycle Gmres for Preconditioning 3D Helmholtz Equation. *GEOPHYSICS* 86, T349–T359. doi:10.1190/geo2020-0901.1

Xuan, K., Ying, S., Xuebao, G., and Shizhu, L. (2014). "Carbonate Reservoir Pre-stack Reverse-Time Migration and Gpu/cpu Heterogeneous Computing Research," in *Beijing 2014 International Geophysical Conference & Exposition*. Beijing, China: Society of Exploration Geophysicists (SEG), 21–24. *April 2014*. 1101–1104. doi:10.1190/IGCBeijing2014-279

Zhan, Q., Sun, Q., Ren, Q., Fang, Y., Wang, H., and Liu, Q. H. (2017). A Discontinuous Galerkin Method for Simulating the Effects of Arbitrary Discrete Fractures on Elastic Wave Propagation. *Geophys. J. Int.* 210, 1219–1230. doi:10.1093/gji/ggx233

Zhan, Q., Wang, Y., Fang, Y., Ren, Q., Yang, S., Yin, W.-Y., et al. (2021). An Adaptive High-Order Transient Algorithm to Solve Large-Scale Anisotropic Maxwell's Equations. *IEEE Trans. Antennas Propagat.*, 1. doi:10.1109/tap.2021.3111639

Zhan, Q., Zhuang, M., Mao, Y., and Liu, Q. H. (2020). Unified Riemann Solution for Multi-Physics Coupling: Anisotropic Poroelastic/elastic/fluid Interfaces. *J. Comput. Phys.* 402, 108961. doi:10.1016/j.jcp.2019.108961

Zhou, H., Liu, Y., and Wang, J. (2021). Optimizing Orthogonal-Octahedron Finite-Difference Scheme for 3D Acoustic Wave Modeling by Combination of taylor-series Expansion and Remez Exchange Method. *Exploration Geophys.* 52, 335–355. doi:10.1080/08123985.2020.1826890

Conflict of Interest: Authors BW, WT, and BL are employed by SINOPEC.

The remaining authors declare that the research was conducted in the absence of any commercial or financial relationships that could be construed as a potential conflict of interest.

Publisher's Note: All claims expressed in this article are solely those of the authors and do not necessarily represent those of their affiliated organizations, or those of the publisher, the editors, and the reviewers. Any product that may be evaluated in this article, or claim that may be made by its manufacturer, is not guaranteed or endorsed by the publisher.

frontiers in Earth Science

ORIGINAL RESEARCH
published: 18 January 2022
doi: 10.3389/feart.2021.771570

High-Resolution Imaging: An Approach by Compensating Absorption and Dispersion in Prestack Time Migration With Effective Q Estimation and Fresnel Zone Identification Based on Deep Learning

Jizhong Wu[1], Ying Shi[1], Aihua Guo[2], Pengfei Lu[2] and Qianqian Yang[1]*

[1]*Bohai Rim Energy Research Institute, Northeast Petroleum University, Daqing, China,* [2]*Institute of Computer Science, East China University of Technology, Nanchang, China*

OPEN ACCESS

Edited by:
Jianping Huang,
China University of Petroleum, Huadong, China

Reviewed by:
Anastasia Nekrasova,
Institute of Earthquake Prediction Theory and Mathematical Geophysics (RAS), Russia
Jiangjie Zhang,
Institute of Geology and Geophysics (CAS), China

****Correspondence:***
Jizhong Wu
wjzkgr@163.com

Specialty section:
This article was submitted to Solid Earth Geophysics, a section of the journal Frontiers in Earth Science

Received: *06 September 2021*
Accepted: *17 December 2021*
Published: *18 January 2022*

Citation:
Wu J, Shi Y, Guo A, Lu P and Yang Q (2022) High-Resolution Imaging: An Approach by Compensating Absorption and Dispersion in Prestack Time Migration With Effective Q Estimation and Fresnel Zone Identification Based on Deep Learning. Front. Earth Sci. 9:771570. doi: 10.3389/feart.2021.771570

We have developed a migration scheme that can compensate absorption and dispersion with effective *Q* estimation and Fresnel zone identification based on deep learning. We use the U-Net neural network technology in deep learning to automatically identify Fresnel zones from compensated migrated dip-angle gathers and obtain the optimal aperture for migration, avoiding the tedious task of manually modifying the boundaries of Fresnel zones. Instead of the interval *Q* factor, we used an effective *Q* parameter to compensate absorption and dispersion. The effective *Q* is estimated using VSP well data and surface seismic velocity data. The proposed scheme can be incorporated into conventional seismic data processing workflow. A field data set was employed to validate the proposed scheme. Higher resolution imaging results with low noise levels are obtained.

Keywords: Q, deep learning, high-resolution, attenuation, PSTM

1 INTRODUCTION

The dissipation of seismic energy is caused by the anelasticity of the subsurface medium, which will decrease the amplitude and modify the phase. In this dissipative medium, as the propagation distance of the seismic wave increases, the attenuation of the seismic wave becomes more serious. Therefore, seismic waves in deep and ultra-deep stratums face the problem of lower resolution due to dissipation. It is crucial to find an appropriate method to eliminate the absorption and dispersion effects of seismic waves for higher resolution. We commonly use the quality factor Q-related methods to compensate absorption and dispersion in seismic data processing, and most of them can be divided into two categories: one is the inverse Q filtering (Hargreaves and Calvert, 1991; Wang, 2002; Ferber, 2005; Cavalca et al., 2011; Chen et al., 2014; Zhang et al., 2014; Dai et al., 2018; Shi et al., 2019; Sangwan and Kumar, 2021), and the other is the anelastic prestack migration based on the viscoacoustic wave equation (Zhang and Wapenaar, 2002; Xie et al., 2009; Zhang et al., 2013; Guo et al., 2016; Wang et al., 2018; Zhang et al., 2021). In the first category, inverse Q filtering is based on the theory of 1-D wave backpropagation and cannot calculate the seismic wave propagation path accurately. In the second category, anelastic prestack depth migration (PSDM) utilizes the viscoacoustic wave equation to simulate wave propagation with dissipation in the wavefield extrapolation, which is a more accurate and consistent way; however, the calculation load is

huge, and the interval Q model is difficult to obtain. Because of the effectiveness of prestack time migration (PSTM) in imaging complex structures without strong velocity variations, various Q-compensated methods based on the PSTM structure have been developed (Zhang et al., 2013; Zhang et al., 2016; Wu et,al., 2019). These methods employ effective Q parameters, rather than the interval Q model used in the depth migration approach, and the estimation of an effective Q model is easier to achieve than that of an interval Q model.

An optimal migration aperture can improve the signal-to-noise ratio (S/N) of imaging results. Schleicher et al. (1997) pointed out that the Fresnel zone is an optimal migration aperture. The signal outside the Fresnel zone does not contribute to imaging but brings noise and artifacts, which reduces the quality of the imaging results (Chen 2004; Marfurt 2006; Klokov and Fomel 2012a; Yu et al., 2013). However, the low S/N of field data and underground complex structures make an accurate Fresnel zone estimation challenging. In recent years, some articles have realized the estimation of Fresnel zones in a simple domain, by constructing a migrated dip-angle gather in the time or depth domains (Zhang et al., 2016; Li et al., 2018; Cheng et al., 2020). Zhang et al. (2016) has applied conventional PSTM to generate migrated dip-angle gathers for Fresnel zone estimation during deabsorption of the PSTM process. Cheng et al. (2020) used a modified VGGNet (A convolutional neural network was developed by the University of Oxford's Visual Geometry Group and Google DeepMind in 2014) to extract Fresnel zones from migrated dip-angle gathers, which is a useful attempt at deep learning for Fresnel zone estimation. However, these Fresnel zone estimation methods are all suitable for dip-angle gathers generated by conventional migration methods, and little research has been carried out on that using compensated dip-angle gathers with a high resolution generated by compensated migration methods.

The quality factor Q is closely related to the rock properties of the formation, water saturation, seismic wave amplitude and frequency, and other factors; therefore, calculating the Q value accurately is very difficult. To meet the demand for Q in seismic data processing, many methods have been developed to estimate Q. The Q estimation method was initially proposed using a vertical seismic profile (VSP) (Tonn, 1991) and crosswell data (Neep et al., 1996). These methods can obtain a small amount of Q values because VSP and cross-well data are not always available in the field, and we prefer to estimate the Q value from surface reflection seismic data. A variety of methods have been proposed to estimate the Q value from surface seismic data, and most of them can be divided into two categories: one is the wavelet information–based method (Quan and Harris, 1997; Dasgupta and Clark, 1998; Zhang et al., 2013; Bettinelli Pet al., 2014), which is employed in the time or frequency domain (e.g., the frequency shift method and spectral-ratio method) and demonstrates good performance for estimation of the Q value, whereas often suffers from noise and wavelet interferences, and the other one is the tomography inversion–based method (Brzostowski and McMechan, 1992; Shen et al., 2018). In the first category, Zhang et al. (2013) estimated the Q value using surface seismic data by constant Q migration scanning; however, the implementation complexity of this method limits its broader application. In the second category, the widely used ray-based tomography can estimate the Q value for the dominant frequency with expensive calculation cost and local instability (Cavalca et al., 2011; Shen and Zhu, 2015; Dutta and Schuster, 2016). Full-waveform inversion (FWI) is another popular inversion approach using waveform rather than travel-time, but it requires an accurate initial model and burdens a huge computational expense (Kamei and Pratt, 2008).

This article takes the estimations of the optimal aperture and effective Q model as the research focus in the compensated PSTM, which is arranged as follows: first, we introduce a modified PSTM scheme with compensation based on the effective Q; second, we propose a Fresnel zone identification scheme based on compensated migrated dip-angle gathers using deep learning; third, we present an estimation approach of the effective Q model for the compensated PSTM. Finally, we demonstrate our scheme with a field data set.

2 PSTM WITH COMPENSATION BASED ON EFFECTIVE Q

By following Zhang et al. (2013), a modified PSTM with compensation based on the effective Q model is expressed as

$$I_Q(x,T) = \sum_{p=1}^{n} \Omega(x, T_S, T_0) \frac{\tau_s}{\tau_g} \int f_p(\omega) \sqrt{\omega} \exp\left(-\frac{i\pi}{4}\right) \exp\left[\mathrm{i}\omega\left(\tau_s + \tau_g\right)\left(1 - \frac{1}{\pi Q_{eff}} \ln \frac{\omega}{\omega_0}\right)\right] \exp\left[\frac{\omega\left(\tau_s + \tau_g\right)}{2Q_{eff}}\right] \mathrm{d}\omega, \quad (1)$$

where $f_p(\omega)$ is the Fourier transform of the p$^{\text{th}}$ prestack trace, τ_s and τ_g represent the travel times from the shot and receiver to the imaging point, respectively, T_0 is the two-way vertical travel time, $\Omega(x, T_S, T_0)$ represents the whole migration aperture, T_s represents the starting travel time of the migration aperture, and Q_{eff} is the effective Q parameter. **Eq. 1** denotes a compensated migration impulse response of a seismic trace. Summation of the impulse responses of all seismic traces yields a compensated migration result. The two Q_{eff}-related terms in **Eq. 1** are the frequency-dependent dispersion and amplitude attenuation correction terms, respectively, which are different from the conventional PSTM. In **Eq. 1**, the size of the migration aperture has an important influence on the signal-to-noise ratio of the imaging result, and the accuracy of effective Q determines the quality of the compensation result. In view of these two aspects, this article proposes a method of using deep learning to pick up the optimal aperture and a method of quickly obtaining the effective Q model using VSP data and seismic velocity data. These two methods, together with the modified PSTM with compensation, form a seismic data imaging workflow that is specifically used for high-resolution imaging of prestack seismic data.

3 IDENTIFICATION OF FRESNEL ZONES USING DEEP LEARNING

Three separate sections are considered to introduce the theory of deep learning–based automated Fresnel zone extraction. The first section makes a review of migrated dip-angle gathers.

The second section introduces the architecture of the deep neural network adopted, including the design of U-Net input and output patterns and different types of layers in the network. The final section gives the loss function and training details in seeking optimal weights and biases of the network.

3.1 Review of Migrated Dip-Angle Gathers

Summing the migrated traces within Fresnel zones can produce a high S/N imaging profile. The migrated dip-angle gather supplies a simple domain that makes a visual pickup of Fresnel zones possible, which are constructed by sorting and summing the migrated results in the time or depth domains according to the dip angle (Zhang et al., 2016; Cheng et al., 2020). Different from the conventional migrated dip-angle gather, the compensated migrated dip-angle gather has the characteristics of high resolution and thin events. Therefore, the label data and training parameters of the trained network for conventional migrated dip-angle gathers must be relabeled and trained respectively when the neural network is applied to identify Fresnel zones using compensated migrated dip-angle gathers. In the next section, we will discuss how to use compensated dip-angle gathers to determine Fresnel zones of 2D seismic data. **Figure 1** shows the geometrical relationship about the dip angle (Zhang et al., 2016). The angle can be expressed as follows:

$$\tan\theta = \left[(x_s - x)\tau_g + \left(x_g - x\right)\tau_s\right] \Big/ \left[TV_{rms}\left(\tau_s + \tau_g\right)\right], \qquad (2)$$

where θ denotes the dip-angle related to travel time at the imaging point I; V_{rms} is the root mean-square velocity at the imaging point; τ_s and τ_g represent the travel times from the shot (x_s) and receiver (x_g) to the imaging point I, respectively; and T represents the one-way vertical travel time. We obtained a 1D dip-angle gather by summing the migrated traces with dip angles (θ) over the 2D imaging result. This process can be expressed as

$$I(x, T, \theta) = \sum_{i=1}^{n} N \frac{\tau_s^2}{\tau_g^2} \tilde{f}_i\left(\tau_s + \tau_g, x_s, x_g\right) \lambda_i\left(\tau_s + \tau_g, Q\right), \qquad (3)$$

where n denotes the number of seismic traces, $\tilde{f}_i$ denotes a half-derivative of the i^{th} prestack seismic trace, and λ_i is the corresponding compensation factor.

The dip-angle gather shows a curved reflected event (Klokov and Fomel 2012b), and its vertex is the stationary-phase point (Cheng et al., 2020). The Fresnel zone is within half a wavelength near the stationary-phase point. Since the Fresnel zone is easy to identify in the dip-angle gather, we can pick it up through the dip-angle gather and obtain a high S/N migrated result by summing the Fresnel zones, but in practice, estimating Fresnel zones through dip-angle gathers will become challenging because dip-angle gathers will become correspondingly more complicated due to the low S/N of field data and underground complex structures, especially for imaging results with compensating absorption and dispersion since their dip-angle gathers differ in S/N and resolution from those generated by conventional migration, which add additional complexity. Many manual modifications to the Fresnel zone boundaries are required, which is a time-consuming and difficult task.

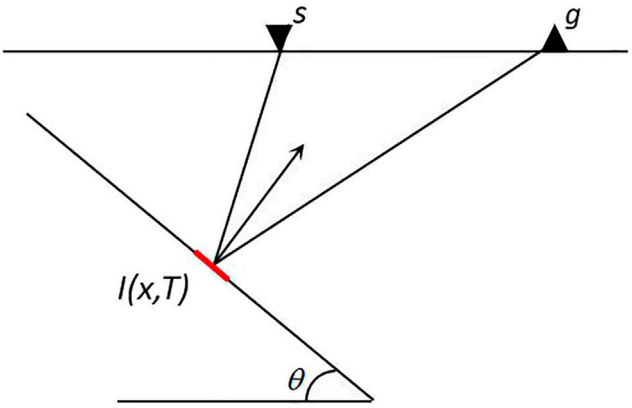

FIGURE 1 | Illustration of the generation of a dip-angle gather. Points s and g denote the shot and receiver, respectively, and point I is the imaging point. θ represents the travel time–related dip-angle at the imaging point I.

3.2 U-Net Architecture

Deep learning can think and process data just like the human brain, showing its superior capability in many fields in recent years (LeCun et al., 2015). It has multi-layer nonlinear activation function, which can discover hidden features in complex high-dimensional data by simulating signal transformation. Convolutional neural networks (CNNs) are currently the most successful and extensive application in deep learning, which connect input and output through multi-layer convolution. U-Net, a special type of CNN, was originally an auto-encoder–decoder network designed for medical image segmentation (Ronneberger, et al., 2015; A. Sevastopolsky, 2017; Wu et al., 2019; Zhang et al., 2021). We use U-Net to identify the left and right boundaries in the dip-angle gathers as the boundaries of Fresnel zones because one important reason is that U-Net can deliver a satisfactory performance even if the size of the training set is not very large. As shown in **Figure 2**, the main structure of the network includes two parts, down (encoder) and up (decoder), presenting a symmetrical form. Different levels of networks have different functions. The shallow layer is employed to solve the pixel positioning problem, while the deep layer is used to classify pixels. In the contraction path on the left, each step consists of two 3 × 3 convolution layers, followed by a rectified linear unit (ReLU) (Nair and Hinton, 2010; Krizhevsky et al., 2012) and a 2 × 2 max-pooling operation with stride 2 for downsampling. Symmetrically, each step on the right expansive path consists of a 2 × 2 upsampling operation with the same stride and two convolutional layers to halve feature channels. The sigmoid activation function is applied to the last channel feature vectors to produce a probability map of the output with the same size as the input. The skip connection is used in each upsampling operation, instead of directly

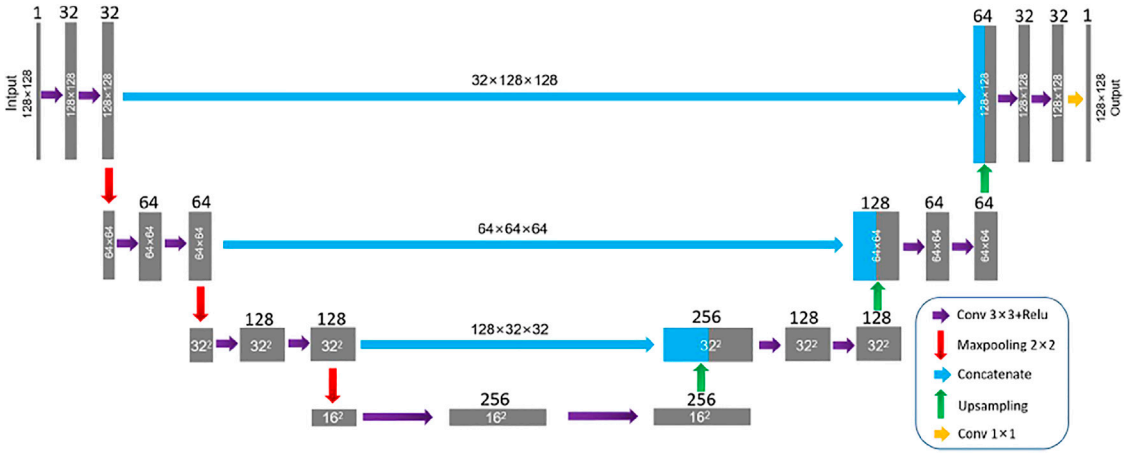

FIGURE 2 | Simplified U-Net architecture. The black number describes the number of channels in feature maps. The purple arrow represents convolution-ReLU operation. The red arrow indicates the max-pooling operation which downsamples feature maps while the green arrow means the upsampling process. The blue arrow is the shortcut concatenating feature maps from shallow to deep layers.

monitoring and loss back-transmission on high-level semantic features, to integrate more low-level features into the finally recovered feature map. After building the network, we feed small volumes of seismic images generated by PSTM with compensation, together with corresponding labels. Each data volume contains 128 2D images with a size of 128 × 128. In order to avoid the odd-sized feature map encountered by the pooling layer, the same-padding convolution process was adopted in each step of the network.

3.3 Loss Function and Training

Network training uses a loss function to represent the difference between the true Fresnel zones and the predictions. The update of the parameters in the network is realized *via* the loss backpropagation (Rumelhart et al., 1986; Hecht-Nielsen, 1989), which is commonly used in the gradient descent optimization algorithm to iteratively adjust weights and biases of the neurons by calculating the gradient of the loss function. We consider the Fresnel zone identification problem as a binary segmentation problem; in other words, the output of the network is a probability distribution of 0–1, and the binary cross-entropy loss function is generally adopted:

$$\text{Loss} = -\sum_{i=1}^{n} (b_i \times \ln a_i + (1 - b_i) \times \ln(1 - a_i)), \quad (4)$$

where n is the number of pixels, b_i denotes the true binary labels (0 or 1), and a_i is the prediction probabilities ($0 < a_i < 1$) computed from the sigmoid activation in the last convolutional layer. The boundary occupies a relatively small proportion of the entire imaging region, resulting in a high imbalance between zero (no boundary) and one (boundary). To overcome this issue, we apply a class-balanced binary cross-entropy loss function (Xie and Tu, 2015; Wu et al., 2021) to adjust the imbalance so that the network is not trained or converged to predicted only zeros.

$$\text{Loss} = -\sum_{i=1}^{n} (\varepsilon \times b_i \times \ln a_i + (1 - \varepsilon) \times (1 - b_i) \times \ln(1 - a_i)), \quad (5)$$

where $\varepsilon = \chi_0/\chi$ and $1 - \varepsilon = \chi_1/\chi$, χ_0 and χ_1 represent the number of pixels of boundaries and non-boundaries in the label data sets, respectively. χ denotes the total number of pixels in the label data sets. The class-balanced binary cross-entropy loss can help the network converge in the correct direction by introducing the class-balancing weight ε on a per-pixel term basis.

Given one thousand images of dip-angle gathers for training and the corresponding true segmentations as labels, training a given model and optimizing the parameters is the goal of training. The labels here are established by manual interpretation and labeling, with labeling ones on true boundaries and zeros elsewhere. **Figure 3** shows three randomly seismic images of different dip angle gathers with their corresponding labels. We prepared another 400 dip-angle gathers for validation and testing, of which 60% are used for validation and 40% for testing. In general, a validation set is used to evaluate the model during the training process, fine-tune hyperparameters, and perform model selection, while the testing set is used to evaluate the model. The network takes in the images and outputs 2D boundary distribution probability maps. Cheng et al. (2020) used a modified VGGNet to identify the Fresnel boundary, and the output of his network is a one-dimensional probability distribution map. In our research, we employ the U-net to identify the Fresnel boundary, and its output is a two-dimensional probability distribution map. The U-Net is essentially a fully convolutional network, and its output is different from the VGGNet's (Wu et al., 2021). Although Cheng's method is suitable for dip-angle gathers generated by conventional migration methods and the U-net proposed is carried out on compensated dip-angle gathers with high resolution, the steps of the two methods in learning and training are roughly the same, and both need to pre-process the data, and both use training to optimize network parameters.

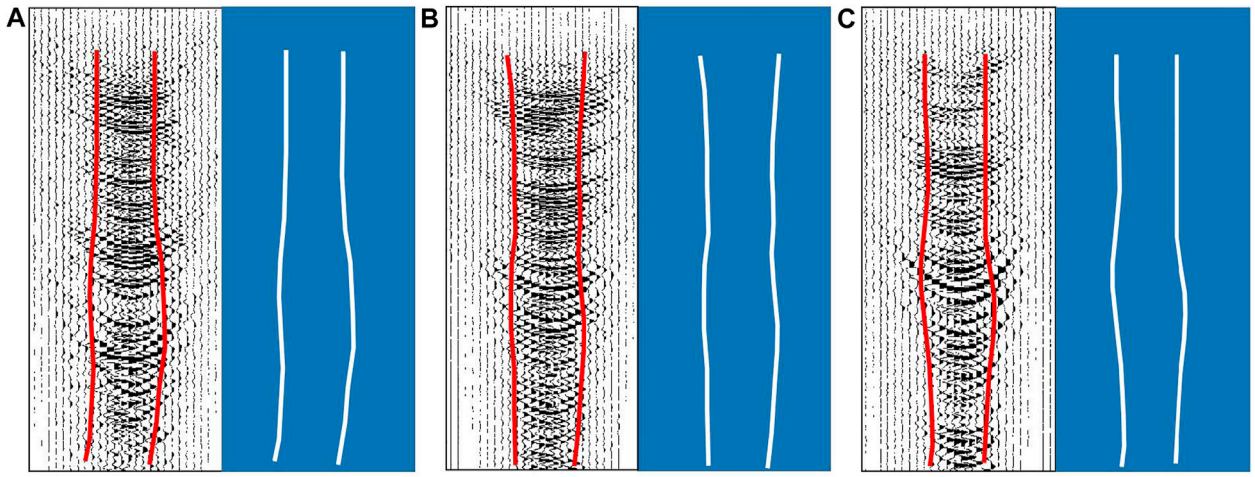

FIGURE 3 | Three randomly seismic images (red lines, the boundaries manually picked) with their corresponding labels (with labeling ones, white line of Fresnel zones and zeros elsewhere) generated by manual interpretation.

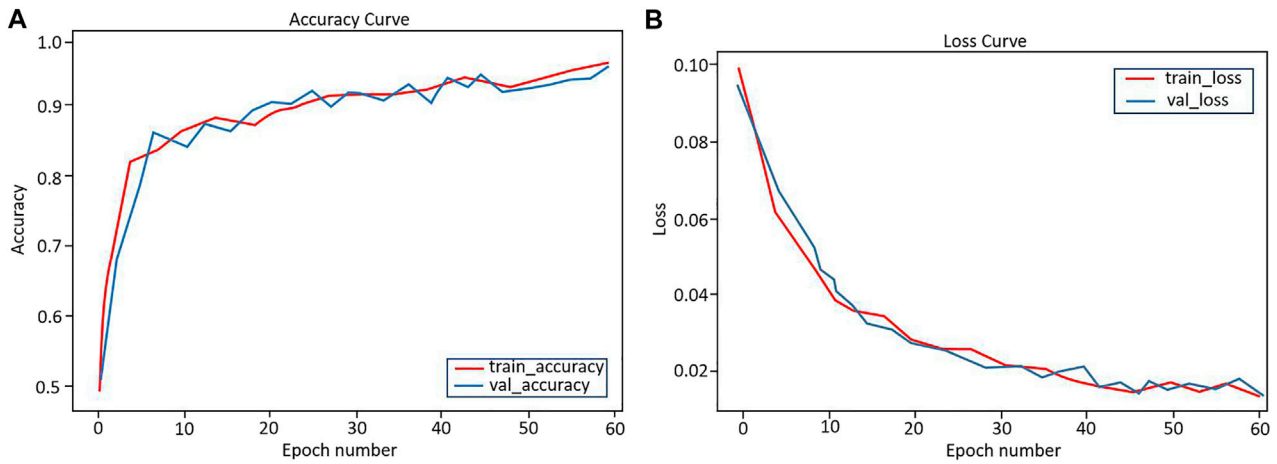

FIGURE 4 | (A) The training and validation accuracy both will increase with epochs, whereas **(B)** the training and validation loss decreases with epochs.

In order to improve the convergence of U-Net training and balance the numerical difference between training data and prediction data, the input image needs to be normalized. Adam method (Kingma and Ba, 2014) was adopted to optimize network parameters, and the default learning rate was set to 0.001. The Adam method is designed to combine the advantages of two methods: AdaGrad (Duchi et al., 2011), which works well with sparse gradients, and RMSProp (Tieleman and Hinton, 2012), which works well in online and non-stationary settings. We can also pick up a proper learning rate manually (Smith L, 2017). We used 60 epochs to train the network, and each epoch processed 1,000 training images. As shown in **Figure 4**, after 60 training epochs of approximately 22 h, the accuracy of training and validation gradually increases to 95%, while the training and validation loss converges to 0.01. It shows that our network has been trained.

4 ESTIMATION OF EFFECTIVE Q

Zhang et al. (2013) introduced the definition of effective Q, which is related to the spatial location of the imaging point with no knowledge of velocities, and proposed a constant Q migration scanning method to obtain the effective Q parameters. However, this method of obtaining Q is complicated in calculation, and the quality of seismic data has a great influence on the accuracy of Q. We need a method that is more suitable for practical applications, taking into account both accuracy and efficiency. To address these issues, we develop an effective Q-model estimation scheme, and the specific implementation steps are as follows:

1) use VSP data to obtain initial Q, expressed as Q_{vsp}. The number of VSP wells should be as many as possible, and the distribution should be as even as possible.

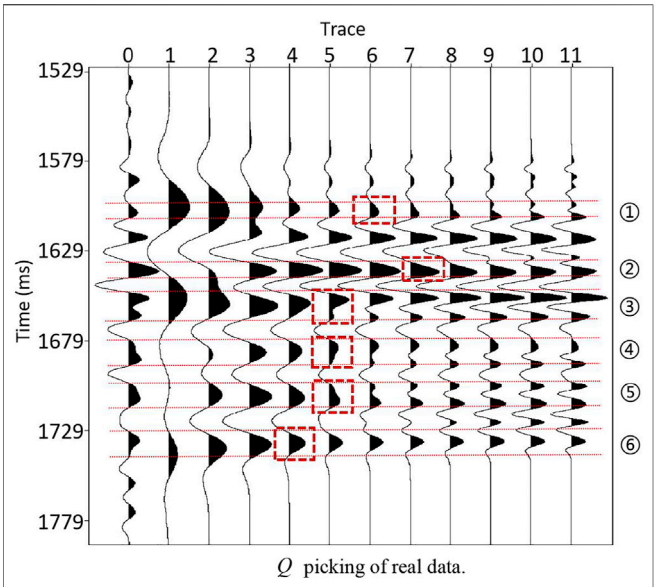

FIGURE 5 | *Q* picking of real data.

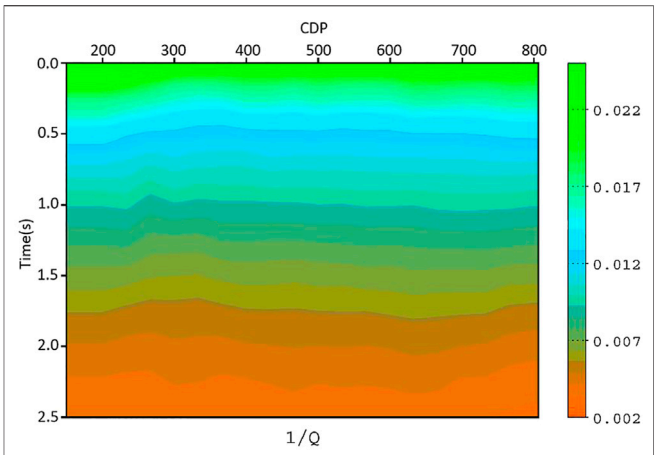

FIGURE 6 | *Q* model of real data.

2) generate a synthetic trace without attenuation and different migrated traces with compensation. *Q* is selected according to the match between the synthetic trace and their corresponding migrated traces and is denoted as Q_{well}.
3) use Lee's empirical formula $Q = 14v^{2.2}$ to get *Q* from seismic data. The *Q* is marked as $Q_{seismic}$. Lee's empirical formula can quickly establish a Q model of the entire work area by using seismic velocity (Tian, 1990).
4) Use all $Q_{well}s$ to calibrate $Q_{seismic}$ and get a *Q* model of the whole work area.

In step 1, we use the centroid frequency shift method (Quan and Harris, 1997) to estimate *Q* that reads

$$Q = \frac{\pi\tau\sigma^2}{f_{shot} - f_{geo}}, \tag{6}$$

where σ^2 is the variance of the source wavelet; τ is the travel time in the layers; and f_{shot} and f_{geo} are the centroid frequencies of the shot point and detection point, respectively. Since this method is sensitive to layering effects and background noise, it is necessary to preprocess the VSP data such as denoising. In addition, try to avoid thin layers, and select some large layers for *Q* calculation.

In step 2, we use a Rick wavelet to generate a synthetic trace without attenuation at the location of this VSP well, first. Because the attenuation of shallow seismic data is weak, its dominant frequency can be used as the dominant frequency of the Rick wavelet. Next, we get different migrated imaging traces corresponding to the synthetic trace using PSTM with compensation under a set of regular variable *Q*. Based on Q_{vsp} and multiplied by different weight coefficients, the variable *Q* was obtained as 0.5, 0.6, 0.7, 0.8, 0.9,1.0, 1.1, 1.2, 1.3, 1.4, and 1.5 times of Q_{vsp}. The optimal *Q* is selected according to the similarity between the synthetic trace and its corresponding seismic imaging traces.

In step 3, the unit of the parameter *v* in Lee's empirical formula is km/s, and it is a root mean square velocity. Lee's formula uses velocity information to estimate the *Q* value, which has the characteristics of high efficiency and easy realization in practical application. However, its estimation accuracy is low, and it needs to be corrected by well information.

In the last step, we use all $Q_{well}s$ to calibrate $Q_{seismic}$ and get a *Q* model of the whole work area. Q_{well} is derived from VSP data, and its accuracy is higher than that of *Q* calculated from Lee's formula. Using all $Q_{well}s$ to calibrate $Q_{seismic}$ can improve the overall accuracy of the *Q* model.

5 RESULT

5.1 Field Data Example

In this section, we directly use a 2D field data line to analyze and discuss the effective *Q* estimation, the identification of Fresnel zones using deep learning, and the imaging with compensation. This line consists of 1,000 CDPs (common depth point) with a CDP spacing of 12.5 m. The data are sampled at 1 ms with a length of 2.5 s.

Figure 5 shows how an optimal *Q* value is obtained from the compensated imaging traces. The specific implementation process is as follows: we get the synthetic seismic trace without attenuation, and then use VSP data to estimate the *Q* value, which is denoted as Q_{vsp}. Next, we get different migrated traces corresponding to the synthetic trace by PSTM with compensation using Q_{vsp} with different weight coefficients. There are eleven weight coefficients used, which are 0.5, 0.6, 0.7, 0.8, 0.9, 1.0, 1.1, 1.2, 1.3, 1.4, and 1.5. Multiply Q_{vsp} by different weight coefficients to obtain the waveforms of compensated imaging traces under different *Q*, and then, compare them with their corresponding synthetic seismic trace without attenuation. When the two waveforms are similar, the corresponding *Q* value is the optimal *Q*. In **Figure 5**, trace 0 represents a synthetic seismic trace without attenuation, which exists as a reference trace during *Q* picking. Trace 1 to trace 11

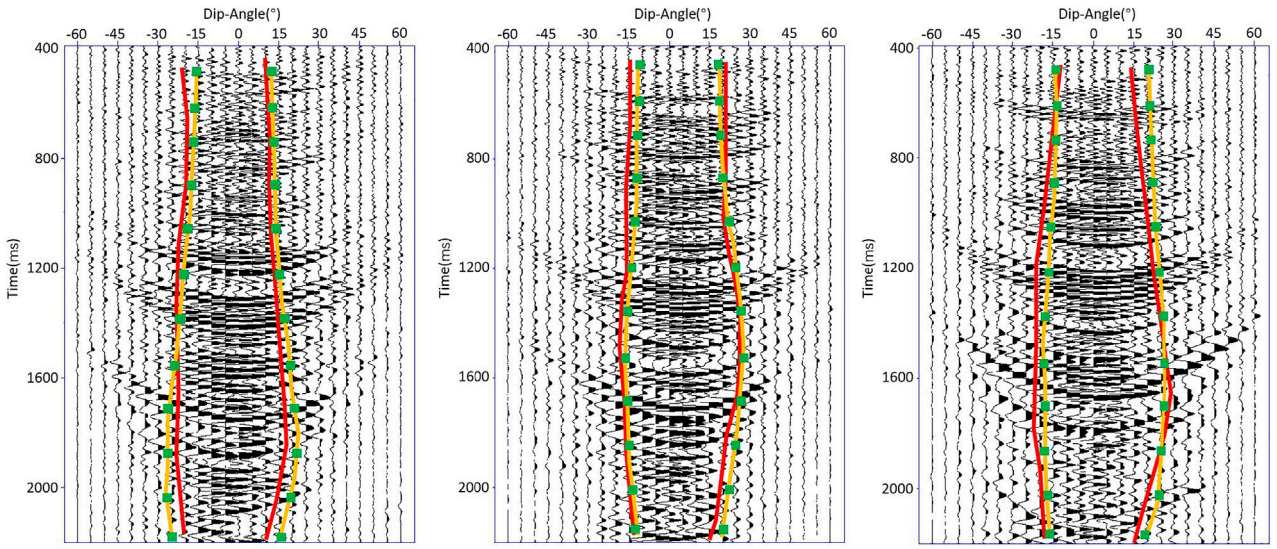

FIGURE 7 | Prediction of the boundaries of the Fresnel zones from the dip-angle gathers at three CDPs (400, 600, and 800). The red lines are the boundaries manually picked, while the green points on yellow lines are the exact points predicted by U-Net. The predicted boundaries of the Fresnel zones are similar to the manually picked ones.

represent the compensated imaging traces under different Q. For example, trace 1 is when Q_{vsp} is multiplied by 1.5, and trace 2 is when Q_{vsp} is multiplied by 1.4, and so on; trace 11 is when Q_{vsp} is multiplied by 0.5. On trace 0, six black typical crests are selected, and each crest is surrounded by a set of red dashed lines. The amplitude of the intersection of two red dashed lines with the wave curve is zero. These six crests represent six events. For each wave crest, two red dashed lines that envelop it extend from trace 0 to trace 11. We judge whether Q is optimal according to whether the two red dashed lines intersect the wave curve at amplitude zero. The principle of picking Q here is that when Q is optimal, the waveform of its compensated imaging trace should be closest to that of its corresponding synthetic seismic trace without attenuation. The six red boxes in **Figure 5** are the best Q-labeled. **Figure 6** shows the final Q model of real data, and the value is displayed as the reciprocal of Q.

Figure 7 shows part of the prediction results, which are the Fresnel zones predicted from the dip-angle gathers at three CDPs (400, 600, and 800). In order to solve the problem of local unsmoothness of Fresnel zones predicted by deep learning, the

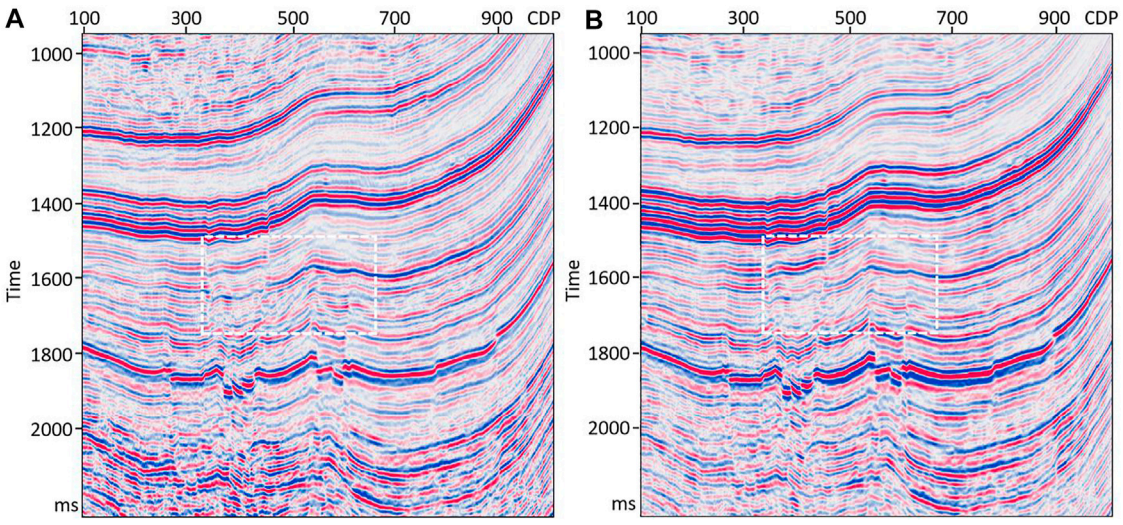

FIGURE 8 | Comparison between the compensated migrated result with different apertures. Panel **(A)** represents the compensated migrated result with a constant aperture ranging from −17 to 17°, while panel **(B)** represents the result with the U-Net predicted optimal aperture. The result with the U-Net predicted optimal aperture has a higher S/N than the result with a constant aperture.

prediction results were sparsely processed and only twelve pairs of equally spaced sample points were retained. The Fresnel zones predicted by deep learning was obtained by connecting the sample points with smooth curves. In **Figure 7**, the red lines are the boundaries manually picked, while the green points on yellow lines are the sample points predicted by U-Net. The predicted boundaries of the Fresnel zones are similar to the manually picked ones, with a smoother curve. After superimposing the Fresnel zones at each CDP within the predicted boundaries, a migrated result with a higher S/N can be obtained. **Figure 8** shows the compensated imaging results with different apertures. While **Figure 9** shows the detailed comparison of two white boxes in **Figure 8**. The result with U-Net predicted an optimal aperture has a higher S/N than the result with a constant aperture. The prediction of each dip-angle gather by the trained U-Net requires approximately 0.6 s when using six TITAN Xp GPUs, which is much more efficient than manual picking. **Figure 10** shows the comparison between the migration results obtained using conventional PSTM and the PSTM with compensation. The conventional PSTM used a constant aperture, and the compensated PSTM used an optimal aperture predicted by deep learning. **Figure 11** shows the detailed comparison of two white boxes in **Figure 10**. We see the overlay events are well separated by the PSTM with compensation. **Figure 12** shows the comparison of dB spectra between the migration sections obtained using conventional PSTM and the PSTM with compensation. The white boxes in **Figure 10** are the time windows of the frequency spectrum. Observe that the high frequencies have been recovered well by the PSTM with compensation.

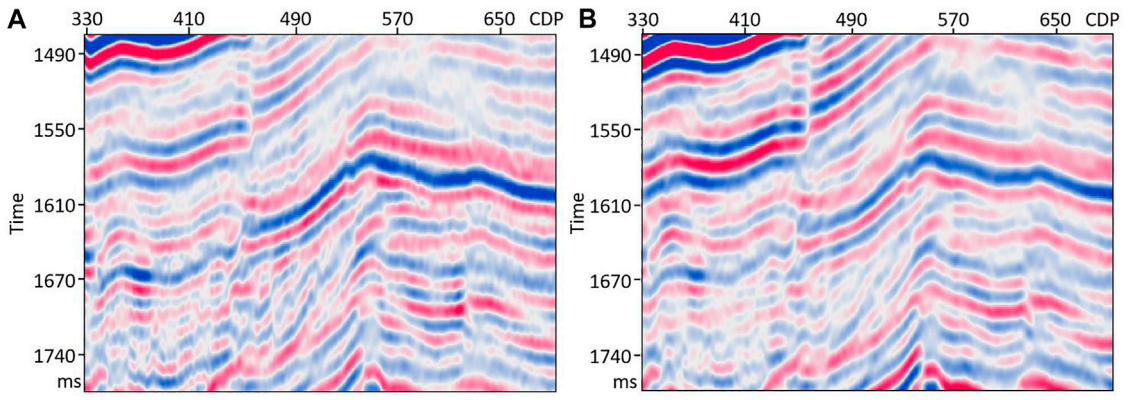

FIGURE 9 | Comparison of the enlarged details inside the boxes of **Figure 8**. Panel **(A)** is the enlarged detail of the compensated migrated result with a constant aperture ranging from −17 to 17°, while panel **(B)** is that with the U-Net predicted optimal aperture.

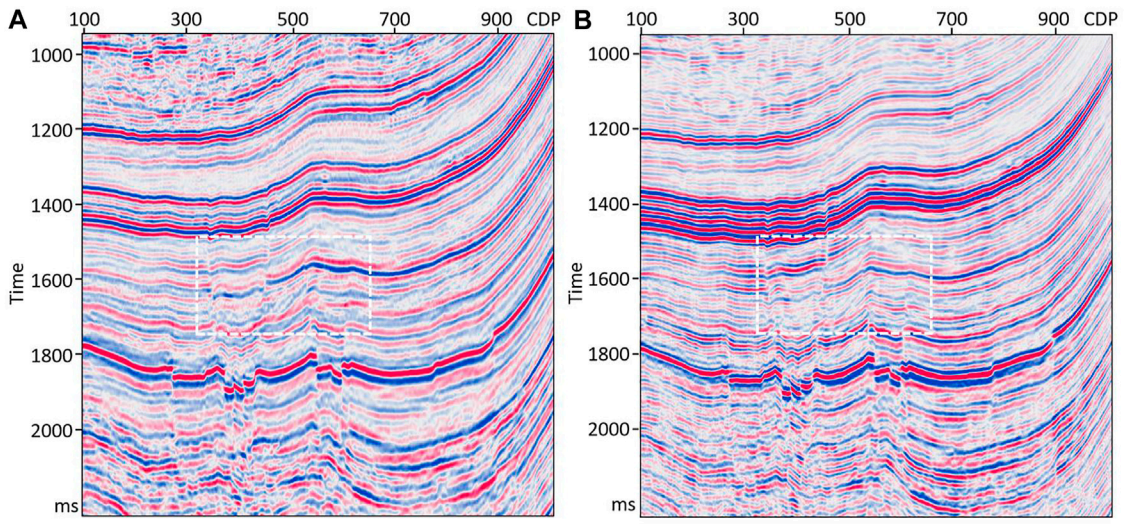

FIGURE 10 | Comparison between the result obtained using conventional PSTM **(A)** and the result obtained using PSTM with compensating absorption and dispersion **(B)**. Panel **(A)** represents the migrated result with a constant aperture ranging from −17 to 17°, while panel **(B)** represents the result with the U-Net predicted optimal aperture.

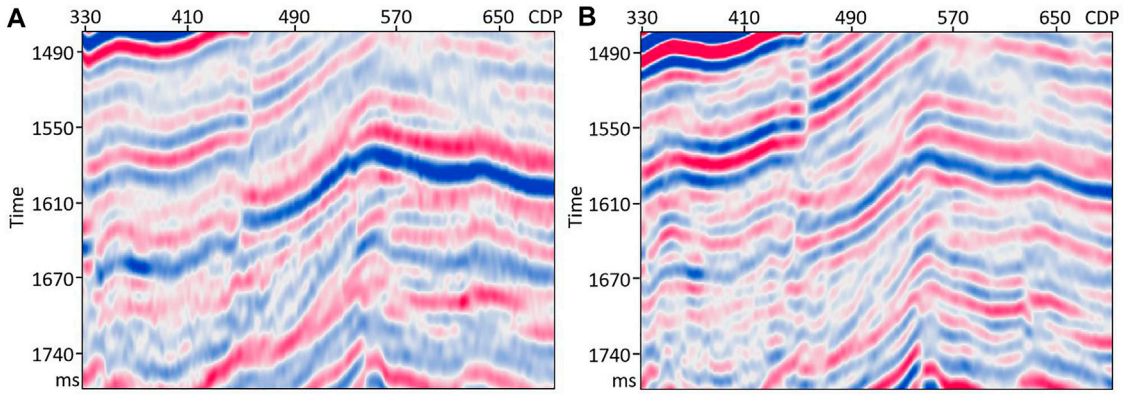

FIGURE 11 | Comparison of the enlarged details in-side the boxes of **Figure 10**. Panel **(A)** is the enlarged detail of the conventional migrated result with a constant aperture ranging from −17 to 17°, while panel **(B)** is that of the compensated migrated result with the U-Net predicted optimal aperture.

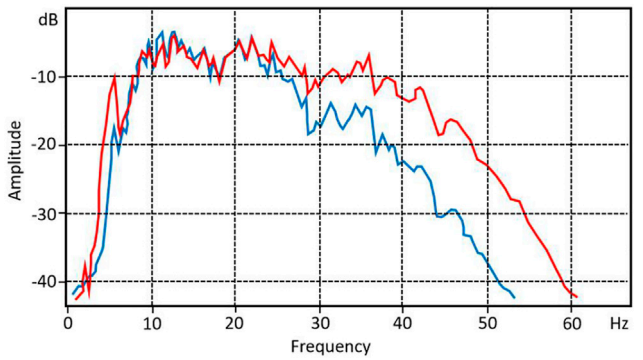

FIGURE 12 | Comparison of amplitude spectra between the migration sections obtained using conventional PSTM (blue) and the PSTM with compensation (red).

6 CONCLUSION

We have presented a PSTM scheme that can compensate absorption and dispersion with effective Q estimation and Fresnel zone identification based on deep learning. Using U-Net to estimate Fresnel zones from compensated migrated dip-angle gathers, we obtain an optimal migration aperture. The predicted boundaries of the Fresnel zones were similar to the manually picked ones, and the migrated result obtained by applying the predicted Fresnel zones exhibited a higher S/N. The effective Q model is constructed using surface seismic velocity data and VSP well data. The optimal Q is selected according to the similarity between the synthetic trace and its corresponding seismic imaging traces, which is a quick and effective method. Since the proposed migration scheme can compensate absorption and dispersion, the real data have been imaged with a higher resolution. Here, we discussed how to obtain 1D Fresnel zones from 1D dip-angle gathers for 2D seismic data using deep learning. Because of the high computation cost and memory requirement for 2D dip-angle gathers, it is difficult to directly estimate 2D Fresnel zones from 2D dip-angle gathers for 3D migration. Although 2D Fresnel zones can be represented by incorporating the inline and crossline 1D Fresnel zones from 1D dip-angle gathers obtained from 3D data, this simplified strategy will bring about inaccuracy of migration apertures in other directions except the inline and crossline directions. Therefore, it will be the next research focus to use deep learning to obtain 2D Fresnel zones from 3D data (Aki and Richards, 1980; Bleistein, 1984; Tian, 1990; Xu and Zhang, 2017; Wu and Zuo, 2019).

DATA AVAILABILITY STATEMENT

The raw data supporting the conclusion of this article will be made available by the authors, without undue reservation.

AUTHOR CONTRIBUTIONS

JW and YS contributed to conceptualization; JW and PL carried out the methodology; JW and AG helped with software; QY and JW performed validation; YS conducted the formal analysis; PL was responsible for investigation; AG and QY carried out data curation; JW wrote the original draft; JW was responsible for review and editing of the draft; QY carried out visualization; JW and PL was responsible for supervision. All authors have read and agreed to the published version of the manuscript.

ACKNOWLEDGMENTS

The authors are grateful to the National Natural Science Foundation of China (41930431) and the China Postdoctoral Science Foundation (2020M680840) for supporting this work.

REFERENCES

Aki, K., and Richards, P. G. (1980). *Quantitative Seismology*. W. H. Freeman.

Bai, J., and Yingst, D.,"Q Estimation through Waveform Inversion," in Proc. London, 75th EAGE Conf. Exhib. Incorporating SPE Europec, London, UK: Extended Abstr., 2013, 348-00601.doi:10.3997/2214-4609.20130112

Bleistein, N. (1984). *Mathematical Methods for Wave Phenomena*. Academic Press.

Brzostowski, M., and McMechan, G. (1992). 3-D Tomographic Imaging of Nearsurface Seismic Velocity and Attenuation. *"Geophysics* 57 (3), 396–403. doi:10.1190/1.1443254

Cavalca, M., Moore, I., Zhang, L., Ng, S. L., Fletcher, R., and Bayly, M. (2011). *Ray-based Tomography for Q Estimation and Q Compensation in Complex media: 81st Annual International Meeting*. Expanded Abstracts: SEG, 3989–3992.

Chen, J. (2004). Specular ray Parameter Extraction and Stationary-phase Migration. *Geophysics* 69, 249–256. doi:10.1190/1.1649392

Chen, Z., Chen, X., Wang, Y., and Jingye, L. (2014). Estimation of Q Factors from Reflection Seismic Data for a Band-Limited and Stabilized Inverse Q Filter Driven by an Average-Q Model. *J. Appl. Geophys.* 101, 86–94. doi:10.1016/j.jappgeo.2013.12.003

Cheng, Q., Zhang, J., and Liu, W. (2020). Extracting Fresnel Zones from Migrated Dip-Angle Gathers Using a Convolutional Neural Network. *Exploration Geophys.* 52. 1-10. doi:10.1080/08123985.2020.1798755

Dai, Y. U., Zhi-Jun, H. E., Yuan, S. U. N., and Wang, Y. A. (2018). A Comparison of the Inverse Q Filtering Methods Based on Wavefield continuation. *J. Geophys. Geochem. Explor.* 42 (2). 331–338.

Dasgupta, R., and Clark, R. (1998). Estimation of Q from Surface Seismic Reflflection Data. *Geophysics* 63 (6), 2120–2128. doi:10.1190/1.1444505

Dutta, G., and Schuster, G. (2016). Wave-equation Q Tomography. *Geophysics* 81 (6), R471–R484. doi:10.1190/geo2016-0081.1

Ferber, R. (2005). *A Filter Bank Solution to Absorption Simulation and Compensation: 75th Annual International Meeting*. Expanded Abstracts: SEG, 2170–2172.

Futterman, W. I. (1962). Dispersive Body Waves. *J. Geophys. Res.* 67 (13), 5279–5291. doi:10.1029/jz067i013p05279,

Guo, P., McMechan, G. A., and Guan, H. (2016). Comparison of Two Viscoacoustic Propagators for Q-Compensated Reverse Time Migration. *Geophys. J. Soc. Exploration Geophysicists* 81 (5), S281–S297. doi:10.1190/geo2015-0557.1

Hargreaves, N. D., and Calvert, A. J. (1991). Inverse Q Filtering by Fourier Transform. *Geophysics* 56, 519–527. doi:10.1190/1.1443067

Hecht-Nielsen, R. (1989). Theory of the Backpropagation Neural Network. *Neural Networks* 11, 593–605. doi:10.1109/IJCNN.1989.118638

Kamei, R., and Pratt, R. G., "Waveform Tomography Strategies for Imaging Attenuation Structure with Cross-Hole Data," in Proc. 70th EAGE Conf. Exhib. Incorporating SPE EUROPEC, 2008.doi:10.3997/2214-4609.20147680

Keers, H., Vasco, D. W., and Johnson, L. R. (2001). Viscoacoustic Crosswell Imaging Using Asymptotic Waveforms. *Geophysics* 66, 861–870. doi:10.1190/1.1444975

Kingma, D. P., and Ba, J. (2014). *Adam: A Method for Stochastic Optimization*.

Kjartansson, E. (1979). Constant Q Wave Propagation and Attenuation. *J. Geophys. Res.* 84 (1), 4737–4748. doi:10.1029/jb084ib09p04737

Klokov, A., and Fomel, S. (2012a). *Optimal Migration Aperturefor Conflicting Dips. 82nd Annual International Meeting*. Expanded Abstracts: SEG.

Klokov, A., and Fomel, S. (2012b). Separation and Imaging of Seismic Diffractions Using Migrated Dip-Angle Gathers. *Geophysics* 77 (6), S131–S143. doi:10.1190/geo2012-0017.1

LeCun, Y., Bengio, Y., and Hinton, G. (2015). Deep learning. *Nature* 521, 436–444. doi:10.1038/nature14539

Li, Z., Zhang, J., and Liu, W. (2018). Diffraction Imaging Using Dipangle and Offset Gathers. *Chin. J. Geophys.* 61 (4), 1447–1459. doi:10.6038/cjg2018K0583

Marfurt, K. J. (2006). Robust Estimates of 3D Reflector Dip and Azimuth. *Geophysics* 71 (4), P29–P40. doi:10.1190/1.2213049

Neep, J., Worthington, M., and O'Hara-Dhand, K. (1996). Measurement of Seismic Attenuation from High-Resolution Crosshole Data. *Geophysics* 61 (4), 1175–1188. doi:10.1190/1.1444037

Quan, Y., and Harris, J. M. (1997). Seismic Attenuation Tomography Using the Frequency Shift Method. *Geophysics* 62 (1), 895–905. doi:10.1190/1.1444197

Ronneberger, O., Fischer, P., and Brox, T. (2015).U-net: Convolutional Networks for Biomedical Image Segmentation in *MICCAI 2015*. Editors N. Navab, J. Hornegger, W. M. Wells, and A. F. Frangi (Cham: LNCSSpringer), 9351, 234–241. doi:10.1007/978-3-319-24574-4_28

Rumelhart, D. E., Hinton, G. E., and Williams, R. J. (1986c). Learning Representations by Back-Propagating Errors. *Nature* 323, 533–536. doi:10.1038/323533a0

Sangwan, P., and Kumar, D. (2021). *A Robust Approach to Estimate Q from Surface Seismic Data and Inverse Q Filtering for Resolution Enhancement*. Houten, Netherlands: First Break.

Schleicher, J., Hubral, P., Tygel, M., and Jaya, M. S. (1997). Minimum Apertures and Fresnel Zones in Migration and Demigration. *Geophysics* 62, 183–194. doi:10.1190/1.1444118

Sevastopolsky, A. (2017). Optic Disc and Cup Segmentation Methods for Glaucoma Detection with Modification of U-Net Convolutional Neural Network. *Pattern Recognition Image Anal.* 27 (3), 618–624. doi:10.1134/s1054661817030269

Shen, Y., Biondi, B., and Clapp, R.,"Q-model Building Using One-Way Wave-Equation Migration Q Analysis—Part 1: Theory and Synthetic Test,"*Geophysics*, 83, 2, 1–64. 2018. doi:10.1190/geo2016-0658.1

Shen, Y., and Zhu, T. (2015). Image-based Q Tomography Using Reverse Time Q Migration. *Proc. 85th Annu. Int. Meeting*. Houston, TX: SEG, Expanded Abstr., 3694–3698. doi:10.1190/segam2015-5852526.1

Shi, Y., Zhou, H.-L., Cong, N., Chun-Cheng, L., and Meng, L.-J. (2019). A Variable Gain-Limited Inverse. *Q. Filtering Method Enhance Resolution Seismic data.Journal Seismic Exploration* 28 (3), 257–276. 10.1190/obnobc2017-22.

Smith, L. (2017). Cyclical Learning Rates for Training Neural Networks[C]. 2017 IEEE Winter Conference on Applications of Computer Vision (WACV). (IEEE).

Tian, S. (1990). Estimating the Q Value in Inverse Q Filtering with Lee's Empirical Formula. *Pet. Geophys. Prospecting(in Chinese)* 3, 354–361. doi:10.1111/1365-2478.12391

Tieleman, T., and Hinton, G. (2012). Lecture 6.5-rmsprop: Divide the Gradient by a Running Average of its Recent Magnitude. *COURSERA: Neural Networks for Machine Learning* 4 (2).

Tonn, R. (1991). The Determination of the Seismic Quality Factor Q from VSP Data: A Comparison of Different Computational Methods. *Geophys. Prospecting* 39 (1), 1–27. doi:10.1111/j.1365-2478.1991.tb00298.x

Wang, Y. (2002). A Stable and Efficient Approach of Inverse Q Filtering. *Geophysics* 67, 657–663. doi:10.1190/1.1468627

Wang, Y., Zhou, H., Chen, H., and Chen, Y. (2018). Adaptive Stabilization for Q-Compensated Reverse Time Migration. *Geophysics*. 83. 1-111. doi:10.1190/geo2017-0244.1

Wu, J., Liu, B., Zhang, H., He, S., and Yang, Q. (2021). Fault Detection Based on Fully Convolutional Networks (FCN). *J. Mar. Sci. Eng.* 9 (3), 259. doi:10.3390/jmse9030259

Wu, J., and Zuo, H. (2019). Attenuation Compensation in Prestack Time Migration and its GPU Implementation. *Oil Geophys. Prospecting* 54 (1), 84–92. doi:10.13810/j.cnki.issn.1000-7210.2019.01.010

Wu, X., Liang, L., Shi, Y., and Fomel, S. (2019). FaultSeg3D: Using Synthetic Data Sets to Train an End-To-End Convolutional Neural Network for 3D Seismic Fault Segmentation. *Geophysics* 84, 35–45. doi:10.1190/geo2018-0646.1

Xie, S. N., and Tu, Z. W. (2015). Holistically-Nested Edge Detection. *Int. Conf. Comp. Vis.* 1. 1395–1403. doi:10.1109/ICCV.2015.164

Xie, Y., Xin, K., Sun, J., Notfors, C., Biswal, A. K., and Balasubramaniam, M. K. (2009). 3D prestack depth migration with compensation for frequency dependent absorption and dispersion: 79th Annual International Meeting. Expanded Abstracts. Houston, TX: SEG, 2919–2922. doi:10.1081/22020586.2010.12041885

Xu, J., and Zhang, J. (2017). Prestack Time Migration of Nonplanar Data: Improving Topography Prestack Time Migration with Dip-Angle Domain

Stationary-phase Filtering and Effective Velocity Inversion. *Geophysics*. 82 (3), S235–S246. doi:10.1190/geo2016-0087.1

Yu, Z., Etgen, J., Whitcombe, D., Hodgson, L., and Liu, H. (2013).Dip-adaptive Operator Anti-aliasing for Kirchhoff Migration. 83rd Annual International Meeting. Expanded Abstracts. Houston, TX: SEG, 3692–3695. doi:10.1190/segam2013-0584.1

Zhang, G., Wang, X., He, Z., Yu, G., Li, Y., Liu, W., et al. (2014). Impact of Q Value and Gain-Limit to the Resolution of Inverse Q Filtering. *J. Geophys. Eng.* 11(4), 45011. doi:10.1088/1742-2132/11/4/045011

Zhang, H., Han, J., Li, Z., and Zhang, H. (2021). Extracting Q Anomalies from Marine Reflection Seismic Data Using Deep Learning. *IEEE Geosci. Remote Sensing Lett.* 1(99), 1–5. doi:10.1109/lgrs.2020.3048171

Zhang, J. F., Wu, J. Z., and Li, X. Y. (2013). Compensation for Absorption and Dispersion in Prestack migration:An Effective Q Approach. *Geophysics* 78 (1), 1–14. doi:10.1190/geo2012-0128.1

Zhang, J., and Wapenaar, K. (2002). Wavefield Extrapolation and Prestack Depth Migration in Anelastic Inhomogeneous media. *Geophys. Prospecting* 50 (1), 629–643. doi:10.1046/j.1365-2478.2002.00342.x

Zhang, J., Li, Z., Liu, L., Wang, J., and Xu, J. (2016). High-resolution Imaging: An Approach by Incorporating Stationary-phase Implementation into Deabsorption Prestack Time Migration. *Geophysics* 81 (5), S317–S331. doi:10.1190/geo2015-0543.1

Conflict of Interest: The authors declare that the research was conducted in the absence of any commercial or financial relationships that could be construed as a potential conflict of interest.

Publisher's Note: All claims expressed in this article are solely those of the authors and do not necessarily represent those of their affiliated organizations, or those of the publisher, the editors, and the reviewers. Any product that may be evaluated in this article, or claim that may be made by its manufacturer, is not guaranteed or endorsed by the publisher.

frontiers in Earth Science

ORIGINAL RESEARCH
published: 11 February 2022
doi: 10.3389/feart.2021.810578

Effect of Velocity Anisotropy in Shale on the Acoustic Emission Events Matching and Location

Peng Wang, Feng Zhang and Xiang-Yang Li*

China University of Petroleum, Beijing, China

Accurate source event location is important in fracturing monitoring and characterization. Velocity anisotropy has a great influence on both events matching and events location. Failure to take into account the velocity anisotropy can lead to huge errors in locating events. In this article, we have presented an experimental study on lower Silurian shale from the Sichuan Basin. The experimental observations include ultrasonic measurements, acoustic emissions (AEs) in a three-point bend experiment, and CT scanning of the original sample and the fractured sample. The ultrasonic measurements show that the shale sample has strong velocity anisotropy. Initially, AEs are analyzed using the conventional event-matching method and event location method (Geiger's method), and the detected events are compared to the X-ray image of the fracture. Event-matching aims to obtain AE signals from the same source event and thus assists in selecting valid AE signals that come from the same source and are received by at least four sensors, to determine the location of the source. Although many reliable signals are obtained by isotropic event-matching, fewer sources were located than expected, and the event location results did not match the fracture distribution. To address this problem, an improved event-matching method is proposed using a stricter matching threshold based on directional velocity rather than a single threshold same for all directions. In addition, we propose an improved Geiger's method using the anisotropic velocity model. The new methods located more sources that better match fracture distribution than the results of the isotropic method. We have concluded that both event-matching and the source location of the fracturing are largely influenced by velocity anisotropy, and thus in practice, the velocity anisotropy information obtained from various measurements (e.g., laboratory measurements, well logs, VSP, and velocity analysis of reflected seismic surveys) should be involved in both processing procedures. This study can be useful to provide some background for monitoring and predicting dynamic geo-hazards in relation to the AE method.

Keywords: acoustic emission, microseismic, shale, anisotropy, event-matching, source location

OPEN ACCESS

Edited by:
Jidong Yang,
China University of Petroleum Huadong, China

Reviewed by:
Song Jln,
China University of Geosciences Wuhan, China
Yaojun Wang,
University of Electronic Science and Technology of China, China
Zhiqi Guo,
Jilin University, China

****Correspondence:***
Feng Zhang
zhangfeng@cup.edu.cn

Specialty section:
This article was submitted to Solid Earth Geophysics, a section of the journal Frontiers in Earth Science

Received: *07 November 2021*
Accepted: *20 December 2021*
Published: *11 February 2022*

Citation:
Wang P, Zhang F and Li X-Y (2022) Effect of Velocity Anisotropy in Shale on the Acoustic Emission Events Matching and Location. Front. Earth Sci. 9:810578. doi: 10.3389/feart.2021.810578

1 INTRODUCTION

Seismic source location is important in earthquake research, fracturing monitoring, and acoustic emission (AE) experiment. Triggering events can be located by minimizing an objective function in terms of the difference between observed and theoretical arrival times (Geiger, 1912; Ge, 2013; Wuestefeld et al., 2018). The reliable location of an event depends on an accurate velocity model.

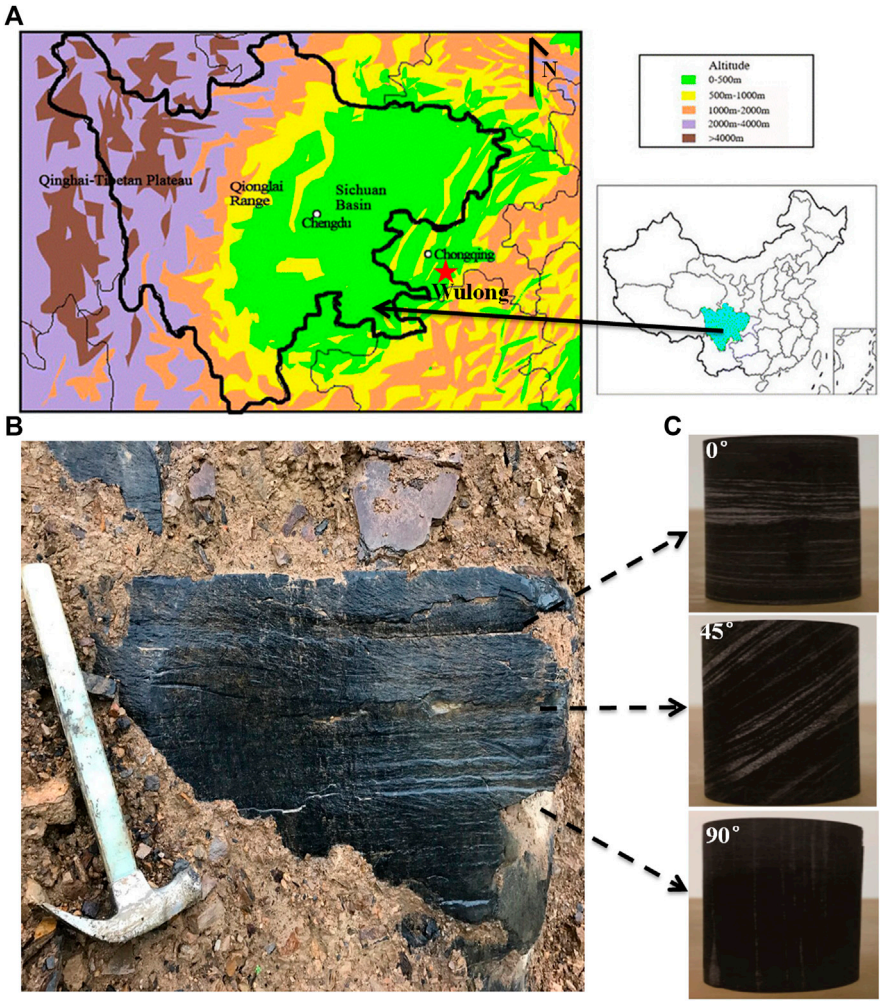

FIGURE 1 | (A) Shale samples collected from Wulong, southeast of Sichuan Basin. **(B)** Silurian Longmaxi shale outcrops. **(C)** Cores are cut in three different directions.

TABLE 1 | Mineral composition of the Silurian Longmaxi shale sample (measured using an X-ray fluorescence spectrometer).

Mineral	Quartz	K-feldspar	Plagioclase	Calcite	Dolomite	Pyrite	Clay
Fraction (%)	58.6	1.9	5.5	2.3	6.9	3.9	20.9

TABLE 2 | Velocities of P- and S-waves measured in three directions.

Angle to bedding (°)	0	45	90
Vp (km/s)	3.54	3.96	4.51
Vs (km/s)	2.24	2.74	2.60
ρ (g/cm^3)	2.51	2.52	2.53

Current source location methods assume homogenous and isotropic velocity models (King and Talebi, 2007; Zhou et al., 2017). However, shale is observed to have strong anisotropy caused by preferentially orientated clay platelets and other integrated factors on a small scale (Vernik and Nur, 1992; Lonardelli et al., 2007; Zhang, 2017; Zhang et al., 2017). Anisotropic shale can be modeled as a VTI (vertical transverse isotropy) medium in which the velocity of the acoustic wave perpendicular to the shale bedding is less than the velocity parallel to the shale bedding. The magnitude of shale anisotropy can be up to 40%, and thus the effect of anisotropy must be taken into account in source location and event-matching.

Event-matching obtaining valid AE signals is a necessary procedure to locate the source. Valid AE signals mean those signals are from the same source and are received by at least four receivers because four unknown source parameters including the location coordinates (x_0, y_0, z_0) and the origin time (t_0) need to be determined. Accurate events matching can be difficult since

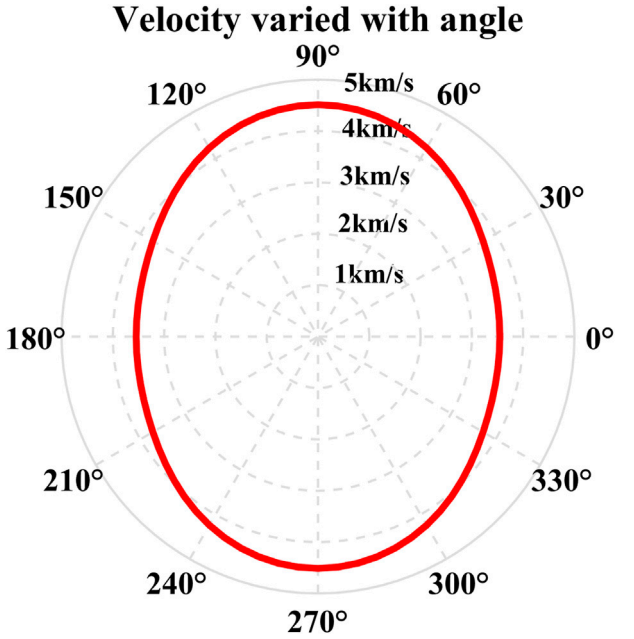

FIGURE 2 | Variation of velocity with an angle to the axis of symmetry.

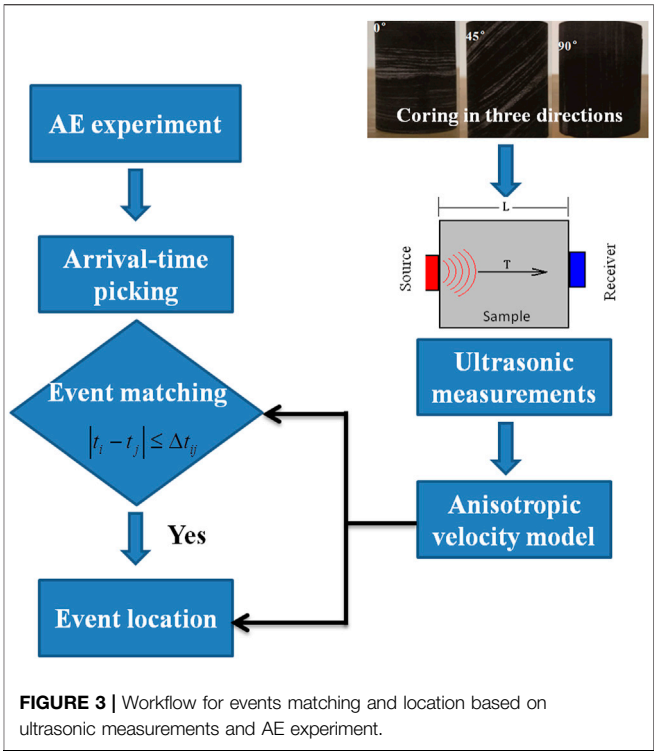

FIGURE 3 | Workflow for events matching and location based on ultrasonic measurements and AE experiment.

signals contain false AE detections, electronic noise, anthropogenic noise, and other signals (López Comino et al.,2017). In addition, AE signals can be mixed with boundary reflections or signals from other sources. The cross-correlation event-matching method uses the similarity of signals received by each channel from the same source (Gibbons and Ringdal, 2006; Song et al., 2010). Another effective method for event-matching is based on the maximum time difference between the earliest and latest arrivals (Feng et al., 2019). The maximum time acts as a threshold and is usually calculated in terms of isotropy. However, sensors are placed in geometries with a wide range of directions, and therefore the presence of anisotropy can have a large impact on the results of event-matching.

An inaccurate velocity model is another factor that leads to uncertainty in locating an event. Current AE and microseismic methods for determining the location of the source often assume that acoustic waves propagate in straight lines at a constant velocity for all sensors, and the location of the source is determined by the average wave velocity or vertical velocity determined from well-logging data (King and Talebi, 2007; Zhou et al., 2017). Thus, the effect of anisotropy must also be included in the source location. The importance of including VTI corrections, when detecting microseismic events, was shown by King and Talebi (2007) and Maxwell et al. (2010). A variable velocity method is proposed to address the location problem of a complex multilayer velocity model (Li and Qi, 2009). Van Dok et al. (2011) discussed some of the fundamental elements of how HTI (horizontal transverse isotropic) and VTI affect the correct location of microseismic imaging points. However, these methods allow obtaining anisotropic parameters using control measurements, cross-well measurement using three-component sensors, and advanced dipole sonic, which is mainly applicable to field microseismic data and makes it difficult to obtain anisotropic parameters in AE experiments in the laboratory; therefore, we use a core measurement method to obtain an anisotropic velocity model. An improved Geiger's method is proposed that corrects the anisotropic velocity instead of using a constant velocity during each iteration.

In this article, we first perform ultrasonic measurements on a shale sample from the lower Silurian shale formation in the southern Sichuan Basin to investigate its elastic properties. An acoustic emission experiment is then carried out on a shale sample. The number of located sources using traditional event-matching and Geiger's method is incompatible with the X-ray image of the fracture. To address this issue, we study the effect of anisotropy on event-matching and propose an improved event-matching method based on a triangulation method considering velocity anisotropy. The newly proposed matching method greatly improves data-processing efficiency by reducing invalid redundant AE events. Finally, we propose an improved Geiger's method by taking into account velocity anisotropy and verify the accuracy of the location results based on a CT scan.

2 ULTRASONIC MEASUREMENTS OF A SHALE SAMPLE

Shale samples are collected from an outcrop of the Longmaxi formation in Wulong County, Chongqing City (**Figure 1A,B**).

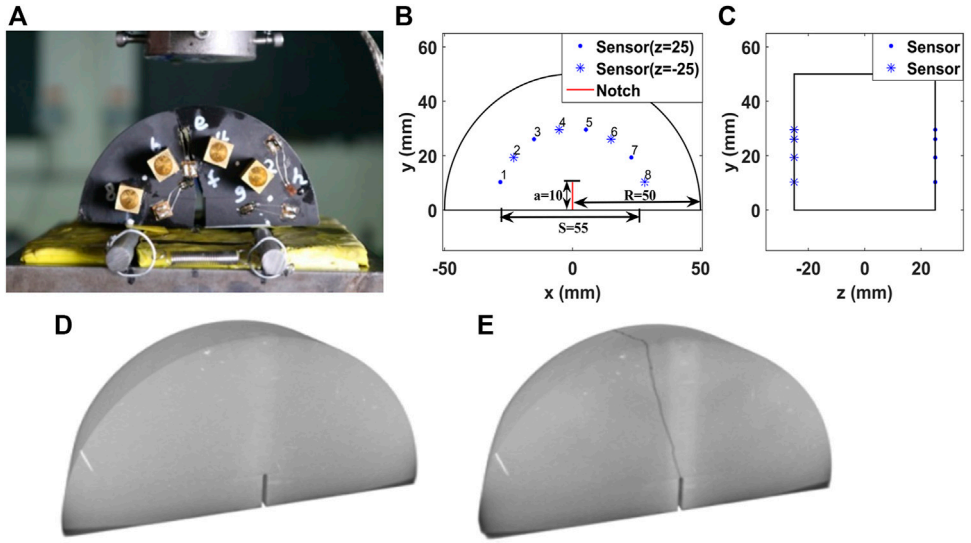

FIGURE 4 | (A) Notched semicircular bend (NSCB) shale sample after unaxial loading. **(B)** The front view of sample geometry and eight AE sensors. The distance between the two supporting(S) is 55 mm and a 10mm notch is made in the middle of the lower part of the sample to cause a directed rupture. **(C)** The side view of sample geometry and four sensors are glued on the z = 25 mm plane (blue point) and the rest are on the z = –2 5mm plane(blue asterisk).X-ray images of CT scanning **(D)** and **(E)** after fracturing.

TABLE 3 | Basic parameters of the AE experiment.

Design parameter	Value
Sample frequency	5,000 kHz
Sample point	4,000
Pre-sampling time	150 μs
Waveform threshold	35 dB
Preamplifiers	40 dB
Filter	100 kHz–400 kHz
Loading rate	0.01 mm/min

The density and porosity of the shale sample are measured as 2.52 g/cm^3 and 3.83%, respectively. The mineral grades are shown in **Table 1**. Although the shale contains a large volume of quartz, the alignment of the clay mineral is considered to be the determining factor in causing the anisotropy of seismic velocities (Liu et al., 2019; Zhang, 2019). We used the method proposed by Vernik and Nur (1992) to measure P- and S-wave velocities for three cylindrical plugs cut in three directions (normal to bedding, 45° to bedding, and parallel to bedding) from the sample (**Figure 1C**).

An ultrasonic pulse testing system is used to measure the velocities of P- and S-waves (SH-wave) in a shale sample. The measurements were carried out at room temperature and pressure, the main frequencies of P- and S-wave transducers were 1 and 0.5 MHz, respectively, and the test error was less than 1%. The measured velocities are shown in **Table 2**. The quantities $V_P(0^\circ)$ and $V_{SH}(0^\circ)$ represent the velocities of the P- and SH-waves along the normal to the bedding, respectively. The quantities $V_P(45^\circ)$ and $V_{SH}(45^\circ)$ represent the velocities of P- and S-waves at an angle of 45° to the bedding, respectively. The quantities $V_P(90^\circ)$ and $V_{SH}(90^\circ)$ represent the velocities of the P- and S-waves parallel to the bedding, respectively. It is seen that $V_P(0^\circ) < V_P(45^\circ) < V_P(90^\circ)$ and $V_{SH}(0^\circ) < V_{SH}(45^\circ) < V_{SH}(90^\circ)$. Thus, a shale sample has an equivalent VTI property and five independent elastic stiffness coefficients C_{ij}, which can be calculated using the measured velocity and density ρ as (Wang, 2002; Mavko et al.,2003)

$$\begin{cases} c_{11} = \rho V_P{}^2(90^\circ), & c_{12} = c_{11} - 2\rho V_{SH}{}^2(90^\circ), \\ c_{33} = \rho V_P{}^2(0^\circ), \quad c_{44} = \rho V_{SH}{}^2(0^\circ), & c_{66} = \frac{1}{2}(c_{11} - c_{12}), \\ c_{13} = -c_{44} + \sqrt{4\rho^2 V_P{}^4(45^\circ) + (c_{11} + c_{44})(c_{33} + c_{44}) - 2\rho V_P{}^2(45^\circ)(c_{11} + c_{33} + 2c_{44})}. \end{cases} \quad (1)$$

The P-wave velocity as a function of angle is calculated using the following equation:

$$V_P(\alpha) = \left(c_{11}\sin^2\alpha + c_{33}\cos^2\alpha + c_{44} + \sqrt{M}\right)^{1/2}(2\rho)^{-1/2}, \quad (2)$$

where α is the phase angle to the bedding normal and $M = [(c_{11} - c_{44})\sin^2\alpha - (c_{33} - c_{44})\cos^2\alpha]^2 + (c_{13} + c_{44})^2\sin^2 2\alpha$. The velocity of P-wave, which varies depending on the direction, is shown in **Figure 2** and is used for further event-matching and location using data from the AE experiment (**Figure 3**). Since in subsequent AE experiments the sensors have only one component, only the P-wave velocity is used to locate events. The kinematics of P-wave in the TI medium weakly depends on the S-wave phase velocity (Alkhalifah, 1998; Jin and Stovas, 2018; Jin and Stovas, 2020). The magnitude of shale anisotropy can be represented by the P-wave velocity anisotropy parameter $\varepsilon = (C_{11} - C_{33})/2C_{33}$ (Thomsen, 1986). The measured shale sample has strong P-wave anisotropy, since its ε is 0.27. The densities of the three samples are almost the same, and slight deviations can be caused by heterogeneity.

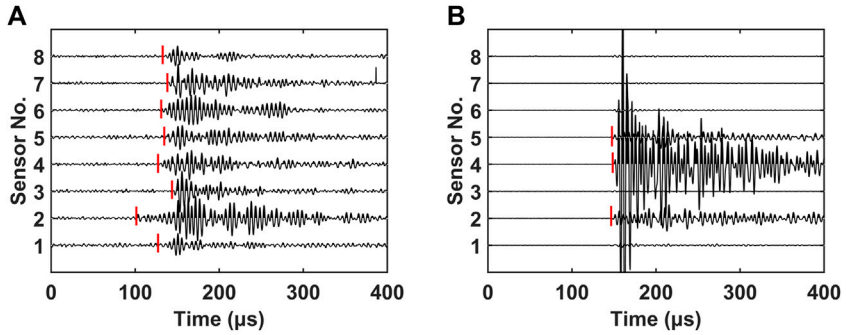

FIGURE 5 | (A) AE event recorded by eight sensors. The red line represents the selected arrival times. **(B)** AE event received by only three sensors (Sensor 2, 4, and 5).

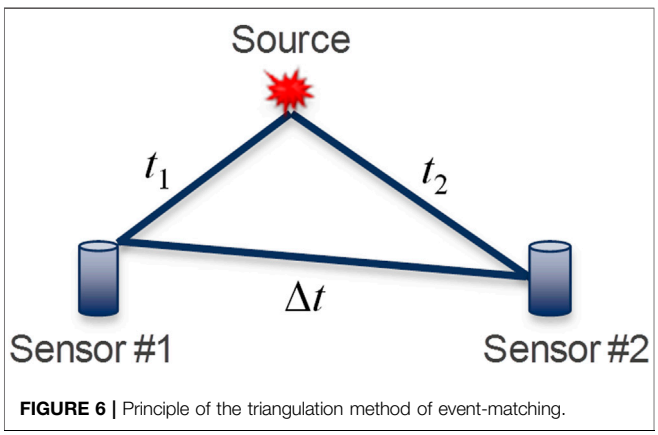

FIGURE 6 | Principle of the triangulation method of event-matching.

3 ACOUSTIC EMISSION EXPERIMENTS

A three-point bend acoustic emission experiment is carried out on a semicylindrical shale sample that is 50 mm thick and has a radius of 50 mm (**Figures 4A,B**). The sample before fracturing did not contain natural fractures. Its axial direction is perpendicular to the bedding. Compressive loads are applied to three points with a ratio of 0.01 mm/min for 1 hour until the destruction of the sample. The AE signals are received by eight resonance-type sensors (SR150S) placed on the surface of the sample (**Figure 4C**). The sensors have a frequency range of 70~280 kHz and a resonance frequency of 150 kHz. The main parameters of the AE experiment are shown in **Table 3**. The AE signal sampling frequency is 5,000 kHz with a sampling interval of 0.2 μs, a waveform threshold of 35 dB, a pre-sampling time of 150 μs, a sampling length of 4,000 points, and a total recording length of 800 μs for each acquisition segment. The eight AE sensors and 40-dB preamplifiers were used in the tests, and AE signals exceeding 40 dB were captured during fracturing. CT scans are performed before and after rock breakdown to determine fracture distribution. The results of the CT X-ray images are shown in **Figures 4D,E**. These results will be used as the true fracture distribution for comparing source locations.

4 EVENT-MATCHING FOR ANISOTROPIC MEDIA

Event-matching aims to obtain AE signals from the same source event. It is carried out after the acquisition of the first arrivals (**Figure 3**). Ideally, an AE event is received and recorded by all eight sensors (**Figure 5A**). However, many AE events are received and recorded by only a few sensors (**Figure 5B**). This may be because these events are not strong enough to trigger all sensors for recording. To determine the location of the AE source, it is necessary to solve four unknown parameters, including the coordinates of the location (x_0, y_0, z_0) and the origin time (t_0). Therefore, valid AE signals are signals from the same source received by at least four sensors. Hence, reliable AE event-matching is crucial to locate the source.

Event-matching can be achieved using a triangulation rule as shown in **Figure 6**. The difference between the AE arrival times from the two sensors is compared with the time threshold Δt to confirm if they are valid. The time threshold is usually constant and is expressed as the difference in travel time between the two farthest points or sensors in the sample (Feng et al., 2019). The arrival times of AE signals received by two sensors (t_1 and t_2) correspond to two sides of the triangle. Knowing the coordinates of two sensors, it is possible to calculate the travel time from one sensor to the other as a "third side" using a known velocity model. The signals can be identified as from the same source event, if the following matching condition is met:

$$|t_1 - t_2| \leq \Delta t. \tag{3}$$

In this three-point bending experiment, assuming the sample is isotropic, Δt is calculated as 30 μs using a constant velocity 3.54 km/s. As shown in **Figure 7A**, signals are received by four sensors, but the differences in arrival times between them are much greater than Δt, so this set of signals is recognized as invalid based on the formula **Eq. 3**. In this article, the Akaike information criterion (AIC) (Maeda, 1985) is used to determine the time of the first

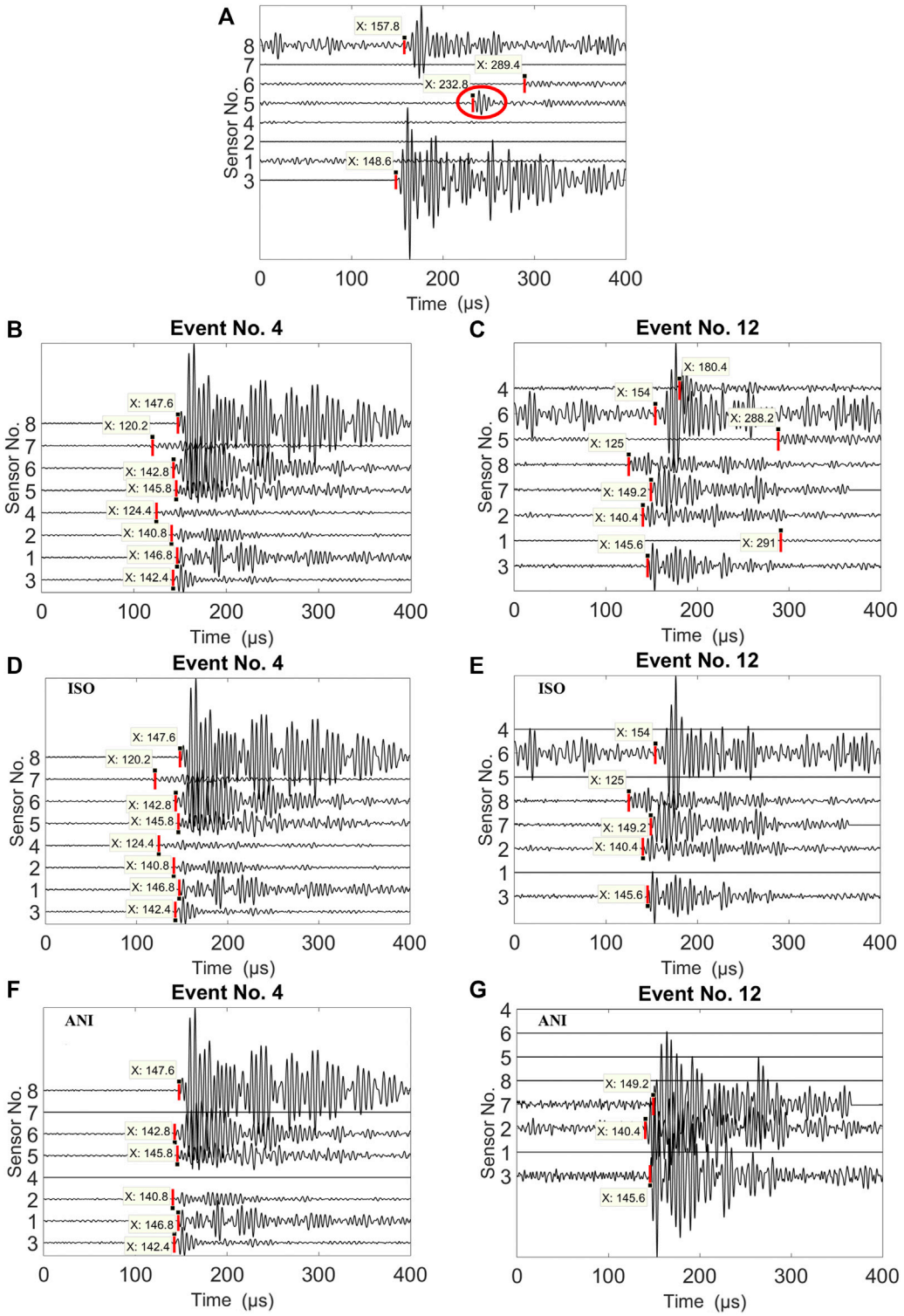

FIGURE 7 | (A) Signals received by four sensors are considered invalid. Red lines represent first arrivals, and the red ellipse in the sensor 5 represents the boundary reflection. **(B)** Event No. 4 and **(C)** Event No. 12 received by all eight sensors before event-matching. **(D)** Event No. 4 and **(E)** Event No. 12 after event-matching using the constant Δt as 30 μs. **(F)** Event No. 4 and **(G)** Event No. 12 after event-matching using Δt calculated using anisotropic velocity.

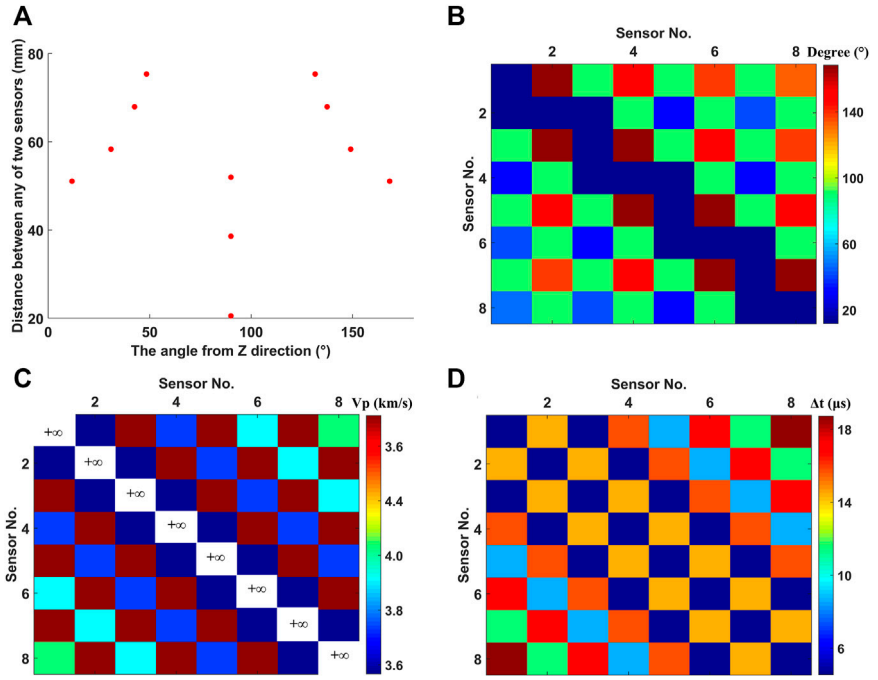

FIGURE 8 | (A) Relationship between the distances between two sensors and the angle from the Z direction in a three-point bend experiment. **(B)** Directions between either of the two sensors. **(C)** Velocity variation between either of the two sensors. **(D)** Differences in travel time between either of the two sensors. It is noted that the time differences (Δt_{ii}) between the same sensors are equal to 0, and the propagation velocity is infinite.

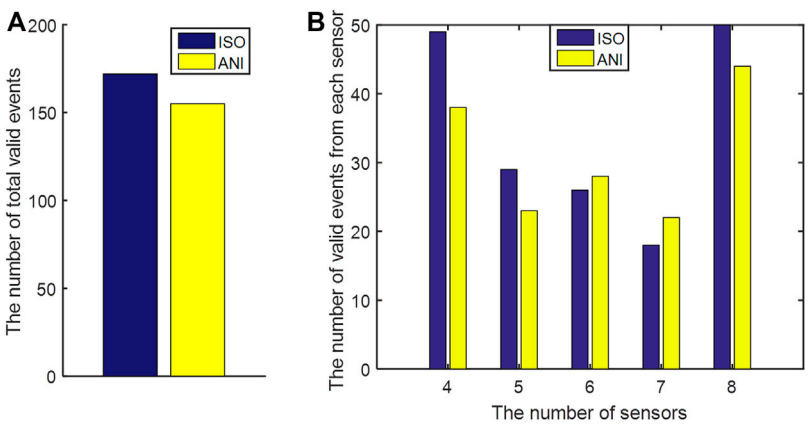

FIGURE 9 | (A) Total number of valid events matched using isotropic (ISO) and anisotropic (ANI) methods. **(B)** Number of valid events from each sensor, matched using ISO and ANI event-matching methods.

arrival of AE events. Although this method is convenient and highly effective, it can match redundant signals because received signals are mixed with boundary reflections or signals from other sources. As shown in **Figures 7B,C**, events No.4 and No.12 contain signals received by all eight sensors. If Δt is used as 30 μs, eight signals and six signals can be matched for events No.4 and No. 12, respectively, and thus both events are considered valid. However, neither of these two events can complete the subsequent location. Either the location result is outside the sample, or an unreliable solution is obtained. This is because redundant invalid events are matched as valid using a constant Δt, ignoring directional velocity variation.

To solve this problem, an improved matching condition is proposed, including the impact of anisotropy. In this AE experiment, sensors are arranged in a semicircle, and their

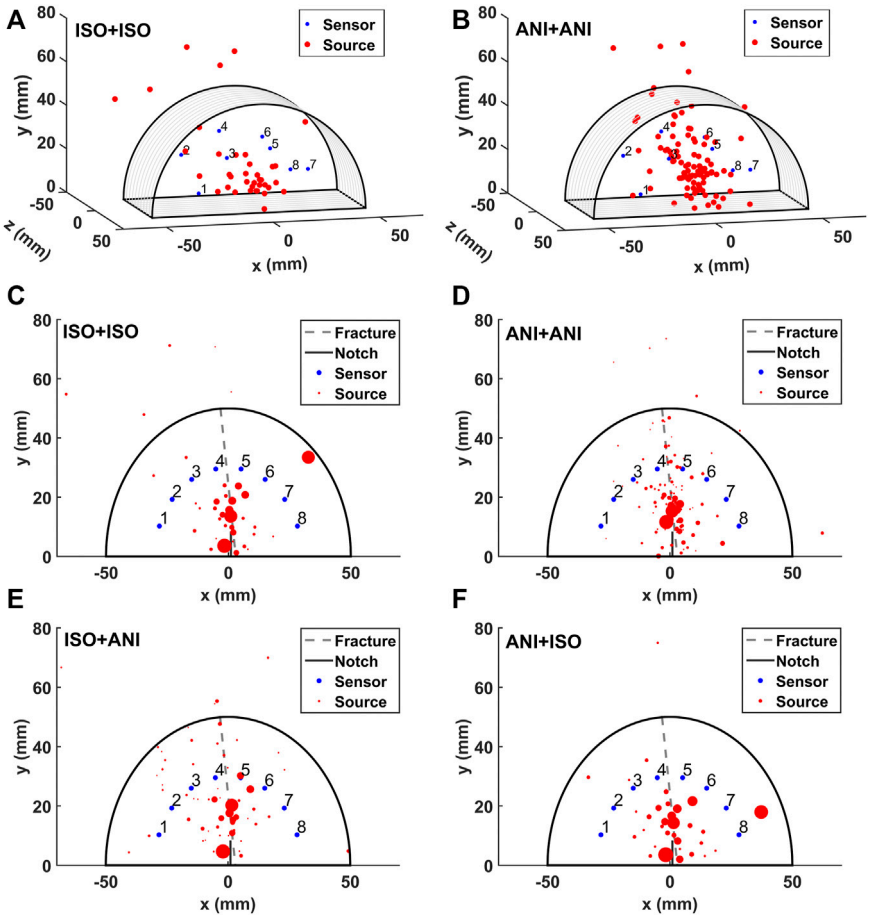

FIGURE 10 | Source location results (3D display) using **(A)** an isotropic matching and isotropic location (ISO+ISO) method and **(B)** an anisotropic matching and anisotropic location (ANI+ANI) method. Comparison of fracture and location results (Front view) using **(C)** isotropic matching and isotropic location (ISO + ISO), **(D)** anisotropic matching and anisotropic location (ANI + ANI), **(E)** isotropic matching and anisotropic location (ISO + ANI), and **(F)** anisotropic matching and isotropic location (ANI + ISO). The gray dashed lines represent the fracture, and the magnitude of source events is displayed using dots of various sizes.

angles are in a wide range (**Figure 8A**). As discussed in **Eq. 2**, the velocity of propagation of signals $V_p(\alpha)$ depends on the phase angle. Directional sines and cosines of the ith sensor relative to the jth sensor are respectively equal,

$$\sin\alpha = \sqrt{\left(x_i - x_j\right)^2 + \left(y_i - y_j\right)^2} \Big/ R_{ij} \; and \; \cos\alpha = \left(z_i - z_j\right) \Big/ R_{ij}, \tag{4}$$

where (x_i, y_i, z_i) and (x_j, y_j, z_j) are the coordinates of the ith and the jth sensor, respectively, and R_{ij} represents the linear distance between any of the two sensors. **Figure 8B** shows the calculated value of α of either of two sensors using **Eq. 4**. **Figure 8C** shows calculated $V_P(\alpha)$ using the formula **Eq. 2** based on ultrasonic measurements. The time threshold Δt is now updated as

$$\Delta t_{ij} = R_{ij} \big/ V_p(\alpha), \tag{5}$$

and the new matching condition is

$$\left|t_i - t_j\right| \le \Delta t_{ij}. \tag{6}$$

The calculated value of Δt_{ij} between any of two sensors is shown in **Figure 8D**. The time differences between the two sensors range from 0 to 20 μs, which are less than the isotropic Δt (30 μs).

Compared to the initial results, using the improved matching condition that takes into account the impact of anisotropy, fewer signals are matched (**Figures 7F,G**). Six signals are matched for event No. 4, which is still recognized as a valid AE event, while only three signals are matched for event No. 12 and thus cannot be used for locating since the number of signals is less than four. In general, the results of anisotropic matching remove redundant events and thus reduce the total number of effective events (**Figure 9A**). A total of 179 valid events were obtained using event-matching without taking into account the anisotropy effect, and a total of 153 valid events are obtained using the new event-matching method taking into account velocity anisotropy. In particular, the number of events received by the four sensors is significantly reduced (**Figure 9B**). The reason is because that the

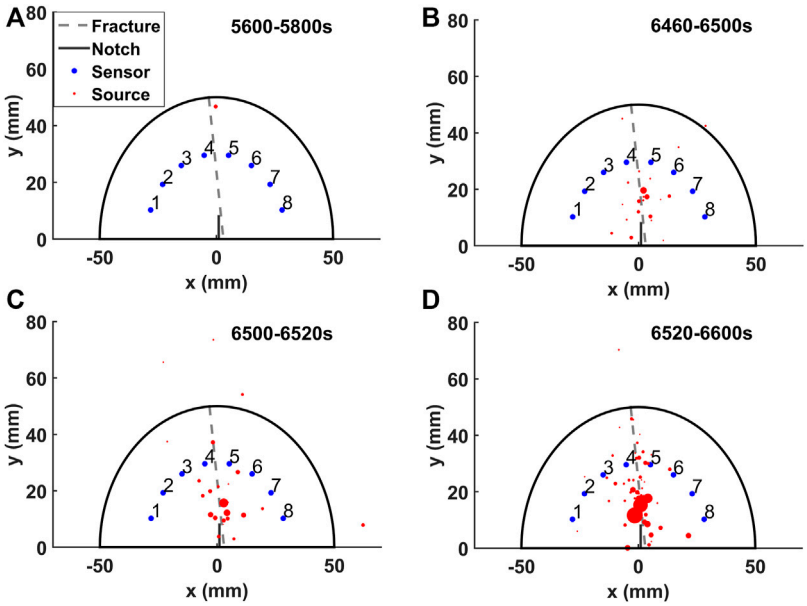

FIGURE 11 | Located AE events at different fracturing times **(A)** 5600–5800s, **(B)** 6460–6500s, **(C)** 6500–6520s, **(D)** 6520–6600s.

anisotropic method uses a stricter threshold (Δt has a lower value) than the isotropic method since the latter's time threshold is calculated using a constant and relatively low velocity measured normal to the layer (0^o as shown in **Figure 2**), while the former's time threshold calculated using higher velocity depending on the direction.

5 SOURCE LOCATION INCLUDING VELOCITY ANISOTROPY

The source location can be determined by the source parameters inversion based on the known observational data. Source parameters, including coordinates and time of fracture initiation, can be estimated by resolving an inconsistent linear system (Geiger, 1912). As for an anisotropic medium, the function of the arrival time of the kth sensor f_k is expressed as

$$f_k(\mathbf{m}) = t + \frac{1}{V(\alpha_k)}\sqrt{(x_k - x)^2 + (y_k - y)^2 + (z_k - z)^2}, \quad (7)$$

where $\mathbf{m} = (t, x, y, z)^T$ is the vector of the source parameters in terms of the origin time t and source coordinates (x, y, z) to be inverted, $V(\alpha_k)$ is the calculated velocity based on ultrasonic measurements, and α_k is the angle of the kth sensor to the Z axis (**Figure 8A**), which can be expressed as

$$\sin\alpha_k = \sqrt{(x_k - x)^2 + (y_k - y)^2}\Big/ l \text{ and } \cos\alpha_k = (z_k - z)/l, \quad (8)$$

where $l = \sqrt{(x_k - x)^2 + (y_k - y)^2 + (z_k - z)^2}$. Given a certain point $\mathbf{m_0} = (t_0, x_0, y_0, z_0)^T$, $f_k(\mathbf{m})$ can be expanded using the first-order Taylor series as

$$f_k(\mathbf{m}) \approx f_k(\mathbf{m}_0) + \mathrm{A}(\mathbf{m} - \mathbf{m}_0), \quad (9)$$

where $\mathrm{A} = \begin{bmatrix} \frac{\partial f_1}{\partial x} & \frac{\partial f_1}{\partial y} & \frac{\partial f_1}{\partial z} & \frac{\partial f_1}{\partial t} \\ \vdots & \vdots & \vdots & \vdots \\ \frac{\partial f_k}{\partial x} & \frac{\partial f_k}{\partial y} & \frac{\partial f_k}{\partial z} & \frac{\partial f_k}{\partial t} \end{bmatrix}$. The source parameter update $\Delta\mathbf{m} = \mathbf{m} - \mathbf{m}_0$ can be recovered as

$$\Delta\mathbf{m} = \left(\mathbf{A}^{\mathrm{T}}\mathbf{A}\right)^{-1}\mathbf{A}^{\mathrm{T}}\Delta f_k, \quad (10)$$

where $\Delta f_k = f_k(\mathbf{m}) - f_k(\mathbf{m}_0)$, and k is greater than or equal to 4. The vector of the source parameters is solved iteratively using the formula **Eq. 11** until the specified error criterion is met

$$\mathbf{m}_{n+1} = \mathbf{m}_n + \Delta\mathbf{m}_n, \quad (11)$$

where n stands for the number of iteration.

This method is applied to experimental AE data. We compare the location results using isotropic velocity and anisotropic velocity, as shown in **Figures 10A,B**. These results are also calibrated with the actual fracture distribution from CT scanning as shown in **Figures 10C,D**, in which the amplitude of source events is displayed using varied size of dots. The valid location results must satisfy in the spatial domain $-50mm \le x \le 50mm$, $0 \le y \le 50mm$ and $-25mm \le z \le 25mm$. Although 179 events are matched using the isotropic condition, only 40 sources are located using the isotropic location method, in which 31 sources are within the valid spatial domain (**Figures 10A,C**); while for 153 events matched

using the anisotropic condition, 99 sources are located using the anisotropic location method, in which 71 sources are inside the valid spatial domain (**Figures 10B,D**). The number of located sources using the isotropic method is much less than that using the anisotropic method. In addition, the located sources using anisotropic velocity are better aligned with the fracture distribution, and the strong source events (displayed with larger dots) are more focused on the starting position of the fractures. To further demonstrate the result, we show four results using different processes (**Figures 10C–F**): isotropic matching and isotropic location (ISO + ISO), anisotropic matching and anisotropic location (ANI + ANI), isotropic matching and anisotropic location (ISO + ANI), and anisotropic matching and isotropic location (ANI + ISO). The located sources of anisotropic matching and anisotropic location show the best agreement with the CT scanning results in terms of fracture distribution and starting position. Therefore, it is very important to take into account the influence of anisotropy on the velocity for both AE event location and event-matching. Although there are several sources of weak-amplitude located outside the semicircle sample (**Figures 10B,D**), this could be improved by more accurate arrival times selection and more receivers with wider geometry (receivers are placed only on planes Z = −25 mm and Z = 25 mm in this study).

Finally, we analyze the located AE events at different stages of fracture, as shown in **Figure 11**. The first AE event is detected at 5800s after loading (**Figure 11A**). After a quiet period of about 10 min, several acoustic emission events occurred during the 6460–6500s period (**Figure 11B**). These events appear around the fracture, but their distribution does not follow the strike of the fracture. In the period of 6500–6600s (**Figures 11C,D**), a large number of acoustic emission events are detected that developed along the fracture.

6 CONCLUSION

Event-matching is a necessary process for pinpointing a location. Traditional methods of event-matching and location can be affected by velocity anisotropy, leading to further unreliable source location results. In the event-matching process, if velocity anisotropy is ignored, many redundant events or false AE events will be matched. Most of the source points detected by these false events are outside the sample, and the location results are incompatible with fracture distribution. In this article, we analyze the effect of anisotropy on the results of event-matching and location based on the three-point bend AE experiment. We achieve the event-matching and location taking into account the correction for anisotropic velocity, increasing the ratio of the number of detected sources to valid events, which may better help us in determining fracture characteristics. Real acoustic emission data applications show a clear improvement in location results over isotropic Geiger's results. The location results are also calibrated by CT scanning results, which show good consistency and confirm the improvement in fracture characteristics. In fact, both the velocity model and the sensor geometry have a large impact on the location results. If the sensors are distributed over a wide range of directions, we must not only take into account the anisotropy of the velocity model but also consider the anisotropy of velocity in event-matching.

DATA AVAILABILITY STATEMENT

The raw data supporting the conclusion of this article will be made available by the authors, without undue reservation.

AUTHOR CONTRIBUTIONS

PW: acquisition and processing of AE data, data presentation, methodology, and original draft; FZ: the conception and design of the study, reviewing and editing, and supervision; X-YL: conceptualization, collected important background information, and manuscript editing.

FUNDING

This work was supported by the National Natural Science Foundation of China (U19B6003, 42122029) and the Strategic Cooperation Technology Projects of CNPC and CUPB (ZLZX2020-03).

REFERENCES

Akram, J., and Eaton, D. W. (2016). A Review and Appraisal of Arrival-Time Picking Methods for Downhole Microseismic Data. *Geophysics* 81 (2), KS67–KS87. doi:10.1190/geo2014-0500.1

Alkhalifah, T. (1998). Acoustic Approximations for Processing in Transversely Isotropic media. *Geophysics* 63 (2), 623–631. doi:10.1190/1.1444361

Feng, X.-T., Young, R. P., Reyes-Montes, J. M., Aydan, Ö., Ishida, T., Liu, J.-P., et al. (2019). ISRM Suggested Method for *In Situ* Acoustic Emission Monitoring of the Fracturing Process in Rock Masses. *Rock Mech. Rock Eng.* 52 (5), 1395–1414. doi:10.1007/s00603-019-01774-z

Ge, M. C. (2013). Analysis of Source Location Algorithms Part II: Iterative Methods. *J. Acoust. Emission* 21, 29–51.

Geiger, L. (1912). Probability Method for the Determination of Earthquake Epicenters from the Arrival Time Only. *Bull. St. Louis Univ.* 8, 60–71.

Gibbons, S. J., and Ringdal, F. (2006). The Detection of Low Magnitude Seismic Events Using Array-Based Waveform Correlation. *Geophys. J. Int.* 165 (1), 149–166. doi:10.1111/j.1365-246x.2006.02865.x

Jin, S., and Stovas, A. (2020). S-wave in 2D Acoustic Transversely Isotropic media with a Tilted Symmetry axis. *Geophys. Prospecting* 68 (2), 483–500. doi:10.1111/1365-2478.12856

Jin, S., and Stovas, A. (2018). S-wave Kinematics in Acoustic Transversely Isotropic media with a Vertical Symmetry axis. *Geophys. Prospecting* 66 (6), 1123–1137. doi:10.1111/1365-2478.12635

King, A., and Talebi, S. (2007). Anisotropy Effects on Microseismic Event Location. *Pure Appl. Geophys.* 164 (11), 2141–2156. doi:10.1007/s00024-007-0266-8

Li, J. H., and Qi, G. (2009). Improving Source Location Accuracy of Acoustic Emission in Complicated Structures. *Journal of Nondestructive Evaluation* 28, 1–8. doi:10.1007/s10921-009-0042-z

Liu, Z., Zhang, F., and Li, X. (2019). Elastic Anisotropy and its Influencing Factors in Organic-Rich marine Shale of Southern China. *Sci. China Earth Sci.* 62, 1805–1818. doi:10.1007/s11430-019-9449-7

Lonardelli, I., Wenk, H.-R., and Ren, Y. (2007). Preferred Orientation and Elastic Anisotropy in Shales. *Geophysics* 72, D33–D40. doi:10.1190/1.2435966

López Comino, J. A., Heimann, S., Cesca, S., Milkereit, C., Dahm, T., and Zang, A. (2017). Automated Full Waveform Detection and Location Algorithm of Acoustic Emissions from Hydraulic Fracturing Experiment. *Procedia Engineering* 191, 697–702. doi:10.1016/j.proeng.2017.05.234

Maeda, N. (1985). A Method for Reading and Checking Phase Time in Auto-Processing System of Seismic Wave Data. *Jssj* 38, 365–379. doi:10.4294/zisin1948.38.3_365

Mavko, G., Mukerji, T., and Dvorkin, J. (2003). *The Rock Physics Handbook-Tools for Seismic in Porous media*. Cambridge University Press.

Maxwell, S. C., Bennett, L., and Jones, M. (2010). *Anisotropic Velocity Modeling for Microseismic Processing: Part 1—Impact of Velocity Model Uncertainty: SEG Technical Program Expanded Abstracts 2010*. Denver,Colorado: Soc. Expl. Geophys., 2130–2134.

Song, F., Kuleli, H. S., Toksöz, M. N., Ay, E., and Zhang, H. (2010). An Improved Method for Hydrofracture-Induced Microseismic Event Detection and Phase Picking. *Geophysics* 75 (6), A47–A52. doi:10.1190/1.3484716

Thomsen, L. (1986). Weak Elastic Anisotropy. *Geophysics* 51 (10), 1954–1966. doi:10.1190/1.1442051

Van Dok, R., Fuller, B., Engelbrecht, L., Sterling, M., and Hipoint, A. (2011). Seismic Anisotropy in Microseismic Event Location Analysis. *The Leading Edge* 30 (7), 766–770. doi:10.1190/1.3609091

Vernik, L., and Nur, A. (1992). Ultrasonic Velocity and Anisotropy of Hydrocarbon Source Rocks. *Geophysics* 57 (5), 727–735. doi:10.1190/1.1443286

Wang, Z. (2002). Seismic Anisotropy in Sedimentary Rocks, Part 1: A Single-plug Laboratory Method. *Geophysics* 67 (5), 1415–1422. doi:10.1190/1.1512787

Wuestefeld, A., Greve, S. M., Näsholm, S. P., and Oye, V. (2018). Benchmarking Earthquake Location Algorithms: A Synthetic Comparison. *Geophysics* 83 (4), KS35–KS47. doi:10.1190/geo2017-0317.1

Zhang, F. (2019). A Modified Rock Physics Model of Overmature Organic-Rich Shale: Application to Anisotropy Parameter Prediction from Well Logs. *J. Geophys. Eng.* 16 (1), 92–104. doi:10.1093/jge/gxy008

Zhang, F. (2017). Estimation of Anisotropy Parameters for Shales Based on an Improved Rock Physics Model, Part 2: Case Study. *J. Geophys. Eng.* 14, 238–254. doi:10.1088/1742-2140/aa5afa

Zhang, F., Li, X.-y., and Qian, K. (2017). Estimation of Anisotropy Parameters for Shale Based on an Improved Rock Physics Model, Part 1: Theory. *J. Geophys. Eng.* 14, 143–158. doi:10.1088/1742-2140/14/1/143

Zhang, H. L., Zhu, G. M., and Wang, Y. H. (2013). Automatic Microseismic Event Detection and Picking Method. *Geophys. Geochemical Exploration* 37 (2), 269–273.

Zhou, Z. L., Zhou, J., Dong, L. J., Cai, X., Rui, Y. C., and Ke, C. T. (2017). Experimental Study on the Location of an Acoustic Emission Source Considering Refraction in Different media. *Sci. Rep.* 7 (1), 7472. doi:10.1038/s41598-017-07371-w

Conflict of Interest: The authors declare that the research was conducted in the absence of any commercial or financial relationships that could be construed as a potential conflict of interest.

Publisher's Note: All claims expressed in this article are solely those of the authors and do not necessarily represent those of their affiliated organizations, or those of the publisher, the editors, and the reviewers. Any product that may be evaluated in this article, or claim that may be made by its manufacturer, is not guaranteed or endorsed by the publisher.

frontiers in Earth Science

ORIGINAL RESEARCH
published: 10 March 2022
doi: 10.3389/feart.2022.846034

Diffraction Extraction and Least-Squares Reverse Time Migration Imaging for the Fault-Karst Structure With Adaptive Sampling Strategy

Liang Chen, Jianping Huang, Cheng Song and Jiale Han*

Key Laboratory of Deep Oil and Gas, China University of Petroleum (East China), Qingdao, China

The ultra-deep fault-karst structure discovered in the Tarim Basin in Western China is a fractured-vuggy carbonate reservoir with great potential for development. The diffraction generated by fractures, small-scale caves and vugs is often used for reservoir identification and seismic interpretation. Since the diffraction is much weaker than the reflection, it is difficult to separate the diffraction from the full wavefield. We use a plane-wave destruction (PWD) filter to extract the diffraction from the full data. In order to obtain a high-accuracy and amplitude-preserving imaging profile, we use the least-squares reverse time migration (LSRTM) method to image the separated diffraction. The large amount of calculation is the most challenging problem of the LSRTM algorithm. In view of this, we develop an adaptive sampling strategy to improve computing efficiency and reduce memory requirement. We use a fault model, a vugs-fractures model, and a fault-karst model to demonstrate the effectiveness and practicability of the proposed method. The numerical examples show that the proposed method can enhance the imaging resolution of the fault-karst structure and save computing cost without losing accuracy. In addition, a test on field data processing demonstrates the advantages of our algorithm.

Keywords: fault-karst structure, ultra-deep reservoir, least-squares reverse time migration, diffraction separation, adaptive sampling

OPEN ACCESS

Edited by:
Nicola Alessandro Pino, National Institute of Geophysics and Volcanology (INGV), Italy

Reviewed by:
Jiangjie Zhang, Institute of Geology and Geophysics (CAS), China
Jiaze He, University of Alabama, United States

****Correspondence:***
Jianping Huang
jphuang@upc.edu.cn

Specialty section:
This article was submitted to Solid Earth Geophysics, a section of the journal Frontiers in Earth Science

Received: *30 December 2021*
Accepted: *31 January 2022*
Published: *10 March 2022*

Citation:
Chen L, Huang J, Song C and Han J (2022) Diffraction Extraction and Least-Squares Reverse Time Migration Imaging for the Fault-Karst Structure With Adaptive Sampling Strategy. Front. Earth Sci. 10:846034. doi: 10.3389/feart.2022.846034

INTRODUCTION

The marine carbonate reservoirs have produced abundant oil and gas resources globally (Loucks and Anderson, 1985; Soudet et al., 1994; Tian et al., 2016). Their formation is related to faulting and dissolution. Different from conventional fractured carbonate reservoirs, the ultra-deep fault-karst reservoirs discovered in the Shunbei area of the Tarim Basin are controlled by large-scale faults, karstification and deep hydrothermal reforming (Li et al., 2019). The reservoirs are dominated by various irregular vugs and fractures occurring along the large-scale strike-slip faults or the associated secondary faults. According to structural features and controlling factors, Lu et al. (2015) first proposed the theoretical concept of fault-karst traps, and divided the fault-karst reservoirs into three categories. Ma et al. (2019) summarized the reflection characteristics of the fault-karst structure using forward modeling, which provides guidance for its identification. However, due to deep burial depth and complex inner structure, the diffraction generated by vugs or fractures is much weaker than the reflection, making it difficult to obtain high-resolution seismic imaging profile (Khaidukov et al.,

2004; Kong et al., 2017). Furthermore, the large amount of computational cost caused by large-scale and high-precision imaging process is inevitable. In view of the above, a more accurate and efficient imaging method is needed to support the exploration and development of the ultra-deep fault-karst reservoirs.

Separating the diffraction from full wavefield is very important for the high-resolution imaging of the fault-karst structure. The differences between reflected waves and diffracted waves in kinematics are substantial in the common-shot gathers, which allows us to extract the diffraction from the shot records (Landa et al., 1987). Dip filtering (Bansal and Imhof, 2005), focusing and defocusing (Khaidukov et al., 2004) hybrid Radon transform (Klokov et al., 2010), and PWD filtering (Fomel, 2002; Taner et al., 2006) have been developed for separating diffraction. These methods utilized the fact that the travel time curve of the diffracted wave is quasi-parabolic in the common-shot gathers while the reflected wave is quasi-linear. The PWD filtering method can effectively eliminate artifacts and retain more diffraction energy. Therefore, it has been successfully applied to several 3D field datasets (Burnett et al., 2015; Tyiasning et al., 2016). Another advantage of the PWD filtering method is that the separated diffraction can be directly used for pre-stack migration, avoiding complex data processing.

Reverse time migration (RTM), which is based on two-way wave equation, can effectively migrate reflection data and describe subsurface geological structures (Baysal et al., 1983; Sun and McMechan, 1986). LSRTM can be regarded as the optimization algorithm of RTM. It employs the least-squares inversion theory that continuously fits the error between the linear demigration data and the observed data (Tarantola, 1984; Nemeth et al., 1999; Dai et al., 2012). Compared to RTM, LSRTM can improve migration resolution, balance imaging amplitude, and reduce image artifacts (Dutta and Schuster, 2014; Yang et al., 2019). Nevertheless, this algorithm requires a huge amount of storage space and computational effort. Some researchers have tried to use different acceleration algorithms to improve LSRTM, such as multi-source and plane-wave encoding methods (Dai et al., 2012; Huang and Schuster, 2012; Dai and Schuster 2013). However, the crosstalk noise caused by different sources is hard to be eliminated.

Variable-grid methods, which are implemented by decreasing the grid points of a model, can reduce memory costs and improve computational efficiency (Moczo, 1989; Jastram and Behle, 1992; Fan et al., 2015; Huang et al., 2015). Several variable-grid methods have shown their potential in imaging. Li et al. (2014) developed a dual-variable grid algorithm and applied it to RTM. Li et al. (2017) introduced the idea of pseudo-time domain (Alkhalifah, 2003; Ma and Alkhalifah, 2013) into LSRTM, which improves imaging efficiency by reducing vertical grid points (Wang et al., 2020). Proposed an adaptive grid discretization strategy and applied it to 3D LSRTM. Most variable-grid methods always resample a local region. Due to the inherent difficulty of automatically discretizing spatial grid, local variable-grid methods have not been widely used in seismic data processing.

Diffraction extraction, high-resolution imaging, and cost control are key to accurate exploration of the ultra-deep fault-karst reservoirs. In this paper, we first apply the PWD filter method (Taner et al., 2006) to extract the diffraction from the full wavefield. Then, the diffraction-based LSRTM (D-LSRTM) algorithm are used to image the diffraction. In order to improve the computing efficiency, we develop an efficient variable-grid D-LSRTM method based on a globally adaptive sampling strategy (AS-D-LSRTM). Finally, four numerical tests are used to prove the effectiveness and robustness of the proposed method.

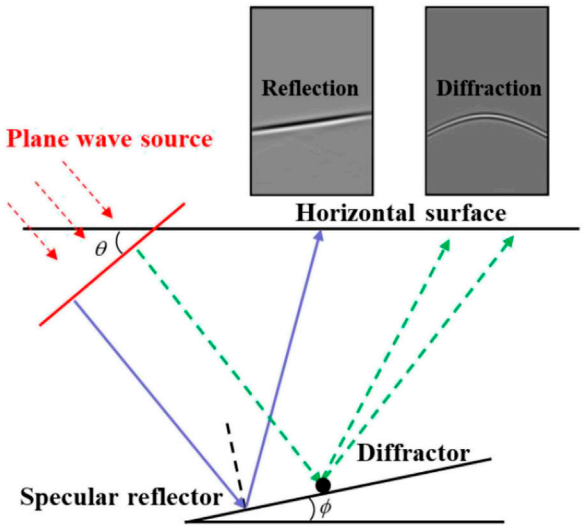

FIGURE 1 | Comparison of the reflection and the diffraction. As illuminated by the plane wave source, the seismic response of the reflection is linear while the response of the diffraction is hyperbolic.

The complete workflow of the AS-D-LSRTM method is divided into the following steps: 1) separating the diffraction from the full wavefield by PWD filter method; 2) performing irregular grid discretization applying adaptive sampling; 3) imaging the diffraction using LSRTM.

The Principle of Diffraction Separation

In the common-shot gathers, the reflection and the diffraction generated by a point source share similar kinematic characteristics, which are difficult to be distinguished (Landa et al., 1987). While when the incident wave is a plane wave, the travel time curve of the reflected wave can be written as:

$$t_R = \frac{\cos\theta \sin(\theta - 2\phi)}{v\cos(\theta - \phi)} \cdot x + \frac{2h}{v}\left[\cos\theta\cos(\theta - \phi) - \frac{cos\phi\cos(\theta - \phi) - \cos\theta}{\cos(\theta - \phi)}\right] \quad (1)$$

where t_R denotes the travel time and v denotes the medium velocity. The specific meaning of θ and ϕ is shown in **Figure 1**.

The travel time curve of the diffracted wave can be expressed as:

$$\frac{(t_D - h/v)^2}{h^2\cos^2\theta/v^2} - \frac{(x - h\sin\theta)^2}{h^2\cos^2\theta} = 1 \quad (2)$$

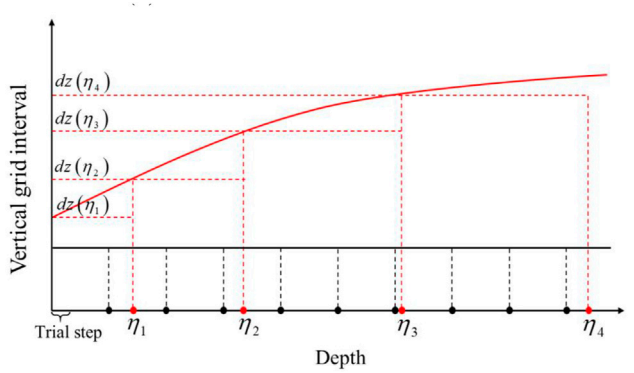

FIGURE 2 | Diagrammatic sketch of the adaptive sampling method.

According to **Eqs. 1**, **2** and **Figure 1**, the seismic response of the reflection is linear while the response of the diffraction is hyperbolic. Therefore, we can separate the reflection and the diffraction based on the difference of kinematic properties in plane-wave gathers. Firstly, we convert the common-shot gathers into common ray-parameter gathers using tau-p transform (Kappus et al., 1990; Zhang et al., 2005). The tau-p transform equation can be expressed as:

$$P(\tau, p) = \int d(t, x)dx = \int d(\tau + px, x)dx \tag{3}$$

where $d(t, x)$ denotes the seismic shot records in the time-offset $t - x$ domain, and $P(\tau, p)$ is the so-called plane-wave gathers with ray parameter p and time axis τ. Then we use the PWD wave filter proposed by Fomel (2002) to estimate the local dip angle of the diffracted wave and separate it in the tau-p domain. After that, we use the inverse tau-p transform to get the diffraction wavefield in the time-offset domain. The inverse tau-p transform equation is expressed as:

$$d_D(t, x) = \int P(\tau, p)dp = \int P(\tau = t - px, p)dp \tag{4}$$

where $d_D(t, x)$ denotes the shot records of the diffracted wave.

Adaptive Sampling Strategy

In Tarim Basin, where the fractured-vuggy carbonate reservoirs are extensively developed, the surface is often covered by desert and gravel layers with low velocity. In forward modeling and migration, a fine spatial grid must be used to avoid numerical dispersion. However, for the deep region with high velocity, using fine grid is a waste of computing resources. We use an adaptive sampling strategy to solve the above problem.

As shown in **Figure 2**, the horizontal axis denotes depth and the vertical axis represents vertical grid interval. The black dots on the x-axis denote initial vertical grid points. The black solid line denotes initial vertical grid interval, which is fixed. According to the medium velocity and the dominant frequency of the source, we use **Eq. 5** to recalculate the optimal vertical grid interval (The red solid line in **Figure 2**):

$$dz(z) = \frac{v_{\min}(z)}{10 f_m} \tag{5}$$

where $v_{\min}(z)$ denotes the minimum velocity along the depth axis z, f_m is the dominant frequency of the source wavelet, and $dz(z)$ denotes the optimal vertical grid spacing.

We use a rectangular sampling method (Wang et al., 2020) to resample the initial migration model. Firstly, we set a small trial step from $z = 0$ and increase it continuously to get the first grid point η_1, where $\eta_1 = dz(\eta_1)$. Then we repeat the previous step to get the second grid point η_2, where $\eta_2 - \eta_1 = dz(\eta_2) - dz(\eta_1)$. Finally, we repeat the above process to the max depth and obtain a new model. The vertical grid interval of the new model is irregular and it varies with velocity. Note that there is a mapping relationship between the initial model and the new model, we use two different coordinate systems to express it:

$$x = x(\xi, \eta) \tag{6}$$

$$z = z(\xi, \eta) \tag{7}$$

where x and z are the coordinate variables in coordinate system $A(x, z)$, ξ and η are the coordinate variables in coordinate system $B(\xi, \eta)$. The initial model is located in $A(x, z)$ and the new model is located in $B(\xi, \eta)$. The derivation process of the mapping relationship is shown in **Supplementary Appendix SA**.

The acoustic wave equation in 2D heterogeneous isotropic medium in coordinate system $A(x, z)$ can be written as:

$$\frac{1}{v^2}\frac{\partial^2 u}{\partial t^2} = \rho\left(\frac{\partial^2 u}{\partial x^2} + \frac{\partial^2 u}{\partial z^2}\right) + f_s(t) \tag{8}$$

where u denotes acoustic pressure field, t denotes time, ρ denotes medium density, v denotes acoustic velocity, and $f_s(t)$ denotes source function.

Substitute Eq. A-9 and A-10 into **Eq. 8**, we get the expression of **Eq. 8** in coordinate system $B(\xi, \eta)$:

$$\frac{1}{v^2}\frac{\partial^2 u}{\partial t^2} = \rho\left(\frac{\partial^2 u}{\partial \xi^2} + \frac{\partial^2 u}{\partial \eta^2}\frac{1}{z_\eta^2} - \frac{\partial u}{\partial \eta}\frac{z_{\eta\eta}}{z_\eta^3}\right) + f_s(t) \tag{9}$$

where $z_\eta = \partial z/\partial \eta$ and $z_{\eta\eta} = \partial^2 z/\partial \eta^2$ they can be solved by finite-difference method.

Compared to **Eq. 8**, one term is added to **Eq. 9**, which increases the computational cost for one grid point. In fact, the omission of the extra term has little effect on the final imaging results. Therefore, **Eq. 9** is further simplified as:

$$\frac{1}{v^2}\frac{\partial^2 u}{\partial t^2} = \rho\left(\frac{\partial^2 u}{\partial \xi^2} + \frac{\partial^2 u}{\partial \eta^2}\frac{1}{z_\eta^2}\right) + f_s(t) \tag{10}$$

Review of the Principle of LSRTM

LSRTM is considered to be a true amplitude imaging method, which can improve imaging resolution, reduce artifacts, and meet the demand for lithological interpretation.

As shown in **Eq. 11**, the seismic wavefield satisfies the superposition principle:

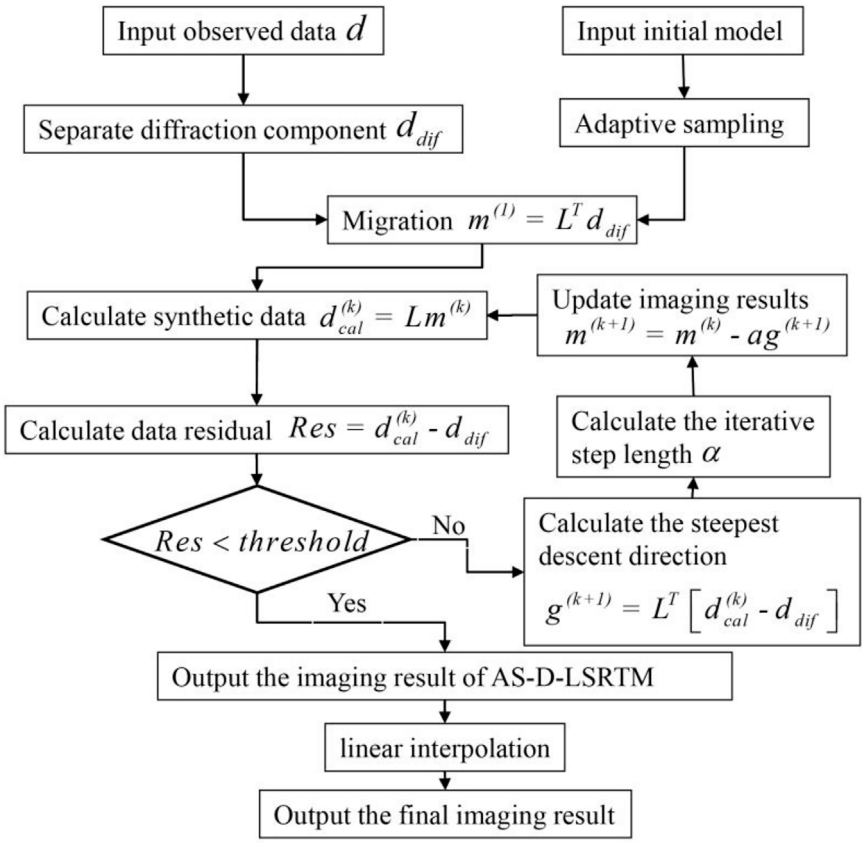

FIGURE 3 | Workflow of AS-D-LSRTM.

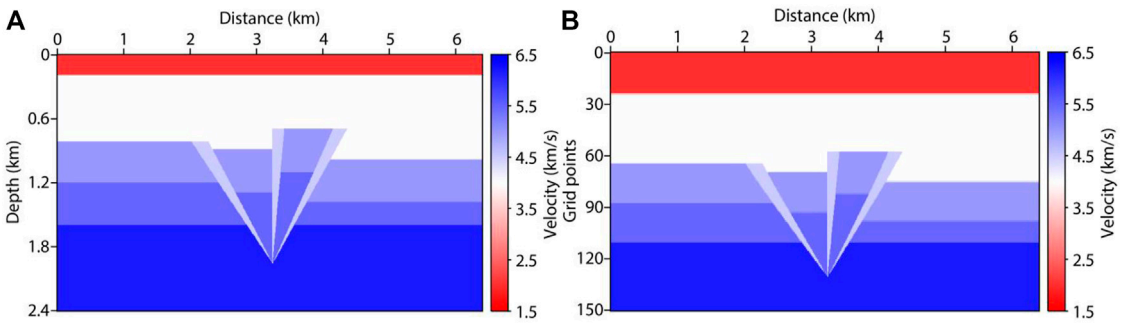

FIGURE 4 | Fault model **(A)** and the resampled model **(B)**.

$$u = u_0 + u_s \tag{11}$$

where u denotes total wavefield, u_0 denotes background wavefield, and u_s denotes perturbation wavefield.

Similarly, the velocity model can be regarded as the superposition of a perturbation model and a smoothed background model,

$$\frac{1}{v^2} = \frac{1}{v_0^2} + \frac{1}{\Delta v^2} \tag{12}$$

u_0 obeys **Eq. 10**:

$$\frac{1}{v^2}\frac{\partial^2 u_0}{\partial t^2} = \rho\left(\frac{\partial^2 u_0}{\partial \xi^2} + \frac{\partial^2 u_0}{\partial \eta^2}\frac{1}{z_\eta^2}\right) + f_s(t) \tag{13}$$

Substitute **Eq. 11** and **Eq. 12** into **Eq. 10**, subtract **Eq. 13**, and apply Born approximation (Dai et al., 2012), we can obtain the control equation of

$$\frac{1}{v_0^2}\frac{\partial^2 u_s}{\partial t^2} = \rho\left(\frac{\partial^2 u_s}{\partial \xi^2} + \frac{\partial^2 u_s}{\partial \eta^2}\frac{1}{z_\eta^2}\right) - \frac{1}{\Delta v^2}\frac{\partial^2 u_0}{\partial t^2} \tag{14}$$

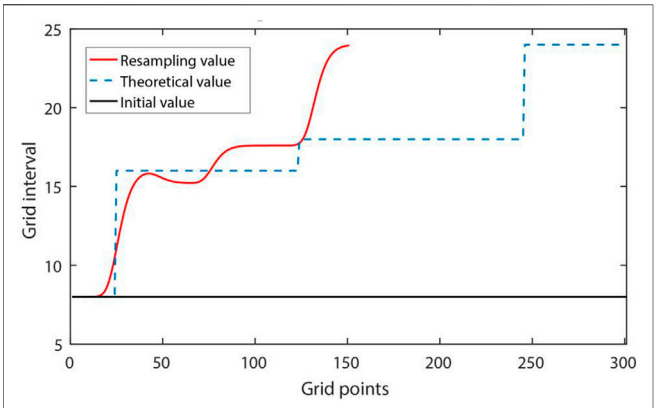

FIGURE 5 | Comparison of vertical grid interval.

Eq. 14 is the Born (linearized) forwarding modeling equation, and it can be rewritten as a matrix:

$$d_s = Lm \tag{15}$$

where L is the Born forwarding modeling operator, m denotes model parameter, and d_s denotes the Born-modeled data. We can get the migration image by using the the RTM operator:

$$m_{mig} = L^T d_s \tag{16}$$

where m_{mig} represents the imaging result. L^T denotes the RTM operator, which is the conjugate transpose of L.

The goal of LSM theory is to minimize the objective function, which is defined as:

$$J(m) = \frac{1}{2}\|Lm - d_{obs}\|_2^2 \tag{17}$$

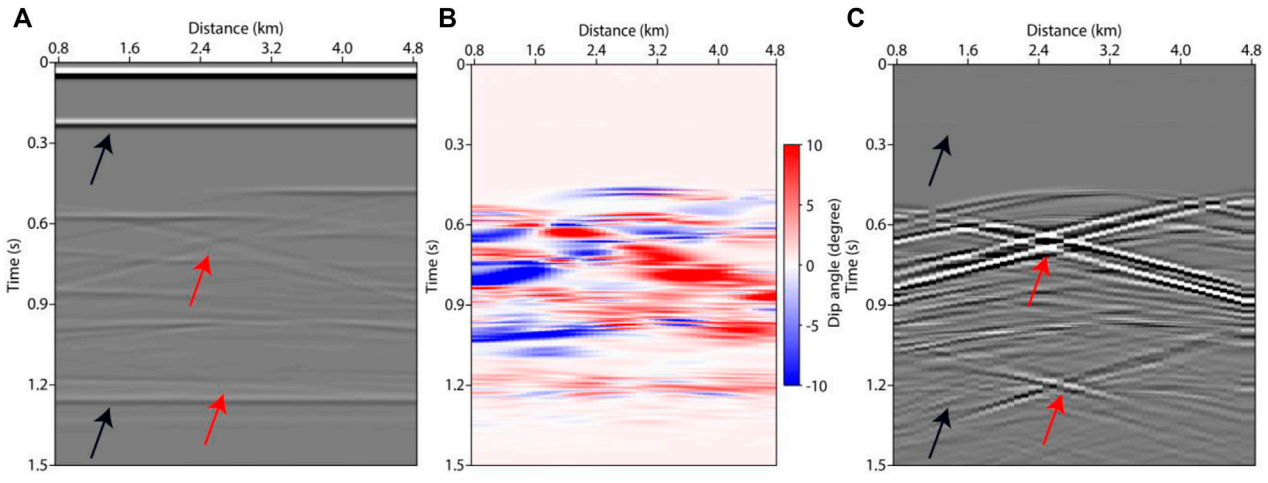

FIGURE 6 | Time sections of the fault model with ray parameter p = 0 ms/m. **(A)** plane-wave section for the full wavefield, **(B)** estimated dip angle field, and **(C)** plane-wave section for the separated diffraction.

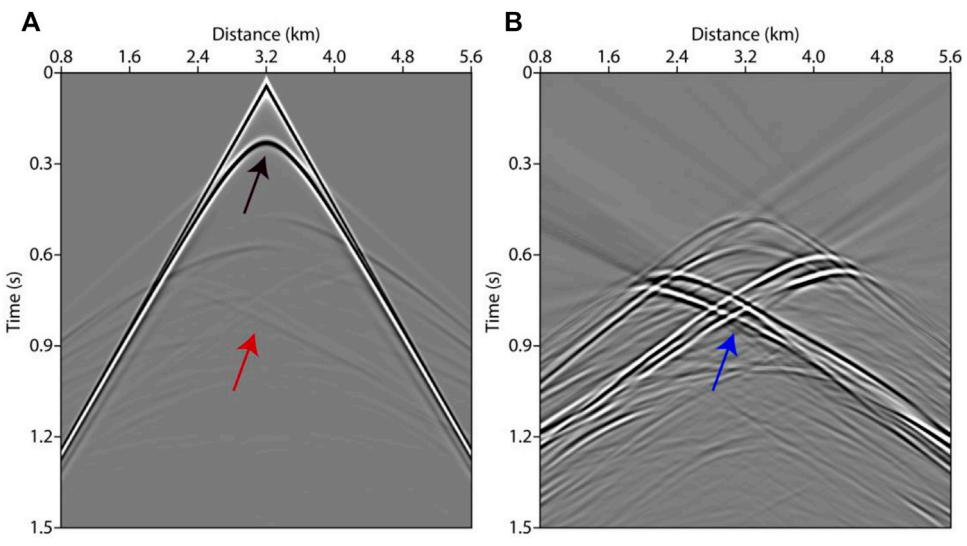

FIGURE 7 | Response of the point source. **(A)** full wavefield, and **(B)** diffraction wavefield.

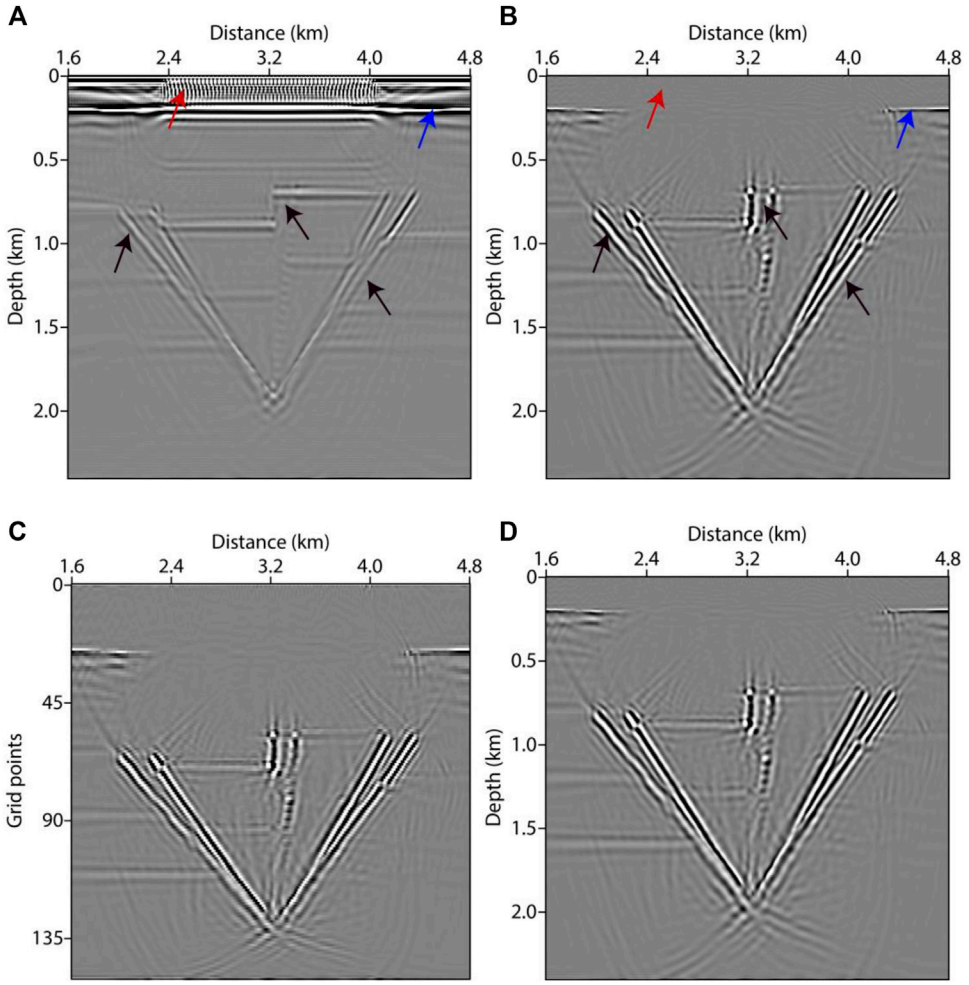

FIGURE 8 | LSRTM images after 30 iterations using different methods. **(A)** F-LSRTM, **(B)** D-LSRTM, **(C)** AS-D-LSRTM, and **(D)** AS-D-LSRTM with linear interpolation.

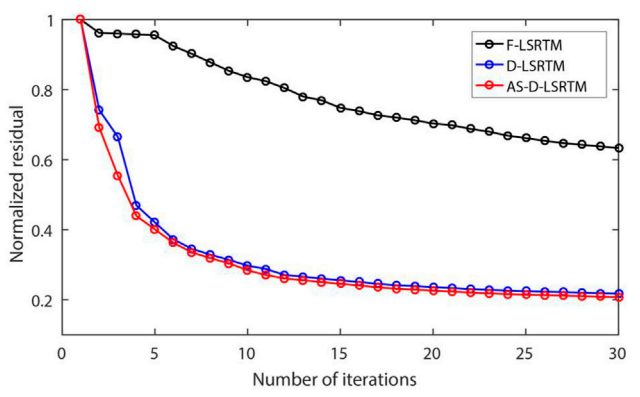

FIGURE 9 | Normalized residual convergence curves of the three methods.

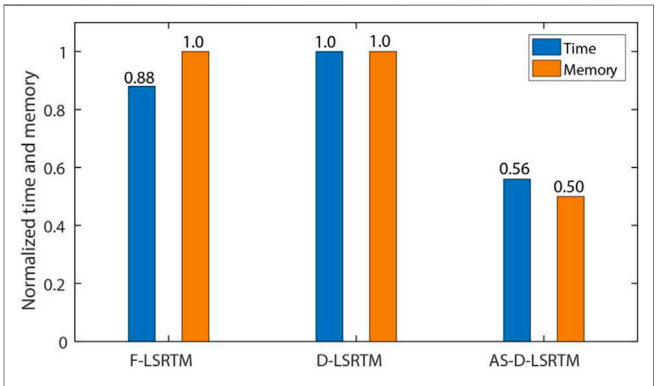

FIGURE 10 | Computing time and memory requirement of the three methods.

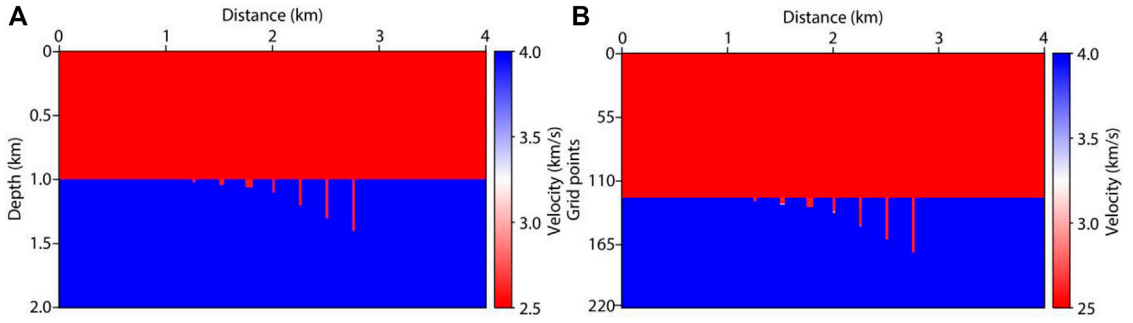

FIGURE 11 | Fractures-vugs model **(A)** and the resampled model **(B)**.

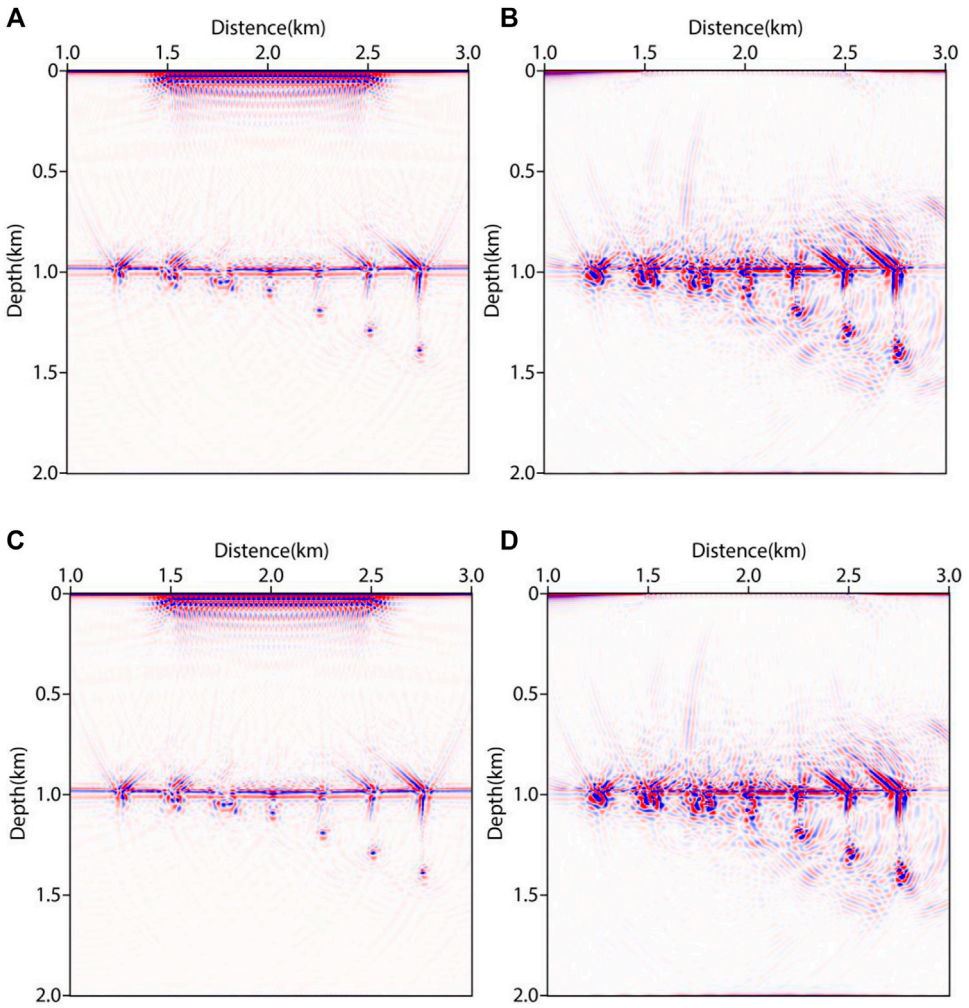

FIGURE 12 | Migration images using different methods after 30 iterations. **(A)** F-LSRTM, **(B)** D-LSRTM, **(C)** AS-F-LSRTM with linear interpolation, and **(D)** AS-D-LSRTM with linear interpolation.

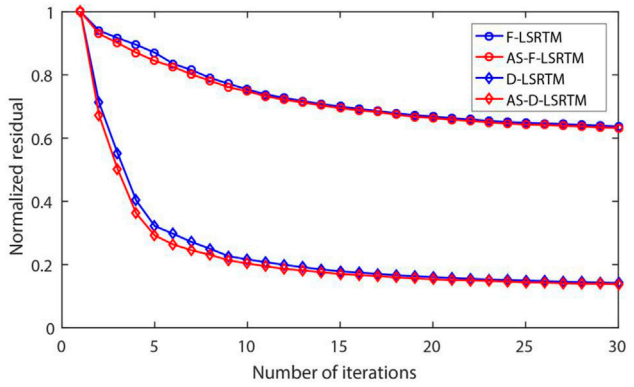

FIGURE 13 | Normalized residual convergence curves of the four methods.

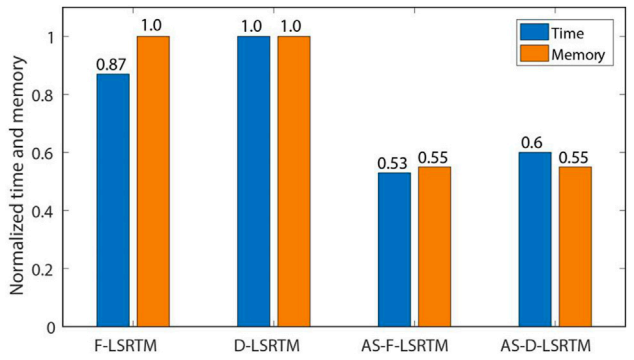

FIGURE 14 | Computing time and memory requirement of the four methods.

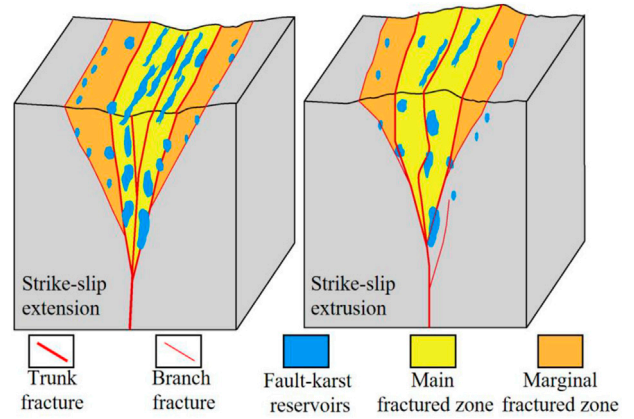

FIGURE 15 | Distribution characteristics of the fault-karst carbonate reservoirs.

where $J(m)$ is the objective function, d_{obs} denotes the observed data, and $\|\cdot\|_2^2$ is the L2-norm of a vector.

We use a conjugate-gradient algorithm (Dai et al., 2012) to solve the model parameter m, which is formulated as:

$$
\begin{aligned}
g^{k+1} &= L^*\left[Lm^k - d_{obs}\right] \\
\beta^{k+1} &= \frac{\left[g^{k+1}\right]^*\left[Cg^{k+1}\right]}{\left[g^k\right]\left[Cg^k\right]} \\
z^{k+1} &= Cg^{k+1} + \beta^{k+1} z^k \\
a^{k+1} &= \frac{\left[z^{k+1}\right]^*\left[g^{k+1}\right]}{\left[Lz^{k+1}\right]^*\left[Lz^{k+1}\right]} \\
m^{k+1} &= m^k - a^{k+1} z^{k+1}
\end{aligned}
\tag{18}
$$

where k and * denote iteration index and conjugate transpose of a matrix, g^k and β^k represent gradient and correction coefficient, z^k and α^k denote conjugate gradient direction and step length, and C denotes precondition operator.

In summary, the implementation of the AS-D-LSRTM method contains four main steps. The first step is to separate diffraction. The second step is to resample the initial model. The third step is to obtain the image after several iterations by LSRTM. Finally, we use linear interpolation to convert the final image from the coordinate system $B(\xi, \eta)$ to coordinate system $A(x, z)$. **Figure 3** shows the complete workflow of AS-D-LSRTM.

NUMERICAL EXAMPLES

In this section, three synthetic examples are used to test the effectiveness of the proposed AS-D-LSRTM in high-resolution imaging. Furthermore, numerical tests on land field data confirm its adaptability for complex structure.

Fault Model

The initial fault model is shown in **Figure 4A**, which has a low-velocity surface layer with velocity of 2000 m/s. It is discretized on a 801 × 301 grid a with grid spacing $dx = dz = 8$ m. The time sampling interval is 0.5 ms and the recording time is 1.5 s. A total of 51 sources are distributed laterally from 2.4 to 4 km. The shot interval is 32 m. There are 601 receivers of each shot and the receiver interval is 8 m. We use a Ricker wavelet as the source, and its dominant frequency is 25 Hz. To improve the computational efficiency, we resample the initial model using the adaptive sampling method. **Figure 4B** shows the resampled model with 151 vertical grid points. From **Figure 4B** we can see that the deep layers with high velocity are compressed. **Figure 5** shows the grid interval comparison of the two models. The black line in **Figure 5** denotes initial vertical grid interval, the blue line denotes theoretical value calculated by **Eq. 5**, and the red line shows the vertical grid interval of the resampled model.

We use the tau-p transform to produce 501 plane-wave time sections with ray parameters ranging from −0.5 to 0.5 ms/m. **Figure 6A** displays a section with ray parameter $p = 0$ ms/m. In **Figure 6A**, the reflection is linear (see the black arrows) and the diffraction is hyperbolic (see the red arrows). **Figure 6B** shows the estimated dip field of **Figure 6A**. Based on the dip angle field shown in **Figure 6B**, we use the PWD filter method to separate the diffraction. **Figure 6C** shows the separated diffraction with ray parameter $p = 0$ ms/m. We can see from **Figure 6C** that the

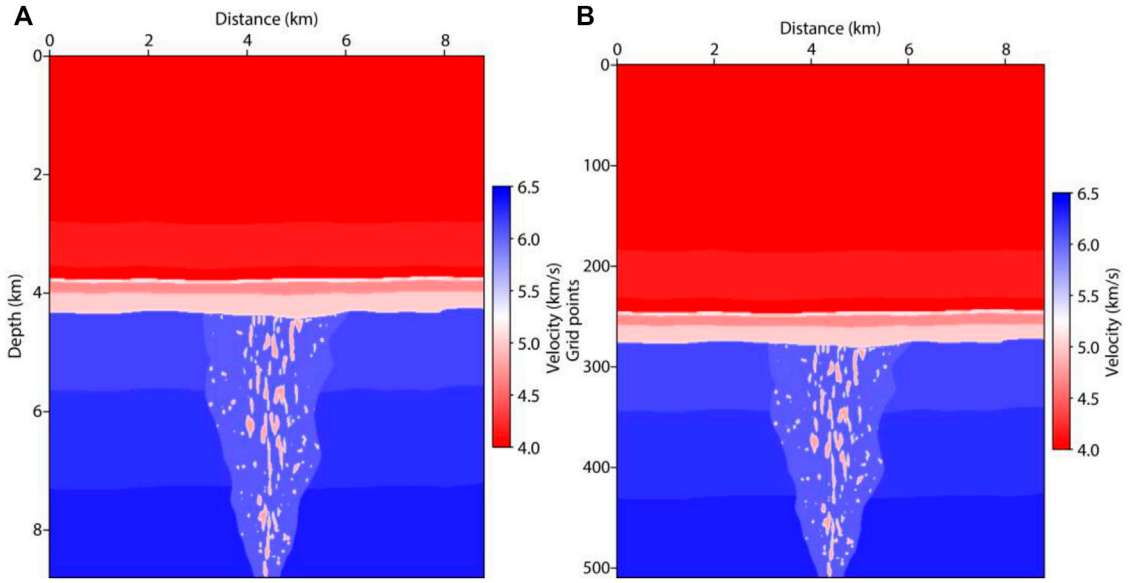

FIGURE 16 | Ultra-deep fault-karst carbonate reservoir model **(A)** and the resampled model **(B)**.

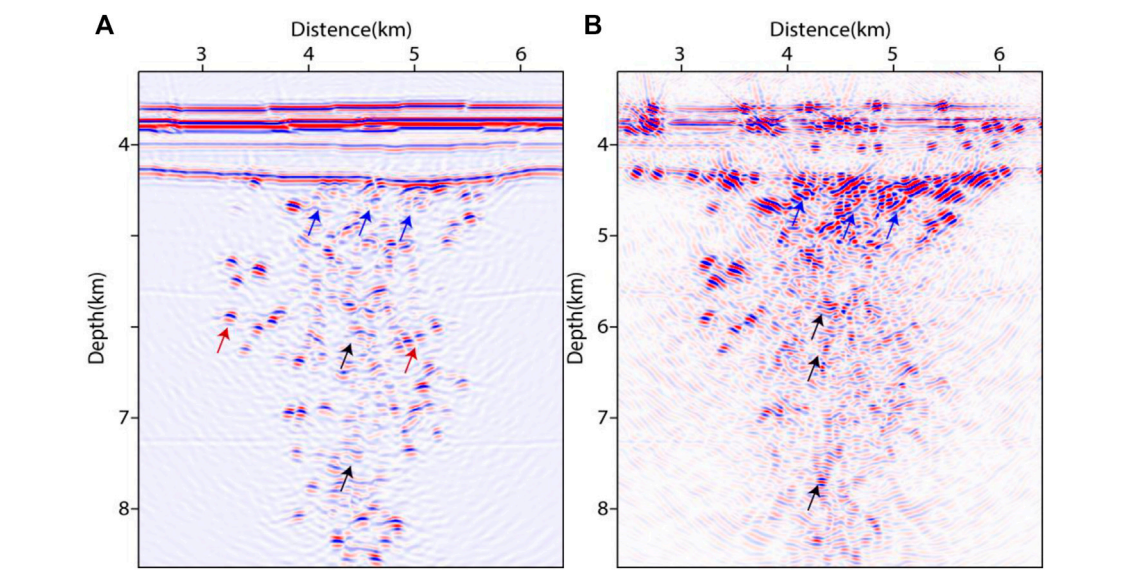

FIGURE 17 | LSRTM images after 20 iterations. **(A)** AS-F-LSRTM and **(B)** AS-D-LSRTM.

reflection is removed while the diffraction is preserved. **Figure 7A** shows the point source response of the full wavefield. In **Figure 7A**, the diffraction energy generated by the inclined faults (the red arrow) is much weaker than that of the layer interface (the black arrow). **Figure 7B** shows the response of the diffraction wavefield. In **Figure 7B**, the reflection is suppressed and the diffraction (the blue arrow) is preserved.

Figures 8A, 8B show the images of full wavefield LSRTM (F-LSRTM) and D-LSRTM after 30 iterations, respectively. In **Figure 8B**, we can see that the acquisition footprints (the red arrow) and the reflection generated by the surface layer (the blue arrow) are almost eliminated. Moreover, the resolution of the fault in **Figure 8B** is higher than that in **Figure 8A** (see the black arrows). **Figure 8C** shows the AS-D-LSRTM image after 30 iterations, and **Figure 8D** shows the final result after linear interpolation. In **Figure 8B**, the artifacts and the diffraction are enhanced simultaneously when the reflection is removed. Nevertheless, the diffraction-based LSRTM results are still focused. **Figure 9** displays the normalized residual convergence curves of F-LSRTM, D-LSRTM, and AS-D-LSRTM. The curves show that the convergence rate of D-LSRTM and AS-D-LSRTM is faster than that of F-LSRTM.

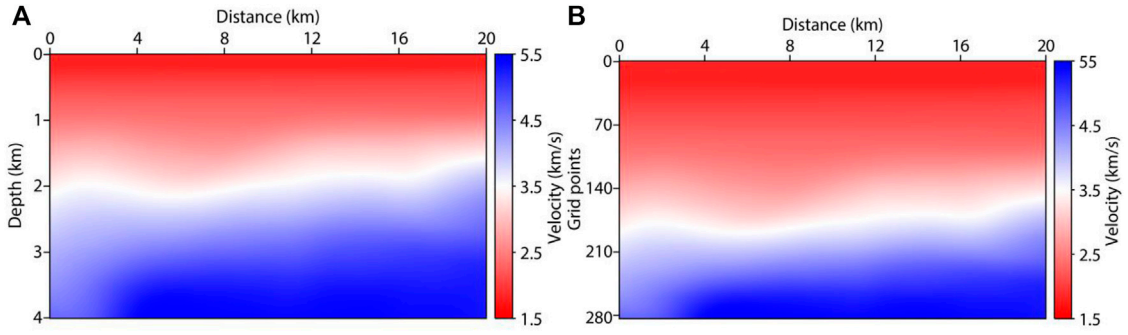

FIGURE 18 | Initial migration velocity model **(A)** and **(B)** the resampled model.

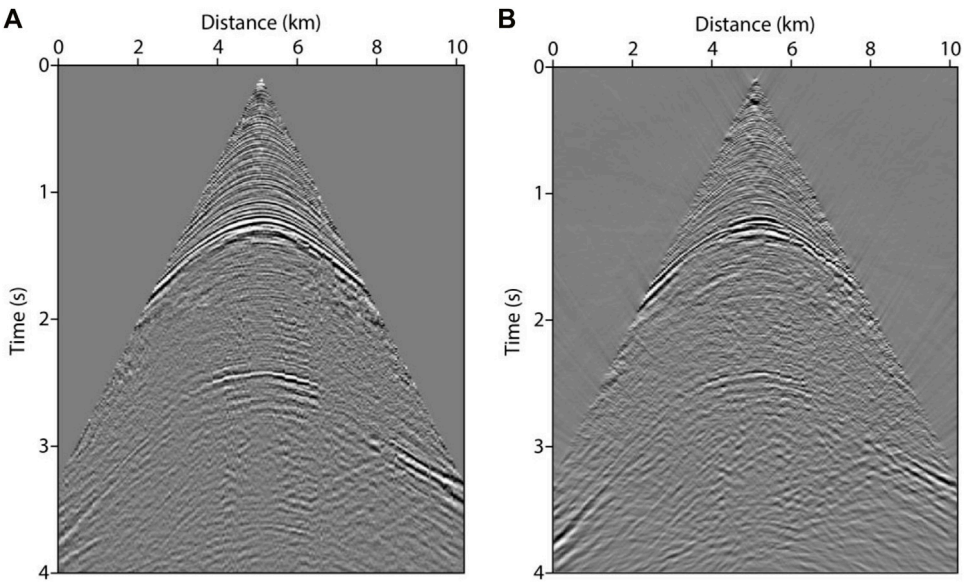

FIGURE 19 | Field shot record. **(A)** full wavefield, and **(B)** diffraction wavefield.

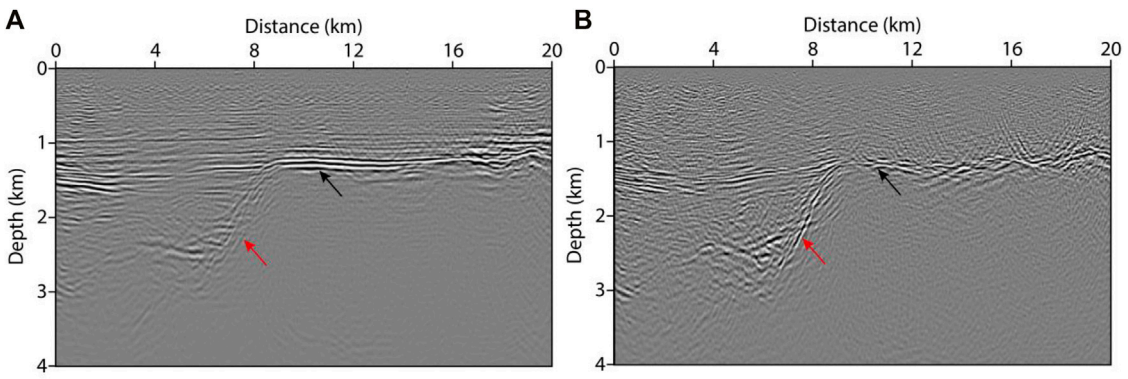

FIGURE 20 | Migration images after 5 iterations using AS-F-LSRTM **(A)** and AS-D-LSRTM **(B)**.

Moreover, the normalized residual of D-LSRTM and AS-D-LSRTM decreases quickly before the 5th iterations and gradually converges to a same value. **Figure 10** shows the normalized computing time and memory footprint of these methods. Compared with D-LSRTM, AS-D-LSRTM can save 44% of computing cost and half of memory requirement without losing accuracy. From the above analysis, we conclude that AS-D-LSRTM is superior to F-LSRTM and D-LSRTM.

Layered Model With Vugs and Fractures

We use a layered model to further verify the effectiveness of the proposed method. **Figure 11A** shows the initial model, which is discretized on a 801 × 401 grid with a grid interval of $dx = dz =$ 5 m. The model has two layers with velocity of 2.5 km/s and 4 km/s, respectively. There are three small-scale vugs and four fractures distributed at the layer interface with velocity of 3 km/s. The vugs are square with side lengths of 20, 40, and 60 m, respectively. The width of the fractures is 20 m and the lengths of them are 100, 200, 300, and 400 m, respectively. **Figure 11B** shows the resampled model (f_m in **Eq. 5** is 30), which has 221 vertical grid points in total. In total, 41 sources are distributed laterally from 1.5 to 2.5 km. Each shot has 601 receivers. The shot interval is 25 m and the receiver interval is 5 m. The time step is 0.3 ms and the recording time is 1.5 s.

In this tests, we apply the adaptive sampling method to F-LSRTM (denoted by AS-F-LSRTM) and D-LSRTM. **Figure 12** shows the images after 30 iterations using different LSRTM methods. In **Figures 12A,C**, the vugs and fractures are imaged successfully, and the bottom of the fractures is shown as a string of beads (Lu et al., 2015). In **Figures 12B,D**, the reflection are restrained and the energy of the diffraction is enhanced.

Figure 13 displays the normalized residual convergence curves of the four methods. The result shows that the convergence rate of D-LSRTM and AS-D-LSRTM is faster than that of F-LSRTM and F-AS-LSRTM. We can see that the convergence curves of D-LSRTM and AS-D-LSRTM are almost coincident after the 16th iteration. **Figure 14** shows the normalized computing cost and storage requirement of the four methods. From **Figures 12–14**, we conclude that the AS-D-LSRTM algorithm is helpful to identify small-scale caves and fractures, and it can greatly save computing resources.

Ultra-Deep Fault-Karst Carbonate Reservoir Model

The fault-karst carbonate reservoirs are usually stripped distribution along the strike-slip fault zone, especially in South Tahe area of Tarim Basin (Ding et al., 2020). According to stress state, the strike-slip fault can be divided into three structural styles, which are translation, extrusion and extension. The oil and gas resources are more abundant in the extension and extrusion section (Cheng et al., 2020). **Figure 15** shows the distribution characteristics of the fault-karst reservoirs. In the extension section (left), large-scale caves are developed near the trunk fracture zone and small-scale vugs are distributed along the branch fracture. In the extrusion section (right), the caves and vugs are mainly distributed along the trunk fracture. According to the characteristics of the fault-karst carbonate reservoirs formed by strike-slip extension, we build an ultra-deep fault-karst model, as shown in **Figure 16A**. The model includes 1101 × 1101 grid points with grid spacing of 8 m. The maximum depth of the fault-karst structure is more than 8 km. **Figure 16B** shows the new model after adaptive sampling. The number of vertical grid points reduces from 1101 to 510.

In numerical tests, a total of 61 sources are distributed laterally from 3.2 to 5.6 km. Each shot has 801 receivers. The shot interval is 40 m and the receiver interval is 8 m. The time step is 0.5 ms and the record time is 4 s. The source is a Ricker wavelet and its dominant frequency is 25 Hz. **Figures 17A,B** show AS-F-LSRTM and AS-D-LSRTM images after 20 iterations, respectively. In **Figure 17A**, some small-scale caves and vugs are shown as strong reflection spots (see the red arrows). However, the reflection energy generated by large-scale caves near the trunk fracture is much weaker (see the black arrows). In addition, the reflection-based LSRTM images cannot correctly describe the distribution and the structural characteristics of the fault-karst reservoirs. For example, the reflection energy of the top of the reservoirs is extremely weak (see the blue arrows in **Figure 17A**). This phenomenon can mislead the prospectors and lead them to miss productive reservoirs. In **Figure 17B**, the diffraction of the trunk fracture is much stronger than that in **Figure 17A** (see the black arrows). Moreover, the top of the reservoirs is easier to identify in **Figure 17B** (see the blue arrows). We conclude that AS-D-LSRTM can enhance the diffraction and improve the imaging resolution of the fault-karst carbonate reservoirs.

Field Data Test

The LSRTM algorithms relies heavily on accurate migration velocity model and high-quality data. In this paper, the proposed AS-D-LSRTM method is also tested on a 2D field dataset to further verify its effectiveness. **Figure 18A** shows the initial migration velocity model, which includes 2001 × 401 grid points with a grid spacing of 10 m. **Figure 18B** shows the variable-grid model after adaptive sampling (n in **Eq. 5** is 10), which is discretized on a 401 × 284 grid. We use the Ricker wavelet with dominant frequency of 20 Hz as the source. Total shots are 100 with irregular distribution and the record time is 4 s. Each shot has 204 receivers and the receiver interval is 50 m. The time sampling interval is 0.5 ms.

Figure 19A shows a single shot record. We apply the PWD filter method to the full-wavefield data and obtain its diffraction component, as shown in **Figure 19B**. **Figures 20A,B** show the AS-F-LSRTM and AS-D-LSRTM images after 5 iterations, respectively. In **Figure 20A**, the diffraction generated by the fault (see the red arrow) is muck weaker than the reflection produced by the horizontal layers (see the black arrow). From the image result of AS-D-LSRTM (**Figure 20B**), we can see that the reflection energy (see the red arrow) is almost eliminated while the diffraction is enhanced (see the black arrow). In addition, about 74% of computing time and 71% of memory space are saved after using the adaptive sampling method. We conclude that our method is still effective for field data.

CONCLUSION

We propose a high-accuracy and high-efficiency AS-D-LSRTM method, which contains three main parts. Firstly, we use the PWD filter to extract the diffraction from the full wavefield. Then we resample the initial migration model using the adaptive sampling strategy. Finally, we image the diffraction and obtain high-resolution migration results after multiple iterations. LSRTM is known to be limited by huge amount of computation when tens of iterations and hundreds of shots are required to be carried out. Numerical tests on synthetic data and field data demonstrate that the proposed AS-D-LSRTM method greatly improves computing efficiency and reduces memory requirement. In addition, our method can effectively image the diffraction produced by faults, fractures, caves and vugs. In summary, AS-D-LSRTM is a potential imaging approach for the interpretation and depiction of the fault-karst carbonate reservoirs in the Tarim Basin in Western China.

DATA AVAILABILITY STATEMENT

The original contributions presented in the study are included in the article/**Supplementary Material**, further inquiries can be directed to the corresponding author.

AUTHOR CONTRIBUTIONS

LC and JH contributed to the conception and design of the study. CS organized the database and performed the statistical analysis. JH modified the manuscript. All authors contributed to manuscript revision and read and approved the submitted version.

FUNDING

This research is supported by the National Key R&D Program of China (no. 2019YFC0605503), the National Outstanding Youth Science Foundation (no. 41922028), and the Major Scientific and Technological Projects of CNPC (no. ZD2019-183-003).

ACKNOWLEDGMENTS

The authors are grateful to the editor and reviewers for reviewing this article.

SUPPLEMENTARY MATERIAL

The Supplementary Material for this article can be found online at: https://www.frontiersin.org/articles/10.3389/feart.2022.846034/full#supplementary-material

REFERENCES

Alkhalifah, T. (2003). Tau Migration and Velocity Analysis: Theory and Synthetic Examples. *Geophysics* 68 (4), 1331–1339. doi:10.1190/1.1598126

Bansal, R., and Imhof, M. G. (2005). Diffraction Enhancement in Prestack Seismic Data. *Geophysics* 70 (3), V73–V79. doi:10.1190/1.1926577

Baysal, E., Kosloff, D. D., and Sherwood, J. W. C. (1983). Reverse Time Migration. *Geophysics* 48 (11), 1514–1524. doi:10.1190/1.1441434

Burnett, W. A., Klokov, A., Fomel, S., Bansal, R., Liu, E., and Jenkinson, T. (2015). Seismic Diffraction Interpretation at Piceance Creek. *Interpretation* 3 (1), SF1–SF14. doi:10.1190/INT-2014-0091.1

Cheng, H., W, Y., and Lu, X. B. (2020). *Acta Petrolei Sinica* 41 (3), 301–309. doi:10.7623/syxb202003005

Dai, W., Fowler, P., and Schuster, G. T. (2012). Multi-source Least-Squares Reverse Time Migration. *Geophys. Prospecting* 60 (4), 681–695. doi:10.1111/j.1365-2478.2012.01092.x

Dai, W., and Schuster, G. T. (2013). Plane-wave Least-Squares Reverse-Time Migration. *Geophysics* 78 (4), S165–S177. doi:10.1190/geo2012-0377.1

Ding, Z. W., Wang, R. J., Chen, F. F., Yang, J. P., Zhu, Z. Q., Yang, Z. M., et al. (2020). *Pet. Exploration Dev.* 47 (2), 286–296. doi:10.11698/PED.2020.02.0710.1016/s1876-3804(20)60048-9

Dutta, G., and Schuster, G. T. (2014). Attenuation Compensation for Least-Squares Reverse Time Migration Using the Viscoacoustic-Wave Equation. *Geophysics* 79 (6), S251–S262. doi:10.1190/geo2013-0414.1

Fan, N., Zhao, L.-F., Gao, Y.-J., and Yao, Z.-X. (2015). A Discontinuous Collocated-Grid Implementation for High-Order Finite-Difference Modeling. *Geophysics* 80 (4), T175–T181. doi:10.1190/geo2015-0001.1

Fomel, S. (2002). Applications of Plane-wave Destruction Filters. *Geophysics* 67 (6), 1946–1960. doi:10.1190/1.1527095

Huang, J.-P., Qu, Y.-M., Li, Q.-Y., Li, Z.-C., Li, G.-L., Bu, C.-C., et al. (2015). Variable-coordinate Forward Modeling of Irregular Surface Based on Dual-Variable Grid. *Appl. Geophys.* 12 (1), 101–110. doi:10.1007/s11770-014-0476-2

Huang, Y., and Schuster, G. T. (2012). Multisource Least-Squares Migration of marine Streamer and Land Data with Frequency-Division Encoding. *Geophys. Prospecting* 60 (4), 663–680. doi:10.1111/j.1365-2478.2012.01086.x

Jastram, C., and Behle, A. (1992). Acoustic Modelling on a Grid of Vertically Varying Spacing1. *Geophys. Prospect* 40 (2), 157–169. doi:10.1111/j.1365-2478.1992.tb00369.x

Kappus, M. E., Harding, A. J., and Orcutt, J. A. (1990). A Comparison Of Tau–P Transform Methods. *Geophysics* 55 (9), 1202–1215. doi:10.1190/1.1442936

Khaidukov, V., Landa, E., and Moser, T. J. (2004). Diffraction Imaging by Focusing-defocusing: An Outlook on Seismic Superresolution. *Geophysics* 69 (6), 1478–1490. doi:10.1190/1.1836821

Klokov, A., Baina, R., Landa, E., Thore, P., and Tarrass, I. (2010). Diffraction Imaging for Fracture Detection: Synthetic Case Study. *SEG Tech. Program Expanded Abstr.* 29, 3354–3358. doi:10.1190/1.3513545

Kong, X., Wang, D.-Y., Li, Z.-C., Zhang, R.-X., and Hu, Q.-Y. (2017). Diffraction Separation by Plane-Wave Prediction Filtering. *Appl. Geophys.* 14, 399–405. doi:10.1007/s11770-017-0634-9

Landa, E., Shtivelman, V., and Gelchinsky, B. (1987). A Method for Detection of Diffracted Waves on Common-Offset Sections*. *Geophys. Prospect* 35 (4), 359–373. doi:10.1111/j.1365-2478.1987.tb00823.x

Li, Q., Huang, J., and Li, Z. (2017). Cross-correlation Least-Squares Reverse Time Migration in the Pseudo-time Domain. *J. Geophys. Eng.* 14 (4), 841–851. doi:10.1088/1742-2140/aa6B33

Li, Y. T., Qi, L. X., Zhang, S. N., Yun, L., and Cao, Z. C. (2019). Characteristics and Development Mode of the Middle and Lower Ordovician Fault-Karst Reservoir in Shunbei Area, Tarim Basin. *Acta Petrolei Sinica* 40, 1470–1484. 10.11743/ogg20150301.

Li, Z., Li, Q., Huang, J., Na, L., and Kun, T. (2014). A Stable and High-Precision Dual-Variable Grid Forward Modeling and Reverse Time Migration Method. *Geophys. Prospecting Pet.* 53 (2), 127–136. doi:10.3969/j.issn.1000-1441.2014.02.001

Loucks, R. G., and Anderson, J. H. (1985). Depositional Facies, Diagenetic Terranes, and Porosity Development in Lower Ordovician Ellenburger Dolomite, Puckett Field, West Texas. *Carbonate Pet. Reservoirs*, 38 19–37. doi:10.1007/978-1-4612-5040-1_2

Lu, X. B., Hu, W. G., Wang, Y., Li, X. H., Li, T., Lv, Y. P., et al. (2015). Characteristics and Development Practice of Fault-Karst Carbonate Reservoirs in Tahe Area, Tarim Basin. *Oil Gas Geology.* 36 (3), 347–355. doi:10.11743/ogg20150301

Ma, N. B., Jin, S. L., Yang, R. Z., Meng, L. B., Wang, L., and Hu, Y. Z. (2019). Seismic Response Characteristics and Identification of Fault-Karst Reservoir in Shunbei Area, Tarim Basin. *Oil Geophys. Prospecting* 54 (2), 398–403. doi:10.13810/j.cnki.issn.1000-7210.2019.02.019

Ma, X., and Alkhalifah, T. (2013). Wavefield Extrapolation in Pseudodepth Domain. *Geophysics* 78 (2), S81–S91. doi:10.1190/geo2012-0237.1

Moczo, P. (1989). Finite-difference Technique forSH-Waves in 2-D media Using Irregular Grids-Application to the Seismic Response Problem. *Geophys. J. Int.* 99 (2), 321–329. doi:10.1111/j.1365-246X.1989.tb01691.x

Nemeth, T., Wu, C., and Schuster, G. T. (1999). Least-squares Migration of Incomplete Reflection Data. *Geophysics* 64 (1), 208–221. doi:10.1190/1.1444517

Soudet, H. J., Sorriaux, P., and Rolando, J. P. (1994). Relationship between Fractures and Karstification- the Oil-Bearing Paleokarst of Rospo Mare (Italy). *Bull. Des Centres De Recherches Exploration-Production Elf Aquitaine* 18 (1), 257–297.

Sun, R., and McMechan, G. A. (1986). Pre-stack Reverse-Time Migration for Elastic Waves with Application to Synthetic Offset Vertical Seismic Profiles. *Proc. IEEE* 74 (3), 457–465. doi:10.1109/PROC.1986.13486

Taner, M. T., Fomel, S., and Landa, E. (2006). Separation and Imaging of Seismic Diffractions Using Plane-wave Decomposition. *SEG Tech. Program Expanded Abstr.* 25 (1), 2401–2405. doi:10.1190/1.2370017

Tarantola, A. (1984). Linearized Inversion of Seismic Reflection Data*. *Geophys. Prospect* 32 (6), 998–1015. doi:10.1111/j.1365-2478.1984.tb00751.x

Tian, F., Jin, Q., Lu, X., Lei, Y., Zhang, L., Zheng, S., et al. (2016). Multi-layered Ordovician Paleokarst Reservoir Detection and Spatial Delineation: A Case Study in the Tahe Oilfield, Tarim Basin, Western China. *Mar. Pet. Geology.* 69, 53–73. doi:10.1016/j.marpetgeo.2015.10.015

Tyiasning, S., Merzlikin, D., Cooke, D., and Fomel, S. (2016). A Comparison of Diffraction Imaging to Incoherence and Curvature. *The Leading Edge* 35 (1), 86–89. doi:10.1190/tle35010086.1

Wang, Z., Huang, J., Li, Z., Liu, D., and Yong, P. (2020). An Efficient and Accurate Finite-Difference Operator Using Adaptively Discretized Grids and its Application for 3D Least-Squares Reverse-Time Migration. *Arab J. Geosci.* 13 (12), 480. doi:10.1007/s12517-020-05417-4

Yang, J., Zhu, H., McMechan, G., Zhang, H., and Zhao, Y. (2019). Elastic Least-Squares Reverse Time Migration in Vertical Transverse Isotropic media. *Geophysics* 84 (6), S539–S553. doi:10.1190/geo2018-0887.1

Zhang, Y., Sun, J., Notfors, C., Gray, S. H., Chernis, L., and Young, J. (2005). Delayed-Shot 3D Depth Migration. *Geophysics* 70 (5), E21–E28. doi:10.1190/1.2057980

Conflict of Interest: The authors declare that the research was conducted in the absence of any commercial or financial relationships that could be construed as a potential conflict of interest.

Publisher's Note: All claims expressed in this article are solely those of the authors and do not necessarily represent those of their affiliated organizations, or those of the publisher, the editors, and the reviewers. Any product that may be evaluated in this article, or claim that may be made by its manufacturer, is not guaranteed or endorsed by the publisher.

frontiers in Earth Science

ORIGINAL RESEARCH
published: 10 March 2022
doi: 10.3389/feart.2022.829846

A New Fluid Mobility Calculation Method Based on Frequency-Dependent AVO Inversion

Xin Luo[1,2], Xuehua Chen[2,3], Yinghao Duan[4], Shizhen Chen[1], Yingkai Qi[3] and Fei Huo[1]**

[1]Institute of Sedimentary Geology, Chengdu University of Technology, Chengdu, China, [2]State Key Laboratory of Oil and Gas Reservoir Geology and Exploitation, Chengdu University of Technology, Chengdu, China, [3]College of Geophysics, Chengdu University of Technology, Chengdu, China, [4]No. 2 Oil Production Plant, Petrochina Dagang Oilfield Company, Tianjin, China

Fluid mobility (i.e., permeability to viscosity ratio) is a key parameter that can evaluate the reservoir permeability and delineate the fluid characteristic in hydrocarbon-saturated reservoirs. Based on the asymptotic representation for the frequency-dependent reflections in the fluid-saturated pore-elastic media and frequency-dependent AVO inversion, we propose a novel method for estimating fluid mobility from poststack seismic data. First, we establish the relationship between fluid mobility and frequency-dependent AVO analysis. Then, the fluid mobility is estimated using the theory of frequency-dependent AVO inversion. Tests on synthetic data reveal that the fluid mobility shows excellent imageability for the fluid-saturated reservoirs and can accurately delineate the spatial distribution shape of the gas-saturated reservoir. The application of field data examples demonstrates that the fluid mobility calculated by the proposed method produces less background interferences caused by elastic layers compared with the conventional frequency-dependent fluid indicator. The frequency-dependent fluid mobility takes into account the dispersion features associated with hydrocarbon reservoirs, and it provides a new way to detect the location of hydrocarbon reservoirs and characterize their spatial distribution.

Keywords: fluid mobility, frequency-dependent inversion, time-frequency decomposition, reservoir delineation, dispersion

OPEN ACCESS

Edited by:
Jidong Yang,
China University of Petroleum, Huadong, China

Reviewed by:
Xilin Qin,
Yangtze University, China
Cai Hanpeng,
University of Electronic Science and Technology of China, China

****Correspondence:***
Xin Luo
luoxin21@cdut.edu.cn
Fei Huo
huofei342099206@163.com

Specialty section:
This article was submitted to Solid Earth Geophysics, a section of the journal Frontiers in Earth Science

Received: *06 December 2021*
Accepted: *17 January 2022*
Published: *10 March 2022*

Citation:
Luo X, Chen X, Duan Y, Chen S, Qi Y and Huo F (2022) A New Fluid Mobility Calculation Method Based on Frequency-Dependent AVO Inversion. Front. Earth Sci. 10:829846. doi: 10.3389/feart.2022.829846

INTRODUCTION

The reservoir permeability is a key parameter for measuring the capacity of fluid flow in porous rock and it is commonly measured through laboratory experiments. The poroelasticity theory indicates that permeability is significantly related to the seismic attenuation induced by the fluid flow when seismic waves penetrate the hydrocarbon-bearing reservoirs (Biot, 1956a; Biot, 1956b). Many studies have demonstrated that the seismic response of reservoirs is closely dependent on permeability (Pride et al., 2003; Kozlov, 2007; Goloshubin et al., 2008; Rubino et al., 2012). However, estimating permeability from real seismic data is a challenge for reservoir geophysicists until now, especially for the data without well data constraints. Fluid mobility (i.e., permeability to viscosity ratio) can reflect the reservoir permeability and fluid flow behaviors in a porous rock simultaneously and can be extracted from the surface seismic data, which provides an indirect factor to evaluate the percolation properties of a porous media (Rusakov et al., 2016). The measurement and numerical simulation illustrate that fluid mobility is a key parameter that can directly affect the seismic responses associated with the hydrocarbon-saturated reservoirs (Batzle et al., 2006; Goloshubin et al., 2008;

Chen et al., 2013a; Ren et al., 2013). The seismic reflection coefficient obtained by the theory of asymptotic representation for the reflection of a seismic wave from a fluid-saturated porous medium provides a basic theory for estimating fluid mobility (Silin et al., 2006; Silin and Goloshubin, 2010). Based on this asymptotic analysis theory, the fluid mobility calculation method using the low-frequency information of the seismic spectrum is proposed by Chen et al. (2012). Further, Chen et al. (2013a) delineated the gas reservoirs and their spatial distribution by integrating the low-frequency shadow and fluid mobility, which greatly reduced the uncertainty of reservoir prediction. In recent years this technology has emerged as a particularly attractive candidate for reservoir prediction. Luo et al. (2018) proposed an integrated prediction strategy for reservoir prediction using the seismic inversion and fluid mobility attribute. Because the fluid mobility calculation is dependent on the time-frequency analysis method, the arrival of new time-frequency transform methods has shown an improvement in spatial resolution of the fluid mobility. Xue et al. (2018) employed the synchrosqueezed wavelet transforms to improve the estimation precision of fluid mobility. Zhang et al. (2020) further use fluid mobility to predict the high-quality reservoir based on a modified high-precision time-frequency transform. These studies illustrate that reservoir-related fluid mobility is a key attribute for reservoir delineation. However, the calculation of these methods mentioned above only uses the seismic information of a single frequency in a low-frequency range and ignores frequency-dependent behaviors associated with the hydrocarbon reservoirs. In the paper, these methods that use the low-frequency information of seismic data for calculating fluid mobility are uniformly defined as the LF-FM. The fluid mobility extracted by the LF-FM commonly indicates the location of the reservoir interface. Therefore, this study is focused on further extracting the fluid mobility from frequency-dependent seismic data to obtain the fluid mobility between the reservoir interfaces.

It is commonly known that the calculation formula of fluid mobility proposed by Chen et al. (2012) is frequency-dependent. So extracting the fluid mobility using frequency-dependent information of seismic data is of great importance for reservoir delineation. Evidence from several studies indicated that the frequency-dependent seismic responses induced by the velocity dispersion and amplitude attenuation occur when the seismic waves pass through the hydrocarbon saturated porous rocks (Chapman et al., 2003; Batzle et al., 2006; Chapman et al., 2006; Gurevich et al., 2010; Dupuy and Stovas, 2013; Chen et al., 2016; Qin et al., 2018). Frequency-dependent effects associated with hydrocarbon-bearing reservoirs provide theoretical supports for computing reservoir-related attributes using seismic data. The frequency-dependent AVO (FDAVO) inversion method provides an approach to estimate the dispersion attribute for reservoir delineation (Wilson et al., 2009; Wu et al., 2012; Chen et al., 2014; Liu et al., 2019; Wang et al., 2019; Luo et al., 2020; Jin et al., 2021). Therefore, the FDAVO inversion is being explored to extract fluid mobility using the frequency-dependent information of seismic data.

In this paper, based on the theory of asymptotic representation of frequency-dependent reflection in the fluid-saturated medium and FDAVO inversion method, we first established the relationship between fluid mobility and FDAVO. And then, the fluid mobility calculation method using frequency-dependent information of post-stack seismic data is proposed. Next, a synthetic data test is used to verify the effectiveness of the proposed approach. Finally, field data examples are further analyzed to illustrate the feasibility of the proposed method.

THEORY AND METHOD

Based on the low-frequency asymptotic analysis theory, Chen et al. (2012) derived the expression of reservoir fluid mobility:

$$F = \frac{\kappa}{\eta} = \frac{1}{C^2}\left(\frac{dR}{d\omega}\right)^2 \omega \tag{1}$$

where k is the reservoir permeability, η denotes the fluid viscosity, R is the reflection coefficient of a planar compression wave from the interface between elastic and fluid-saturated porous media, ω denotes the angular frequency, parameter C is a function of the bulk density and can be regarded as a constant.

Wilson et al. (2009) and Wu et al. 2010, Wu et al., 2012) extended the two-term AVO linear approximation proposed by Smith and Gidlow (1987) to frequency domain. The frequency-dependent reflection coefficient has the following form

$$R(\theta,\omega) \approx A(\theta)\frac{\Delta v_p}{v_p}(\omega) + B(\theta)\frac{\Delta v_s}{v_s}(\omega) \tag{2}$$

where θ is incident angle, v_p and v_s with the units of m/s represent P-wave velocity and S-wave velocity, respectively. The expressions of $A(\theta)$ and $B(\theta)$ are as follows:

$$A(\theta) = \frac{5}{8} - \frac{1}{2}\frac{v_s^2}{v_p^2}\sin^2\theta + \frac{1}{2}\tan^2\theta,\ B(\theta) = -4\frac{v_s^2}{v_p^2}\sin^2\theta \tag{3}$$

Due to the reflection coefficient R in **Eq. 1** is the normal reflection of a compression wave, we let $\theta = 0$ to pursue a simplified version of **Eq. 2** that is an approximation of the normal reflection coefficient. Then, we obtain

$$R(\omega) \approx \frac{5}{8}\frac{\Delta v_p}{v_p}(\omega) \tag{4}$$

Taking the derivative of **Eq. 4** with respect to the angular frequency ω, we obtain

$$\frac{dR}{d\omega} \approx \frac{5}{8}\frac{d}{d\omega}\left(\frac{\Delta v_p}{v_p}\right) \tag{5}$$

By virtue of **Eqs 1**, **5**, we can get the new frequency-dependent expression of the fluid mobility:

$$F(\omega) \approx P^2\left[\frac{d}{d\omega}\left(\frac{\Delta v_p}{v_p}\right)\right]^2 \omega \tag{6}$$

where P is a new constant with $P = \frac{5}{8C}$. Here, the parameter P can be regarded as a scale factor. Therefore, the **Eq. 6** can be further rewritten as:

$$F(\omega) \approx \omega \left[\frac{d}{d\omega} \left(\frac{\Delta v_p}{v_p} \right) \right]^2 \tag{7}$$

Expanding **Eq. 4** as first-order Taylor series at a reference frequency ω_0 without considering the higher-order terms, we can get:

$$R(\omega) \approx \frac{5}{8} \frac{\Delta v_p}{v_p} (\omega_0) + (\omega - \omega_0) \frac{5}{8} \frac{d}{d\omega} \left(\frac{\Delta v_p}{v_p} \right) \tag{8}$$

In general, the value of ω_0 is determined by the spectral decomposition and the dominant frequency of the seismic signal is usually selected as the reference frequency.

By virtue of **Eqs 7**, **8**, we can obtain a new expression of frequency-dependent reflection coefficient relating to the fluid mobility, that is:

$$R(\omega) \approx \frac{5}{8} \frac{\Delta v_p}{v_p} (\omega_0) + \frac{5}{8} \frac{(\omega - \omega_0)}{\omega} \frac{1}{D_p} F(\omega) \tag{9}$$

where, D_p represents the derivatives of frequency-dependent velocity of P-wave and its expression is $D_p = \frac{d}{d\omega} (\frac{\Delta v_p}{v_p})$.

Eq. 8 can be further rewritten as:

$$R(\omega) - \frac{5}{8} \frac{\Delta v_p}{v_p} (\omega_0) \approx \frac{5}{8} \frac{(\omega - \omega_0)}{\omega} \frac{1}{D_p} F(\omega) \tag{10}$$

Considering m angular frequencies $[\omega_1, \omega_2, \ldots, \omega_m]$, the vectors **r** and **e** can be expressed in matrix form:

$$\mathbf{r} = \begin{bmatrix} R(t, \omega_1) - \frac{5}{8} \frac{\Delta v_p}{v_p} (\omega_0) \\ \vdots \\ R(t, \omega_m) - \frac{5}{8} \frac{\Delta v_p}{v_p} (\omega_0) \end{bmatrix} \tag{11}$$

$$\mathbf{e} = \begin{bmatrix} \frac{5}{8} \frac{(\omega_1 - \omega_0)}{\omega_1} \frac{1}{D_p} \\ \vdots \\ \frac{5}{8} \frac{(\omega_m - \omega_0)}{\omega_m} \frac{1}{D_p} \end{bmatrix} \tag{12}$$

Then, we obtain:

$$\mathbf{r} = \mathbf{e}F \tag{13}$$

At last, the least-squares inversion method can be used to estimate the frequency-dependent fluid mobility F:

$$F = \left(\mathbf{e}^{\mathrm{T}} \mathbf{e} \right)^{-1} \mathbf{e}^{\mathrm{T}} \mathbf{r} \tag{14}$$

where the T indicates the transpose of the matrix.

In the **Eq. 10**, the D_p is also calculated by the least-squares inversion method:

$$D_p = \left(\mathbf{d}^{\mathrm{T}} \mathbf{d} \right)^{-1} \mathbf{d}^{\mathrm{T}} \mathbf{r} \tag{15}$$

where, the form of vector **d** is:

$$\mathbf{d} = \begin{bmatrix} \frac{5}{8} (\omega_1 - \omega_0) \\ \vdots \\ \frac{5}{8} (\omega_m - \omega_0) \end{bmatrix} \tag{16}$$

To extract the frequency-dependent information from the reflected seismic waves, the time-frequency decomposition method is used in the fluid mobility inversion. The seismic reflection amplitude $R(t)$ can be transformed into data sets $S(t, f)$ at different frequencies using generalized S-transform (GST) (Chen et al., 2009), that is

$$R(t) \xrightarrow{GST} S(t, f) \tag{17}$$

where, the expression of GST is:

$$S(f, \tau) = \int_{-\infty}^{+\infty} x(t) \frac{|\lambda| |f|^p}{\sqrt{2\pi}} \exp\left[-\frac{\lambda^2 (t - \tau)^2 f^{2p}}{2} \right] \exp(-i2\pi f t) dt \tag{18}$$

where $x(t)$ is the original seismic signal, τ is the time shift parameter, λ and p are the adjustable parameters and control the Gaussian window, $S(f, \tau)$ is the expression of a 2D time-frequency variable with regard to f and τ.

THE APPLICATION TO SYNTHETIC AND FIELD DATA EXAMPLES

Synthetic Data Test

To illustrate the effectiveness of the proposed method, we design a simple gas-saturated permeable reservoir model (**Figure 1A**) to test the feasibility of the frequency-dependent fluid mobility to delineate reservoirs. In the model, the gas-saturated reservoir is marked with ③, and other layers are dry strata. The black curve indicates the reservoir location. The model parameters are given in **Table 1**. We perform the forward modeling and migration to produce the synthetic seismic records (**Figure 1B**) by employing the DVWE (diffusive and viscous wave equation)-based method (He et al., 2008; Chen et al., 2013b; Chen et al., 2016). In the modeling, the frequency-dependent velocity of the gas-saturated reservoir is calculated by the theory proposed by Chapman et al. (2003). The synthetic seismic records were generated using a Ricker wavelet with the dominant frequency of 40 Hz. The seismic records shown in **Figure 1B** indicate that the top interface of gas-saturated reservoir show strong seismic reflection anomalies. However, the seismic reflections of the reservoir bottom interface show obviously time delay and phase distortion. Besides, the seismic reflections at the bottom of the gas-saturated sand reservoir show noticeable amplitude attenuation and phase delay due to the seismic effects of velocity dispersion.

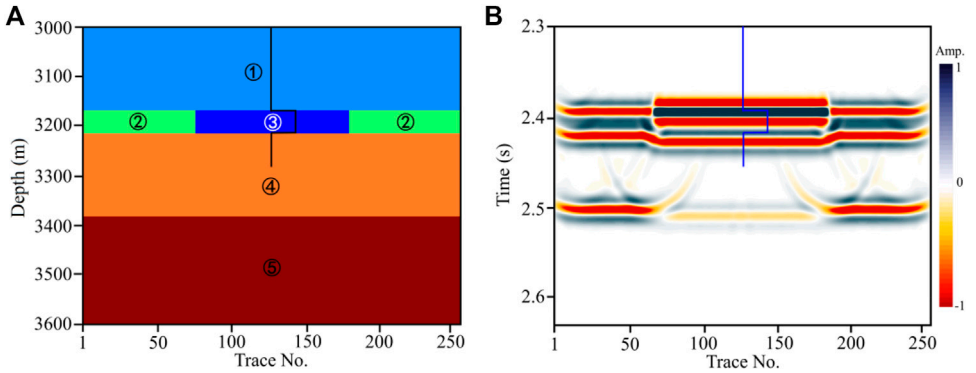

FIGURE 1 | (A) The gas-saturated permeable sand reservoir model and **(B)** its synthetic seismic section.

TABLE 1 | Physical parameters used in the modeling.

Layer	V_P/(m·s^{-1})	Thickness/(m)
①	3,500	170
②	3,700	50
③	3,600	50
④	3,900	150
⑤	4,100	230

Then, we calculate the frequency-dependent fluid mobility of the model using the proposed method and compare it with the result of LF-FM, and the estimation results are shown in **Figure 2**. As shown in **Figure 2A**, the high value of fluid mobility calculated by the LF-FM indicates the top interface rather than the actual spatial distribution shape of the gas-saturated reservoir. However, in **Figure 2B**, the fluid mobility estimated using our method shows clear anomalies in the reservoir region and the gas storage space correlates well with the reservoir shape. The test for the synthetic data illustrates that the fluid mobility calculated by the frequency-dependent inversion method can accurately delineate the location of the gas-saturated reservoir.

To further analyze the influence of the tuning effect on the fluid mobility calculation, we also make a model (**Figure 3A**) with thickness of the gas-saturated reservoir less than a quarter wavelength. In the new model, the reservoir thickness is 20 m, and other parameters are the same to the model shown in **Figure 1A**. The synthetic seismic record (**Figure 3B**) indicates that the reflection interfaces of the thin reservoir are difficult to distinguish from the seismic events due to the tuning effect. As can be seen in **Figures 3C,D**, the fluid mobility calculated by the LF-FM and our method can both accurately delineate the reservoir location and its shape.

Field Data Applications

In this section, we apply the proposed method to field seismic data to further demonstrate the performance of the proposed method. The reservoirs in the study area are mainly marine sandstone reservoirs with different gas saturations. **Figure 4** shows the two well-logs through the sandstone reservoirs, including water saturation (S_w), P-wave, S-wave, density and porosity curves. As shown in **Figure 4**, the velocities of S-wave show high values in the third column and the porosity in the reservoir zones is about 18%. However, compared to the non-reservoir zones, the velocity curves of P-wave in the second

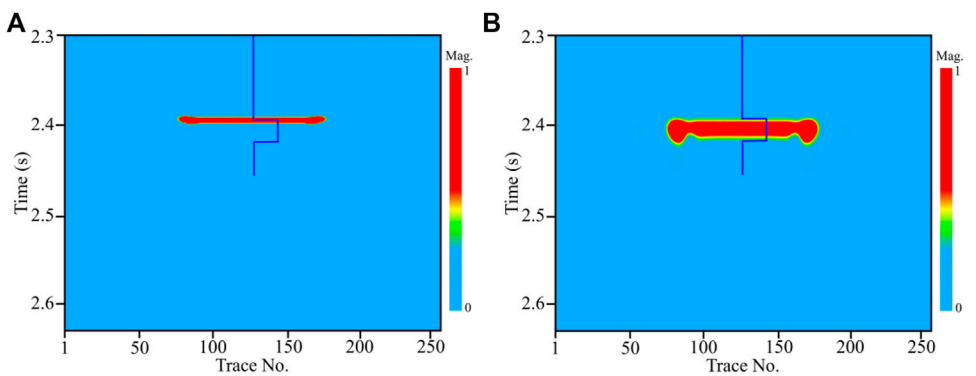

FIGURE 2 | The fluid mobility sections calculated by **(A)** the LF-FM method and **(B)** our method.

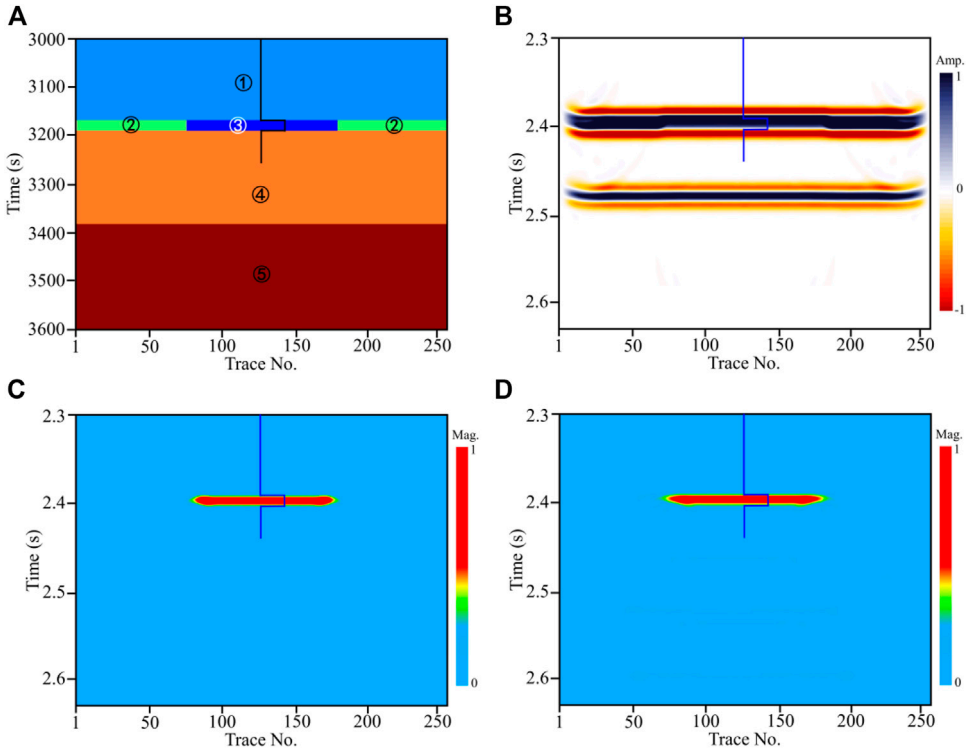

FIGURE 3 | (A) The gas-saturated reservoir model with the reservoir thickness is 20 m and **(B)** its synthetic seismic record. The fluid mobility calculated by **(C)** LF-FM and **(D)** our method.

column and the density curves in the fourth column are both show a change to lower values. The reservoirs with high gas saturation are outlined by cyan rectangles. We choose two seismic profiles across the two wells for analysis. The seismic profile shown in **Figure 5A** intersecting well-1 is extracted from the line marked with M to M' in a three-dimensional (3D) area. **Figure 5B** is the seismic trace extracted at the well-1 location (CDP No.178) and **Figure 5C** is its time-frequency spectrum after the GST. In the **Figure 5C**, we can observe strong energy at the reservoir zone. The section shown in **Figure 5D** intersecting well-2 is extracted from the line marked with N to N'. **Figure 5E** is the seismic trace extracted at the well-2 location (CDP No.146) and **Figure 5F** is its time-frequency spectrum after the GST. In **Figure 5F**, there are two strong energy clusters in the reservoir zone. The amplitude spectra shown in **Figures 5G,H** of the two seismic traces (**Figures 5B,E**) illustrate that the frequency band is approximately 5–50 Hz, and the dominant frequency is about 20 Hz.

To evaluate the ability for imaging the reservoirs, we calculated the fluid mobility of the two seismic sections and compared it with the dispersion attribute of P-wave obtained by frequency-dependent AVO inversion (Wilson et al., 2009; Wu et al., 2012; Chen et al., 2014; Luo et al., 2020). The comparison results are shown in **Figure 6**. For the results of the section across the Well-1, the dispersion attribute (**Figure 6A**) delineates the reservoir zone while the results are greatly affected by the other anomalies. However, the fluid mobility result in **Figure 6B** shows a high value at the location of the reservoir zone and the background interference unrelated to the reservoirs are very weak. For the results of the section across the Well-2, the result of dispersion attribute (**Figure 6C**) of P-wave is also affected by the other interference, which results in difficulty for accurately discriminating the reservoirs. As shown in **Figure 6D**, the fluid mobility calculated by our method can exhibit the location of the gas reservoirs and degrades the background interference of elastic layers to the most extent. Meanwhile, the result has a high resolution for delineating reservoirs. The two sets of reservoirs shown in **Figure 4B** are both identified from the fluid mobility section (**Figure 6D**).

To further illustrate the accuracy of the method, we choose the dispersion and fluid mobility curves at the location of the Well to compare with the log curve. **Figure 7A** is the seismic trace chosen from the location of Well-1. **Figure 7B** shows the water saturation curve, which can significantly distinguish the reservoir (outlined by the yellow shadow) with high gas saturation. **Figures 7C,D** show the comparison result of the dispersion curve and fluid mobility curve. Both the curves show significant anomalies in the gas-saturated reservoir. However, the dispersion curve is greatly affected by the other anomalies (indicated by black arrows) unrelated to reservoirs. The fluid mobility curve obtained by our method only shows significant anomalies in the gas-saturated zone, whereas the background interference of the other layers is very weak. Similarly, **Figure 8** shows the analysis result of the curves chosen from the location of Well-2. The S_w curve in **Figure 8B** illustrates that there develop two sets of reservoirs with

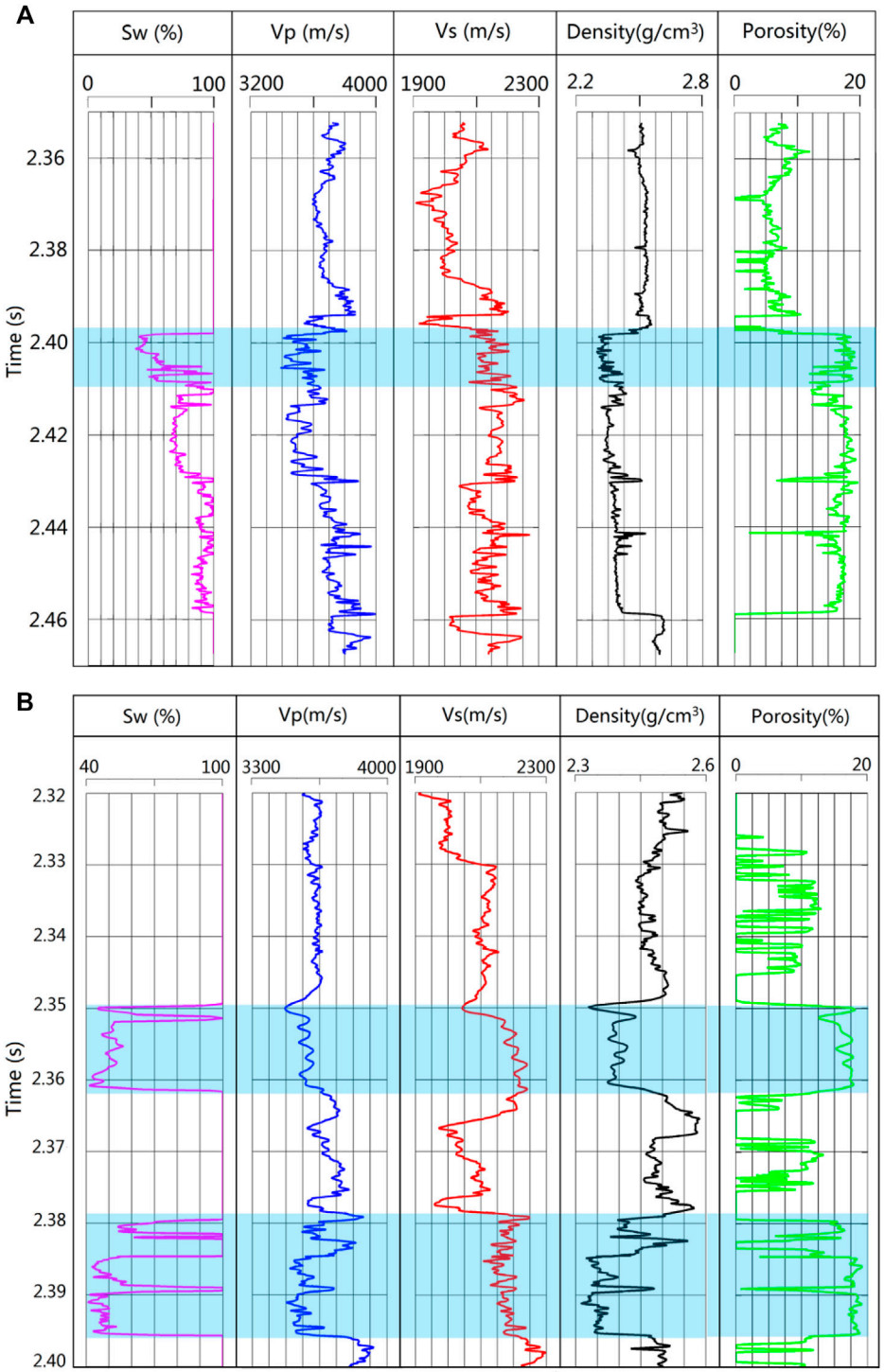

FIGURE 4 | Well logs of the sandstone reservoir for **(A)** well-1 and **(B)** well-2. The reservoir in the study area is gas-saturated sandstone and the cyan rectangle outlines the fluid-saturated reservoirs saturated with high gas saturation (Sg ≥ 0.4).

high gas saturation in the vertical direction. As shown in **Figure 8C**, the dispersion curve shows the strongest anomalies at the lower reservoir while the dispersion anomalies of the upper reservoir are not evident. Meanwhile, the dispersion curve is also affected by the other anomalies (indicated by the black arrows) unrelated to reservoirs. However, both reservoirs show strong anomalies in the fluid mobility curve (**Figure 8D**) and correlate well with the reservoir location. In addition, the anomalies of

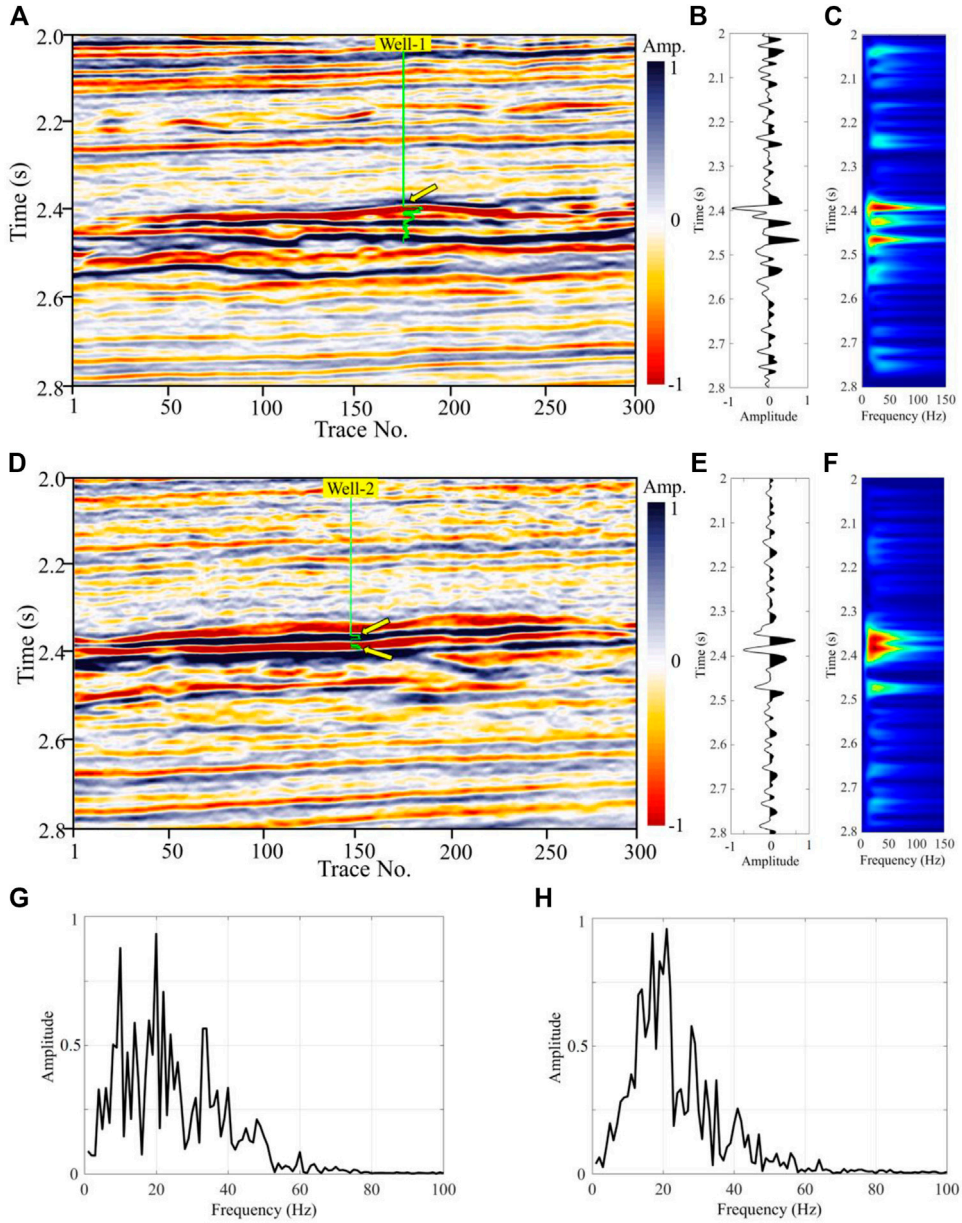

FIGURE 5 | (A) The stacked section across the Well-1. **(B)** The seismic trace extracted at the Well-1 location and **(C)** its time-frequency spectrum calculated by GST. **(D)** The stacked section across the Well-2. **(E)** The seismic trace extracted at the Well-2 location and **(F)** its time-frequency spectrum calculated by GST. **(G)** and **(H)** are the amplitude spectra of **Figures 5B,E**, respectively. In the two sections, the reservoir zones are indicated with the yellow arrows.

background interference are suppressed to the greatest extent. The analysis in **Figure 7** and **Figure 8** illustrates that the fluid mobility calculated by our method can accurately delineate the location of the reservoir and degrade the background interference of other layers unrelated to reservoirs to the most extent.

Finally, we use the proposed method to calculate the fluid mobility for 3D seismic data volume. The target interval slices extracted from the data volume are shown in **Figure 9**. **Figure 9A** is the seismic amplitude slice and **Figure 9B** is the fluid mobility slice corresponding to the **Figure 9A**. As shown in **Figure 9B**, both wells in the zone show strong anomalies that correlate well with the known production according to the logging interpretation results. Moreover, the fluid mobility slice clearly delineates the spatial distribution and the edge of the gas-saturated reservoirs.

DISCUSSION AND CONCLUSION

Based on the calculation formula of fluid mobility and frequency-dependent AVO inversion theory, a methodology for calculating frequency-dependent fluid mobility using post-stacked seismic

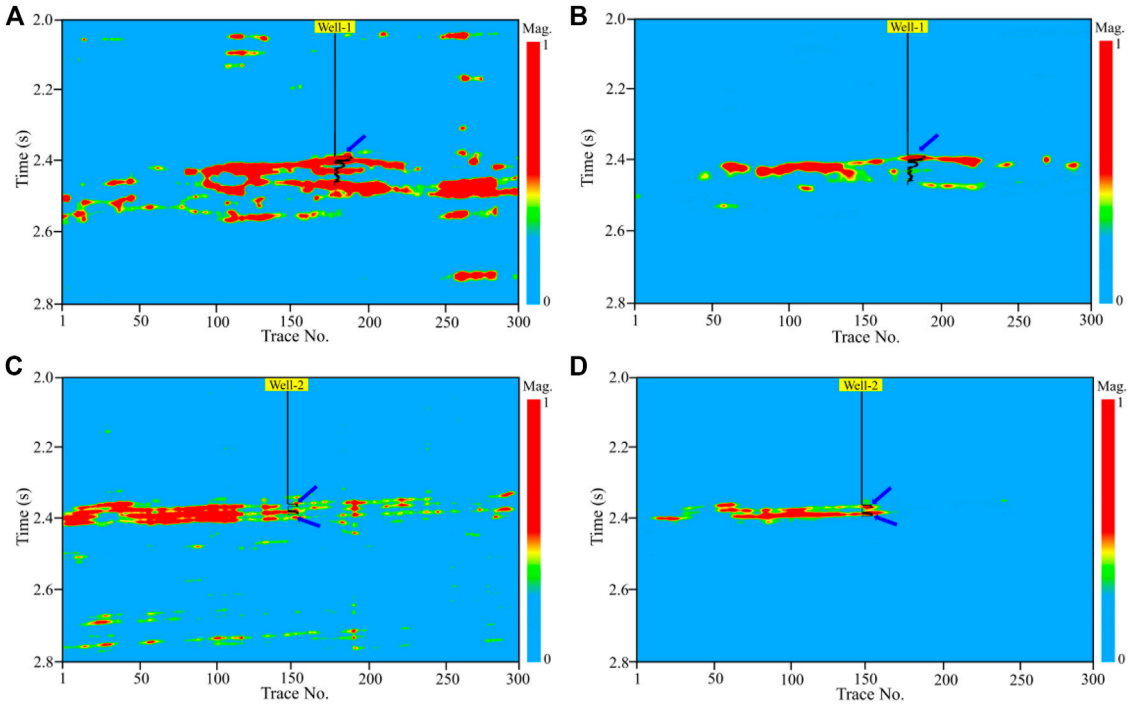

FIGURE 6 | The comparison of the dispersion attribute section of P-wave and the fluid mobility. **(A)** and **(C)** are the dispersion attribute sections of P-wave. **(B)** and **(D)** are the fluid mobility sections calculated by the proposed method. The results of **(A)** and **(B)** correspond to the stacked section in **Figure 5A**, and the results of **(C)** and **(D)** correspond to the stacked section in **Figure 5D**.

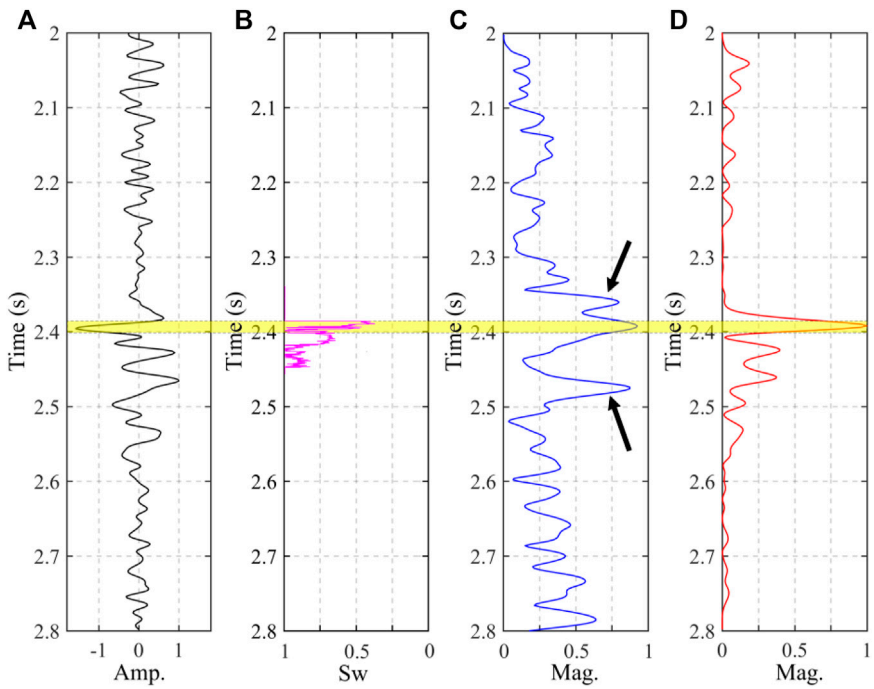

FIGURE 7 | The analysis of the single trace at the location of well-1. **(A)** The seismic trace. **(B)** The log curve of water saturation. **(C)** The dispersion curve and **(D)** the fluid mobility curve correspond to the **(A)**.

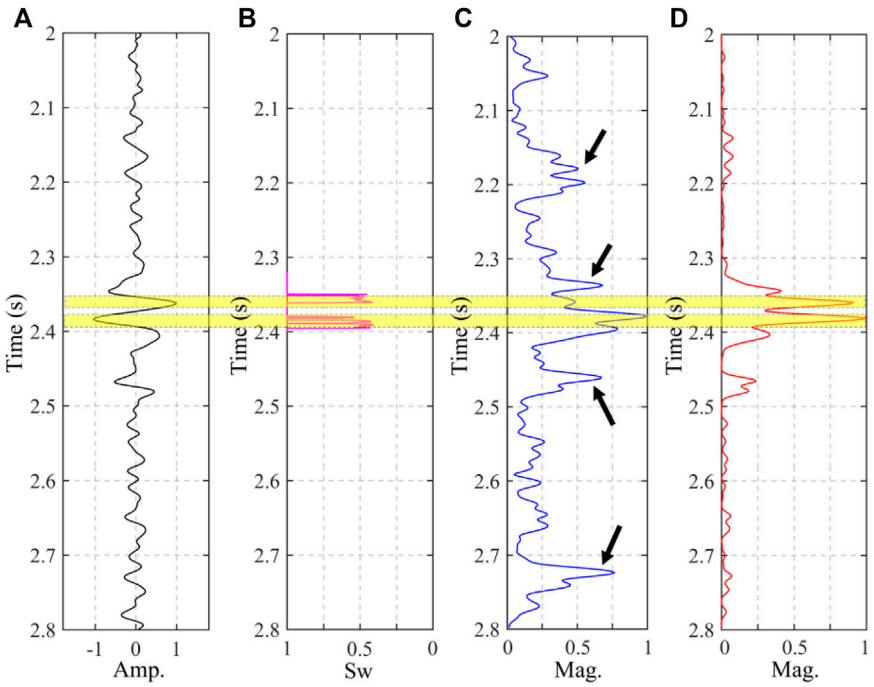

FIGURE 8 | The analysis of the single trace at the location of well-2. **(A)** The seismic trace. **(B)** The log curve of water saturation. **(C)** The dispersion curve and **(D)** the fluid mobility curve correspond to the **(A)**.

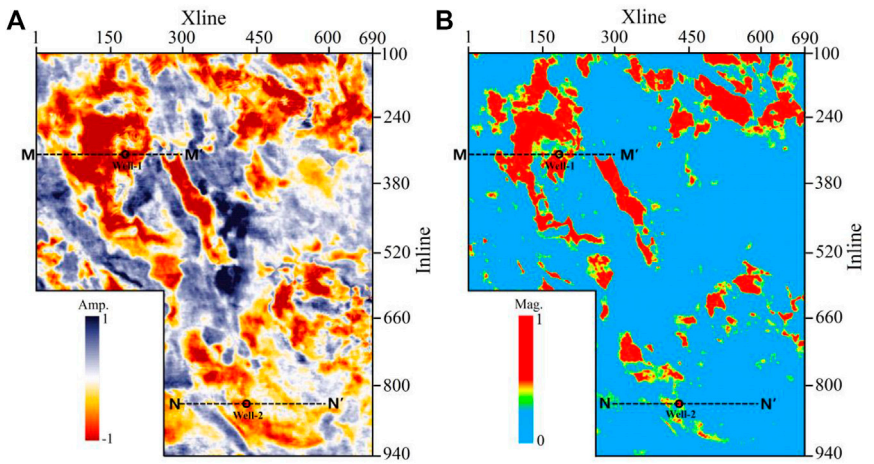

FIGURE 9 | (A) Seismic slice extracted through the gas reservoir in the target interval and **(B)** its fluid mobility slice calculated by the proposed method. The M, M', N and N' donate the location of the seismic sections in the study.

data is proposed. In comparison with the LF-FM method, the fluid mobility calculated by the proposed method can better delineate the spatial distribution shape. Furthermore, compared with the prestack dispersion attribute inversion method (Wilson et al., 2009; Wu et al., 2012; Chen et al., 2014; Luo et al., 2020), the computation time is significantly reduced. For the seismic data corresponding to **Figure 5A**, it needs 41.28 s to get the results of dispersion parameters using prestack dispersion AVO inversion. However, the computation time only costs 5.92 s when obtaining the fluid mobility result. This illustrates that the proposed method is advantageous if we need to compute the large-scale seismic data volume to delineate reservoirs in a 3D area. In addition to significant computation time reductions, the fluid mobility calculated by the proposed method has a higher accuracy for reservoir characteristics compared with the dispersion attribute, which can better

delineate the reservoir location. However, the prestack data contains more abundant information related to the reservoirs. If the frequency-dependent fluid mobility attribute can be extracted from the prestack seismic data, the accuracy of reservoir prediction and fluid identification will be further improved. It is worth further studying to deduce the AVO approximation related to reservoir fluid mobility from the theory of fluid-saturated porous media.

In addition, the time-frequency analysis method can directly affect the spatial resolution of the calculation result. In the proposed method, the time-frequency decomposition is conducted by the generalized S-transform proposed by Chen et al. (2009). Combining the high-precision time-frequency transform methods with the proposed method to improve the resolution and accuracy of calculation requires further investigations.

Synthetic and field data examples illustrate that the fluid mobility attribute calculated by the proposed method shows excellent imaging quality for gas-saturated reservoirs and is less affected by the anomalies unrelated to the reservoirs, which can accurately delineate the spatial distribution of hydrocarbon reservoirs. This methodology provides a new approach to extract frequency-dependent information related to the hydrocarbon reservoirs from seismic data. The calculation results can provide technical support for subsequent high-precision exploration such as fine reservoir evaluation and drilling deployment. It is noteworthy that the proposed method for calculating fluid mobility is not constrained by the well data, which also provides a new way for reservoir characterization in the case of no drilling.

DATA AVAILABILITY STATEMENT

The modeling data that the findings of this study are based on are available from the corresponding author upon reasonable request. The authors do not have the legal right to release the real seismic data, and it is used for research purposes only.

AUTHOR CONTRIBUTIONS

XL and XC contributed to the conception and design of the study. XL prepared the original draft. YD and SC prepared some Figures. YQ contributed to the data modeling. FH organized the study and modified the manuscript. All authors contributed to the article and approved the submitted version.

FUNDING

This work was supported by the Central Funds Guiding the Local Science and Technology Development (Grant No. 2021ZYD0037).

REFERENCES

Batzle, M. L., Han, D.-H., and Hofmann, R. (2006). Fluid Mobility and Frequency-dependent Seismic Velocity - Direct Measurements. *Geophysics* 71, N1–N9. doi:10.1190/1.2159053

Biot, M. A. (1956b). Theory of Propagation of Elastic Waves in a Fluid-Saturated Porous Solid. II. Higher Frequency Range. *The J. Acoust. Soc. America* 28, 179–191. doi:10.1121/1.1908241

Biot, M. A. (1956a). Theory of Propagation of Elastic Waves in a Fluid-Saturated Porous Solid. I. Low-Frequency Range. *J. Acoust. Soc. America* 28, 168–178. doi:10.1121/1.1908239

Chapman, M., Liu, E., and Li, X.-Y. (2006). The Influence of Fluid-Sensitive Dispersion and Attenuation on AVO Analysis. *Geophys. J. Int.* 167, 89–105. doi:10.1111/j.1365-246X.2006.02919.x

Chapman, M., Maultzsch, S., Liu, E., and Li, X.-Y. (2003). The Effect of Fluid Saturation in an Anisotropic Multi-Scale Equant Porosity Model. *J. Appl. Geophys.* 54, 191–202. doi:10.1016/j.jappgeo.2003.01.003

Chen, S., Li, X. Y., and Wu, X. (2014). Application of Frequency-dependent AVO Inversion to Hydrocarbon Detection. *J. Seism. Explor.* 23, 241–264.

Chen, X.-H., He, Z.-H., Zhu, S.-X., Liu, W., and Zhong, W.-L. (2012). Seismic Low-Frequency-Based Calculation of Reservoir Fluid Mobility and its Applications. *Appl. Geophys.* 9, 326–332. doi:10.1007/s11770-012-0340-6

Chen, X., He, Z., Gao, G., He, X., and Zou, W. (2013a). "A Fast Combined Method for Fluid Flow Related Frequency-Dependent AVO Modeling," in 83th Annual International Meetting Expanded Abstracts. Houston, TX: SEG, 3454–3459. doi:10.1190/segam2013-0007.1

Chen, X., He, Z., Pei, X., Zhong, W., and Yang, W. (2013b). Numerical Simulation of Frequency-dependent Seismic Response and Gas Reservoir Delineation in Turbidites: A Case Study from China. *J. Appl. Geophys.* 94, 22–30. doi:10.1016/j.jappgeo.2013.04.005

Chen, X. H., He, Z. H., Huang, D. J., and Wen, X. T. (2009). Low Frequency Shadow Detection of Gas Reservoirs in Time-Frequency Domain. *Chin. J. Geophys.* 52, 215–221.

Chen, X., Qi, Y., He, X., He, Z., and Chen, H. (2016). Phase-Shifted Based Numerical Method for Modeling Frequency-dependent Effects on Seismic Reflections. *Pure Appl. Geophys.* 173, 2899–2912. doi:10.1007/s00024-016-1290-3

Dupuy, B., and Stovas, A. (2014). Influence of Frequency and Saturation on AVO Attributes for Patchy Saturated Rocks. *Geophysics* 79, B19–B36. doi:10.1190/geo2012-0518.1

Goloshubin, G., Silin, D., Vingalov, V., Takkand, G., and Latfullin, M. (2008). Reservoir Permeability from Seismic Attribute Analysis. *The Leading Edge* 27, 376–381. doi:10.1190/1.2896629

Gurevich, B., Makarynska, D., de Paula, O. B., and Pervukhina, M. (2010). A Simple Model for Squirt-Flow Dispersion and Attenuation in Fluid-Saturated Granular Rocks. *Geophysics* 75, N109–N120. doi:10.1190/1.3509782

He, Z., Xiong, X., and Bian, L. (2008). Numerical Simulation of Seismic Low-Frequency Shadows and its Application. *Appl. Geophys.* 5, 301–306. doi:10.1007/s11770-008-0040-4

Jin, H., Liu, C., Guo, Z., Zhang, Y., Niu, C., Wang, D., et al. (2021). Rock Physical Modeling and Seismic Dispersion Attribute Inversion for the Characterization of a Tight Gas Sandstone Reservoir. *Front. Earth Sci.* 9, 1–11. doi:10.3389/feart.2021.641651

Kozlov, E. (2007). Seismic Signature of a Permeable, Dual-Porosity Layer. *Geophysics* 72, SM281–SM291. doi:10.1190/1.2763954

Liu, J., He, Z.-L., Liu, X., Wu, H., Liu, X.-w., Huo, Z.-z., et al. (2019). Using Frequency-dependent AVO Inversion to Predict the "sweet Spots" of Shale Gas Reservoirs. *Mar. Pet. Geology.* 102, 283–291. doi:10.1016/j.marpetgeo.2018.12.039

Luo, X., Chen, X., Sun, L., Zhang, J., and Jiang, W. (2020). Optimizing Schemes of Frequency-dependent Avo Inversion for Seismic Dispersion-Based High Gas-Saturation Reservoir Quantitative Delineation. *J. Seism. Explor.* 29, 173–199.

Luo, Y., Huang, H., Yang, Y., Hao, Y., Zhang, S., and Li, Q. (2018). Integrated Prediction of deepwater Gas Reservoirs Using Bayesian Seismic Inversion and Fluid Mobility Attribute in the South China Sea. *J. Nat. Gas Sci. Eng.* 59, 56–66. doi:10.1016/j.jngse.2018.08.019

Pride, S. R., Harris, J. M., Johnson, D. L., Mateeva, A., Nihel, K. T., Nowack, R. L., et al. (2003). Permeability Dependence of Seismic Amplitudes. *The Leading Edge* 22, 518–525. doi:10.1190/1.1587671

Qin, X., Li, X.-y., Chen, S., and Liu, Y. (2018). The Modeling and Analysis of Frequency-dependent Characteristics in Fractured Porous media. *J. Geophys. Eng.* 15, 1943–1952. doi:10.1088/1742-2140/aac130

Ren, Y., Chapman, M., Wu, X., Guo, Z., U, J., and Li, X. (2013). "Estimation of Fluid Mobility From Frequency Dependent Azimuthal AVO - A Modelling Study," in 83th Annual International Meetting Expanded Abstracts. Houston, TX: SEG, 473–477. doi:10.1190/segam2013-1364.1

Rubino, J. G., Velis, D. R., and Holliger, K. (2012). Permeability Effects on the Seismic Response of Gas Reservoirs. *Geophys. J. Int.* 189, 448–468. doi:10.1111/j.1365-246X.2011.05322.x

Rusakov, P., Goloshubin, G., Tcimbaluk, Y., and Privalova, I. (2016). An Application of Fluid Mobility Attribute for Permeability Prognosis in the Crosswell Space with Compensation of the Reservoir Thickness Variations. *Interpretation* 4, T157–T165. doi:10.1190/INT-2015-0096.1

Silin, D. B., Korneev, V. A., Goloshubin, G. M., and Patzek, T. W. (2006). Low-frequency Asymptotic Analysis of Seismic Reflection from a Fluid-Saturated Medium. *Transp Porous Med.* 62, 283–305. doi:10.1007/s11242-005-0881-8

Silin, D., and Goloshubin, G. (2010). An Asymptotic Model of Seismic Reflection from a Permeable Layer. *Transp Porous Med.* 83, 233–256. doi:10.1007/s11242-010-9533-8

Smith, G. C., and Gidlow, P. M. (1987). Weighted Stacking for Rock Property Estimation and Detection of Gas*. *Geophys. Prospect.* 35, 993–1014. doi:10.1111/j.1365-2478.1987.tb00856.x

Wang, P., Li, J., Chen, X., Wang, K., and Wang, B. (2019). Fluid Discrimination Based on Frequency-dependent AVO Inversion with the Elastic Parameter Sensitivity Analysis. *Geofluids* 2019, 1–13. doi:10.1155/2019/8750127

Wilson, A., Chapman, M., and Li, X. Y. (2009). Frequency-dependent AVO Inversion. *79th Annu. SEG Meet. Expand. Abstr.*. Houston, TX: SEG 28, 341–346.

Wu, X., Chapman, M., and Li, X.-Y. (2010). Estimating Seismic Dispersion from Pre-stack Data Using Frequency-Dependent AVO Inversion. *80th Annu. Int Meet. Expand. Abstr.*. Denver, CO: SEG, 425–429. doi:10.1190/1.3513759

Wu, X., Chapman, M., and Li, X.-Y. (2012). Frequency-dependent AVO Attribute: Theory and Example. *First Break*. Denver, CO: SEG 30, 67–72. doi:10.3997/1365-2397.2012008

Xue, Y.-J., Cao, J.-X., Zhang, G.-L., Cheng, G.-H., and Chen, H. (2018). Application of Synchrosqueezed Wavelet Transforms to Estimate the Reservoir Fluid Mobility. *Geophys. Prospecting* 66, 1358–1371. doi:10.1111/1365-2478.12622

Zhang, Y., Wen, X., Jiang, L., Liu, J., Yang, J., and Liu, S. (2020). Prediction of High-Quality Reservoirs Using the Reservoir Fluid Mobility Attribute Computed from Seismic Data. *J. Pet. Sci. Eng.* 190, 107007. doi:10.1016/j.petrol.2020.107007

Conflict of Interest: Author YD is employed by No.2 Oil Production Plant, Petrochina Dagang Oilfield Company.

The remaining authors declare that the research was conducted in the absence of any commercial or financial relationships that could be construed as a potential conflict of interest.

Publisher's Note: All claims expressed in this article are solely those of the authors and do not necessarily represent those of their affiliated organizations, or those of the publisher, the editors and the reviewers. Any product that may be evaluated in this article, or claim that may be made by its manufacturer, is not guaranteed or endorsed by the publisher.

frontiers in Earth Science

ORIGINAL RESEARCH
published: 28 March 2022
doi: 10.3389/feart.2022.851379

The Inverse Fresnel Beam XSP-CDP Stack Imaging in Crosswell Seismic

Fei-Long Yang[1,2,3,4]*, *Guang-Ying Ren*[1], *Feng-Ming Yao*[1] and *Chong Zhao*[1]

[1]School of Earth Sciences and Engineering, Xi'an Shiyou University, Xi'an, China, [2]State Key Laboratory of Oil and Gas Reservoir Geology and Exploitation, Chengdu University of Technology, Chengdu, China, [3]Academician and Expert Workstation, Xi'an Shiyou University, Xi'an, China, [4]Shaanxi Key Laboratory of Petroleum Accumulation Geology, Xi'an, China

In order to overcome the shortcomings of serious arc drawing and low computational efficiency in the crosswell seismic migration method and the problems of the inaccurate velocity model and sparse distribution of reflection points in the traditional stack imaging method, the article proposes an inverse Fresnel beam XSP-CDP stack imaging method based on first-arrival wave velocity tomography combined with the characteristics of crosswell seismic wave field. Firstly, an accurate crosswell velocity model is established by the first-arrival wave tomography inversion method based on the characteristics of high energy and easy pick-up of the first-arrival wave in crosswell seismic. Secondly, the velocity model is optimized, and the energy contribution weights of effective rays to the receiver point are calculated through the crosswell seismic Fresnel beam wave field forward numerical simulation method. Then, the reflected wave field is dynamically migrated to the reflection points within the first Fresnel zone according to the weight function, and the intensive common reflection point (CRP) gather after normal moveout (NMO) correction is generated. Finally, an appropriate bin is selected for stacking. In this article, the inverse Fresnel beam method is used to decompose the single-channel seismic wave field into the effective reflection points in the Fresnel zone, which makes the fold of the reflection point more uniform and improves the imaging accuracy. The model test and actual data processing results proved the validity and robustness of this method.

Keywords: crosswell seismic, inverse Fresnel beam, weight function, tomography, stack imaging

OPEN ACCESS

Edited by:
Jidong Yang,
China University of Petroleum, China

Reviewed by:
Hui Sun,
Southwest Jiaotong University, China
Li Xingwang,
Chang'an University, China

***Correspondence:**
Fei-Long Yang
feilongy@xsyu.edu.cn

Specialty section:
This article was submitted to Solid Earth Geophysics, a section of the journal Frontiers in Earth Science

Received: *09 January 2022*
Accepted: *28 February 2022*
Published: *28 March 2022*

Citation:
Yang F-L, Ren G-Y, Yao F-M and Zhao C (2022) The Inverse Fresnel Beam XSP-CDP Stack Imaging in Crosswell Seismic. Front. Earth Sci. 10:851379. doi: 10.3389/feart.2022.851379

INTRODUCTION

The field of oil and gas exploration is extending to complex reservoirs, complex structures, deep layers, unconventionality, and oceans. It is facing exploration and development problems such as complex surface, complex underground structures, changeable sedimentary facies, strong reservoir heterogeneity, thin thickness, deep burial, and small trap scale. Seismic imaging needs to further broaden the frequency band urgently to improve spatial resolution, identify thinner reservoirs (2–10 m) and smaller faults (less than 5 m), improve the imaging accuracy of complex structures, and serve new areas of oil and gas exploration (Zhao et al., 2017). As a high-resolution seismic exploration method, crosswell seismic technology has become a bridge and link connecting multidisciplinary oil and gas exploration methods (Cai, 2021). With the continuous innovation of the distributed optical fiber sensing instrument and the continuous progress of the optical fiber data processing method, the optical fiber borehole seismic technology has achieved good application effect in the fine exploration of the complex structure area, thin layer oil and gas exploration area, complex surface structure area, and carbonate reservoir area (Ma et al., 2020). Crosswell seismic

plays a role in resolution compensation, fine horizon calibration, and logging curve correction between drilling and seismic exploration. In the exploration method of time domain and depth domain, it plays a role of well-controlled time-depth conversion and formation depth prediction. In the process of extending from seismic exploration to fine reservoir development, it plays the role of seismic geological guidance, fine structure interpretation, and reservoir fracturing monitoring. At the same time, it builds a bridge between static reservoir description and dynamic monitoring (Cai et al., 2022).

The imaging methods of crosswell seismic mainly include migration based on the numerical solution of the wave equation and stack imaging based on the ray theory. Gaussian beam migration (GBM), the most important seismic data imaging method, is a flexible, accurate, and robust imaging technique (Hill, 1990, 2001; Hale, 1992; Gray, 2005; Nowack et al., 2005; Gray and Bleistein, 2009; Yue et al., 2012, 2019a, 2019b, 2019c). It not only solves the problems of multiple arrivals and imaging in caustic zones but also preserves high efficiency. Nevertheless, GBM produces numerous swing noises and migration artifacts when the signal-to-noise ratio and fold number of seismic data are low. Therefore, many new beam methods have been proposed, such as focused beam (Nowack, 2008; Wang and Yang, 2015; Yang J.-D. et al., 2015), complex beam (Zhu, 2013), fast beam (Gao et al., 2006), and Fresnel beam (Yang J. D. et al., 2015; Huang et al., 2016). A traditional method to reduce the artifacts is to limit the imaging zones in which reflection events are smeared either in a model-driven or a data-driven way (Chauris and Salomons, 2004). The model-driven method strongly depends on a *priori* information and is inaccurate when the prior information is unreliable (Koren et al., 2008). The data-driven approach does not need a *priori* information and is more reliable (Hua and McMechan, 2001, 2003; Sun and Schuster, 2001, 2003; Buske et al., 2009). In order to suppress migration artifacts, Hu and Stoffa (2009) designed a Fresnel-weighted function to control the contributions of each beam to the final migration results, which ensures that the beams adjacent to the specular rays have dominant smearing energies. Han et al. (2018) introduced a wavelength-dependent Fresnel beam propagator, which is constructed based on the frequency-dependent travel times and provides accurate wave-propagating directions. The crosswell seismic stack imaging method based on the ray theory can effectively avoid the migration artifacts and has higher computational efficiency. Its theoretical basis is the VSP-CDP conversion theory proposed by Wyatt (1981). This technology was first developed based on the horizontal layer. Therefore, the traditional stacking method is only suitable for simple geological structures. In order to overcome the complex structure and lithology imaging problems, different ray tracing methods are applied to VSP-CDP wave field conversion. Yan et al. (2000) combined ray-tracing algorithm for heterogenous media with VSP-CDP conversion to solve the imaging problem of crosswell seismic reflection in anisotropic media. Li and Qiang (2016) optimized the complex structures by using the block iterative segment by the segment method first and then carried out VSP-CDP conversion based on the ray tracing results to solve the reflection wave imaging problem of the complex structures between wells. Kong et al. (2007) sorted the reflected waves in the CDP gather according to the incident angle, calculated the critical angle by using the logging acoustic velocity, and determined the effective stack imaging angle by angle scanning. This method solves the imaging problem of the wide angle reflection of crosswell seismic. Yang et al. (2015, 2016, 2020b) introduced the Gaussian beam method into VSP-CDP conversion, calculated the coordinate of the reflection point and energy weight of the effective ray by Gaussian beam wave field forward modeling, and performed inverse Gaussian beam decomposition on crosswell seismic wave field during imaging. This method is not only suitable for the imaging of complex structures but also can increase the fold numbers of reflection points based on the effective proximate wave field approximation theory, which effectively improves the imaging effect of crosswell seismic-reflected wave field. Yang et al. (2020a) found that the energy distribution of Gaussian beam wave field stacking meets the normal distribution law and proposed the Gaussian beam stack imaging method based on normal distribution by comparing Gaussian beam operator and normal distribution function.

This article presents a crosswell seismic XSP-CDP stack imaging method using the Fresnel beam propagator for common shot records. Crosswell seismic first-arrival wave tomography and the method of wave field interaction analysis are used to establish the velocity model. Based on the theory of wave approximation in the vicinity of central rays (Červený and Pšenčík, 1984), we use the Fresnel beam forward modeling method to calculate the coordinate of the reflection point and energy weight of effective rays in the first Fresnel zone. Then, the Fresnel beam weight function is used to extract intensive CRP gathers in inverse Fresnel beam XSP-CDP conversion.

This article is organized as follows: First, the representation of first-arrival wave travel-time tomography is presented. Next, the Fresnel beam ray operator is deduced by comparing the Gaussian beam propagation method, and the energy weight function of the effective ray is calculated based on the Fresnel–Huygens propagation theory. Then, we apply the inverse Fresnel beam XSP-CDP stack method to convert the CSG gather into intense CRP gather. Finally, synthetic and field data examples are used to illustrate the performance of the proposed method.

METHODS

The First-Arrival Wave Travel-Time Tomography

Accurate velocity is the key to imaging. Considering that the energy of the crosswell seismic first-arrival wave field is prominent and easy to pick up, the initial velocity model is obtained by using the crosswell seismic first-arrival wave tomography (compared with the full waveform inversion, first-arrival velocity tomography is easy to realize and its accuracy can meet the requirements of imaging), and the velocity field is adjusted by the interactive velocity analysis method based on wave field forward modeling, which provides an accurate velocity model for crosswell seismic wave field imaging. The first step of tomography is to establish an initial velocity model according to the geological model range. The model is discretized, and N pixels are obtained by arranging the first and last columns of the rectangular grid. We assume that the slowness in each grid

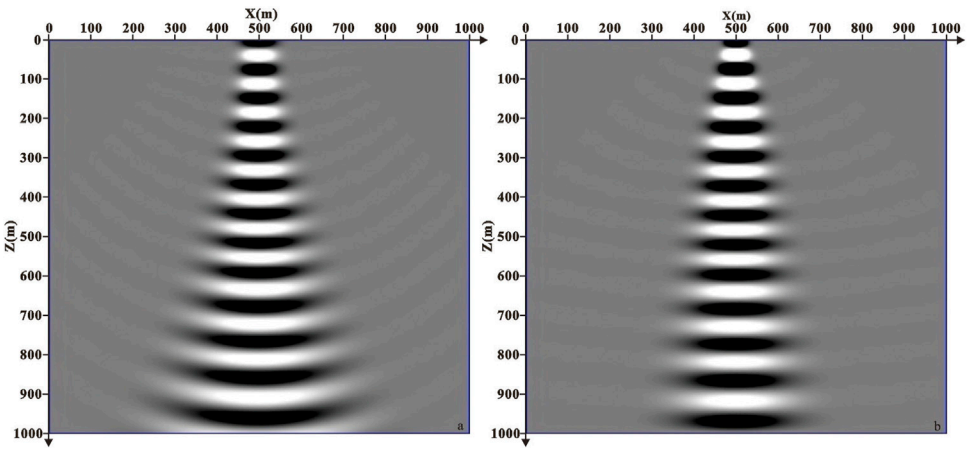

FIGURE 1 | Comparison diagram of beam propagation in the constant velocity model. **(A)** Gaussian beam and **(B)** Fresnel beam.

cell is a constant and can be illustrated as s_j (j = 1.2,. . .,N). An imaging base function for each j is defined as,

$$g_j(x,z) = \begin{cases} 1, (x,z) \in \text{The } j^{th} \text{ pixel} \\ 0, (x,z) \notin \text{The } j^{th} \text{ pixel} \end{cases}. \quad (1)$$

The seismic wave slowness s (x,z) of underground media can be represented by the linear combination of s_j and g_j, namely,

$$s(x,z) = \sum_{j=1}^{N} s_j g_j(x,z) \quad (j = 1,2,...,N). \quad (2)$$

It is assumed that the number of the first-arrival ray path is I, each ray can be expressed as I (i = 1.2,. . .,I), and it also corresponds to a first-arrival travel time and is represented by b_i (i = 1.2,. . .,I). b_i is equal to the curve integral of s (x,z) along the ith ray. Therefore, b_i can be regarded as the generalized Radon positive transformation of s (x,z), namely,

$$b_i = \int_{L_i} \sum_{j=1}^{N} s_j g_j(x,z) ds = \sum_{j=1}^{N} s_j \int_{L_i} g_j(x,z) ds \quad (i = 1,2,...,I). \quad (3)$$

According to the definition of g_j (x,z), $\int_{L_i} g_j(x,z) ds$ is the length of first-arrival ray in the ith trace and in the j grid, which is represented by a_{ij} (i = 1.2, . . . ,I,j = 1.2, . . . ,N). Thus, the first-arrival wave travel-time tomography equations can be illustrated as,

$$\begin{bmatrix} a_{11} & a_{12} & \cdots & a_{1j} & \cdots & a_{1N} \\ a_{21} & a_{22} & \cdots & a_{2j} & \cdots & a_{2N} \\ \vdots & \vdots & \cdots & \vdots & \cdots & \vdots \\ a_{i1} & a_{i2} & \cdots & a_{ij} & \cdots & a_{iN} \\ \vdots & \vdots & \cdots & \vdots & \cdots & \vdots \\ a_{I1} & a_{I2} & \cdots & a_{Ij} & \cdots & a_{IN} \end{bmatrix} \begin{bmatrix} s_1 \\ s_2 \\ \vdots \\ s_j \\ \vdots \\ s_N \end{bmatrix} = \begin{bmatrix} b_1 \\ b_2 \\ \vdots \\ b_j \\ \vdots \\ b_I \end{bmatrix}. \quad (4)$$

Noted as,

$$As = b, \quad (5)$$

where $A = [a_{ij}]$ is the length of every ray of the first-arrival wave in each grid and is obtained by LTI linear interpolation in inversion. s is a vector composed of reciprocals of seismic wave velocity in each grid, which is the result of tomography and can be expressed as $s = (s_1, s_2, \cdots, s_N)^T$. b is a vector of the first-arrival time of each ray and can be expressed as $b = (b_1, b_2, \cdots, b_I)^T$.

The process of crosswell seismic first-arrival wave tomography is to solve **Eq. 5**, which is a large sparse matrix. In this article, the damped LSQR method with the advantages of fast convergence, memory saving, and small calculation amount is used for solving the equation. Coefficient matrix A is any coefficient matrix with I line and N column, that is, $A = A_{I \times N}$, $s \in R^N$, $b \in R^I$. First, the coefficient matrix A is converted into a set of equations whose coefficient matrix is a square matrix. Then, the Lanczos method and QR decomposition method are used to solve the equations. The least squares problem of $As = b$ can be illustrated as,

$$\min \|As - b\|^2. \quad (6)$$

By adding the damping factor (λ), it becomes a damped LSQR problem,

$$\min \left\| \begin{bmatrix} A \\ \lambda I \end{bmatrix} s - \begin{bmatrix} b \\ 0 \end{bmatrix} \right\|^2. \quad (7)$$

The solution satisfies the symmetric equation system,

$$\begin{bmatrix} I & A \\ A^T & -\lambda^2 I \end{bmatrix} \begin{bmatrix} r \\ 0 \end{bmatrix} = \begin{bmatrix} b \\ 0 \end{bmatrix}, \quad (8)$$

where I is the unit matrix, and r is the residual vector and can be expressed as $r = b\text{-}AS$. As the number of iterations increases, the solution obtained by iteration does not change significantly, that is, the solution x_m after the mth iteration satisfies $\|As_m - b\| < \varepsilon$, and the iteration stops. ε is the estimation of the minimum travel time b, which indicates that the data obtained by iteration are in good agreement with the actual data.

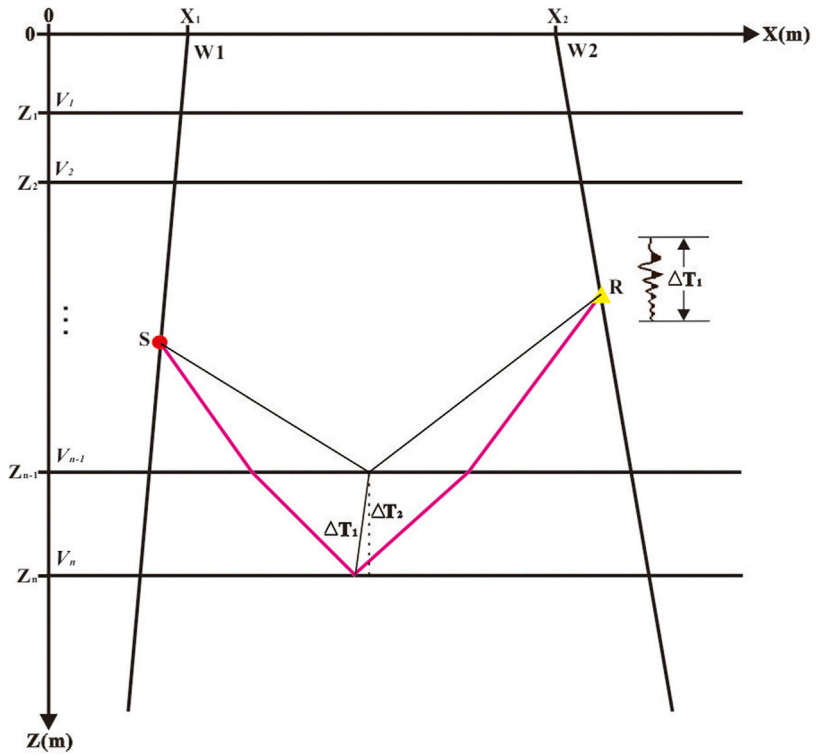

FIGURE 2 | Schematic diagram of XSP-CDP wave field conversion.

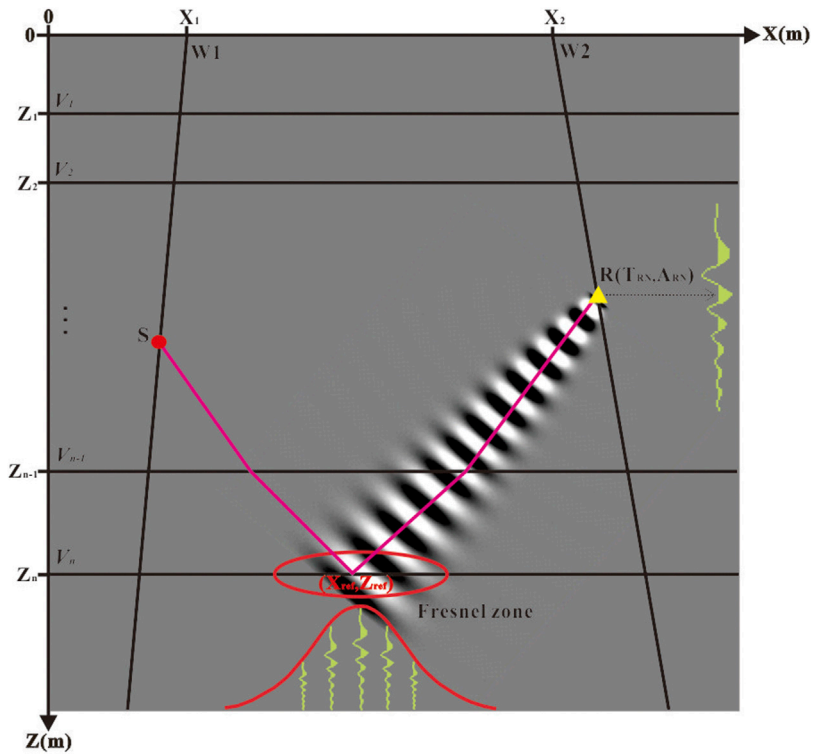

FIGURE 3 | Schematic diagram of inverse Fresnel beam XSP-CDP wave field conversion.

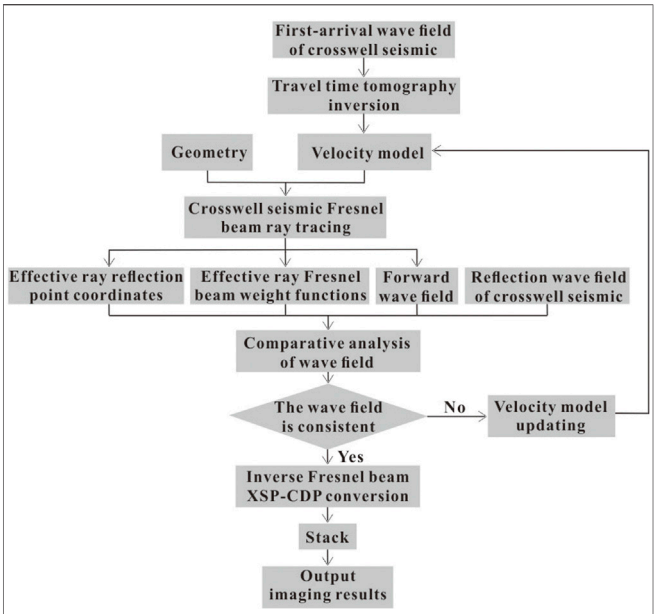

FIGURE 4 | Workflow of the inverse Fresnel beam XSP-CDP stack imaging method.

Fresnel Beam Operator

Based on the Huygens–Fresnel wave field propagation theory, the wave field at the receiver point is the Gaussian-weighted stacking of the effective ray energy in the first Fresnel zone. The weight function can be used to describe the contribution weight of the effective ray to the energy of the receiver point. The Fresnel beam method is an improvement of the Gaussian beam method, which limits the effective half width of the Gaussian beam in the first Fresnel zone. Thus, in order to make the energy of seismic beam conform to the Huygens–Fresnel principle, the Gaussian beam method is constrained to make the finite half width of the Gaussian beam equal to the first Fresnel zone radius. It can be expressed as,

$$\left[\frac{\omega}{2}\mathrm{Im}\left(\frac{\varepsilon(s)p_1(s)+p_2(s)}{\varepsilon(s)q_1(s)+q_2(s)}\right)\right]^{-1/2}=\sqrt{\frac{\pi}{\omega}\frac{q_2(s)}{p_2(s)}+\frac{\lambda_{ave}^2}{16}}. \quad (9)$$

The initial parameters $\varepsilon(s)$ can be obtained by solving **Eq. 9** and expressed as,

$$\varepsilon(s)=-i\frac{\xi+\sqrt{\xi^2-4q_1^2(s)q_2^2(s)}}{2q_1^2(s)}, \quad (10)$$

where $\xi=(\pi q_2(s)/p_2(s)+\pi^2 v_{ave}/(4\omega_{ref}))/2$. p and q are the ray parameters in the dynamic ray tracing equation, v_{ave} is the average velocity, and ω_{ref} is the reference frequency.

It can be seen from **Eq. 10** that the initial parameter of the ray constrained by the Fresnel zone is no longer a constant but a function dynamically changing with the ray arc length. It is a dynamic selection method, which can constrain the main energy of the seismic beam in the first Fresnel zone (Yang, 2016). Therefore, based on the expression of Gaussian beam seismic wave field propagation, the calculation formula of Fresnel beam seismic wave field can be obtained as,

$$U(s,n)=\sqrt{\frac{v(s)}{\varepsilon(s)q_1(s)+q_2(s)}}\exp\left\{i\omega\left[\tau(s)+\frac{1}{2}\frac{\varepsilon(s)p_1(s)+p_2(s)}{\varepsilon(s)q_1(s)+q_2(s)}n^2\right]\right\}, \quad (11)$$

where $v(s)$ is the velocity of the central ray, n is the component of the ray central coordinate system, and $\tau(s)$ is the travel time of the seismic wave.

Therefore, the 2D Green's function of any point M can be expressed as the stacking of Fresnel beams in different emission directions. It can be expressed as,

$$G(M)=\int_0^{2\pi}\phi(\varphi,s)U_\varphi(s,n)d\varphi, \quad (12)$$

where φ is the exit angle of the central ray, $U_\varphi(s,n)$ is the wave field of the Fresnel beam, and $\phi(\varphi,s)$ is the Fresnel beam weight function.

The Green's function in a two-dimensional homogenous medium can be expressed as,

$$G\approx\frac{\exp[i\omega r/v_0+i\mathrm{sgn}(\omega)\pi/4]}{2\sqrt{2\pi|\omega|r/v_0}}, \quad (13)$$

where v_0 is the velocity of the homogenous medium.

The Fresnel beam weight function can be obtained by comparing the analytical solution of the Green's function and the approximate solution represented by the Fresnel beam in the homogenous medium. It can be illustrated as,

$$\phi(\varphi,s)=\frac{i}{4\pi}\left[\frac{\varepsilon(s)}{v_0}\right]^{1/2}. \quad (14)$$

The propagation of the real part of the amplitude in an isotropic medium is shown in **Figure 1**. **Figure 1A** is the Gaussian beam, and **Figure 1B** is the Fresnel beam. They have the same parameters, such as the starting point of the ray beam is located at (500 m, 0 m), the initial direction of the ray beam is 0°, the frequency of the ray beam is 20 Hz, the reference frequency is 30 Hz, the propagation velocity is 1500 m/s, and the initial beam width is 40 m. It can be found from **Figure 1** that the Gaussian beam width increases rapidly with the increase of the distance, while the Fresnel beam can control the beam width very well.

The Inverse Fresnel Beam XSP-CDP Stack Imaging

The traditional crosswell seismic reflection XSP-CDP stack imaging method is to transform the sample value of the record in each CSG (or CRG) from the depth-time domain to the reflection point depth-offset domain. Each sample point in CSG can only be converted into one sample point in CRP gather. In this article, the wave field energy of each receiver is derived

TABLE 1 | Geometry parameters.

Shot parameter				**Receiver parameter**			
Total shot number		11		Total trace (1shot)		101	
Shot interval (m)		100		Trace interval (m)		10	
First shot coordinate (m)		(100,0)		First trace coordinate (m)		(700,0)	
Last shot coordinate (m)		(100,1,000)		Last trace coordinate (m)		(700,1,000)	
Sample interval (ms)		1		Sample number		1,000	
Left well coordinate	X(m)	Y(m)	Z(m)	Right well coordinate	X(m)	Y(m)	Z(m)
Well top	100	0	0	Well top	700	0	0
Well bottom	100	0	1,000	Well bottom	700	0	1,000

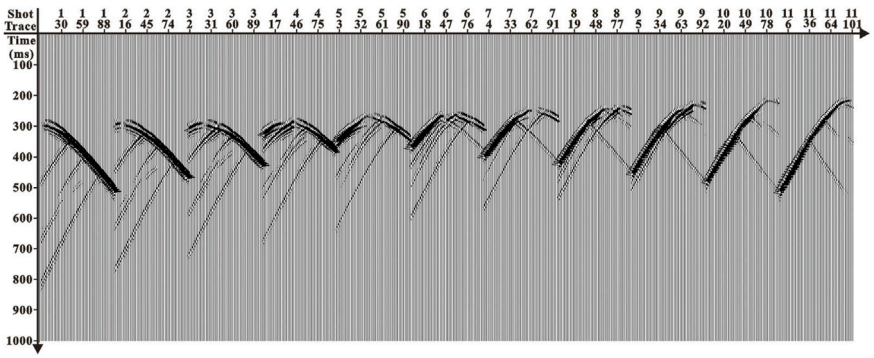

FIGURE 5 | Original field seismic data.

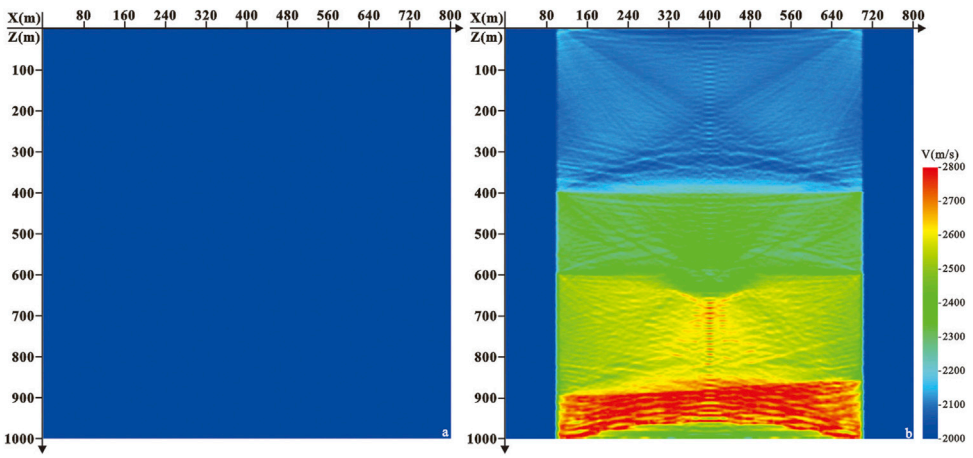

FIGURE 6 | Velocity model. **(A)** Initial velocity model and **(B)** velocity of first-arrival wave tomography.

from the Fresnel beam energy weight of the effective rays in its Fresnel zone. Therefore, based on the Huygens–Fresnel wave field theory, the single channel record in CSG (or CRG) is converted and decomposed into multichannel CRP wave field records in the Fresnel zone under the constraint of the wave theory, and the number of reflection points is adaptively increased to improve the imaging accuracy.

The process of XSP-CDP wave field conversion is similar to NMO correction, that is, each sample point of the CSG is converted to the corresponding CRP gather. In the CSG data, ΔT_1 is the travel time difference of the reflection wave from adjacent strata. The XSP-CDP conversion is to convert the wave field of ΔT_1 into the wave field of ΔT_2 in the adjacent strata of CRP gather, as shown in **Figure 2**. In order to eliminate the time difference between ΔT_1 and ΔT_2, ΔT_1 is corrected according to the coordinates of reflection points and the depth of strata, and the corresponding wave field is converted into the wave field with the time difference of ΔT_2.

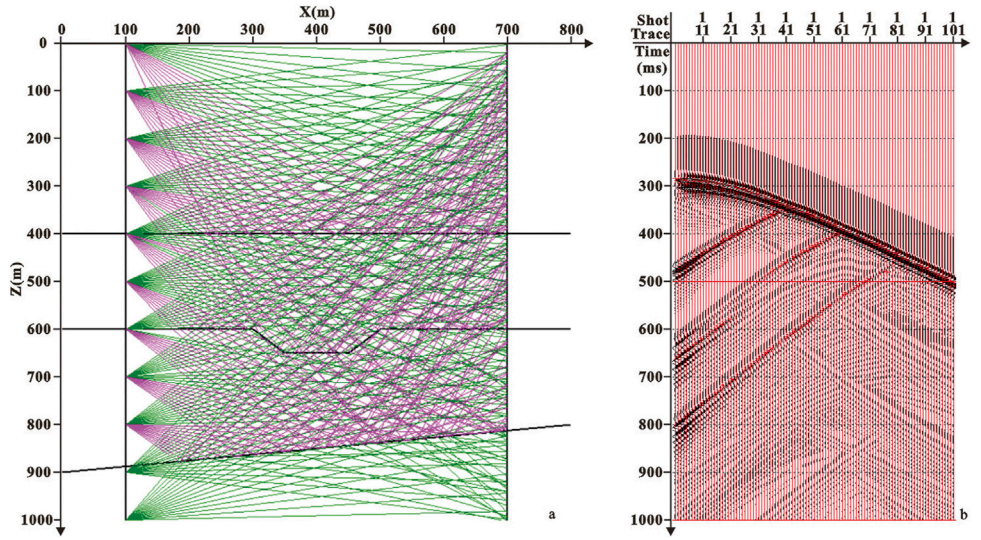

FIGURE 7 | Ray path diagram and comparison diagram of wave field interaction. **(A)** Ray path and **(B)** wave field interaction comparison diagram of the 1st shot.

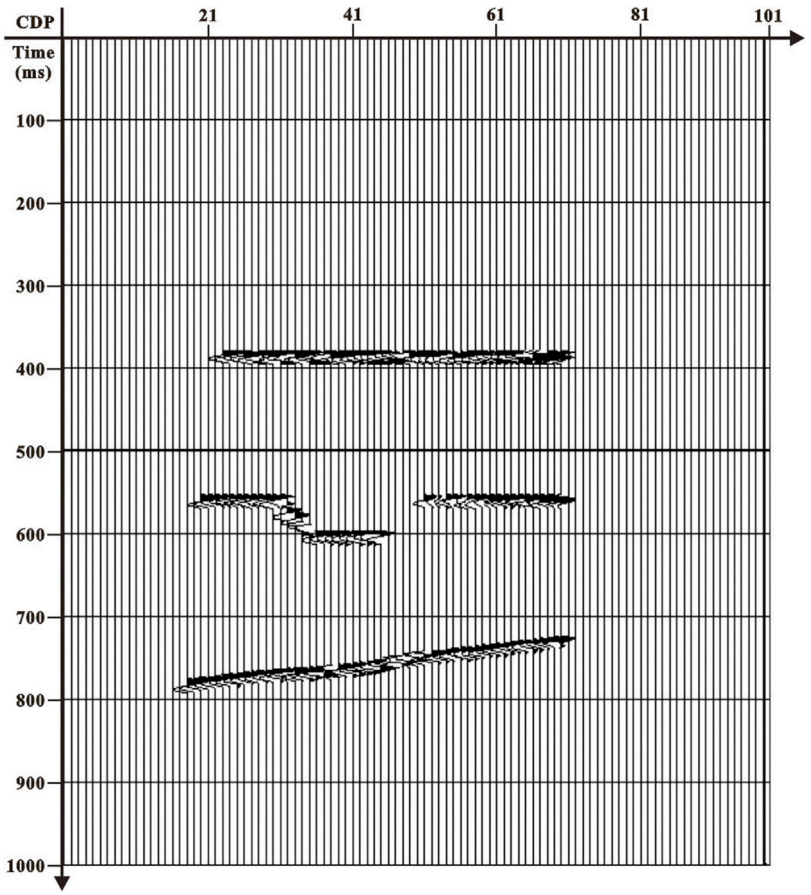

FIGURE 8 | Section of crosswell seismic inverse Fresnel beam stack imaging.

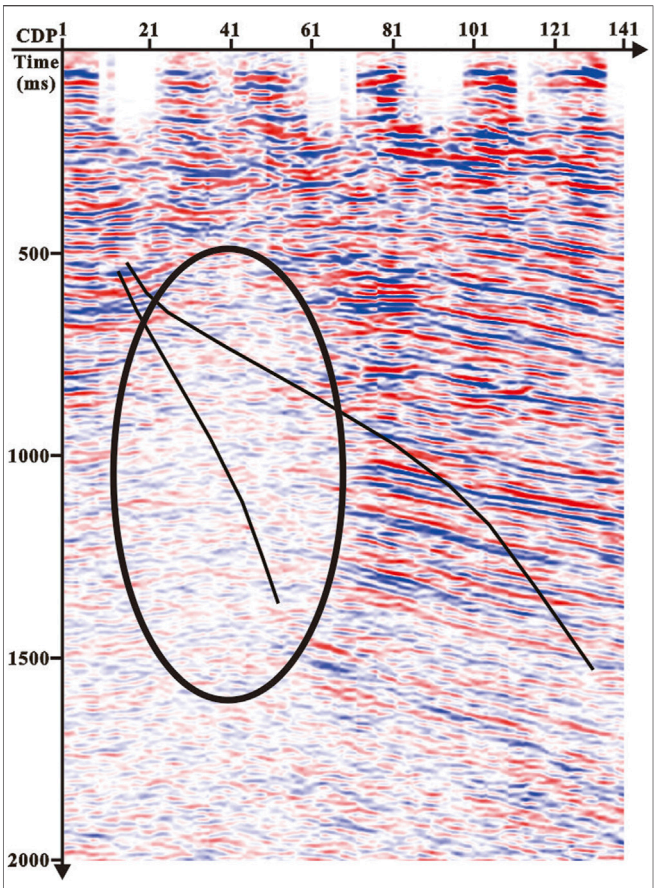

FIGURE 9 | Seismic imaging section across the wells.

As shown in **Figure 3**, T_{RN} is the sample point time when the R-channel receives the reflected wave field from the n-set stratigraphic interface, and A_{RN} is its wave field size. The inverse Fresnel beam XSP-CDP wave field conversion is to migrate the wave field at T_{RN} time into the reflection points belonging to the first Fresnel zone by preserving amplitude. The coordinates and weight functions of the effective rays that contribute to the A_{RN} can be obtained through the wave field forward modeling. If the coordinate of a reflection point is (X_{ref}, Z_{ref}), the inverse Fresnel beam XSP-CDP transformation can be expressed as,

$$\begin{cases} T_{NMO} = \dfrac{2 \cdot Z_{ref}}{\bar{V}} = 2 \cdot \sum_{i=1}^{n} \dfrac{Z_i}{V_i} \\ N_{CDP} = \dfrac{X_{ref} - X_{\min}}{\Delta X} \\ A\left(X_{ref}, Z_{ref}\right) = \phi\left(X_{ref}, Z_{ref}\right) A_{Rn} \end{cases}, \tag{15}$$

where T_{NMO} is the two-way travel time of the reflection point relative to the surface after the inverse Fresnel beam XSP-CDP wave field conversion. ΔX is the CDP bin size. N_{CDP} is the CDP value of the reflection point. A is the amplitude of the sample point. ϕ is the Fresnel beam weight function. Z_i and V_i are the depth and velocity of every stratum corresponding to the reflection point, respectively.

The crosswell seismic inverse Fresnel beam XSP-CDP stack imaging calculation steps are as follows: First, the spatial position of CRP, which belongs to the first Fresnel zone corresponding to the receiver point, and its Fresnel beam weight functions are calculated through the Fresnel beam forward modeling method combined with the velocity model established by the first-arrival wave tomography.

The Second step is carried out by calculating the NMO time based on the VSP-CDP conversion idea and migrating the amplitude of input trace to the imaging grid points of the output channel in the first Fresnel zone adaptively. This process decomposes and converts the single trace wave field of CSG (or CRG) into multichannel CRP wave field records in the Fresnel zone under the constraint of the wave theory.

Finally, the bins are divided according to a certain interval (including in X and t directions). If the sample point (x, t) after the inverse Fresnel beam XSP-CDP conversion falls into a CDP bin, then the sample point belongs to the CDP. All samples are migrated as mentioned previously, and the number of samples falling into each bin is counted, and their amplitudes are stacked as the output samples of the CDP point. Until all samples are completed, the final stack imaging profile is obtained.

The workflow of the inverse Fresnel beam XSP-CDP stack imaging method in crosswell seismic is shown in **Figure 4**.

RESULTS

Model Test

Based on the crosswell seismic inverse Fresnel beam stack imaging method, this section will test the correctness and robustness of the method through theoretical data. The parameters of geometry are shown in **Table 1**. The original field seismic data are shown in

TABLE 2 | Geometry parameters.

Shot parameter				**Receiver parameter**			
Total shot number	60			Total trace (1shot)	120		
Shot interval (m)	15			Trace interval (m)	10		
First shot coordinate (m)	(401.7,659)			First trace coordinate (m)	(293.8,612.5)		
Last shot coordinate (m)	(1550.4,1544)			Last trace coordinate (m)	(3595,1802.5)		
Sample interval (ms)	1			Sample number	1,000		
Left well coordinate	X(m)	Y(m)	Z(m)	Right well coordinate	X(m)	Y(m)	Z(m)
Well top	40	0	6	Well top	40	0	6
Well bottom	1,610	0	1,580	Well bottom	3,695	0	1,850

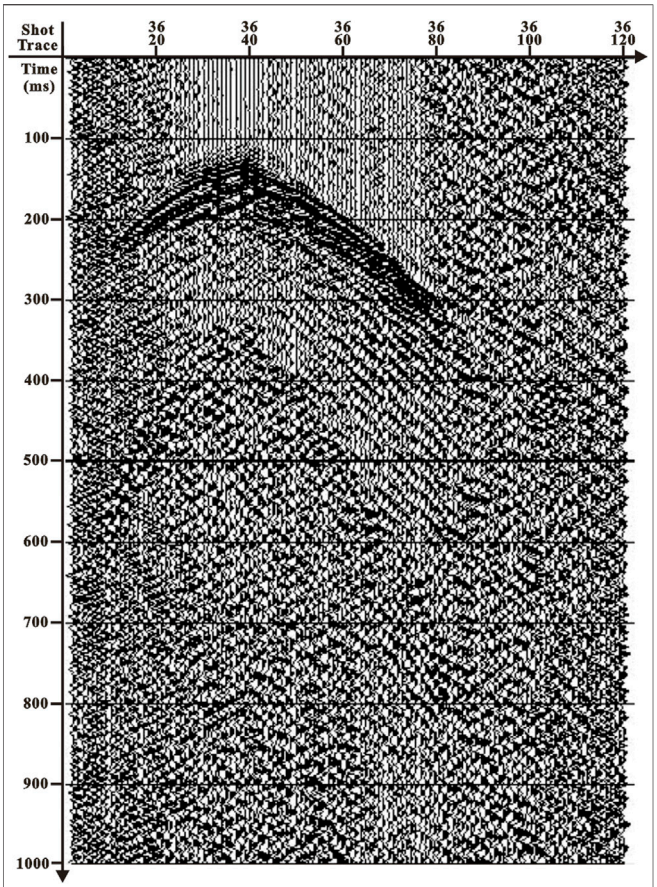

FIGURE 10 | Wave field records of crosswell seismic.

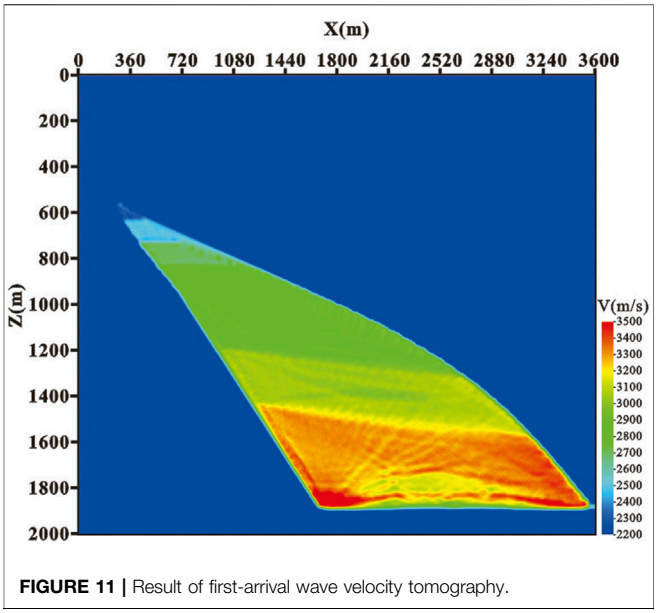

FIGURE 11 | Result of first-arrival wave velocity tomography.

Figure 5. It can be seen from the figure that the first-arrival wave energy of the crosswell seismic is prominent and easy to pick up. The constant velocity model is used as the initial velocity (as shown in **Figure 6A**), and **Figure 6B** is the result of tomography. The crosswell seismic Fresnel beam forward modeling method is carried out with geometry shown in **Table 1** based on the aforementioned velocity model, and the ray path and wave field record diagram are shown in **Figure 7**. As shown in **Figure 7B**, the velocity field is checked and optimized by interactively comparing the wave field records of the forward simulation (in red color) with the seismic records collected in the field (in black color). The crosswell seismic inverse Fresnel beam XSP-CDP wave field conversion method is used to image the original seismic data, and the CDP bin is 10 m for stacking. The imaging result is shown in **Figure 8**. We can see that the crosswell seismic first-arrival wave velocity tomography provides an accurate velocity field for reflection wave imaging. The Fresnel beam forward numerical simulation method not only optimizes the velocity model but also provides the Fresnel beam weight function of the effective ray for the imaging, which makes the fold number of the reflection point more uniform and improves the imaging effect.

Practical Application

This part employs practical data to test the effectiveness of the proposed inverse Fresnel beam stacking method. We apply the method to a crosswell seismic field data in the Bohai oilfield in China. **Figure 9** is the imaging section of the ground seismic passing through the wells. Affected by the gas cloud, the internal wave field energy of the imaging section is weak (as shown in the circle in **Figure 9**), and the event axis is not clear, which is difficult to reflect the structural characteristics of the gas cloud area. Therefore, crosswell seismic exploration is carried out near the gas cloud area. The geometry parameters of crosswell seismic are shown in **Table 2**, and the original P-wave field record is shown in **Figure 10** (the 36th shot after three-component synthesis). The travel time of the first-arrival wave is picked up and used for velocity tomography inversion, and the crosswell velocity model is obtained as shown in **Figure 11**. The geological model was established based on the results of ground seismic imaging and velocity tomography, and the Fresnel beam wave field numerical simulation of the crosswell seismic was carried out. The ray path and wave field record are shown in **Figure 12**. **Figure 12B** is the wave field interaction diagram between the forward modeling seismic records of the 39th shot (in red color) and the field seismic records after wave field separation (in black color). In the actual data processing, the crosswell seismic Fresnel beam forward simulation can not only optimize the velocity field and calculate the Fresnel beam weight function of effective rays but also guide the wave field separation of crosswell seismic. The result of crosswell seismic inverse Fresnel beam stack imaging is shown in **Figure 13A**. It can be seen that the crosswell seismic imaging results can effectively solve the problem of unclear geological structures in the gas cloud area. As shown in **Figure 13B**, the crosswell seismic imaging results (CDP bin is 6.25 m) are embedded in the ground seismic imaging profile (CDP bin is 25 m). We can see that the crosswell seismic imaging results effectively compensate for the presence of ground seismic, and the crosswell seismic imaging results outside the gas cloud area are consistent with the ground seismic imaging results.

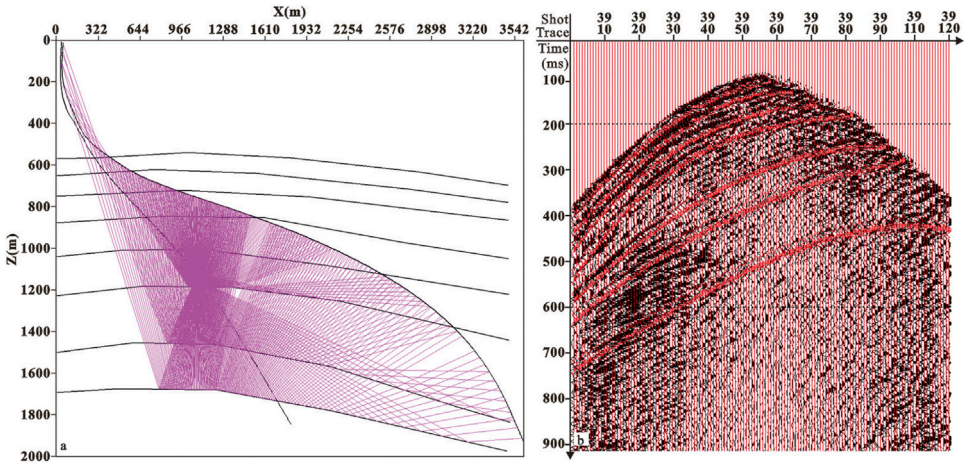

FIGURE 12 | Ray path diagram and comparison diagram of wave field interaction. **(A)** Ray path and **(B)** wave field interaction comparison diagram.

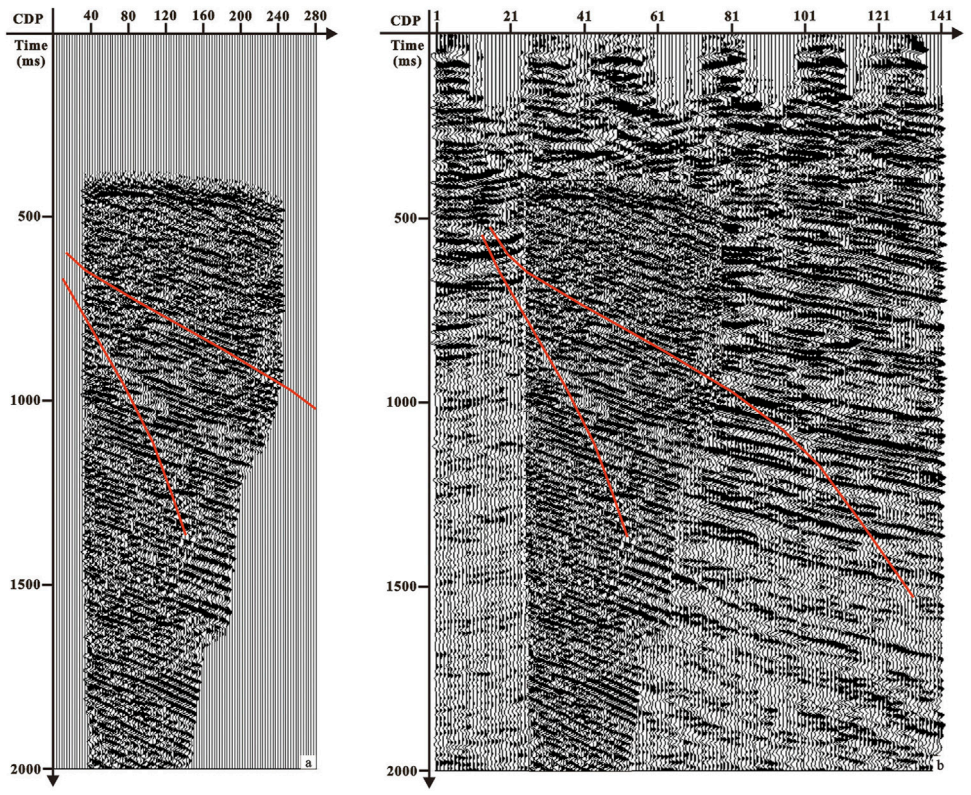

FIGURE 13 | Imaging results. **(A)** Section of crosswell seismic inverse Fresnel beam stack imaging and **(B)** overlapping map of crosswell seismic and ground seismic imaging.

DISCUSSION

Based on the Huygens–Fresnel wave field propagation theory, an inverse Fresnel beam stack imaging method suitable for crosswell seismic complex structures is proposed. The effectiveness and stability of the proposed method are verified by a theoretical model and practical data example. By studying the properties and characteristics of the Fresnel beam, the weight function formula based on the Fresnel beam stacking is derived, and it is applied to crosswell seismic stack imaging, which adaptively increases the fold number of the reflection point and improves the lateral resolution of seismic imaging. The results of model calculation

and actual data processing show that this method can finely image crosswell seismic data and effectively improve the lateral resolution of imaging. It has a potential value to become one of the effective tools for crosswell seismic wave field imaging.

DATA AVAILABILITY STATEMENT

The original contributions presented in the study are included in the article/Supplementary Material, further inquiries can be directed to the corresponding author.

AUTHOR CONTRIBUTIONS

F-LY, G-YR, F-MY, and CZ contributed to the conception and design of the study. F-LY deduced the algorithm and implemented the core algorithm of this manuscript. G-YR carried out the main work in the establishment of the theoretical model. The theoretical model is used to verify the correctness of the proposed method. F-MY and CZ have performed great work in practical data collation and trial calculations. All authors contributed to manuscript revision and read and approved the submitted version.

FUNDING

This work was funded by the Open Fund (PLC. 20211106) of State Key Laboratory of Oil and Gas Reservoir Geology and Exploitation (Chengdu University of Technology) and the Natural Science Basic Research Plan in Shaanxi Province of China (grant no. 2021JQ-588).

REFERENCES

Buske, S., Gutjahr, S., and Sick, C. (2009). Fresnel Volume Migration of Single-Component Seismic Data. *Geophysics* 74 (6), WCA47–WCA55. doi:10.1190/1.3223187

Cai, Z. (2021). Borehole Seismic: A Bridge Connecting Multiple Oil and Gas Exploration Methods. *Oil Geophys. Prospecting* 56 (4), 922–934. doi:10.13810/j.cnki.issn.1000-7210.2021.04.025

Cai, Z., Yang, B., and Wang, Y. (2022). Application of Optical Fiber Bore Hole Seismic Technology in Western China. *Geophys. Prospecting Pet.* 61 (1), 122–131. doi:10.3969/j.issn.1000-1441.2022.01.013

Červený, V., and Pšenčík, I. (1984). Gaussian Beams in Elastic 2-D Laterally Varying Layered Structures. *Geophys. J. Int.* 78, 65–91. doi:10.1111/j.1365-246X.1984.tb06472.x

Chauris, H., and Salomons, B. (2004). "Seismic Applications of One-Way Acoustic Reciprocity," in Proceedings of the 66th Annual International Conference and Exhibition, Paris, France, 7-11 June, 2004 (Houten, Netherlands: EAGE), G026. Extended Abstracts.

Gao, F., Zhang, P., Wang, B., and Dirks, V. (2006). "Fast Beam Migration - A Step toward Interactive Imaging," in Proceedings of the 76th Annual International Meeting, New Orleans, Louisiana, 1-6 October 2006 (Tulsa, Oklahoma, United States: SEG), 2470–2474. Expanded Abstracts. doi:10.1190/1.2370032

Gray, S. H., and Bleistein, N. (2009). True-amplitude Gaussian-Beam Migration. *Geophysics* 74 (2), S11–S23. doi:10.1190/1.3052116

Gray, S. H. (2005). Gaussian Beam Migration of Common-Shot Records. *Geophysics* 70 (4), S71–S77. doi:10.1190/1.1988186

Hale, D. (1992). "Migration by the Kirchhoff, Slant Stack, and Gaussian Beam Methods," Report 121 (Golden, Colorado: Colorado School of Mines, Center for wave phenomena).

Han, B., Gu, H., Liu, S., Yan, Z., Tang, Y., and Liu, C. (2018). Wavelength-dependent Fresnel Beam Propagator and Migration in VTI media. *J. Appl. Geophys.* 155, 176–186. doi:10.1016/j.jappgeo.2018.06.010

Hill, N. R. (1990). Gaussian Beam Migration. *Geophysics* 55, 1416–1428. doi:10.1190/1.1442788

Hill, N. R. (2001). Prestack Gaussian-beam Depth Migration. *Geophysics* 66, 1240–1250. doi:10.1190/1.1487071

Hu, C., and Stoffa, P. L. (2009). Slowness-driven Gaussian-Beam Prestack Depth Migration for Low-fold Seismic Data. *Geophysics* 74 (6), WCA35–WCA45. doi:10.1190/1.3250268

Hua, B. L., and McMechan, G. A. (2001). Parsimonious 2-D Poststack Kirchhoff Depth Migration. *Geophysics* 66, 1497–1503. doi:10.1190/1.1487095

Hua, B., and McMechan, G. A. (2003). Parsimonious 2D Prestack Kirchhoff Depth Migration. *Geophysics* 68, 1043–1051. doi:10.1190/1.1581075

Huang, J., Yang, J., Liao, W., Wang, X., and Li, Z. (2016). Common-shot Fresnel Beam Migration Based on Wave-Field Approximation in Effective Vicinity under Complex Topographic Conditions. *Geophys. Prospecting* 64, 554–570. doi:10.1111/1365-2478.12276

Kong, Q., Wang, Y., Jianjun, Z., Guohua, W., and Hongquan, W. (2007). Study and Application of Finite Angle Stack Approachincross-Hole Seismology. *Oil Geophys. Prospecting* 42 (3), 256–262. doi:10.3321/j.issn:1000-7210.2007.03.004

Koren, Z., Ravve, I., Ragoza, E., Bartana, A., Geophysical, P., and Kosloff, D. (2008). "Full-azimuth Angle Domain Imaging," in Proceedings of the 78th Annual International Meeting, Las Vegas, Nevada, 9-14 November 2008 (Tulsa, Oklahoma, United States: SEG), 2221–2225. Expanded Abstracts. doi:10.1190/1.3059327

Li, H., and Qiang, N. (2016). Forward Simulation Method for Crosswell Seismic of 3D Block Forward Modeling. *Pet. Geology. Eng.* 30 (3), 17–20. doi:10.3969/j.issn.1673-8217.2016.03.005

Ma, G., Cao, D., Yin, J., and Zhu, Z. (2020). Numerical Simulation of Detecting Seismic Signals in DAS wells. *Oil Geophys. Prospecting* 55 (2), 311–320. doi:10.13810/j.cnki.issn.1000-7210.2020.02.012

Nowack, R. L. (2008). "Focused Gaussian Beams for Seismic Imaging," in Proceedings of the 78th Annual International Meeting, Las Vegas, Nevada, 9–14 November 2008 (Tulsa, Oklahoma, United States: SEG), 2376–2380. Expanded Abstracts. doi:10.1190/1.3059356

Nowack, R. L., Sen, M. K., and Stoffa, P. L. (2003). "Gaussian Beam Migration for Sparse Common-shot and Common-receiver Data," in Proceedings of the 75th Annual International Meeting, The Breakers Hotel, September 16-21, 2003 (Tulsa, Oklahoma, United States: SEG), 1114–1117. Expanded Abstracts. doi:10.1190/1.1817470

Sun, H., and Schuster, G. T. (2001). 2-D Wavepath Migration. *Geophysics* 66, 1528–1537. doi:10.1190/1.1487099

Sun, H., and Schuster, G. T. (2003). 3D Wavepath Migration. *Geophys. Prospecting* 51, 421–430. doi:10.1046/j.1365-2478.2003.00380.x

Wang, X., and Yang, J. (2015). "Prestack Depth Migration Using Adaptive Focused Beams," in Proceedings of the 85th Annual International Meeting, New Orleans, Louisiana, USA, 18-23 October 2015 (Tulsa, Oklahoma, United States: SEG), 4293–4297. Expanded Abstracts. doi:10.1190/segam2015-5801751.1

Wyatt, K. D. (1981). Synthetic Vertical Seismic Profile. *Geophysics* 46 (6), 880–891. doi:10.1190/1.1441227

Yan, Y., Yi, M., Xin, W., and Wan, W. (2000). The Imaging and Interpretation of Reflection Waves in Cross-Hole Seismic Data. *Oil Geophys. Prospecting* 35 (1), 36–41. doi:10.13810/j.cnki.issn.1000-7210.2000.01.006

Yang, F., Li, H., Sun, H., Zhang, X., Luo, H., and Zhao, C. (2020b). VSP-CDP Stack Imaging Based on the Weight Function of normal Distribution. *Oil Geophys. Prospecting* 55 (1), 101–110. doi:10.13810/j.cnki.issn.1000-7210.2020.01.012

Yang, F., Sun, Y., Lu, J., Ma, D., Jing, Y., and Pei, D. (2015). The Gaussian Beam Stack Imaging Method of VSP[J]. *Geophys. Geochemical Exploration* 39 (3), 627–632. doi:10.11720/wtyht.2015.3.33

Yang, F., Zhao, C., Zhengrong, W., Sun, H., Li, H., Zhao, C., et al. (2020a). A Research on Inverse Gaussian Beam Stack Imaging in 3D Crosswell Seismic of

Deviated Well and its Application[J]. *Appl. Geophys.* 17 (5), 629–638. doi:10.1007/s11770-019-0830-x

Yang, F., Zhengrong, W., and Li, Q. (2016). "The Inverse Gaussian Beam Common-Reflection-point Stack Imaging in Crosswell Seismic[C]," in The 86th SEG Technical Program, Dallas, Texas, USA, 16-21 October 2016 (Tulsa, Oklahoma, United States: SEG), 840–845. Expanded Abstracts. doi:10.11720/wtyht.2015.3.33

Yang, J.-D., Huang, J.-P., Wang, X., and Li, Z.-C. (2015a). An Amplitude-Preserved Adaptive Focused Beam Seismic Migration Method. *Pet. Sci.* 12, 417–427. doi:10.1007/s12182-015-0044-7

Yang, J. D., Huang, J. P., Wang, X., and Li, Z. C. (2015c). "Fresnel Beam Depth Migration from the Irregular Topography," in Proceedings of the 85th Annual International Meeting, New Orleans, Louisiana, USA, 18-23 October 2015 (Tulsa, Oklahoma, United States: SEG), 4318–4322. Expanded Abstracts. doi:10.1190/segam2015-5747594.1

Yang, J. (2016). *The Research of Seismic Beam Migration Limited by Dynamic Parameters*. Beijing, China: School of Geosciences China University of Petroleum.

Yue, Y., Li, Z., Qian, Z., Zhang, J., Sun, P., and Ma, G. (2012). Amplitude-preserved Gaussian Beam Migration under Complex Topographic Conditions. *Chin. J. Geophys.* 55, 1376–1383. doi:10.6038/j.issn.0001-5733.2012.04.033

Yue, Y., Qian, Z., Zhang, X., Wang, D., Yue, Y., and Chang, W. (2019a). Gaussian Beam Based Born Modeling Method for Single-Scattering Waves in Acoustic Medium. *Chin. J. Geophys.* 62, 648–656. doi:10.6038/cjg2019M0367

Yue, Y., Sava, P., Qian, Z., Yang, J., and Zou, Z. (2019c). Least-squares Gaussian Beam Migration in Elastic media. *Geophysics* 84 (4), S329–S340. doi:10.1190/geo2018-0391.1

Yue, Y., Sun, P., Wang, D., Sun, P., Guo, Z., and Liu, Z. (2019b). Gaussian Beam Based Modeling Method for Single-Scattering Waves in Elastic Isotropic Medium. *Chin. J. Geophys.* 62, 657–666. doi:10.6038/cjg2019M0396

Zhao, B., Dong, S., and Zeng, Z. (2017). Borehole Seismic Development, Status Quo and Future: Application prospect of Borehole Seismic. *Oil Geophys. Prospecting* 52 (5), 1112–1123. doi:10.13810/j.cnki.issn.1000-7210.2017.05.026

Zhu, T. (2013). "Complex-beam Migration: Formulation and Comparisons," in Proceedings of the 83rd Annual International Meeting, Houston, Texas, USA, 22-27 September 2013 (Tulsa, Oklahoma, United States: SEG), 3687–3691. Expanded Abstracts. doi:10.1190/segam2013-0217.1

Conflict of Interest: The authors declare that the research was conducted in the absence of any commercial or financial relationships that could be construed as a potential conflict of interest.

Publisher's Note: All claims expressed in this article are solely those of the authors and do not necessarily represent those of their affiliated organizations, or those of the publisher, the editors, and the reviewers. Any product that may be evaluated in this article, or claim that may be made by its manufacturer, is not guaranteed or endorsed by the publisher.

frontiers | Frontiers in Earth Science

ORIGINAL RESEARCH
published: 11 April 2022
doi: 10.3389/feart.2022.850766

Two Improved Acquisition Systems for Deep Subsurface Exploration

Nengchao Liu[1,2], Gang Yao[1,3], Zhihui Zou[4,5]*, Shangxu Wang[1,2]*, Di Wu[1,2], Xiang Li[1,3] and Jianye Zhou[1,2]*

[1]State Key Laboratory of Petroleum Resources and Prospecting, China University of Petroleum (Beijing), Beijing, China, [2]College of Geophysics, China University of Petroleum (Beijing), Beijing, China, [3]Unconventional Petroleum Research Institute, China University of Petroleum (Beijing), Beijing, China, [4]Key Lab of Submarine Geosciences and Prospecting Techniques MOE, Ocean University of China, Qingdao, China, [5]College of Marine Geosciences, Ocean University of China, Qingdao, China

Present land seismic surveys mainly focus on acquiring reflection data. The maximum offset is usually 1–1.5 times the depth of targets. Limited offset results in that the acquired diving waves only penetrate the shallow parts of the Earth model, far from targets. Thus, the reflection data are used to build the deep part of the velocity model with migration velocity analysis. However, two issues challenge the success of velocity model building. First, incomplete information. Limited offsets lead to a narrow aperture of observation, which results in an under-determined inversion system. One manifestation is the trade-off between the depth of interfaces/reflectors and the average velocity above them. Second, low signal-to-noise (S/N) ratios. Complex near-surface conditions and geologic structures lead to low S/N ratios for reflection data, which fails to build velocity with reflection data. The fundamental solution to these two issues is to acquire better data with an improved acquisition system. In this work, we propose two types of modified geometries to enhance the penetration depth of the diving waves, especially the first arrivals, which can be used to build a deeper velocity model effectively. Type-I geometry adds extra sparse sources on the extension line of the normal acquisition geometry, whereas Type-II geometry deploys extra sparse receivers on the extension line. Consequently, the new acquisition system includes ultra-large offsets, which acquire diving waves from the deep subsurface. These diving waves, including waveform and first-break time, are particularly useful for recovering deeper velocity, which has paramount significance for the exploration of deep and ultra-deep hydrocarbon reservoirs. Synthetic and field data examples preliminarily demonstrate the feasibility of this improved acquisition system.

Keywords: seismic acquisition geometry, diving wave, velocity model building, nodal seismometer, seismic vibrator

OPEN ACCESS

Edited by:
Jianping Huang,
China University of Petroleum, Huadong, China

Reviewed by:
Qiang Guo,
China Jiliang University, China
Xiangchun Wang,
China University of Geosciences, China
Tengfei Wang,
Tongji University, China
Chenhao Yang,
TGS, United States

****Correspondence:***
Gang Yao
yaogang@cup.edu.cn
Zhihui Zou
zouzhihui@ouc.edu.cn
Shangxu Wang
wangsx@cup.edu.cn

Specialty section:
This article was submitted to Solid Earth Geophysics, a section of the journal Frontiers in Earth Science

Received: *08 January 2022*
Accepted: *28 February 2022*
Published: *11 April 2022*

Citation:
Liu N, Yao G, Zou Z, Wang S, Wu D, Li X and Zhou J (2022) Two Improved Acquisition Systems for Deep Subsurface Exploration. Front. Earth Sci. 10:850766. doi: 10.3389/feart.2022.850766

INTRODUCTION

Active-source seismic surveys are the main geophysical method for the exploration of subsurface geological structures and reservoir characteristics. Current seismic surveys are often designed to acquire the reflection waves, which are the seismic energy bounced back at the interfaces between rock layers. Since oil/gas reservoirs are mainly found in sedimentary rocks dominated by the flat layer feature, the seismic surveys set the maximum offset to 1–1.5 times the depth of targets (Yilmaz, 2001). As a result, the surveys are adequate for recording reflection data.

The conventional seismic data processes aim at utilizing reflections, especially primary reflections. Other types of events, including direct arrivals and refractions, are treated as noise; therefore, they are

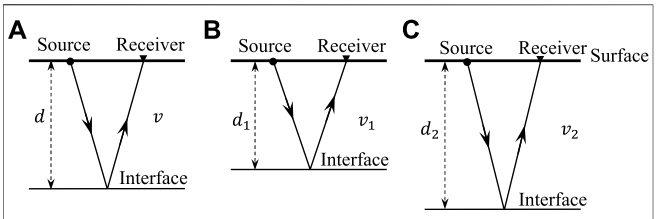

FIGURE 1 | Schematic illustration for the trade-off between the depth of interface and velocity above it. **(A)** The true scenario: both depth d and velocity v are correct. **(B)** The trade-off scenario 1: $d_1 < d$, $v_1 < v$. **(C)** The trade-off scenario 2: $d_2 > d$, $v_2 > v$. The two trade-off scenarios give the same travel time as the true scenario.

suppressed during data processing (Yilmaz, 2001). The main steps of the data processing include velocity model building and migration. The data processing can be performed either in the time domain or the depth domain. The time-domain data process is still popular because of its high efficiency and robustness. However, it suffers from low accuracy. Its migration profiles only show the travel time from the surface to the interfaces. Thus, the migration profiles do not provide the depth of the interfaces. In addition, time-domain migration assumes that the rocks are homogenous above an interface in the aperture of one common-middle-point (CMP) gather. Consequently, time-domain migration could produce artificial geological structures, especially in the region where the velocity possesses strong variation. Thus, time-domain migration results are inappropriate for tasks requiring high accuracy imaging, for example, bore well-drilling design.

By contrast, the depth-domain migration provides the image of geological structures matching the real world (Zhang and Sun, 2008; Liu et al., 2011; Li et al., 2021). Its migration profiles, therefore, are ideal for subsequent processes and interpretation. However, depth migration needs an accurate depth velocity. The migration velocity does not need to contain fine details but must provide an accurate background velocity, which gives the correct travel time and wave paths of reflections. Therefore, building the accurate migration velocity is crucial for depth migration. Limited by the offset, reflections are the only information source for building velocity reaching the depth of targets. Reflection-waveform inversion (RWI) (Xu et al., 2012; Wu and Alkhalifah, 2015; Zhou et al., 2015; Yao and Wu, 2017; Yao et al., 2020) and reflection-traveltime tomography (Sherwood et al., 1986; Kosloff et al., 1996) can be used to achieve this goal. Currently, reflection-traveltime tomography is the mainstream tool for velocity building in the industry. The principle is to utilize the move out residual to update the velocity above the selected reflection interfaces.

Two factors hamper the success of velocity building based on reflections: first, the trade-off between the depth of reflectors and velocity above reflectors. This phenomenon is illustrated in **Figure 1**: if a reflector is moved up/down by reducing/increasing the velocity above the reflector, the travel time keeps the same as that for the true depth and velocity. One symptom in practical applications is that the inverted velocity has strong fluctuation along the strata, which leads to artificial undulated reflectors in the migration image. This undulation becomes more severe in deep parts of the model than its shallow parts due to fewer data constraints as depth increases, for example, Figure 7A of Yao et al. (2019). The fundamental reason for this phenomenon is that inadequate information is used in the inversion. In other words, the inversion system is under-determined. To mitigate this issue, it is necessary to incorporate more information into the system. For instance, structural smoothing is a common constraint used for this purpose (Lewis et al., 2014; Yao et al., 2019).

The second factor is the low S/N ratio. This is common in land seismic surveys. **Figure 2** shows one typical shot gather with a low S/N ratio. The reflection events are barely seen in the profile. The low S/N ratio is caused by the near-surface complexity and complex structures. Consequently, it is almost impossible to build a correct velocity model using reflections in such a scenario.

These two factors lead to a paradox: time migration gives even better migration images than depth migration in this type of scenario, but the migration theory tells that depth migration is more accurate than time migration. One reason why time migration works better here is that it can build an optimal velocity by scanning the semblance of stacking velocity, resulting in plausible migration images.

The analysis above indicates that building an accurate velocity model is the key to reliable depth migration. To achieve this goal, the fundamental solution is to acquire adequate and reliable data. The company BP set such a pioneering example for full-waveform inversion (FWI). BP created a marine vibrator, called WolfSpar, which can generate reliable signals as low as about 1.6 Hz at an offset of 30 km (Dellinger et al., 2016). By combining with ocean bottom nodes (OBN), the acquired dataset successfully delivered much more accurate velocity models with FWI than with reflection travel-time tomography, resulting in stunning migration images (Shen et al., 2018; Zhang et al., 2018).

In this article, we propose an improved acquisition system for building more reliable velocity models for deep subsurface exploration. The basic idea is to add extra spare sources or receivers along the extension line of the normal geometry. As a result, this acquisition system includes ultra-large offsets, which are the foundation to acquire diving waves from the deep subsurface. The diving waves are refraction waves that bend back to the surface due to the velocity gradient of the Earth (Sheriff, 2002). Their waveform and first-arrival time are particularly useful for recovering deeper velocity, which has paramount significance for the exploration of deep and ultra-deep hydrocarbon reservoirs.

The rest of this article will be organized as follows: the improved acquisition geometry will be introduced first; examples then will be demonstrated; and finally, the discussion and conclusion will be given.

METHODOLOGY

Currently, reflection waves are the main objective for active seismic surveys. Thus, the maximum offset is usually about 1–1.5 times the depth of targets. Due to the two factors, which are elaborated in the section of introduction, it is still difficult for reflection-based travel time tomography to build an acceptable velocity model for

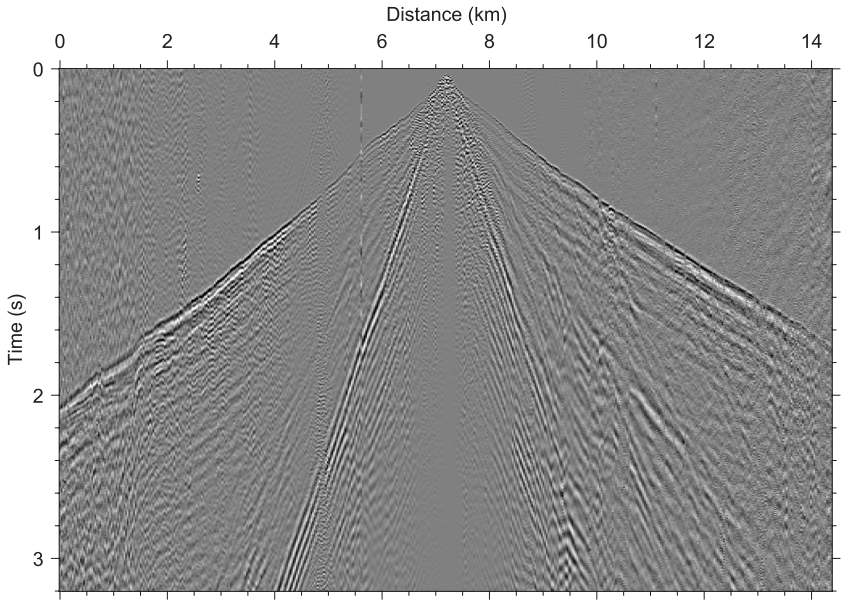

FIGURE 2 | A typical shot profile acquired from the foothills around the Tarim Basin. Trace equalization was applied. Reflection events are barely seen while the first arrival is clear.

migration imaging. By contrast, the diving waves, which are the transmitted waves turning back to the surface due to the velocity increase with depth, are the more robust signals for velocity building than the reflection waves. The reasons are two folds: first, it does not suffer from the trade-off between the depth of reflectors and velocity above reflectors because changing the depth of reflectors does not alter the travel time of diving waves significantly; second, the S/N ratio of diving waves is higher than reflection waves. There are also two other reasons. Diving waves are concentrated on the early arrivals in each trace so that they are not interfered with ground roll noise, which is strong and usually masks reflection signals (Yilmaz, 2001). In addition, reflection coefficients are much smaller than transmission coefficients (Berkhout, 1980). Consequently, the diving waves are robust for velocity building.

There are two ways to utilize the diving waves for velocity building. First-arrival travel time tomography is a robust way to invert the first arrivals of diving waves. The rest of the diving waves is the result of interference of multiple events and multi-path events. Due to the interference, it is impossible to distinguish the travel time of each event. Consequently, travel time tomography cannot be used for these data. One solution for the interfered diving waves is full-waveform inversion (FWI) (Tarantola, 1984; Virieux and Operto, 2009; Warner et al., 2013). In this article, we use travel time tomography (Zhou, 2003) to verify the concept of the improved acquisition geometry, so that the travel time of first arrivals is the information for velocity building.

Improved Acquisition Geometry

The maximum offset of the conventional acquisition geometry usually has 1–1.5 times the depth of the target. The penetration of diving waves is about 1/5–1/3 times the maximum offset (Zhou et al., 2015). Simple math implies that an adequate offset is the key for acquiring the diving waves reaching the depth of targets. Herein, we propose two means to extend the offset range: 1) Type-I modified geometry—exciting extra shots and 2) Type-II modified geometry—deploying extra receivers along the extension line of the normal geometry. **Figure 3** shows the schematic sketches of the two types of modified geometries for acquiring both shallow and deep diving waves.

The normal acquisition geometry part, that is, the red star source and yellow receivers in **Figure 3**, aims to acquire reflections and shallow diving waves. Its receiver interval is set about two times the interval of CMPs, which is related to the horizontal resolution. Usually, the receiver interval is small, for example, 20 m.

In Type-I modified geometry, the first extra source is set at a distance of h_1 to the nearest receiver, where h_1 indicates the maximum offset of the normal geometry part. The interval of the rest of the extra sources is two times h_1. With this setting, no source–receiver pair repeats the survey. This is demonstrated in **Section 2.2**. By contrast, in Type-II modified geometry, the extra receivers are installed along the extension line of the normal geometry. The extra receivers can be very sparsely positioned, which might lead to inaccurate shallow-region updates if this region is complex. This can be fixed by the diving waves that are recorded by dense receivers in the normal geometry. Therefore, the two parts of diving waves are complementary to each other for velocity building. The maximum offset of both modified geometries is set to acquire the diving waves from the targeted depth.

The Characteristics of the Modified Acquisition Geometries

The two types of modified geometries have different characteristics. Type-I modified geometry adds extra sources. The extra sources can

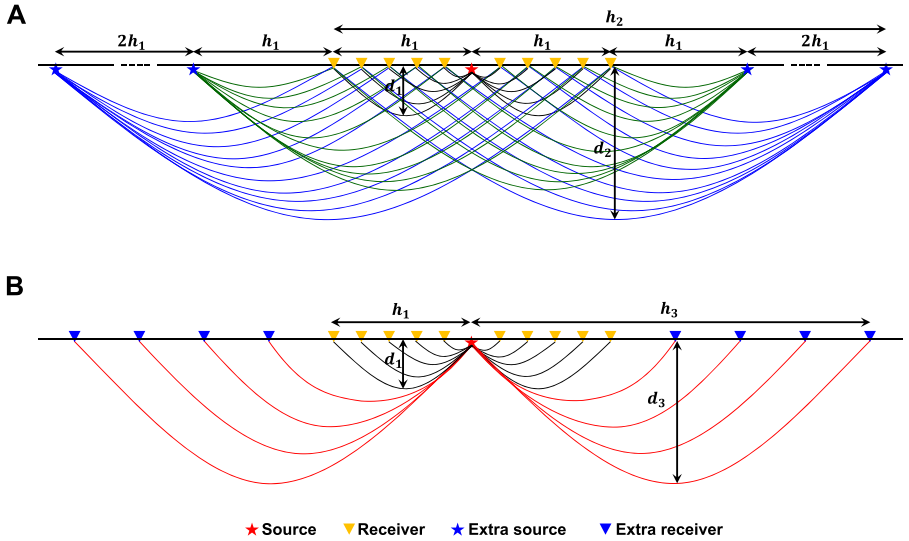

FIGURE 3 | (A) Type-I modified geometry: extra sources are added into the normal geometry, that is, the red star source and yellow receivers. h_1 represents the maximum offset of the receiver array in the normal geometry part. The first extra source is set at a distance of h_1 to the nearest receiver. The interval of the rest of the extra sources is $2h_1$. **(B)** Type-II modified geometry: extra receivers are added into the normal geometry. The interval of the extra receivers is much sparser than the receivers of the normal geometry part. h_2 and h_3 indicate the maximum offset of the modified geometries for acquiring diving waves. d_1, d_2 and d_3 represent the maximum penetration depth of the diving waves.

be different from the source for acquiring reflections. In order to acquire long-distance traveling diving waves, the source energy, for example, the amount of dynamite or the number of seismic vibrators, can be increased to generate stronger and lower-frequency seismic signals. This modification increases the number of shots several times compared with the normal geometry. Thus, one cost-effective way is to apply seismic vibrators instead of dynamite.

By contrast, Type-II modified geometry adds extra receivers. It is inconvenient to achieve this acquisition geometry with cable-connected geophones due to the large offset. The most efficient way to implement this geometry is to use nodal seismometers, which do not need a cable for connection. However, this modified geometry needs to select appropriate sources that ensure diving waves reach the extra receivers. If the extra sources and receivers are the same as that used in the normal geometry, then the two modified geometries are in fact equivalent. **Figure 4** illustrates this equivalence. Type-I geometry with only two extra sources shown in **Figure 4A** turns into Type-II geometry shown in **Figure 4D**. However, if the sources and receivers are different, the acquired data with the two geometries have different dynamics characteristics, for example, amplitude and frequency, but share similar travel time information. If the waveform is used for velocity building, match filtering can be used to remove the difference.

Workflow for Geometry Design

The improved geometries can be designed in three steps:

1) *Determining the maximum offset and interval for acquiring reflections.* Many studies have been done for this purpose. The general principle is that the maximum offset is set as about 1) 1.5 times the depth of targets, and the receiver interval is two times the expected horizontal resolution.
2) *Determining the maximum offset for acquiring the diving waves.* As a rule of the thumb, the maximum offset should be about 3–5 times the depth of the target. A more elegant way is to use ray tracing: building a background velocity model based on existing information about the survey area and then shooting rays into the velocity model to determine the offset that can receive the rays from the depth of the target.
3) *Determining the interval of the extra receivers or sources.* For Type-I geometry, the extra source interval is illustrated in **Figure 3A**: the first extra source is set at a distance of h_1 from its nearest receiver while the interval of rest of the extra sources is two times h_1. For Type-II geometry, an appropriate receiver array setting can achieve the condition that the rays should be dense in the shallow region but can be sparse in the deep region. This is because the width of the first Fresnel zone is narrow, that is, w is small, in the shallow but wide, that is, w is large, in the deep, which is illustrated in **Figure 5**. The shallow region is covered by the dense rays from the normal geometry for recording reflections so that the intervals of the extra receivers can be very sparse. However, it is hard to give exact criteria for the interval of the extra receivers and sources. One practical means is to do simulations with different parameters.

EXAMPLES

Synthetic Data Example

One synthetic model shown in **Figure 6A** is applied to demonstrate the two modified acquisition geometries for

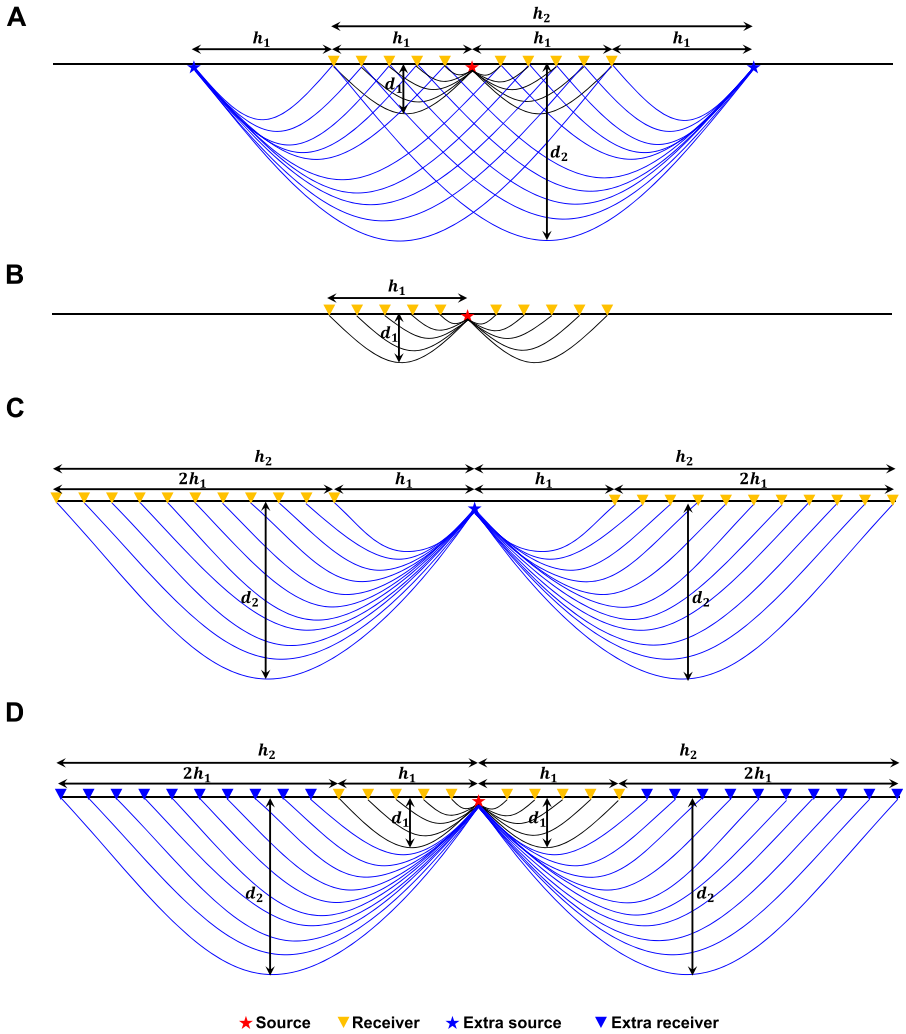

FIGURE 4 | Equivalence between the two types of modified geometry. **(A)** Type-I modified geometry with only two extra sources added at two ends. This geometry is equal to the summation of **(B)** and **(C)**. Consequently, Type-I geometry is equivalent to a Type-II geometry shown in **(D)**. h_1 represents the maximum offset of the receiver array for the normal geometry part. It also denotes the offset of the extra sources to the nearest receivers. h_2 indicates the maximum offset generated by the extra sources. d_1 and d_2 represent the maximum penetration depth of the diving waves recorded by the receivers in the normal geometry and extra sources and receivers, respectively.

building velocity models and corresponding migration imaging. The initial velocity model is a 1D model shown in **Figure 6B**.

Since the deepest interface is at a depth of about 9 km, we set the maximum offset for acquiring reflections as 10 km, and choose a receiver interval of 20 m. The shot interval is set as 200 m. Then, we apply ray tracing on the initial model to determine the maximum offset for acquiring the diving wave that can penetrate to the depth of 9 km. The test indicates that an offset of 50 km is required. Consequently, Type-I modified geometry requires two extra sources at each side of the normal geometry. Type-II modified geometry needs extra receivers to cover 40-km extra offsets. Here, we set the extra receiver interval as 1 km. A 10-Hz Ricker wavelet is used as the source wavelet. One shot record is shown in **Figure 7**.

We picked up the first breaks from the records and then used travel time tomography to recover the velocity model. First, we inverted the first-arrival travel time of the record from the normal geometry, which has a maximum offset of 10 km. The recovered velocity model and its ray density map are shown in **Figure 8**. As can be seen, the inversion only recovers the top 1 km of the model because the diving wave only penetrates such a depth, which is indicated by the ray coverage area in **Figure 8B**.

We then inverted the first breaks of the dataset from Type-I geometry. The recovered model is depicted in **Figure 9A**. As can be seen, it recovers the background velocity of the true model and the shallow low-velocity anomalies, correctly. As analyzed in the previous section, Type-I geometry is equivalent to Type-II geometry with a trace interval of 20 m for extra receivers. As a result, this recovered model can be treated as

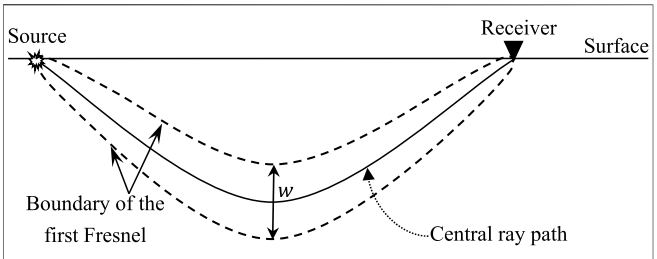

FIGURE 5 | Schematic illustration of the first Fresnel zone for one source–receiver pair. *w* indicates the width of the first Fresnel zone.

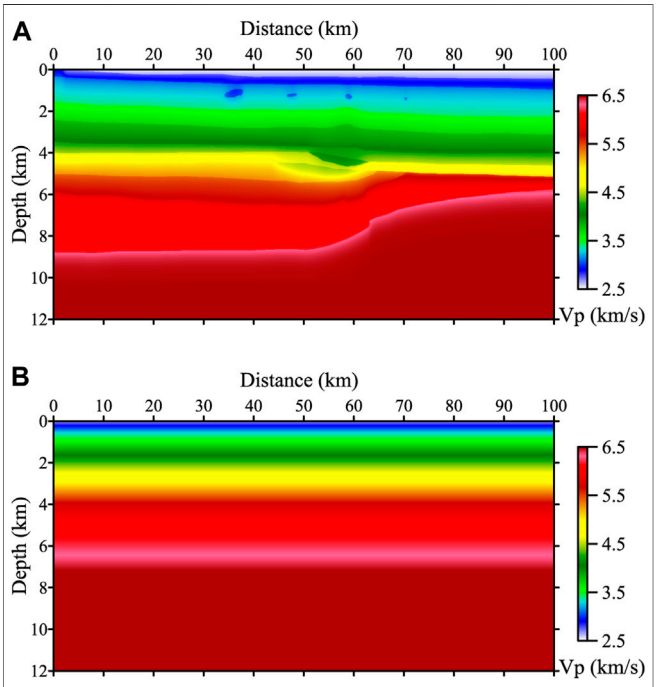

FIGURE 6 | The velocity models for the numerical test. **(A)** The true velocity model. **(B)** The initial velocity model for velocity model building.

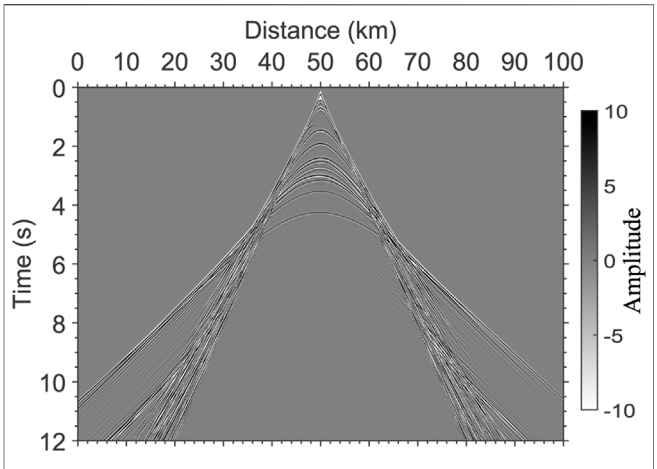

FIGURE 7 | One shot record acquired in the middle of the model. The maximum offset is 50 km.

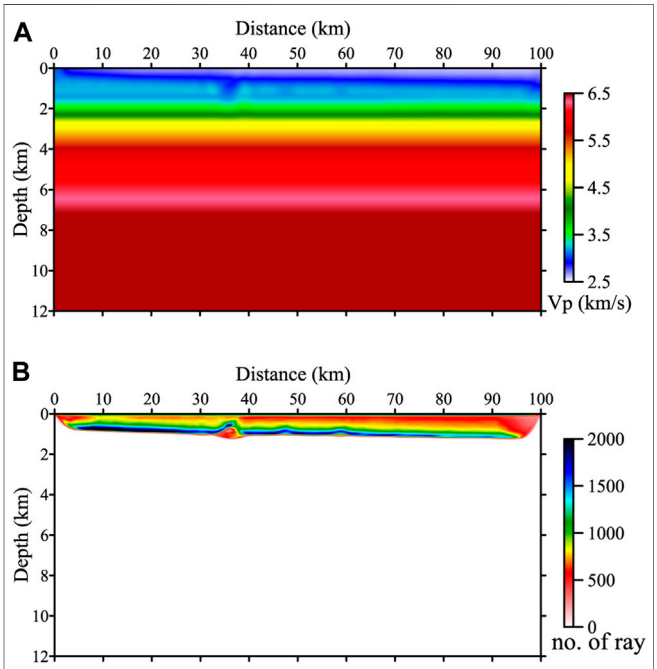

FIGURE 8 | The inverted velocity model **(A)** with a maximum offset of 10 km and **(B)** its ray density map.

that of Type-I geometry with the densest trace interval for the extra receivers.

Next, we inverted the first breaks of the dataset from Type-II geometry, in which the receiver interval is 1 km for the extra receivers. The recovered model is shown in **Figure 10A**. Compared with the model from Type-I geometry, they share a similar background trend. This implies that the extra receivers can be very sparse. We also carried out tests with smaller intervals for the extra receivers, for example, 100 and 500 m. Results show that denser extra receivers give slightly better details but share a similar background velocity trend.

To investigate the significance of the diving waves in the normal geometry, that is, the first 10-km offset in this example, we repeated the inversion but without the first 10-km offset data. The result is shown in **Figure 11A**. Compared with the model shown in **Figures 9A**, **10A**, it is clear that the shallow part of the model, that is, top 1 km part, was not recovered correctly. This means that the diving wave recorded by the normal geometry is important for recovering the shallow region of the model.

To verify the accuracy of the recovered velocity models, we carried out Kirchhoff pre-stack depth migration (PSDM). These migration images are shown in **Figure 12**. A corresponding common image gather (CIG) extracted at a distance of 50 km is depicted in **Figure 13**. As can be seen, both modified geometries acquired adequate diving waves resulting in

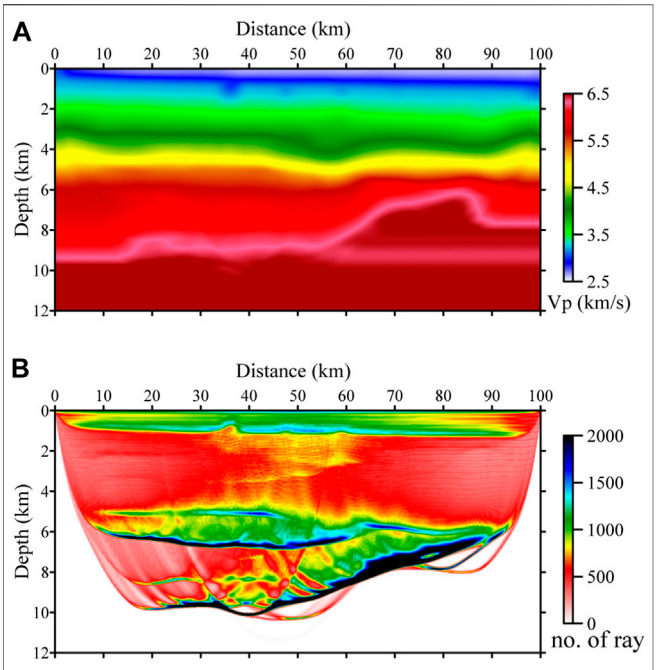

FIGURE 9 | The inverted velocity model **(A)** with Type-I modified geometry and **(B)** its ray density map. The maximum offset of the normal geometry part is 10 km. Two extra sources were excited at both sides of the receiver array.

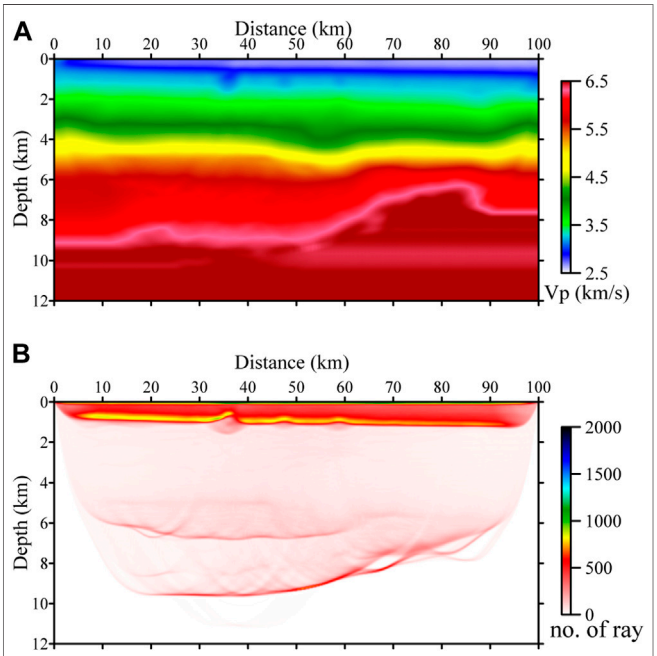

FIGURE 10 | The inverted velocity model **(A)** with Type-II modified geometry and **(B)** its ray density map. The maximum offset of the normal geometry part is 10 km. The interval of extra receivers is 1 km. The maximum offset of the modified geometry is 50 km.

successfully recovering the background velocity. In addition, the diving waves recorded by the normal geometry are crucial for the shallow region recovery.

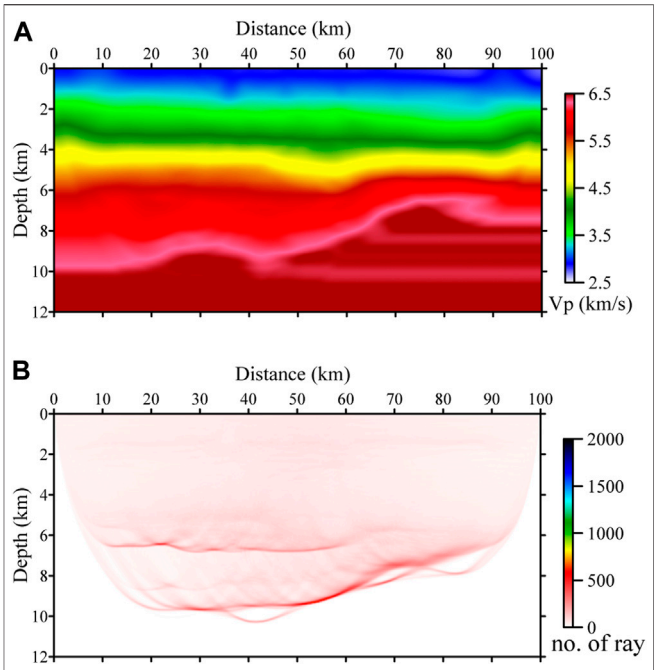

FIGURE 11 | The inverted velocity model **(A)** with Type-II modified geometry but without the 10-km receiver arrays in the normal geometry and **(B)** its ray density map. The interval of extra receivers is 1 km. The maximum offset of the modified geometry is 50 km.

Field Data Example

To validate our concept, we applied Type-II geometry in a seismic survey in East China for constructing the velocity model of a sedimentary basin. The conventional acquisition geometry utilizes a split spread. The shot interval is 250 m. The maximum offset is 4.7 km with a receiver interval of 6.25 m. The nodal seismometers were deployed every 3 km along the whole 21-km survey line, which can give a maximum penetration depth of about 5 km.

We carried out the first-arrival tomography to recover the background velocity, which is shown in **Figure 14B**. The first-arrival data from both conventional geometry and the sparse nodal seismometers were used in the tomography. The ray density map is shown in **Figure 14C**. Note that the small receiver interval in the conventional geometry part provides dense ray coverage in the shallow region, which is crucial for correctly recovering the region's velocity. The initial velocity model is the stacking velocity (**Figure 14A**) from the contractor company. The stacking velocity is created by depth conversion from the NMO velocity through the semblance velocity analysis. Although the semblance velocity analysis is not the cutting-edge method of velocity model building, the stacking velocity is still widely used in seismic exploration as a good initial estimation of the underground velocity.

It shows that the tomographic velocity model constructed by our Type-II geometry contains more details in deep regions than the stacking velocity model constructed by semblance velocity analysis. The tomographic velocity has

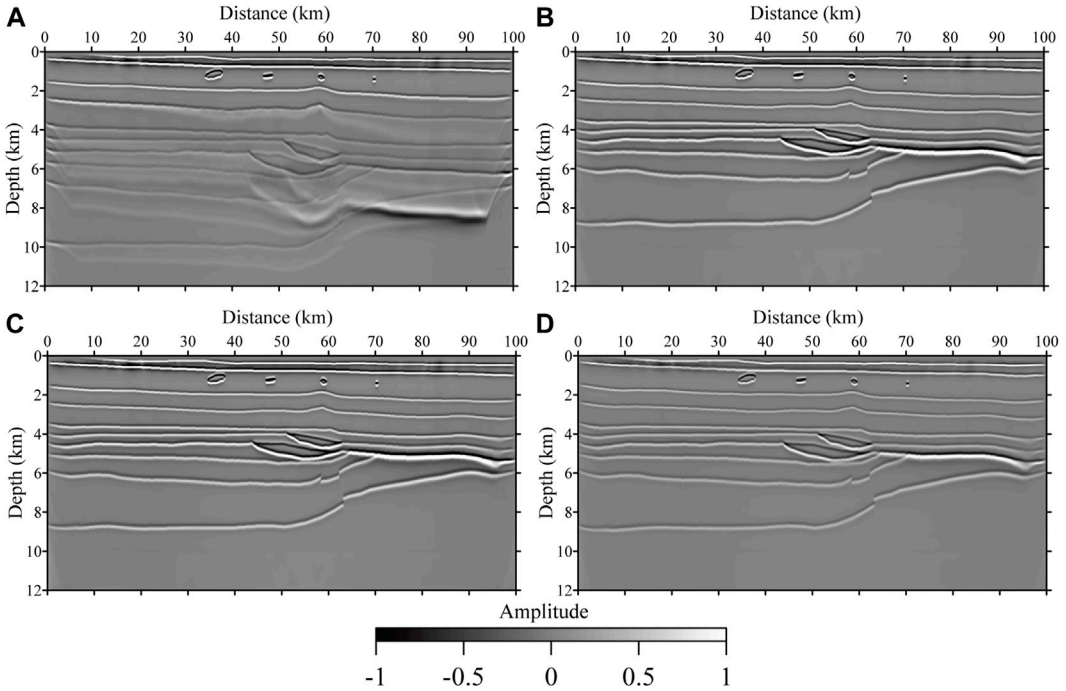

FIGURE 12 | Kirchhoff PSDM profiles: migration velocity shown in **(A) Figure 8A**, **(B) Figure 9A**, **(C) Figure 10A**, and **(D) Figure 11A**.

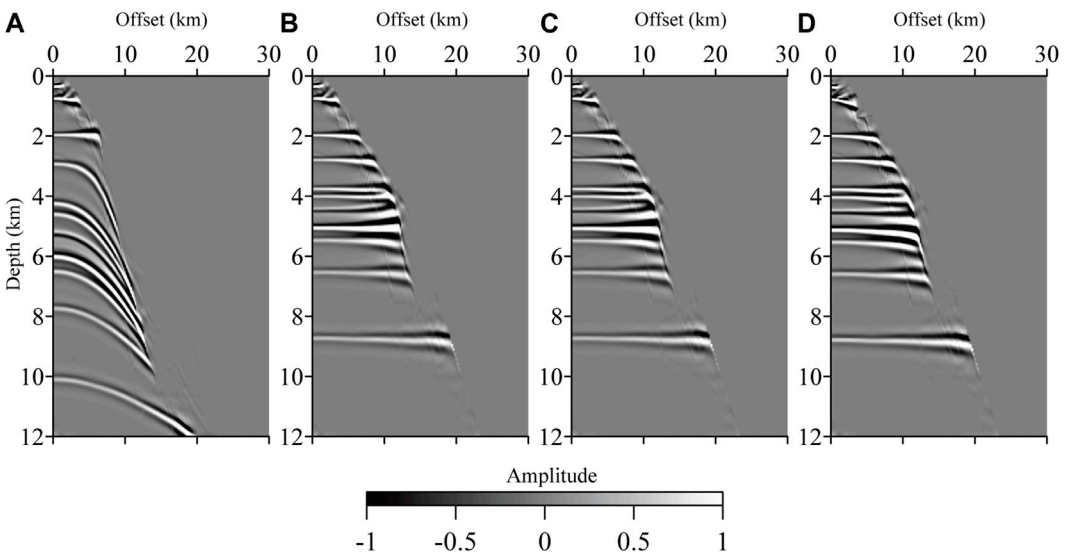

FIGURE 13 | CIG profiles at a distance of 50 km. **(A–D)** corresponds to **(A–D)** in **Figure 12**, respectively.

higher values than the stacking velocity at the bottom of the sedimentary basin. Those differences in the velocity models lead to a noticeable improvement in the migration results shown in **Figure 15**. The migration used the reflection data recorded with the conventional geometry. The migration profile using the tomographic velocity shows better continuity of reflection events (green arrows) and convergence of faults (red arrows) than that using the stacking velocity. The results indicate that our proposed modified geometry through the combination of nodal seismometers and the conventional seismic cable shall be suitable for constructing a deep velocity model.

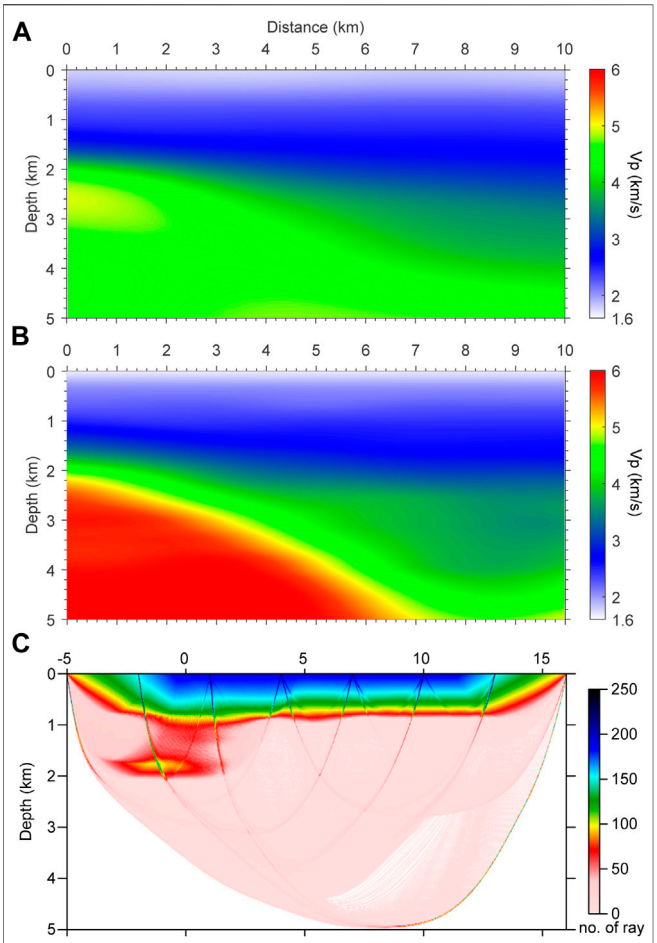

FIGURE 14 | Velocity models: **(A)** the stacking velocity using reflection data from the normal geometry and **(B)** first-arrival tomographic velocity with Type-II geometry. **(C)** The ray density map.

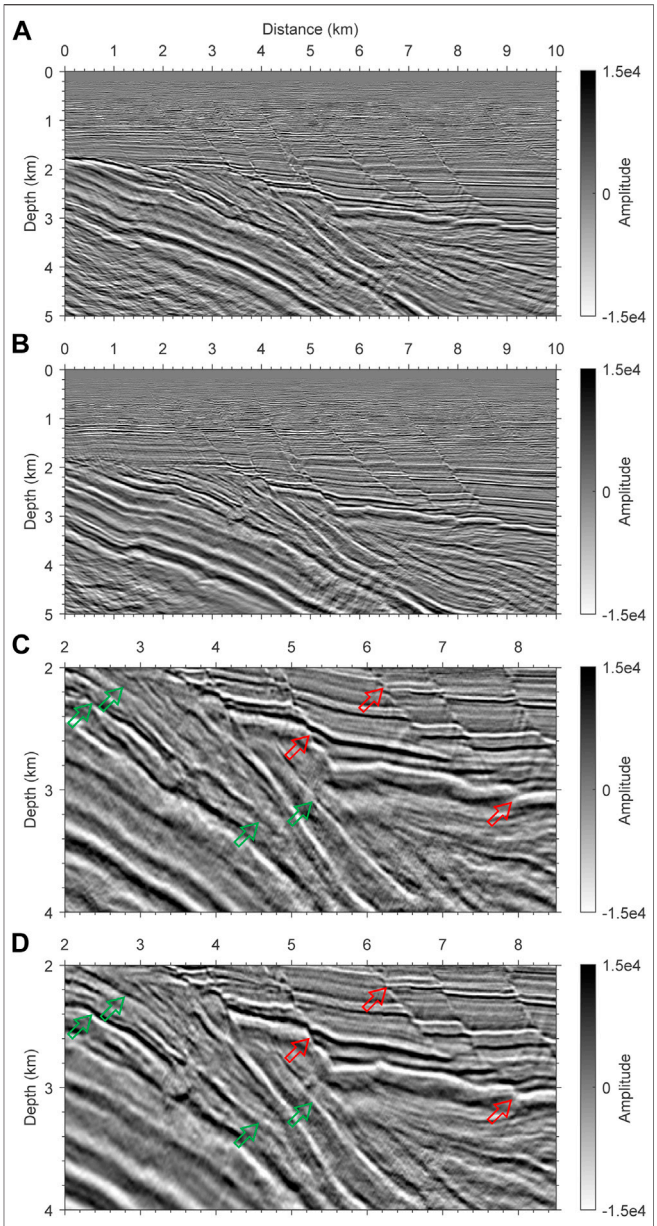

FIGURE 15 | The Kirchhoff PSDM migration images with **(A)** the stacking velocity and **(B)** the tomographic velocity. **(C)** and **(D)** are the enlarged view of the migration images shown in **(A,B)**, respectively. The red arrows indicate better-focused faults. The green arrows point out better-imaged reflectors.

DISCUSSION

In this article, we only analyzed the modified geometries for a 2D seismic survey. However, it is straightforward to extend the two types of modified geometries to a 3D seismic survey. Extra sources and extra receivers were deployed around the 2D receiver arrays. For Type-I geometry, extra sources were deployed not only along inlines but also in crosslines; consequently, the number of extra sources increases significantly compared to that for the 2D seismic survey. According to the analysis before, Type-I geometry is equivalent to the densest receiver interval in Type-II geometry. Thus, two means can mitigate this issue: the first one is to reduce the extra source number; the second one is to use a cost-effective seismic source, for example seismic vibrators. For Type-II geometry, the most cost-effective way is to use nodal seismometers for recording the large-offset diving waves. As demonstrated by the field data example, an interval of 3 km still delivered a good velocity model. Thus, one nodal seismometer can cover a 9 km^2 area. The modified geometries, therefore, are practical for a large 3D seismic survey.

CONCLUSION

Building accurate seismic velocity models is the key for seismic migration imaging. Current seismic surveys are mainly designed for acquiring reflections. Due to limited

offsets, the recorded diving waves in a normal geometry have limited penetration depth. Consequently, the velocity model building relies on reflections. The low S/N ratio and incomplete information of reflection data prevent successful velocity model building. Building velocity models with diving waves can tackle this problem. We, therefore, propose two types of modified geometries to record the diving waves at a large offset, which can penetrate to a large depth. Type-I geometry adds extra sources along the extension line of the receiver array, whereas Type-II geometry deploys extra receivers along the extension line. Analysis shows that the two geometries have different characteristics. Seismic vibrators are a cost-effective choice for Type-I geometry, whereas nodal seismometers are a convenient choice for Type-II geometry. We also provide the workflow for designing the geometries. Both synthetic and field data examples demonstrate that the proposed improved acquisition geometries can record the diving waves from the deep subsurface. Their first arrivals are used to successfully build velocity models that are enough to imaging deep targets. By contrast, the diving wave from conventional geometry only recovers the shallow velocity.

DATA AVAILABILITY STATEMENT

The original contributions presented in the study are included in the article/Supplementary Material, further inquiries can be directed to the corresponding authors.

AUTHOR CONTRIBUTIONS

GY, ZZ, SW, and NL invented the idea of the article. NL, JZ, DW, and XL carried out the test and draw the figures. GY drafted the article. All authors reviewed the article.

FUNDING

This work was partially supported by the National Key R&D Program of China (grant no. 2018YFA0702502), the National Natural Science Foundation of China (grant nos 41974142 and 42074129), Fundamental Research Funds for the Central Universities (grant nos 201964017 and 202072002), Science Foundation of China University of Petroleum (Beijing) (grant no 2462020YXZZ005), and State Laboratory of Petroleum Resource and Prospecting (grant no. PRP/indep-4-2012).

REFERENCES

Berkhout, A. J. (1980). *Seismic Migration Imaging of Acoustic Energy by Wave Field Extrapolation*. Newyork: Elsevier.

Dellinger, J., Ross, A., Meaux, D., Brenders, A., Gesoff, G., Etgen, J., et al. (2016). "Wolfspar, an "FWI-Friendly" Ultralow-Frequency marine Seismic Source," in SEG Technical Program Expanded Abstracts 2016 (October 17, 2016; Dallas, Texas). doi:10.1190/segam2016-13762702.1

Kosloff, D., Sherwood, J., Koren, Z., Machet, E., and Falkovitz, Y. (1996). Velocity and Interface Depth Determination by Tomography of Depth Migrated Gathers. *Geophysics* 61 (5), 1511–1523. doi:10.1190/1.1444076

Lewis, W., Amazonas, D., Vigh, D., and Coates, R. (2014). "Geologically Constrained Full-Waveform Inversion Using an Anisotropic Diffusion Based Regularization Scheme: Application to a 3D Offshore Brazil Dataset," in SEG Technical Program Expanded Abstracts 2014 (October 28, 2014. Denver, Colorado). doi:10.1190/segam2014-1174.1

Li, W., Liu, Y.-K., Chen, Y., Liu, B.-J., and Feng, S.-Y. (2021). Active Source Seismic Imaging on Near-Surface Granite Body: Case Study of Siting a Geological Disposal Repository for High-Level Radioactive Nuclear Waste. *Pet. Sci.* 18, 742–757. doi:10.1007/s12182-021-00569-8

Liu, F., Zhang, G., Morton, S. A., and Leveille, J. P. (2011). An Effective Imaging Condition for Reverse-Time Migration Using Wavefield Decomposition. *Geophysics* 76 (1), S29–S39. doi:10.1190/1.3533914

Shen, X., Ahmed, I., Brenders, A., Dellinger, J., Etgen, J., and Michell, S. (2018). Full-waveform Inversion: The Next Leap Forward in Subsalt Imaging. *Leading Edge* 37 (1), 67b1–67b6. doi:10.1190/tle37010067b1.1

Sheriff, R. E. (2002). *Encyclopedic Dictionary of Applied Geophysics*. 4th Ed. Oklahoma: Society of Exploration Geophysicists. doi:10.1190/1.9781560802969

Sherwood, J., Chen, K. C., and Wood, M. (1986). "Depths and Interval Velocities from Seismic Reflection Data for Low Relief Structures," in SEG Technical Program Expanded Abstracts 1986 (November 5, 1986; Houston, Texas). doi:10.1190/1.1892903

Tarantola, A. (1984). Inversion of Seismic Reflection Data in the Acoustic Approximation. *Geophysics* 49 (8), 1259–1266. doi:10.1190/1.1441754

Virieux, J., and Operto, S. (2009). An Overview of Full-Waveform Inversion in Exploration Geophysics. *Geophysics* 74 (6), WCC1–WCC26. doi:10.1190/1.3238367

Warner, M., Ratcliffe, A., Nangoo, T., Morgan, J., Umpleby, A., Shah, N., et al. (2013). Anisotropic 3D Full-Waveform Inversion. *Geophysics* 78 (2), R59–R80. doi:10.1190/geo2012-0338.1

Wu, Z., and Alkhalifah, T. (2015). Simultaneous Inversion of the Background Velocity and the Perturbation in Full-Waveform Inversion. *Geophysics* 80 (6), R317–R329. doi:10.1190/geo2014-0365.1

Xu, S., Wang, D., Chen, F., Lambaré, G., and Zhang, Y. (2012). "Inversion on Reflected Seismic Wave," in SEG Technical Program Expanded Abstracts 2012. November 6, 2012. Las Vegas, Nevada. doi:10.1190/segam2012-1473.1

Yao, G., and Wu, D. (2017). Reflection Full Waveform Inversion. *Sci. China Earth Sci.* 60 (10), 1783–1794. doi:10.1007/s11430-016-9091-9

Yao, G., da Silva, N. V., and Wu, D. (2019). Reflection-Waveform Inversion Regularized with Structure-Oriented Smoothing Shaping. *Pure Appl. Geophys.* 176 (12), 5315–5335. doi:10.1007/s00024-019-02265-6

Yao, G., Wu, D., and Wang, S.-X. (2020). A Review on Reflection-Waveform Inversion. *Pet. Sci.* 17 (2), 334–351. doi:10.1007/s12182-020-00431-3

Yilmaz, Ö. (2001). *Seismic Data Analysis: Processing, Inversion, and Interpretation of Seismic Data*. Oklahoma: Society of Exploration Geophysicists. doi:10.1190/1.9781560801580

Zhang, Y., and Sun, J. (2008). "Practical Issues of Reverse Time Migration - True-Amplitude Gathers, Noise Removal and Harmonic-Source Encoding," in 70th EAGE Conference & Exhibition - Rome (June 10, 2008. Rome). doi:10.3997/2214-4609.20147708

Zhang, Z., Mei, J., Lin, F., Huang, R., and Wang, P. (2018). "Correcting for Salt Misinterpretation with Full-Waveform Inversion," in SEG Technical Program Expanded Abstracts 2018 (October 16, 2018. Anaheim California). doi:10.1190/segam2018-2997711.1

Zhou, W., Brossier, R., Operto, S., and Virieux, J. (2015). Full Waveform Inversion of Diving & Reflected Waves for Velocity Model Building with Impedance Inversion Based on Scale Separation. *Geophys. J. Int.* 202 (3), 1535–1554. doi:10.1093/gji/ggv228

Zhou, H. w. (2003). Multiscale Traveltime Tomography. *Geophysics* 68 (5), 1639–1649. doi:10.1190/1.1620638

Conflict of Interest: The authors declare that the research was conducted in the absence of any commercial or financial relationships that could be construed as a potential conflict of interest.

Publisher's Note: All claims expressed in this article are solely those of the authors and do not necessarily represent those of their affiliated organizations, or those of the publisher, the editors, and the reviewers. Any product that may be evaluated in this article, or claim that may be made by its manufacturer, is not guaranteed or endorsed by the publisher.

frontiers | Frontiers in Earth Science

METHODS
published: 14 April 2022
doi: 10.3389/feart.2022.851206

Gaussian Beam Migration for Free-Surface Multiples in VSP

Dai Yu[1], *Feilong Yang*[2]*, *Bo Wen*[3], *Ying Wang*[4], *Dezhi Huang*[5] *and Chi Zhao*[6]

[1]College of Geology Engineering and Geomatics Chang'an University, Xi'an, China, [2]School of Earth Sciences and Engineering Xi'an Shiyou University, Xi'an, China, [3]BGP Offshore of China National Petroleum Corporation, Tianjin, China, [4]Docan Tech (Xi'an) Co., Ltd., Xi'an, China, [5]School of Mining Engineering Heilongjiang University of Science and Technology, Harbin, China, [6]Sinopec Northwest Oilfield Company, Urumqi, China

The vertical seismic profiling (VSP) Gaussian beam migration is a seismic imaging method with both computational efficiency and imaging precision. It can get high-resolution structural features near the well. However, the VSP migration based on primary reflection imaging is limited by the observation system, which makes it unable to image for the shallow structure at far offset. The free-surface multiples in VSP can expand the illumination range for far offset effectively. Therefore, Gaussian beam migration (GBM) for free-surface multiples imaging in VSP is proposed. Firstly, based on the ground Gaussian beam pre-stack depth migration, the method for decomposing the plane wave is improved and adapted into VSP geometry. We decompose the seismic records received by the well into plane waves in different directions according to different window centers and image the plane wave of each direction independently. Secondly, through the mirror image of both the velocity model and VSP receivers, the VSP free-surface multiples are converted into VSP primary reflections which are involved in the VSP Gaussian beam migration method, and thus, the method of the primaries is used to image the free-surface multiples. Finally, the effectiveness and robustness of the proposed method are verified by the theoretical model and practical data.

Keywords: vertical seismic profiling, Gaussian beam migration (GBM), velocity mirror image, far offset, free-surface multiples

OPEN ACCESS

Edited by:
Jidong Yang,
China University of Petroleum, China

Reviewed by:
Maysam Abedi,
University of Tehran, Iran
Subin Zhuang,
China University of Petroleum, China

***Correspondence:**
Feilong Yang
feilongy@xsyu.edu.cn

Specialty section:
This article was submitted to Solid Earth Geophysics, a section of the journal Frontiers in Earth Science

Received: *09 January 2022*
Accepted: *14 March 2022*
Published: *14 April 2022*

Citation:
Yu D, Yang F, Wen B, Wang Y, Huang D and Zhao C (2022) Gaussian Beam Migration for Free-Surface Multiples in VSP. Front. Earth Sci. 10:851206. doi: 10.3389/feart.2022.851206

INTRODUCTION

There are many difficulties in exploration and development, such as surface-complicated, complex underground structure, strong reservoir heterogeneity, thin reservoir thickness, and small reservoir traps. Seismic imaging technology needs a high-precision method which can broaden the frequency band so as to improve spatial resolution and identify thinner reservoirs and faults as well as some complex structures. The receivers of VSP exploration are close to the geologic objects, and seismic wave information from VSP can directly reflect the geological attributes of strata, reservoirs, or targets. The exploration precision and detection range of VSP are between ground seismic and logging methods. VSP is the spatial expansion and effective supplement of these two technologies, which is mainly used to study the formation process and the spatial structure around the well. Compared with ground seismic migration, VSP migration improves the resolution and provides the corresponding relationship between the underground strata structure and subsurface measurement parameters.

For a long time, the primaries have been used in imaging and the multiples have been suppressed as interference waves. However, the multiples also contain plentiful geological

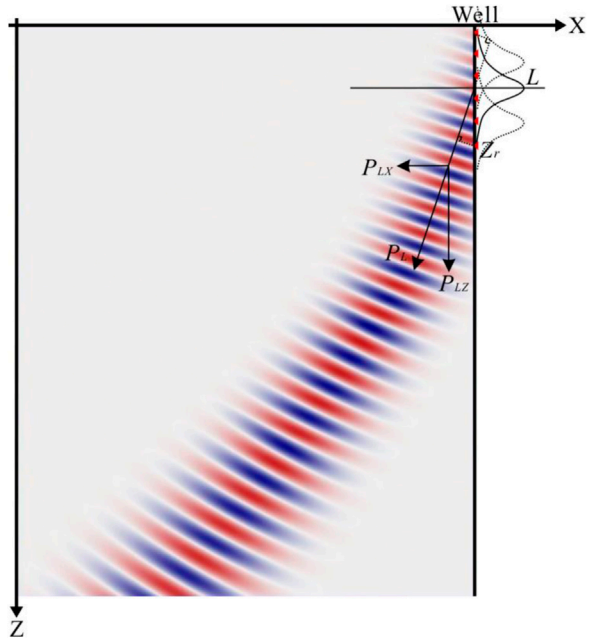

FIGURE 1 | Local plane wave decomposition.

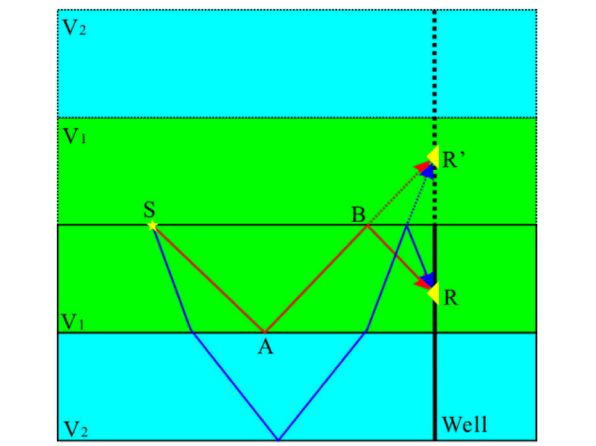

FIGURE 2 | Ray path of VSP first-order free-surface multiples.

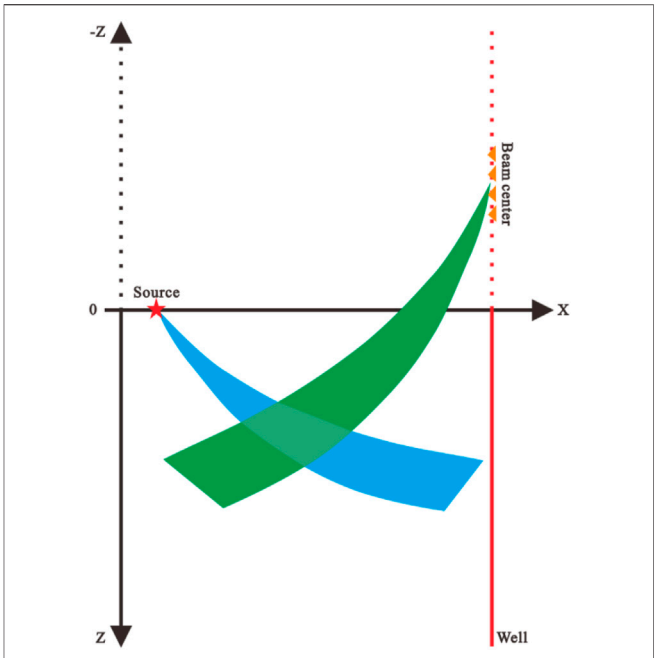

FIGURE 3 | Arrangement of the receivers in GBM for VSP free-surface multiples imaging. The red star indicates the source location, orange inverted triangles indicate the receivers in the velocity mirror image, the blue beam is emitted from the source, the green beam is emitted from the window center point, and the light green area is the region where the ray pairs coincide.

structure information. Reiter et al. (1991) tried to mine the useful information from the multiples and added the first-order water-bottom reflection operator into Kirchhoff pre-stack time migration. The method is difficult to obtain the up-going and down-going components of the towline data in submarine, so it is limited to deep water data processing. Based on this idea, many researchers have done much research on multiples imaging. Until now, the multiples have been regarded as effective information and applied effectively, which are significant to the fine description of underground structure information. Berkhout and Verschuur (1994) proposed a method to realize multiples imaging by using the received records as the sources and the separated multiples as the received records. Based on this idea, Guitton (2002) used the shot-profile method to migrate the multiples. Shan (2003) used source–receiver depth migration to realize multiples imaging. Shan and Guitton (2004) used the multiples to construct a pseudo-primary wave and realize the imaging of the multiples and proved that this method is equivalent to the above method which images the multiples by modifying boundary conditions. Berkhout and Verschuur (2006) combined surface-related multiple elimination (SRME) theory and focal transformation theory to convert the multiples into the primaries, and thus, multiples imaging can also be realized indirectly by extracting the multiples in the focal transformation domain. Lou et al. (2007) presented a new method to perform the 3C vector Kirchhoff pre-stack depth migration for the first-order free-surface multiples in VSP data by the velocity mirror image and the virtual receivers. It can accurately produce a much wider seismic image zone than the conventional VSP migration which uses primary reflections only. Liu et al. (2011) used the reverse time migration (RTM) to image the multiples by separating the multiples to realize multiples imaging through the primaries imaging method. However, the precision of separating the primaries and the multiples may reduce the quality of multiples imaging. Zhang and Schuster (2014) did multiples imaging and achieved the results based on the least square reverse time migration (LSRTM). But it involves huge calculation cost and the

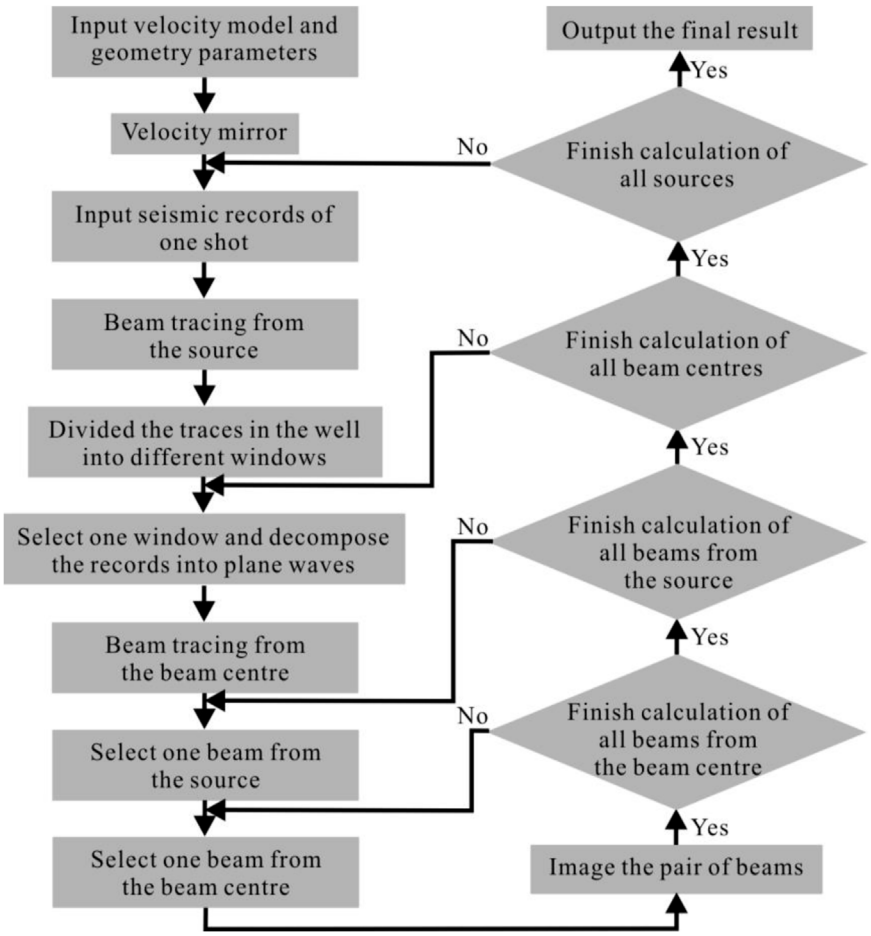

FIGURE 4 | Workflow of GBM for VSP imaging.

elimination of the noise. Liu et al. (2018) proposed the fast LSRTM to image the down-going free-surface multiples in VSP, which greatly expands the imaging illumination range of VSP.

Non-zero offset VSP imaging commonly uses VSP-CDP transform and Kirchhoff migration. Since the VSP-CDP transform and stack method use the ray method for model building in the depth domain and are based on the hypothesis of layered and uniform medium, it is difficult to image the complex structures. The Kirchhoff migration also leads to poor amplitude conservation and low imaging precision. To solve these problems, wave equation pre-stack depth migration was proposed, and it has been demonstrated effective when imaging complex structures (Wang J et al., 2008; Fang et al., 2016). RTM is based on the two-way wave equation and is distinguished by its high imaging and migration homing accuracy (Chen et al., 2018). The Gaussian beam migration (GBM) overcomes the shortcomings of Kirchhoff migration and retains its flexibility and efficiency at the same time. It also leads to the results as accurate as these by RTM. In summary, it has a fast calculation speed and high accuracy (Hill, 1990; Huang et al., 2014; Yu et al., 2018). In order to improve the quality of VSP imaging, Wang Y. G et al. (2008) applied the GBM to VSP for the first time (VSP-GBM for short). VSP-GBM not only considers both computational efficiency and imaging accuracy but also calculates multi-arrival travel time. Besides, it is a ray method, which has a weak dependence on the velocity model, so it has strong imaging ability. In this paper, VSP-GBM is used to calculate the free-surface multiples, and this method is verified by forward seismic data and actual seismic data.

METHODS

VSP-GBM

In a 2D scalar isotropic medium, the surface is horizontal and the receiving well is vertical. $X_s = (x_s, 0)$ is the seismic source, $X_r = (x_r, z_r)$ is the receiver point, $X = (x, z)$ is the imaging point, ω is the angular frequency, and $U(X_r, X_s, \omega)$ is the received seismic wave field. According to the method of Gaussian beam characterizing Green's function, Green's function of the ray beam propagating from the seismic source to the imaging point can be described as

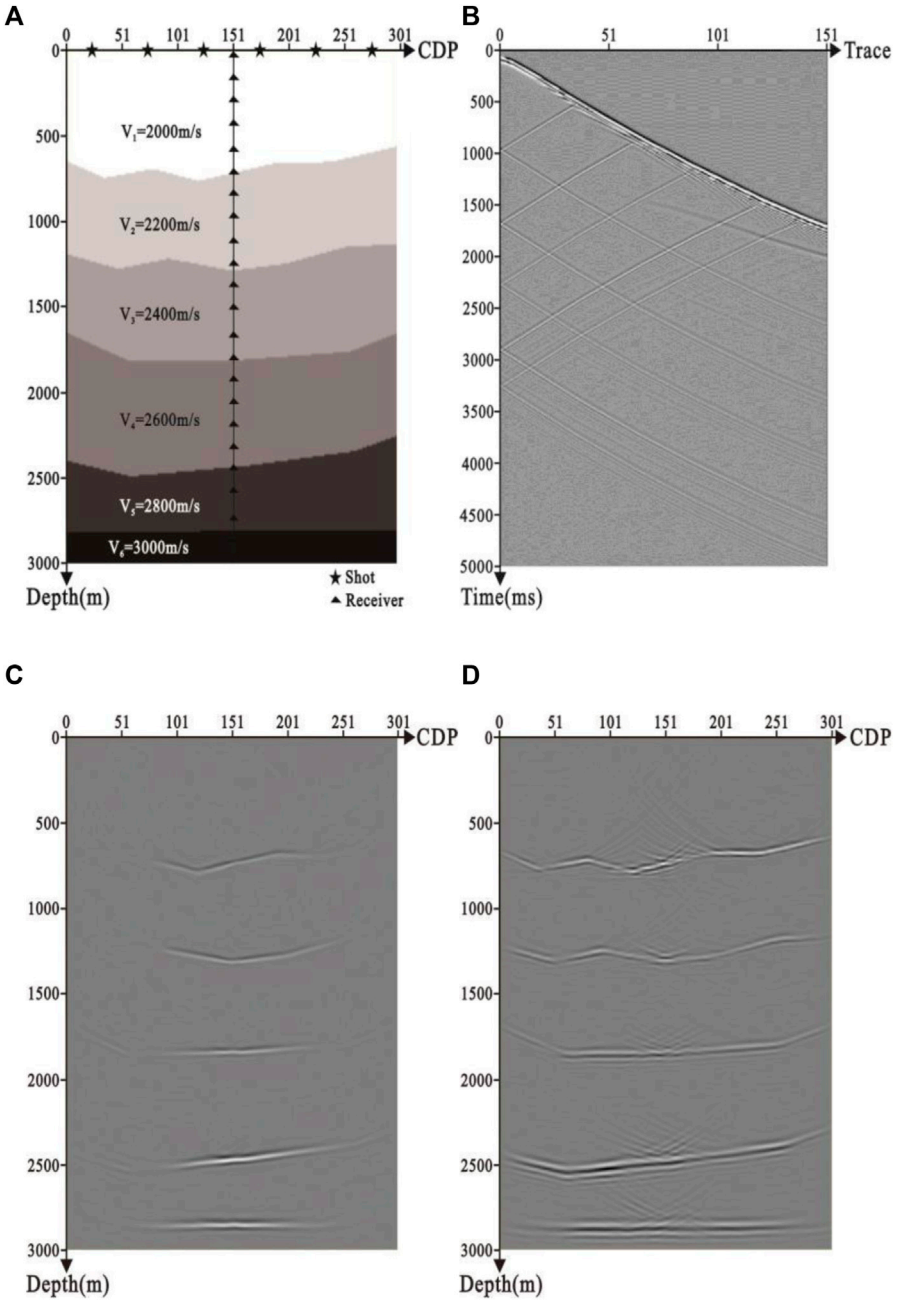

FIGURE 5 | VSP-GBM result of the complex model: **(A)** complex model, **(B)** shot record of the numerical example, **(C)** migration result of the primaries, and **(D)** combined migration result of the first-order free-surface multiples and the primaries.

$$G(\mathbf{X}, \mathbf{X}_s, \omega) = \frac{i}{4\pi} \int \frac{dp_x}{p_z} u_{GB}(\mathbf{X}, \mathbf{X}_s, \boldsymbol{P}, \omega) = \frac{i}{4\pi} \int \frac{dp_x}{p_z} A \exp(i\omega T), \quad (1)$$

where p_x and p_z represent the horizontal and vertical components of initial slowness in the central ray, respectively; $\boldsymbol{P} = (p_x, p_z)$; and $T = \tau(s) + \frac{1}{2}\frac{P(s)}{Q(s)}n^2$ and $A = \sqrt{\frac{\varepsilon V(s)}{V(0)Q(s)}}$ represent the complex-valued travel time and amplitude, respectively. The reverse continuation seismic wave field $U(\mathrm{X}, \mathrm{X_s}, \omega)$ from the source point to the imaging point can be shown by Rayleigh II integral as

$$U(\mathbf{X}, \mathbf{X}_s, \omega) = 2i\omega \int dx_r \frac{\cos\theta_r}{V_r} G^*(\mathbf{X}, \mathbf{X}_r, \omega) U(\mathbf{X}_r, \mathbf{X}_s, \omega), \quad (2)$$

where $\mathrm{G(X, X_r, \omega)}$ is Green's function from the receiving point $\mathrm{X_r}$ to the imaging point X, θ_r is the emergent angle of ray, V_r is the velocity of the receiver point, and * represents the complex conjugate.

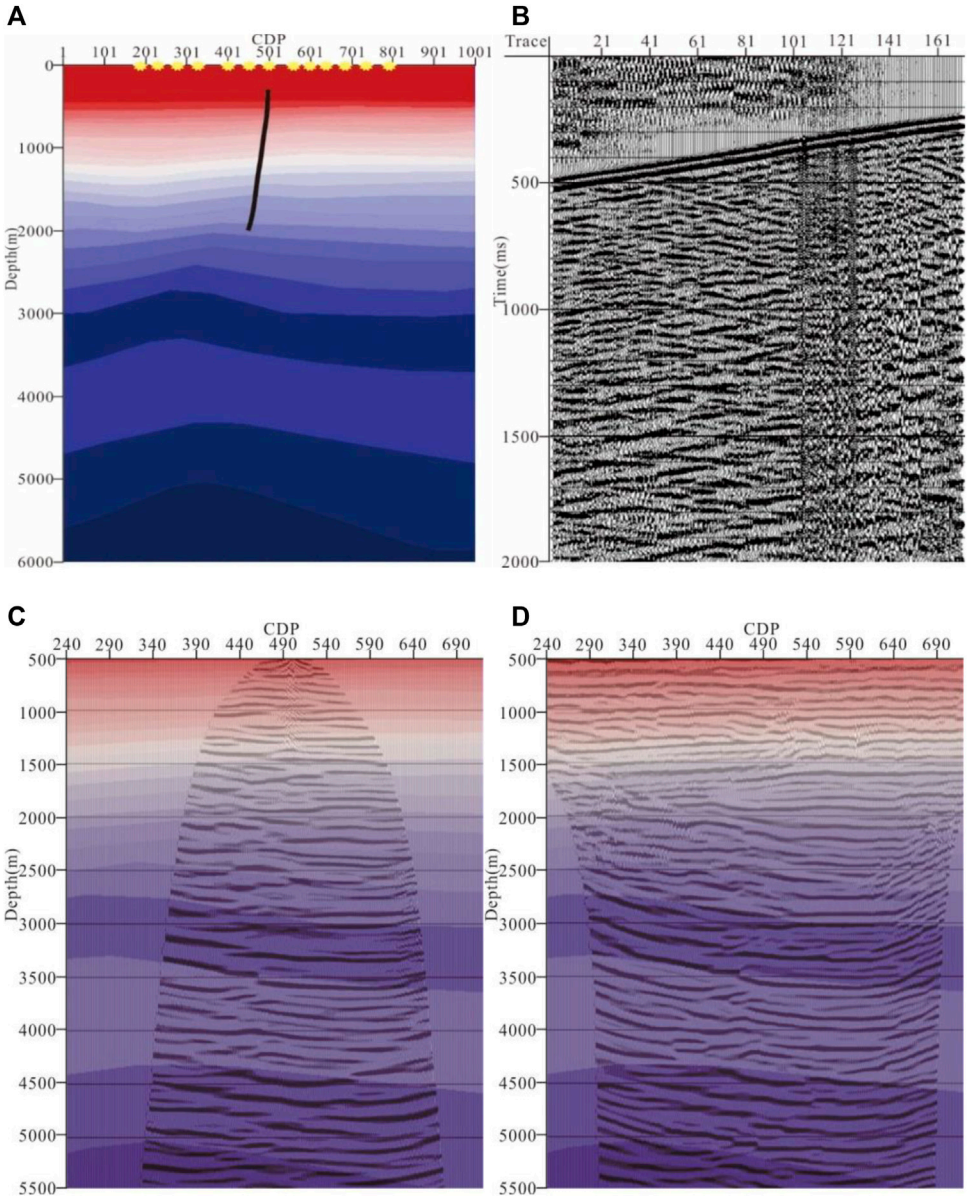

FIGURE 6 | VSP-GBM result of the practical data: **(A)** velocity model, **(B)** shot record, **(C)** migration result of the primaries, and **(D)** combined migration result of the first-order free-surface multiples and the primaries.

If we add Gaussian window into the seismic records $U(X_r, X_s, \omega)$ received from receivers, and use the emitted Gaussian beam from the window center to represent Green's function $G(X, X_r, \omega)$ (as shown in **Figure 1**), then **Eq. 2** can be transformed into

$$U(\mathbf{X}, \mathbf{X}_s, \omega) \approx \frac{\Delta L \omega_r}{(2\pi)^{3/2}\omega_0} \frac{\cos\theta_L}{V_L} \sum_L \int \frac{dp_{Lx}}{p_{Lz}} A_L^* \exp(-i\omega T_L^*) D_s(L, p_{Lz}, \omega), \tag{3}$$

where the one-dimensional (1D) Gaussian window function in the vertical well VSP has the properties shown in

$$\frac{\Delta L}{\sqrt{2\pi}\omega_0} \sqrt{\left|\frac{\omega}{\omega_r}\right|} \sum_L \exp\left[-\left|\frac{\omega}{\omega_r}\right| \frac{(z_r - L)}{2\omega_0^2} \right] \approx 1. \tag{4}$$

$D_s(L, p_{Lz}, \omega)$ is the slant stacking of seismic wave field in the Gaussian window which takes (x_r, L) as its center. It is expressed as

$$D_s(L, p_{Lz}, \omega) = \left|\frac{\omega}{\omega_r}\right|^{3/2} \int dz_r U(\mathbf{X}_r, \mathbf{X}_s, \omega) \exp\left[i\omega p_{Lz}(z_r - L) - \left|\frac{\omega}{\omega_r}\right| \frac{(z_r - L)^2}{2\omega_0^2} \right]. \tag{5}$$

Here, we need to use the deconvolution imaging conditions in order to get the amplitude-preserving migration results in the shot domain:

$$\boldsymbol{I}(\mathbf{X}, \mathbf{X}_s) = \frac{1}{2\pi} \int \frac{U(\mathbf{X}, \mathbf{X}_s, \omega) G^*(\mathbf{X}, \mathbf{X}_s, \omega)}{G(\mathbf{X}, \mathbf{X}_s, \omega) G^*(\mathbf{X}, \mathbf{X}_s, \omega)} d\omega, \tag{6}$$

where $I(X, X_s)$ is the imaging value of one shot and $G(X, X_s, \omega)$ is Green's function of the source spreading in the forward direction. Upon substituting **Eqs 1**, **3** into **Eq. 6**, we get

$$I(\mathbf{X}, \mathbf{X}_s) = -\frac{\Delta L \omega_r}{16\pi^3 \sqrt{2\pi}\omega_0} \sum_L \int d\omega \frac{i}{G(\mathbf{X}, \mathbf{X}_s, \omega) G^*(\mathbf{X}, \mathbf{X}_s, \omega)}$$
$$\int \frac{dp_{sx}}{p_{sz}} A_s^* \exp(-i\omega T_s^*) \times \frac{\cos\theta_L}{V_L} \sum_L \int \frac{dp_{Lx}}{p_{Lz}} A_L^* \exp(-i\omega T_L^*) D_s(L, p_{Lz}, \omega). \tag{7}$$

Eq. 7 is the 2D VSP amplitude-preserving Gaussian beam imaging formula in the shot domain.

Velocity Mirror

In order to solve the issue of first-order free-surface multiples migration, we convert VSP first-order free-surface multiples into primary reflections based on the idea of velocity mirror image. As shown in **Figure 2**, the mirror point of the receiver point R is R'. The path of first-order free-surface multiples ($\overrightarrow{SABR}$) can be converted to the travel path of primary reflection ($\overrightarrow{SAR'}$). VSP-GBM is employed in first-order free-surface multiples, and thus, the beam center is located at the mirror point R'. First, the seismic records are divided into a series of local regions. Then, the seismic records of local regions are decomposed into plane waves (amount to the beam) in different directions by using slant stacking. Finally, we map imaging the plane wave through the travel time and amplitude of rays (as shown in **Figure 3**).

The workflow of the VSP-GBM algorithm is shown in **Figure 4**.

NUMERICAL EXAMPLE

This section employs the complex model to test the VSP-GBM in free-surface multiples.

Figure 5A is the complex model, which is composed of a 301 (in the *x* dimension) by 3,001 (in the *z* dimension) grid, with grid spacings 10.0 m (in the *x* dimension) and 1.0 m (in the *z* dimension), respectively. The well is vertical and locates at the position of (1500 m, 0 m), and the triangles represent part of the receivers. The dataset has 16 shots at intervals of 200 m. The first shot locates at the position of (0 m, 0 m), and the stars represent part of the shot points. Each shot consists of 151 traces, and the receiver interval is 20.0 m (as shown in **Figure 5B**). It can be found from **Figures 5C,D** that the VSP free-surface multiples effectively expand the lateral imaging range, especially in the shallow structure at the far offset. Therefore, it not only fully utilizes VSP free-surface multiples but also effectively compensates the deficiency of primaries imaging in the shallow structure at the far offset.

PRACTICAL DATA TEST

This section employs the practical data to test the effectiveness between primaries and first-order free-surface multiples in the VSP-GBM method.

The geological model is shown in **Figure 6A** with a size of 10000 m × 6000 m. The grid spacing is 10.0 m in the *x* dimension and 10.0 m in the *z* dimension. The well is not vertical, and the black curve indicates the receivers' distribution range. The dataset has 110 shots, and the first shot locates at (1929 m, 0 m); note that the shot intervals are unequal and that the explosion signs are part of the shot points. The minimum offset is 130 m, and the maximum offset is 3070 m. The shot consists of 171 traces, and the receivers locate from 297 to 1967 m in depth. Note that the receiver intervals are also unequal. The wave field is shown in **Figure 6B**. The method can effectively avoid the errors from wave field separation. **Figures 6C,D** show the VSP-GBM results of primaries and first-order free-surface multiples. It can be seen that the VSP-GBM result of first-order free-surface multiples effectively compensates the imaging deficiency of VSP primaries in the shallow structure at the far offset. By comparing the VSP-GBM results shown in **Figures 6C,D**, the feasibility and effectiveness of the proposed method are verified.

CONCLUSION

In this paper, the ground GBM method is extended to VSP geometry, and the idea of velocity mirror image is applied to VSP-GBM. This method can directly image the primary reflection waves and first-order free-surface multiple waves of VSP without wave field separation and effectively use the multiples wave field information of VSP to improve the imaging accuracy of VSP. The results of the theoretical model and practical data show that the first-order free-surface multiples can expand the lateral imaging range of VSP-GBM and effectively compensate the imaging deficiency of VSP primaries in the shallow structure at the far offset.

DATA AVAILABILITY STATEMENT

The original contributions presented in the study are included in the article/Supplementary Material, further inquiries can be directed to the corresponding author.

AUTHOR CONTRIBUTIONS

FY and DY contributed to conception and design of the study and wrote the first draft of the manuscript. BW provided practical data. YW and DH performed data analysis. BW, YW, and CZ wrote sections of the manuscript. All authors contributed to manuscript revision and read and approved the submitted version.

FUNDING

This research was funded by the Natural Science Basic Research Plan in the Shaanxi Province of China (No. 2021JQ-588).

REFERENCES

Berkhout, A. J., and Verschuur, D. J. (1994). "Multiple Technology: Part 2 ,migration of Multiple Reflections[C]," in 64th Annual International Meeting, Los Angeles, CA, October 23-28, 1994 (SEG, Expanded Abstracts), 1497–1500.

Berkhout, A. J., and Verschuur, D. J. (2006). Imaging of Multiple Reflections. *Geophysics* 71 (4), SI209–SI220. doi:10.1190/1.2215359

Chen, Y. Z., Zhang, R. F., Tang, C. Z., Zhang, Y. B., Wang, X. J., and Wang, G. (2018). A Joint VSP and Surface Seismic Survey for Marlstones in Shulu, Huabei Oilfield[J]. *Oil Geophys. Prospecting (in Chinese)* 53 (Suppl. 2), 50–57. doi:10.13810/j.cnki.issn.1000-7210.2018.S2.009

Fang, T. E., Huang, X. R., and Ma, S. F. (2016). VSP Migration Based on High Angle One-Way Wave Equation in Time-Space Domain and its Applications[J]. *Chin. J. Geophys. (in Chinese)* 59 (9), 3459–3469. doi:10.6038/cjg20160928

Guitton, A. (2002). "Shot-profile Migration of Multiple Reflections[C]," in 72th Annual International Meeting, Salt Lake City, UT, October 6-11, 2002 (SEG, Expanded Abstracts), 1296–1299.

Hill, N. R. (1990). Gaussian Beam Migration. *Geophysics* 55 (11), 1416–1428. doi:10.1190/1.1442788

Huang, J. P., Zhang, Q., Zhang, K., Li, Z. C., Yue, Y. B., and Yuan, M. L. (2014). Reverse Time Migration with Gaussian Beams Based on the Green Function[J]. *Oil Geophys. Prospecting (in Chinese)* 49 (1), 101–106. doi:10.13810/j.cnki.issn.1000-7210.2014.01.012

Liu, X. J., Liu, Y. K., and Khan, M. (2018). Fast Least-Squares Reverse Time Migration of VSP Free-Surface Multiples with Dynamic Phase-Encoding Schemes[J]. *Geophysics* 83, 321–332. doi:10.1190/geo2017-0419.1

Liu, Y. K., Chang, X., Jin, D., He, R. Q., Sun, H. C., and Zheng, Y. C. (2011). "Reverse Time Migration of Multiples[C]," in 81st Annual International Meeting, San Antonio, TX, September 18-23, 2011 (SEG, Expanded Abstracts), 3326–3331.

Lou, M., Zhao, X., Doherty, F., and Jackson, J. (2007). "Vector Kirchhoff Migration of First Order Downgoing Multiples from VSP Data [C]," in 77th Annual International Meeting, San Antonio, TX, September 23-28, 2007 (SEG, Expanded Abstracts), 3059–3063.

Reiter, E. C., Toksöz, M. N., Keho, T. H., and Purdy, G. M. (1991). Imaging with Deep-water Multiples. *Geophysics* 56 (7), 1081–1086. doi:10.1190/1.1443119

Shan, G. J., and Guitton, A. (2004). "Migration of Surface-Related Multiples: Tests on the Sigsbee2B Dataset[C]," in 74th Annual International Meeting, Denver, CO, October 10-15, 2004 (SEG, Expanded Abstracts), 1285–1288.

Shan, G. J. (2003). "Source-receiver Migration of Multiple Reflections[C]," in 73nd Annual International Meeting, Dallas, TX, October 26-31, 2003 (SEG, Expanded Abstracts), 1008–1011.

Wang, J., Qiao, Y. L., Yao, Z. R., and Li, R. Z. (2008). Vertical Seismic Profile Imaging by Gaussian Beam Migration [J]. *J. China Univ. Pet.* 32 (4), 29–33. (in Chinese). doi:10.3969/j.issn.1673-5005.2008.04.006

Wang, Y. G., Wang, Y. C., Wei, X. C., Yang, Z. R., and Zhang, D. L. (2008). Improvement of Non-zero Offset VSP Imaging Method[J]. *Oil Geophys. Prospecting (in Chinese)* 43 (6), 641–644. doi:10.13810/j.cnki.issn.1000-7210.2008.06.015

Yu, D., Yang, F. L., Sun, Y., Bian, R. F., and Wang, Y. (2018). The Study of Cross-Well Seismic Gaussian Beam Pre-stack Migration Imaging in Depth Domain[J]. *Comput. Tech. Geophys. Geochemical Exploration (in Chinese)* 40 (2), 141–149. doi:10.3969/j.issn.1001-1749.2018.02.01

Zhang, D., and Schuster, G. T. (2014). Least-squares Reverse Time Migration of Multiples. *Geophysics* 79 (1), S11–S21. doi:10.1190/geo2013-0156.1

Conflict of Interest: BW was employed by BGP Offshore of China National Petroleum Corporation. YW was employed by Docan Tech (Xi'an) Co., Ltd. CZ was employed by Sinopec Northwest Oilfield Company.

The remaining authors declare that the research was conducted in the absence of any commercial or financial relationships that could be construed as a potential conflict of interest.

Publisher's Note: All claims expressed in this article are solely those of the authors and do not necessarily represent those of their affiliated organizations, or those of the publisher, the editors, and the reviewers. Any product that may be evaluated in this article, or claim that may be made by its manufacturer, is not guaranteed or endorsed by the publisher.

frontiers | Frontiers in Earth Science

ORIGINAL RESEARCH
published: 26 May 2022
doi: 10.3389/feart.2022.851828

The State-of-the-Art Techniques of Hydrocarbon Detection and Its Application in Ultra-Deep Carbonate Reservoir Characterization in the Sichuan Basin, China

Junxing Cao[1,2], *Xudong Jiang*[1,2,3]*, *Yajuan Xue*[4], *Renfei Tian*[1,2], *Tao Xiang*[1,2] and *Ming Cheng*[1,2]

[1]The State Key Laboratory of Oil and Gas Reservoir Geology and Exploitation, Chengdu University of Technology, Chengdu, China, [2]College of Geophysics, Chengdu University of Technology, Chengdu, China, [3]Post Doctoral Research Station of Geophysics, Chengdu University of Technology, Chengdu, China, [4]School of Communication Engineering, Chengdu University of Information Technology, Chengdu, China

OPEN ACCESS

Edited by:
Wei Zhang,
Southern University of Science and Technology, China

Reviewed by:
Jianyong Xie,
Chengdu University of Technology, China
Zhaoyun Zong,
China University of Petroleum, Huadong, China
Sanyi Yuan,
China University of Petroleum, Beijing, China

***Correspondence:**
Xudong Jiang
jiangxd@cdut.edu.cn

Specialty section:
This article was submitted to Solid Earth Geophysics, a section of the journal Frontiers in Earth Science

Received: 10 January 2022
Accepted: 19 April 2022
Published: 26 May 2022

Citation:
Cao J, Jiang X, Xue Y, Tian R, Xiang T and Cheng M (2022) The State-of-the-Art Techniques of Hydrocarbon Detection and Its Application in Ultra-Deep Carbonate Reservoir Characterization in the Sichuan Basin, China. Front. Earth Sci. 10:851828. doi: 10.3389/feart.2022.851828

The Sichuan Basin is one of the most important gas-bearing basins in China, and its production accounts for more than a quarter of the country. In the past 10 years, major natural gas exploration discoveries in the basin were in ultra-deep ancient carbonate formations. The discovery of large marine gas fields has gone through a long period of exploration. For example, the Anyue gas field was discovered after more than 40 years of exploration. The main difficulty stems from deep burial, old age, and the complex geological evolution history of the carbonate rock and the resulting difficulty in identifying gas-bearing reservoirs. Although state-of-the-art reservoir prediction techniques have been used, the success rate of the exploration wells is relatively low. At present, the success rate of the ultra-deep exploration wells is about 30%. To enhance the reliability of the hydrocarbon detection of the ultra-deep carbonate reservoirs, we have developed a few novel methods in the last 10 years, including seismic-print analysis (SPA), depth-domain seismic dispersion analysis (DDSDA), and deep learning seismic analysis Applications to field data show that the results obtained by the new methods are in better agreement with the drilling results. This article presents the methods and their applications in the identification of the ultra-deep carbonate gas-bearing reservoirs in the Sichuan Basin, China. Key issues in hydrocarbon detection of ultra-deep carbonate reservoirs, which have not been solved well, are also discussed.

Keywords: Sichuan Basin, hydrocarbon detection, seismic-print, deep learning, carbonate reservoirs

1 INTRODUCTION

Reliable reservoir hydrocarbon detection techniques are silver bullets expected in the hydrocarbon detection field (Fawad et al., 2020). Since the 1970s, seismic exploration experts have developed a series of seismic-based reservoir gas detection methods. These methods and technologies can be roughly divided into three categories (Cao et al., 2019): bright spot technology (Hammond, 1974), AVO analysis technology (Castagna and Backus, 1993), and seismic dispersion analysis technology

(Robinson, 1979). AVO analysis is based on the Zoeppritz equation which is complex. Therefore, scholars obtained the approximate simplified equation of the Zoeppritz equation by introducing different approximate conditions (Chopra and Castagna, 2014). From these approximate equations, we can develop a variety of pre-stack seismic inversion methods (Veeken et al., 2004), obtain a variety of physical parameters (Li et al., 2008), such as P–S wave velocity and density (Jin et al., 2000), Poisson's ratio (Zong et al., 2013), and relative wave impedance (Cui et al., 2010), and thus, develop a variety of hydrocarbon detection methods. Bright spot technology is the strong reflection on the seismic profile relative to the background. The emergence of bright spot technology is largely due to the invention of automatic gain technology, which highlights the change of reflection amplitude on the seismic profile and improves the success rate of gas layer identification from about 12% to 60%–80% (Cao and Tian, 2019). Other methods and technologies with various names can be regarded as derivative methods of these methods and technologies. For example, the fluid factor method (Smith and Sutherland, 1996; Russell et al., 2003) can be attributed to AVO analysis technology; PG parameter prediction (Jiang et al., 2020b) and the low-frequency shadow phenomenon (Castagna et al., 2003) is essentially dispersion. These methods and technologies have both successful cases and failure lessons. The main reason for the failure is that these methods have certain applicable conditions, such as bright spot technology is mainly applicable to the shallow (Hammond, 1974) unconsolidated clastic reservoir; AVO analysis technology is mainly suitable for the situation of relatively simple and gentle formation structure, while dispersion analysis technology is suitable for the situation of known lithology. When the applicability conditions of these methods and technologies are not satisfied, the obtained results will naturally deviate from the real situation.

This article selects the actual data of ultra-deep carbonate reservoirs located in the Sichuan Basin as the experimental data. The Sichuan Basin is the most important gas-bearing basin in China, and the annual output of natural gas accounts for more than a quarter of the total annual output of the country. In the past 10 years, major discoveries of natural gas exploration in the Sichuan Basin are basically concentrated in the ultra-deep ancient carbonate strata. The discovery of ultra-deep huge marine gas fields in the Sichuan Basin has experienced a long exploration period. The reasons why it is difficult to identify gas-bearing reservoirs are deep burial, old age, long history of the geological evolution of carbonate strata in the Sichuan Basin, many control factors of natural gas accumulation, strong reservoir heterogeneity, and a complex gas–water relationship of gas reservoirs. For example, the Anyue gas field was discovered after more than 40 years of exploration. Although the most advanced method and technology will be used for reservoir prediction and gas detection before drilling, the success rate of exploration wells has been increasing slowly, and the achievement rate of ultra-deep exploration wells is only about 30% (Cao et al., 2019). Actual demand is the main driving force of scientific research. To meet the needs of natural gas exploration in ultra-deep ancient carbonate formations in the Sichuan Basin, we have continued to study and develop a variety of reservoir gas detection methods in the past 10 years, including the seismic-print analysis method (Cao et al., 2011b; Cao and Tian, 2011; Cao and Tian, 2019), depth-domain dispersion analysis method (He et al., 2018), seismic deep learning method (Cao, 2017; Cao and Wu, 2017; Cao et al., 2017), and new time–frequency analysis methods (Xue et al., 2013; Xue et al., 2014) to identify ultra-deep carbonate gas reservoirs more reliably. These methods and technologies are basically data-driven, without petrophysics and seismic response mechanism modeling, and have better applicability to a weak seismic response of the ultra-deep strong inhomogeneous medium. The practical application results also show that these methods can more reliably identify ultra-deep carbonate gas reservoirs. This article reviews the principle and application effect of these new reservoir gas detection methods and discusses the development direction of future reservoir gas detection methods.

2 SEISMIC-PRINT ANALYSIS

Seismic-print is a new term borrowed from voiceprint around 2011 (Cao et al., 2011a). The initial concept of the seismic-print is called seismic voiceprint (Cao et al., 2011b). Voiceprint is widely used to identify the speaker (Kersta, 1962). Speaker identification technology based on the voiceprint characteristic analysis was first applied to the field of intelligence listeners approximately in the 1970s, and it began widely used in the civil alignment system at the end of the 20th century (Li and Zhang, 2021). A seismic wave has an intrinsic consistency with an acoustic wave. Therefore, in theory, the geological properties of seismic data volume can be identified through research on seismic wave characteristics using voiceprint analysis method, such as judging whether the reflective layer contains hydrocarbons. We call the seismic attributes analysis method borrowed from voiceprint analysis as seismic voiceprint analysis, referred to as seismic-print analysis.

Almost all of signal analysis methods, from classic to modern, are used in the voiceprint analysis which has the sound characteristics analysis as a target, which are also used in the seismic signal analysis and seismic attribute extraction. People listen to sound, and identify the "accent" of the speaker. "Accent" is not determined on the sound signal record, but is in the ripple of the sound. The core of the voiceprint analysis aimed at the speaker identification is to find out the characteristic signal parameters for the speaker's "accent," and such parameters are called voiceprint parameters. After decades of exploration, currently, only a few parameters such as MEL cepstrum coefficient (MFCC) can effectively identify the "accent" of the speaker (Campbell, 1997; Das and Prasanna, 2018).

The purpose of reservoir prediction is to find oil and gas reservoirs. The hydrocarbon store in the pore/crack of rocks, and their volume and quality only account for a very small portion of the reservoir rock. The seismic responses of the hydrocarbon are very weak, which can only be reflected in the fine ripple structure of the seismic record. Similar to the "accent" signal in the sound

record, it is difficult to intuitively identify the hydrocarbon, and it is also difficult to use the resolving method to calculate or use the numerical method to simulate the hydrocarbons. Based on the intrinsic consistency of the acoustic wave and the seismic wave, it is possible to identify the pore fluid characteristics of the reservoir by referencing to the sound pattern of "accent" signal characteristics.

The key to the seismic-print analysis method is to find better seismic-print parameters which can stably identify the geological properties such as hydrocarbon reservoirs. The intrinsic consistency of seismic waves and acoustic waves determines the various voiceprint analysis methods such as cepstrum. MEL cepstrum can also be applied to the seismic data for the seismic-print analysis. Cepstrum, MEL cepstrum, and the other voiceprint parameters can be derived for characterizing the seismic-print features. However, the objective difference of seismic records and sound records determines that we are unlikely to use the voiceprint parameters to directly characterize reservoir fluids. The difference in seismic signals and sound signals is mainly reflected in repetitiveness, attenuation, frequency, and the other parameters. The source of the voice signal is the human being and the voice signal does not decay with the change of time. However, the source of the seismic records is the reflection signal of the seismic source signals. It is a secondary source. With the increase of time, the seismic signal will be decayed. Although the formation mechanisms of the seismic records and the voice records are the same, the physical meanings of the parameters in the wave equation have a big difference in the details. In addition, the frequency of the voice signal is generally in the range of 100 Hz–7 kHz while the frequency of the seismic signal ranges from several Hz to more than one hundred Hz. The most important feature is that the "accent" features in sound records can be characterized by repetition while the characteristics response of the target body such as gas-bearing formation in the seismic records is a small section of the whole seismic records and is often transient. The similarity between the sound records and seismic records determines that we can borrow the voiceprint analysis method for analyzing the seismic records. We have adopted the voiceprint analysis method to analyze the cepstrum coefficents', Mel cepstrum coefficients', and linear prediction cepstral coefficients' (LPCC) parameters of the seismic Ricker wavelet, the seismic responses of the hydrocarbon reservoir model, and the field data, and we obtained the following conclusions (Xue et al., 2016): (1) The seismic-print parameters of the Ricker wave have a non-linear relationship with the change of the wavelet frequency. (2) Seismic-print parameters are sensitive to the change of the reservoir parameters. (3) It is initially believed that the intersection of the low value of the first-order cepstrum coefficient and the high value of the second-order cepstrum coefficient can be used as a seismic-print criterion for gas-bearing reservoirs.

2.1 Hydrocarbon Detection Based on Seismic-Print Analysis

The key to hydrocarbon detection based on the seismic-print analysis is to find the seismic-print parameters that can identify the gas reservoir. Therefore, we systematically tested the speaker identification parameters used in the field of voiceprint analysis and found that the first and second cepstrum coefficients of the seismic records have good identifications on the gas reservoir.

Cepstrum is a kind of homogeneous transform, and the cepstrum $c(n)$ of a time series signal $x(n)$ can generally be expressed as (Cao et al., 2011b)

$$c(n) = T^{-1}\{\ln\{T[x(n)]\}\}, \tag{1}$$

where T denotes the Z transform or Fourier transform. We define the first-order cepstrum coefficient C_1 as $c(0)$, the second-order cepstrum coefficient C_2 as $c(1)$, and the rest is the same.

Generally the seismic data are represented by the convolution of the reflection coefficients $r(t)$ and the seismic wavelet $w(t)$:

$$s(t) = w(t) * r(t), \tag{2}$$

in which Ricker wavelet is the generally used wavelet $t = 0, 1, \ldots, N-1$.

Taking the discrete Fourier transform of **Eq. 2**, we obtain

$$S(k) = \left\{\sum_{n=0}^{N-1} w(k) e^{-j\frac{2\pi}{N}nk}\right\} \cdot \left\{\sum_{n=0}^{N-1} r(k) e^{-j\frac{2\pi}{N}nk}\right\}, \tag{3}$$

in which $k = 0, 1, \ldots, N-1$.

Then, taking the absolute value on both sides of **Eq. 3**, we transform **Eq. 3** by using a logarithmic operation into

$$\ln|S(k)| = \left\{\ln\left|\sum_{n=0}^{N-1} w(k) e^{-j\frac{2\pi}{N}nk}\right|\right\} \cdot \left\{\ln\left|\sum_{n=0}^{N-1} r(k) e^{-j\frac{2\pi}{N}nk}\right|\right\}. \tag{4}$$

Finally, we apply the inverse Fourier transform to **Eq. 4** and obtain the cepstrum of the seismic data:

$$c(n) = F^{-1}\left\{\ln\left|\sum_{n=0}^{N-1} w(k) e^{-j\frac{2\pi}{N}nk}\right|\right\} + F^{-1}\left\{\ln\left|\sum_{n=0}^{N-1} r(k) e^{-j\frac{2\pi}{N}nk}\right|\right\}$$

$$= \left\{\frac{1}{N}\sum_{k=0}^{N-1}\left[\ln\left|\sum_{n=0}^{N-1} w(k) e^{-j\frac{2\pi}{N}nk}\right|\right] e^{j\frac{2\pi}{N}nk}\right\} + \left\{\frac{1}{N}\sum_{k=0}^{N=1}\left[\ln\left|\sum_{n=0}^{N-1} r(k) e^{-j\frac{2\pi}{N}nk}\right|\right] e^{j\frac{2\pi}{N}nk}\right\}. \tag{5}$$

Equation 5 is the general form of the cepstrum of the discrete seismic data. Obviously, when $n = 0$, we have

$$C_1 = \ln|w(0)| + \ln|r(0)|, \tag{6}$$

$$C_2 = \left\{\frac{1}{N}\sum_{k=0}^{N-1}\left[\ln\left|\sum_{n=1}^{N-1} w(k) e^{-j\frac{2\pi}{N}1k}\right|\right] e^{j\frac{2\pi}{N}1k}\right\} + \left\{\frac{1}{N}\sum_{k=0}^{N=1}\left[\ln\left|\sum_{n=1}^{N-1} r(k) e^{-j\frac{2\pi}{N}1k}\right|\right] e^{j\frac{2\pi}{N}1k}\right\}. \tag{7}$$

Especially, if the seismic wavelet is assumed as

$$w(t) = \cos(\pi f_m t) e^{-\pi^2 f_m^2 t^2}, \tag{8}$$

Eq. 6 will turn into

$$C_1 = \ln|r(0)|, \tag{9}$$

in which f_m is the dominant wavelet frequency. **Equation 9** illustrates that the first-order cepstrum coefficient is the logarithm of the reflection coefficient. Since the absolute value

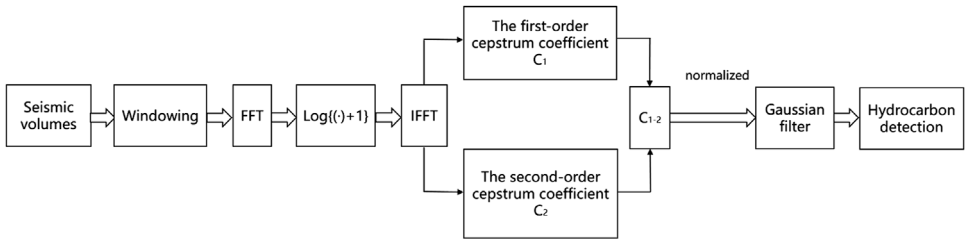

FIGURE 1 | Seismic-print analysis flow.

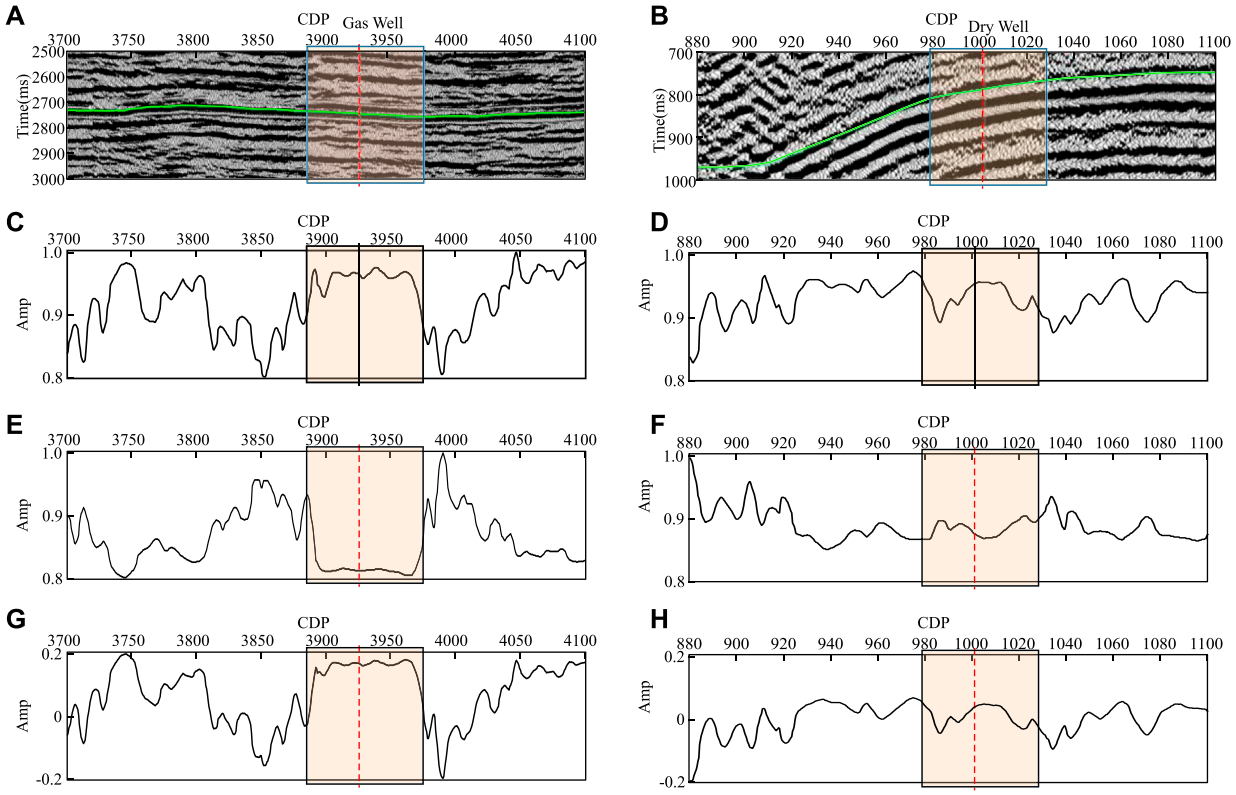

FIGURE 2 | The Seismic-print characteristics of two seismic sections intersecting different wells. **(A)** The seismic section intersecting the gas well. **(B)** The seismic section intersecting the dry well. **(C)** The first-order cepstrum coefficient's volume of the seismic section in **(A)**. **(D)** The first-order cepstrum coefficient's volume of the seismic section in **(B)**. **(E)** The second-order cepstrum coefficient's volume of the seismic section in **(A)**. **(F)** The second-order cepstrum coefficient's volume of the seismic section in **(B)**. **(G)** The result of the new parameter C_{1-2} in **(A)**. **(H)** The result of the new parameter C_{1-2} in **(B)**.

is used, the smaller reflection coefficient will lead to a larger cepstrum coefficient. For example, when r (0) = 0.1, we get C_1 = 2.3; however, when we set r (0) = 0.01, we get C_1 = 4.6. This fact shows that the first-order cepstrum coefficient is sensitive to weak reflection. The high value anomaly of the first-order cepstrum coefficient means a relatively weak reflection, that is, it indicates a "dark spot." **Equation 7** shows that the second-order cepstrum coefficient is a complex function of the high-order logarithmic reflection coefficients and wavelet, and it reflects the strength of the scatter wave. Similarly, the low value anomaly means a strong scattering. Therefore, based on the symmetrical mirror symmetry that is shown between the first-order cepstrum coefficient abnormality and the second-order cepstrum coefficient abnormality of the seismic response in the gas reservoir, we introduced a new parameter C_{1-2} (defined as the difference between the first-order and the second-order cepstrum coefficients) as a reservoir gas-bearing evaluation parameter for the seismic cepstrum feature. The workflow of hydrocarbon detection based on the seismic-print analysis is shown in **Figure 1**. In the seismic-print analysis method, the window length N is a key factor which determines the frequency ranges for a common cepstrum coefficient section. Generally, the

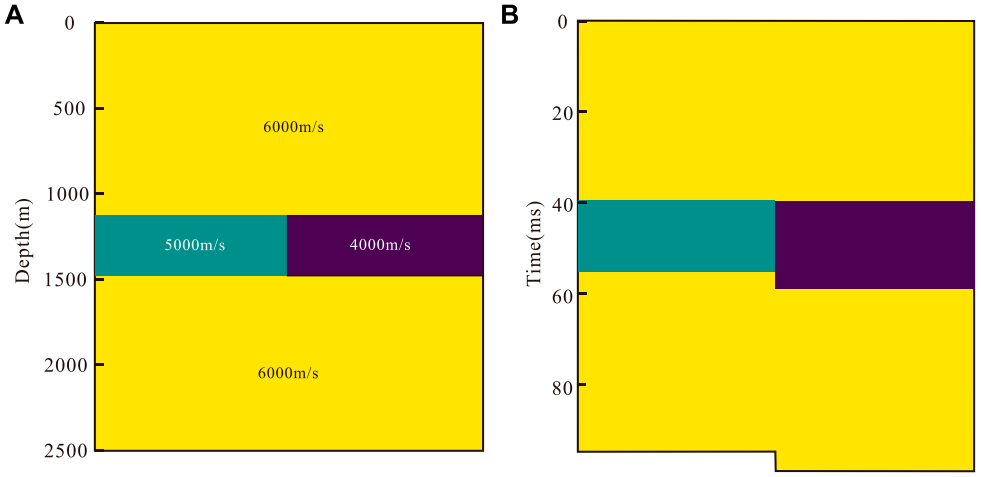

FIGURE 3 | Model comparison diagram. **(A)** Depth-domain model. **(B)** Time-domain model.

first-order cepstrum coefficient section will be in the frequency range of (0, *fs*/2*N*), and the second-order cepstrum coefficient section will be in the frequency range of (*fs*/2*N*, *fs*/*N*) (Xue et al., 2016), in which fs is the sampling frequency.

Hydrocarbon detection technology based on the seismic-print analysis directly extracts the rock's pore–fluid information from the seismic data, which do not explicitly involve the formation mechanism of the seismic response, and have no approximate problem with the numerical model. These features are the main differences between seismic-print analysis-based hydrocarbon detection technology and the other hydrocarbon detection technologies based on forward modeling and the inversion of the wave equation.

Figure 2 shows the seismic-print characteristics of two seismic sections intersecting different wells: gas well (**Figure 2A**) and dry well (**Figure 2B**) from marine carbonate reservoirs in Sichuan, China. The target horizon is shown by a green line. The first- and second-order cepstrum coefficients' volumes of the seismic section intersecting gas well show the mirror symmetry relations in the reservoir area as shown by a rectangular box in **Figures 2C,E** while the first- and second-order cepstrum coefficients' volumes of the seismic section intersecting the dry well do not represent the similar characteristics as shown by **Figures 2D,F**. And the result of the new parameter C_{1-2} is shown by **Figures 2G,H**.

3 DEPTH-DOMAIN SEISMIC DISPERSION ANALYSIS

Since Futterman (1962) first discussed in detail that the absorption and attenuation of seismic waves by rocks (frequency dispersion phenomenon) is the fundamental characteristic of the formation, people have paid more and more attention to the attenuation of seismic waves. Winkler and Nur (1982) pointed out that the leading causes of seismic wave attenuation in rocks are friction, liquid flow, viscous relaxation, and diffusion. Different lithologies have different absorption degrees of seismic waves. The stronger the absorption of the stratum, the faster the attenuation of the high-frequency component of the seismic wave (Pujol and Smithson, 1991; Helle et al., 2003). According to the close relationship between formation absorption properties and lithofacies, porosity, and oil-gas composition, lithology can be predicted, and the existence of oil and gas can be directly predicted under favorable conditions (He et al., 2008). Dilay and Eastwood (1995) discussed the frequency spectrum inside, above, and below the reservoir and analyzed the influence of the hydrocarbon property on the power spectrum. The research and application practice shows that the frequency attenuation gradient is an attribute that is more sensitive to hydrocarbon reactions. According to the theory of viscoelasticity, the amplitude of seismic waves attenuates exponentially as the propagation distance of the seismic waves increases due to the absorption effect generated by uniform incompletely elastic media, that is,

$$A = A_0 e^{-\alpha x}, \tag{10}$$

where A is the amplitude of the seismic wave after propagating for a certain distance; A_0 is the initial amplitude of seismic wave; α is the absorption coefficient; and x is the propagation distance of seismic wave.

The absorption coefficient of different lithologies shows a colossal difference. For example, the absorption coefficient of sandstone layers is larger than that of other rock layers (such as limestone layers). Therefore, the spread of seismic waves in the long-distance, its amplitude decay is severe, especially when with the underlying cracks in filling the hydrocarbon, the amplitude attenuation is more intense, which is the theoretical basis for applying the frequency attenuation property to predict the hydrocarbon properties of the formation (Berryman and Wang, 2000).

At present, the measurement of dispersion is carried out in the time domain, but the time-domain dispersion has the

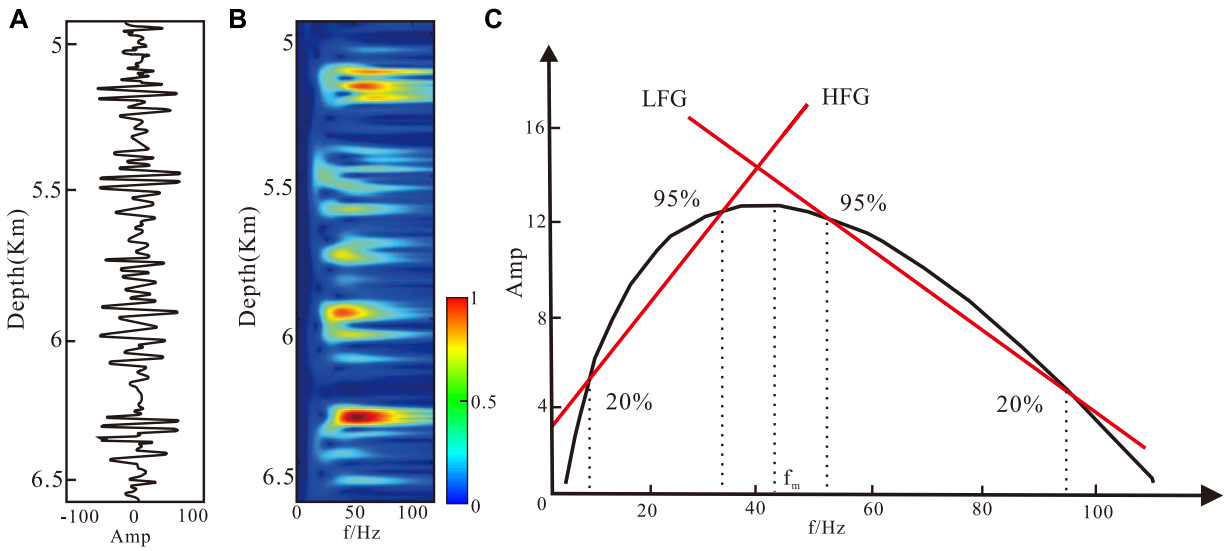

FIGURE 4 | Diagram of the EAA calculation method in the depth domain. **(A)** Deep seismic gathers; **(B)** depth time–frequency analysis diagram; **(C)** EAA extraction instructions.

problem of inaccurate construction (Wu et al., 2007), and the time profile and depth profile will not be completely consistent. Because of the speed difference, the depth with higher speed is greater than the depth with lower speed in the same second and the time profile and depth profile will not be completely consistent. Because of the speed difference, the depth with higher speed is greater than the depth with lower speed in the same second as shown in **Figure 3**, within the same depth interval in the depth domain (e.g., 120 m, due to different rock velocities (e.g., 5 and 4 km/s respectively), The thickness of the form shown on the seismic profile in the time domain can vary widely (in the case of 48 and 60 ms (two-way travel time), a difference of 12 ms), and the dispersion measured in the time domain can be used to estimate the spatial distribution of the reservoir, resulting in incorrect results.

Depth-domain seismic attributes are similar to time-domain seismic attributes in that they derive special measurements of geometry, kinematics, dynamics, and statistical characteristics from seismic data. The dynamic attributes reflect the amplitude variation of seismic data and the variance, gradient, and energy curvature extended by the amplitude (energy) (Singh, 2012; Zhang et al., 2017). The meaning of the depth domain is consistent with that of the time domain. Also, due to the more accurate positioning of imaging points in the depth domain, the more accurate spatial position of the measured attributes can better serve the reservoir prediction (Zhang et al., 2017; Cavalca et al., 2015).

3.1 Time-Depth Conversion of Seismic Data

The time-depth conversion converts a two-way time-domain seismic record to the depth domain, in effect transforming a time-domain seismic wavelet into a depth-domain seismic wavelet. A discrete expression for a two-way time–sine decay wavelet in the time domain is given as

$$x_w(i\Delta t) = A_0 e^{-ai\Delta t} \sin 2\pi\left(f_m - f_n i/N\right) i\Delta t \,(i = 0, \ldots, N), \tag{11}$$

where f_m and f_n denote the starting principal frequency and frequency decay values of the wavelet, respectively; α is the time decay exponents; and N is the number of wavelet points. Similarly, we also give a discrete expression for the depth-domain sinusoidal decay wavelet:

$$y_w(iM) = A_0 e^{-\beta i\Delta h} \sin 2\pi\left(k_m - k_n i/N\right) iAh \,(i = 0, \ldots, N), \tag{12}$$

where k_m and k_n denote the initial main wave number and the wave number attenuation value of the wavelet, respectively, β is the spatial attenuation index, which is desirable for the sake of consistency $\beta\Delta h = \alpha\Delta t$.

Since the time domain is two-way time and the depth domain is one-way depth, the frequency of the time domain to the wave number of the depth-domain conversion relation should not be the usual relation:

$$f = kv. \tag{13}$$

Also, it should be written as

$$f = \frac{1}{2}kv. \tag{14}$$

Here v is the time-depth velocity of logging interpretation, f is the frequency, and k is the wave number. So, **Eq. 11** can also be written as

$$\begin{aligned} y_w(i\Delta h) &= A_0 e^{-\beta i\Delta h} \sin 2\pi\left(f_m - f_n i/N\right) i2\Delta h/v \\ &= A_0 e^{-ai\Delta t} \sin 2\pi\left(f_m - f_n i/N\right) i\Delta t \end{aligned}. \tag{15}$$

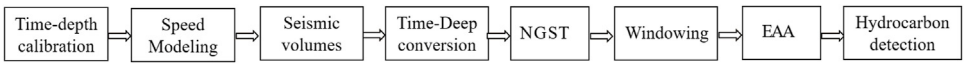

FIGURE 5 | Flow of the depth-domain seismic wave frequency dispersion analysis.

From this, we get a conclusion that the sampling interval relation satisfies

$$\Delta t = 2\Delta h/v. \tag{16}$$

Then, after the wavelet frequency in the time domain is given, the wavelet in the time domain and the depth domain are numerically equal, that is,

$$x_w(i\Delta t) = y_w(i\Delta h). \tag{17}$$

3.2 Calculation Method of Seismic Dispersion Attenuation in the Depth Domain

Mitchell et al. (1996) proposed an analysis method for calculating the energy attenuation of a seismic signal. The core of this technology is to obtain the high-frequency exponential attenuation coefficient of the signal spectrum. Due to the attenuation of waves during propagation, seismic waves are expressed as

$$A = A_0 e^{-ax} e^{i(k_x x \pm ut)}, \tag{18}$$

where $k_r = k - i\alpha$, k is the plural; α is the attenuation coefficient of the signal, which is also what we want to calculate. The calculation process of the energy absorption analysis (EAA) technology is to continuously analyze the spectrum of seismic channels with a series of small windows and calculate the attenuation coefficient. The guiding ideology of EAA technology is to eliminate regular and uniform energy attenuation in the spectrum analysis to retain the abnormal part of attenuation.

The depth-domain-specific algorithm of EAA is as follows: first of all, for each seismic record do a depth frequency analysis (**Figure 4A**), on the deep frequency section detect the maximum energy frequency as the initial attenuation frequency (**Figure 4B**), then calculate the frequency corresponding to 20 and 95% of the seismic wave energy and the corresponding frequency in the frequency range, according to the frequency of the corresponding energy, fitting of the frequency and energy attenuation gradient. The amplitude attenuation gradient factor is obtained (**Figure 4C**). The process of EAA dispersion measurement method based on the aforementioned steps is shown in **Figure 5**. The main key points are the conversion of depth-domain data and the extraction of dispersion parameters.

4 SEISMIC DEEP LEARNING

The advent of the era of artificial intelligence provides new ideas and methods for many hydrocarbon exploration problems. Deep learning forms more abstracted high-level attribute categories or feature representations through a layer-by-layer combination of low-level features, so it can deeply dig into the essential information of data and show its unique advantages and characteristics in recognition and classification (Goodfellow et al., 2016). At present, the main applications of deep learning in seismic exploration are fault recognition (Gan et al., 2016), first arrival picking (Liao et al., 2019), noise suppression (Liu et al., 2018), and velocity model construction (Yang and Ma, 2019), which have good results. Gao et al. (2020) using the transfer learning method for seismic reservoir gas prediction, Song et al. (2022) proposed a kNN-based gas-bearing prediction method by k nearest neighbor (kNN) method, both having good results. Through the block processing of seismic images and combining the respective characteristics of supervised and unsupervised learning, it is successfully applied in the hydrocarbon identification of 3D seismic data. These successful examples have laid the advantages of deep learning in establishing the non-linear mapping relationship between two datasets. At present, there are few applications in gas prediction, so the introduction of deep learning to hydrocarbon detection has a long-term development significance. Pre-stack seismic data have always been the key data basis for hydrocarbon detection. The amplitude change information contained in one time point of pre-stack data includes reservoir gas and water information, which is also the theoretical basis of AVO inversion. If the relationship between pre-stack data and hydrocarbon is to be established directly, the quality of pre-stack data is particularly important. To solve this problem, we also developed a pre-stack trace set optimization method based on bi-dimensional empirical mode decomposition (BEMD) to improve the effective information of the trace set and enhance the matching degree with a gas-bearing property (Jiang et al., 2020a), and the method of removing the strong reflection prominent effective signal (Jiang et al., 2021). The network selects the fully-connected network to deeply mine information and establish the non-linear mapping relationship between pre-stack data and hydrocarbon.

4.1 Overview of Deep Neural Network Algorithms

Establish the relationship between the labeled dataset and the training dataset using a deep neural network algorithm (DNN) to form a prediction network. Neural network technology originated in the fifties and sixties of the last century, called perceptron, with input, output, and a hidden layer. The input feature vector is transformed to the output layer through the hidden layer, and the classification results are obtained at the output layer. DNN can be understood as a neural network with many hidden layers. According to the position of the different layers, the inner

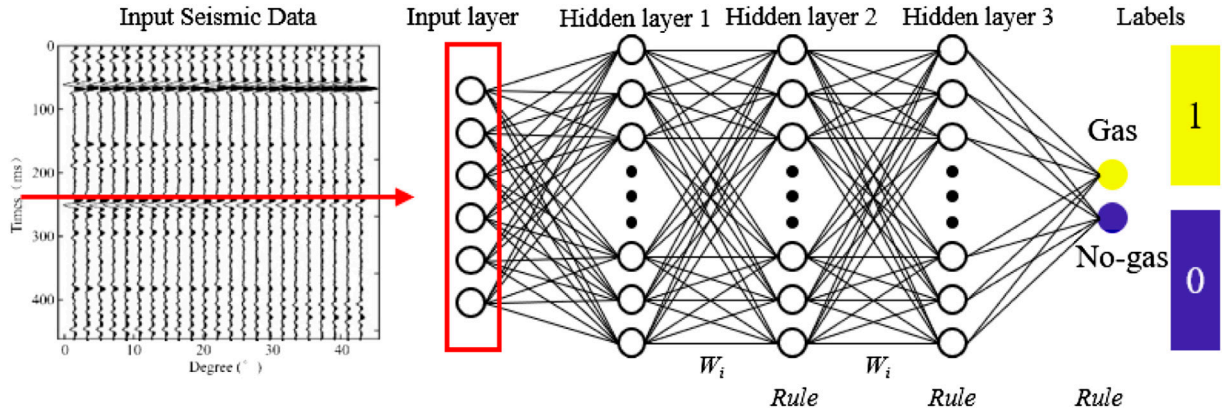

FIGURE 6 | DNN network structure.

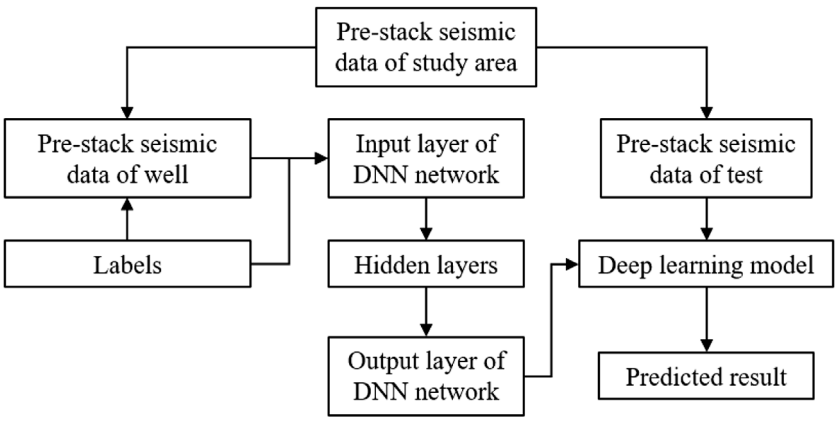

FIGURE 7 | Flow chart of DNN hydrocarbon detection method.

neural network layer of DNN can be divided into three categories: input layer, hidden layer, and output layer. Generally speaking, the first layer is the input layer, the last layer is the output layer, and the middle layer is the hidden layer. One layer and another layer are fully connected, in other words, any neuron in layer i must be connected with any neuron in layer i+1. Although DNN looks pretty complex, it is still the same as perceptron from a small local model, that is, a linear relationship:

$$z = \sum w_i x_i + b, \tag{19}$$

where z is the output layer, w_i is the weight value, x_i is the input layer, b is the bias, and then the final activation function $\sigma(z)$ is added to form the basic structure of DNN. DNN is a neural network algorithm with multiple hidden layers. In the forward propagation phase, the hidden layer takes the output of the former layer as the input for the latter layer:

$$b_k^L = \sum_{i=0}^{n} w_i^L \cdot a_i^{L-1} + d_k^L, \tag{20}$$

$$a_k^L = f\left(b_k^L\right), \tag{21}$$

where b_k^L represents the output before the activation of the k neurons in the L layer of DNN, a_k^L represents the output after the activation of the k neurons in the L layer of DNN, w_{ik}^L represents the linear transfer coefficient from a_i^{L-1} to b_k^L, d_k^L represents the bias constant of the forward propagation function of b_k^L, and f is the activation function. Select Relu function as activation function. Firstly, the Relu function is one of the common activation functions expressed as follows:

$$f(x) = \max(0, x). \tag{22}$$

The Relu function is a piecewise linear function, which changes all negative values to 0, while the positive values remain unchanged. This operation is called a unilateral suppression. If the input is negative, the output will be 0. The neuron will not be activated, which means that only part of the neurons will be started simultaneously, making the network very sparse and efficient for computing. Taking pre-stack seismic data as inputs and hydrocarbon as labels, a direct non-linear mapping relationship is established through the multi-hidden full connection network (DNN) to realize hydrocarbon detection.

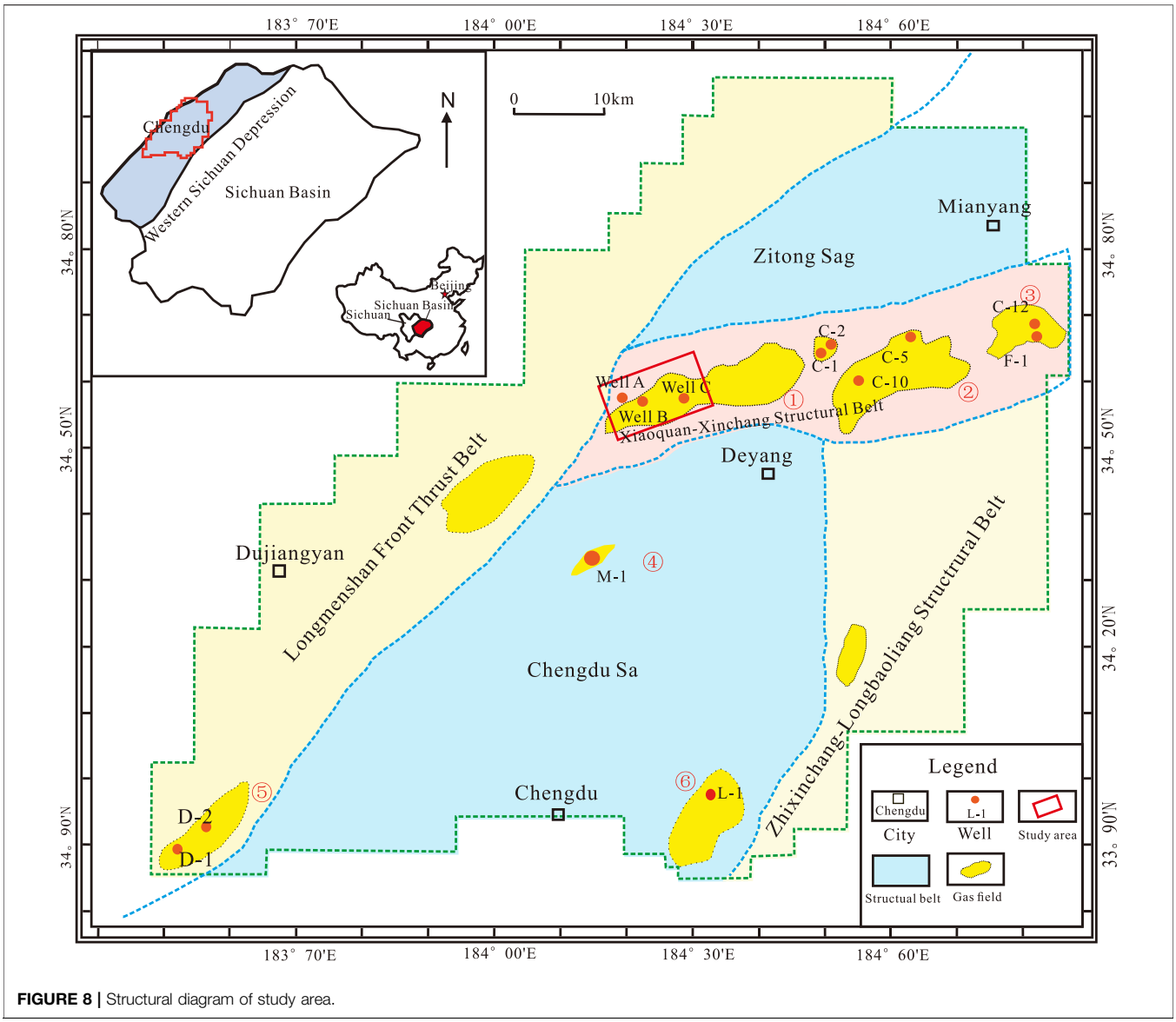

FIGURE 8 | Structural diagram of study area.

Similarly, when we input AVO features as labels, we can take a certain time window vertically and select AVO features within the time window as input features, such as 5 *ms*, which will help to improve the stability and continuity of the results. The network structure is shown in **Figure 6**. The number of network layers and neurons can be set according to the complexity of the data to improve the adaptability and accuracy of the algorithm.

4.2 The Construction Principle of the Gas Prediction Method Based on Deep Neural Network

The classical AVO inversion analysis theory builds a non-linear relationship between amplitude variation with offset and gas-bearing properties. However, due to the universality of the mapping relationship established by the classical method and the strong approximation of the non-linear mapping relationship, the prediction accuracy is often low, and the adaptability is worse under deep conditions. The continuous development of deep neural networks in recent years has shown a unique advantage in non-linear mapping problems. Therefore, according to the relationship between AVO characteristics and the gas-bearing property, the deep neural network is selected as a bridge to build its non-linear relationship. Combined with the traditional AVO analysis technology, the calculation accuracy and efficiency are improved. Based on AVO characteristics, the input layer of the deep neural network is defined as the amplitude variation of the processed gather with offset, and the gas-bearing and non-gas-bearing results of the output layer are the output. A multi-layered deep neural network structure is defined. The whole algorithm flow is shown in **Figure 7**. The deep neural network algorithm greatly simplifies the screening

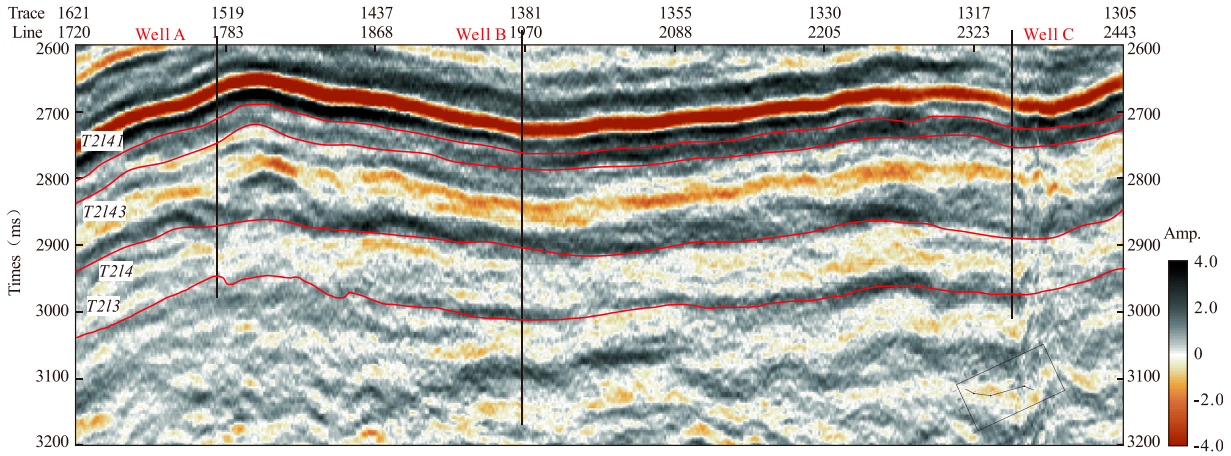

FIGURE 9 | Seismic profile of the wells in the study area.

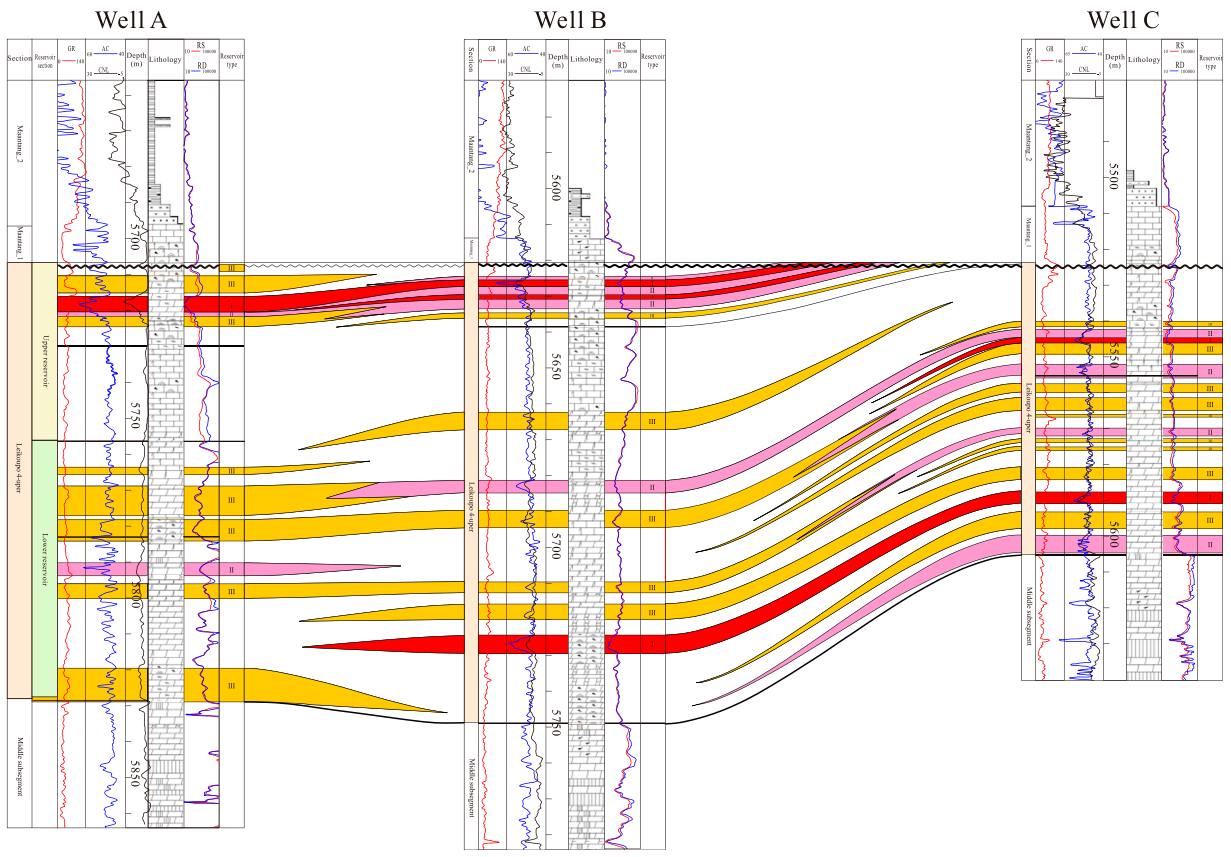

FIGURE 10 | Profile of the drilled wells in the study area.

process of the traditional AVO analysis method. It directly establishes the non-linear mapping relationship between pre-stack gather and hydrocarbon. The results obtained through the established network reduce the interference of human factors and improve the accuracy and reliability of the results.

5 A CASE STUDY

5.1 Area Introduction

The study area is located in the Xiaoquan–Xinchang tectonic belt of the western Sichuan exploration area, with 150 km^2 as shown

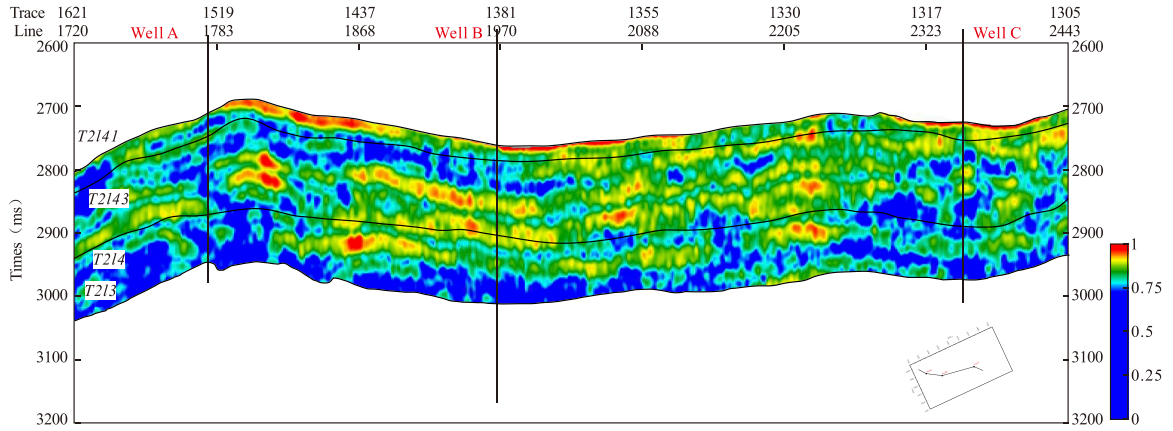

FIGURE 11 | Seismic-print analysis result.

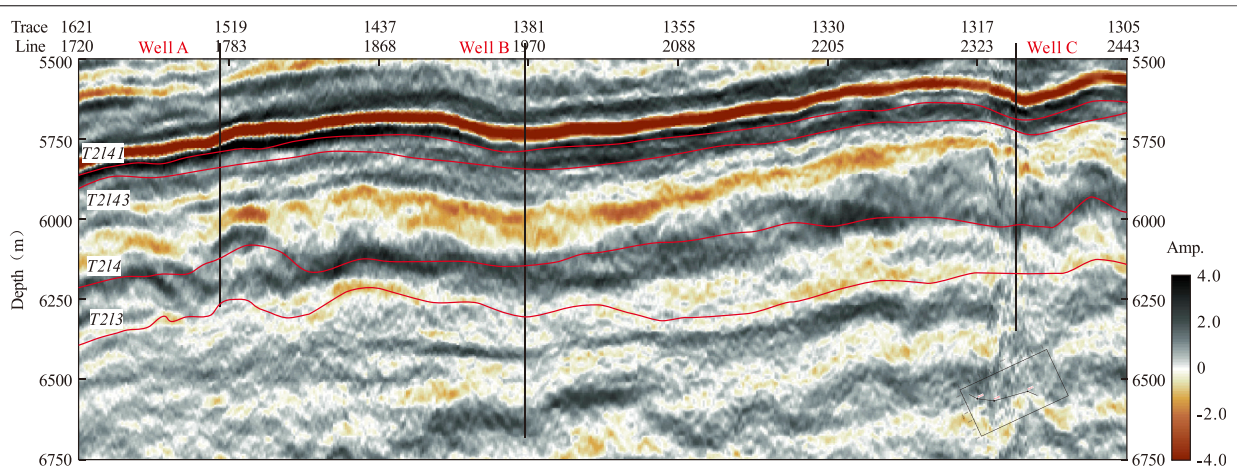

FIGURE 12 | Results of the profile after time-depth conversion.

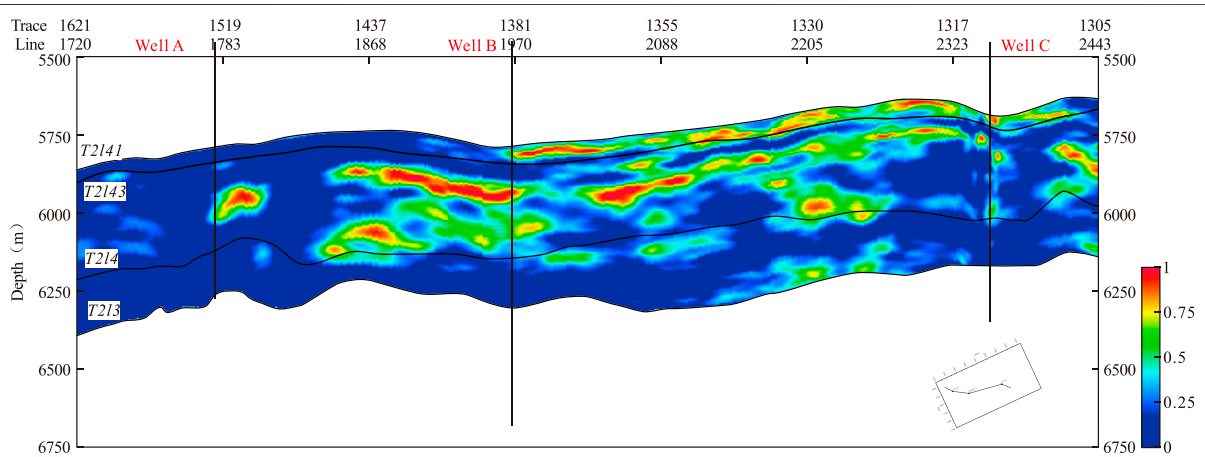

FIGURE 13 | Prediction results of depth threshold dispersion hydrocarbon.

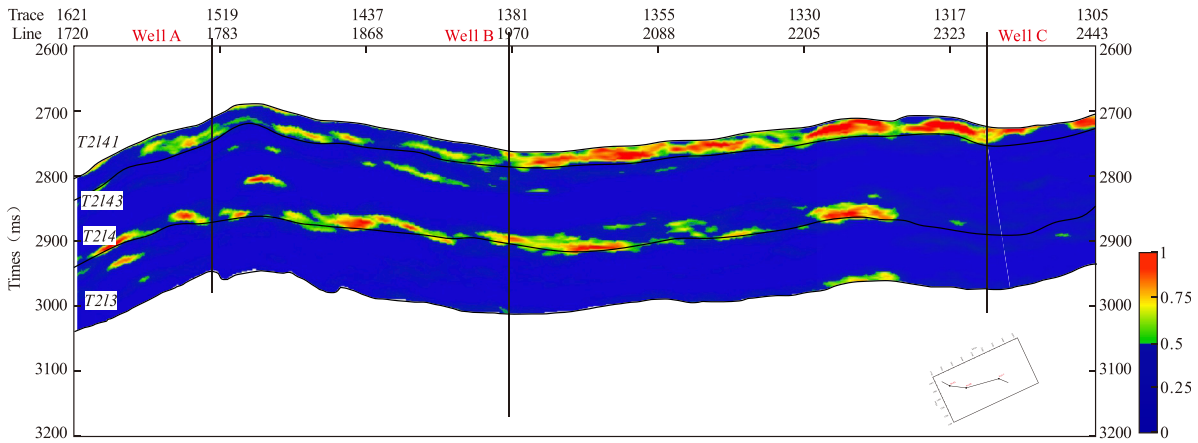

FIGURE 14 | DNN hydrocarbon detection results.

in **Figure 8**. The Xiaoquan–Xinchang tectonic zone is mainly zonal distribution located in the Longmenshan foreland basin. Among them, the collision and contact area of the Qinghai–Tibet Plateau and the Yangtze Block, two important tectonic parts of China, is the Longmenshan thrust belt–Longmenshan foreland basin mountain basin system. The specific shape of the Longmenshan foreland basin is a general zonal depression located at the core of China's abundant natural gas resources. It gradually appeared in the Late Triassic period. The thickness of the continental debris deposited in the basin differed, and some areas could be more than 5,000 m. The main target interval was the deep carbonate rock of the Leikoupo Formation. Three wells have been drilled in the study area, and the seismic profile of the wells is shown in **Figure 9** where T2*l*41 is the top of the upper reservoir of the fourth member of the Leikou profile group, and T2*l*43 is the bottom of the lower reservoir of the fourth member of the Leikoupo group. T2*l*4 is the bottom of the fourth member of the Leikoupo Formation, and T2*l*3 is the bottom of the third member of the Leikoupo Formation. The main target interval of this study is T2*l*41 – T2*l*43. From the seismic profile, it can be seen that the reservoir is thin, and the signal is relatively weak, and the seismic signal difference of the three wells is small. Well A, well B, and well C's drilling profiles are shown in **Figure 10**. The drilling section mainly shows the upper and lower reservoir information of the upper sub-member of the fourth Leikoupo formation. From the logging interpretation results, the reservoir location contains many thin reservoirs, and the reservoir conditions are good, but the drilling results showed that not all of the high quality reservoirs contain gas. Well B had a good gas-bearing property in the upper sub-member of the fourth Leikoupo formation, well A was a water well, well C was a gas–water mixed well; well C had a good gas-bearing property in the upper and lower reservoirs of the fourth Leikoupo formation, well A was still a water well, and well B had a relatively weak gas-bearing property. Both seismic data and drilling profiles show the difficulty of hydrocarbon detection, and also indicate the demand for gas prediction.

5.2 Results

5.2.1 Seismic-Print Analysis

The seismic-print analysis method is used to calculate the profile in the study area, and the hydrocarbon detection results are obtained. In **Figure 11**, the strong amplitude anomaly area indicates that in the hydrocarbon area, the stronger the amplitude, the stronger the hydrocarbon. It can be seen from the results in T2*l*41–T2*l*43 that Well A is a water well, and the amplitude anomaly is relatively weak, which is consistent with the results. The hydrocarbon of wells B and C shows a strong amplitude anomaly. The strong amplitude anomaly position is in good agreement with the hydrocarbon position, and the overall hydrocarbon detection distribution is in good agreement with the geological distribution characteristics, which verifies the method's effectiveness.

5.2.2 Depth-Domain Seismic Dispersion Analysis

Firstly, the time-depth conversion of the seismic data is carried out to obtain the results of **Figure 12**. It can be seen that after conversion, the actual structural distribution of the three wells is more conducive to gas distribution and migration and a more intuitive display of reservoir distribution. The EAA algorithm is used to calculate the dispersion based on the depth-domain data, and the results are shown in **Figure 13**. The same strong amplitude represents the gas-bearing strength. The results further demonstrate the non-hydrocarbon nature of well A and the hydrocarbon nature of wells B and C, which have a higher accuracy and can measure the hydrocarbon to some extent in the horizon from T2*l*41 to T2*l*43.

5.2.3 Seismic Deep Learning

The pre-stack seismic gathers of well B and well C are used to establish a training dataset corresponding to the gas-bearing property after time-depth conversion (1 is gas-bearing, 0 is non-gas-bearing). The dataset size is 24,000 training samples (using the whole profile data set, the profile time range is 2,400–3,600 ms, and the number of samples corresponding to

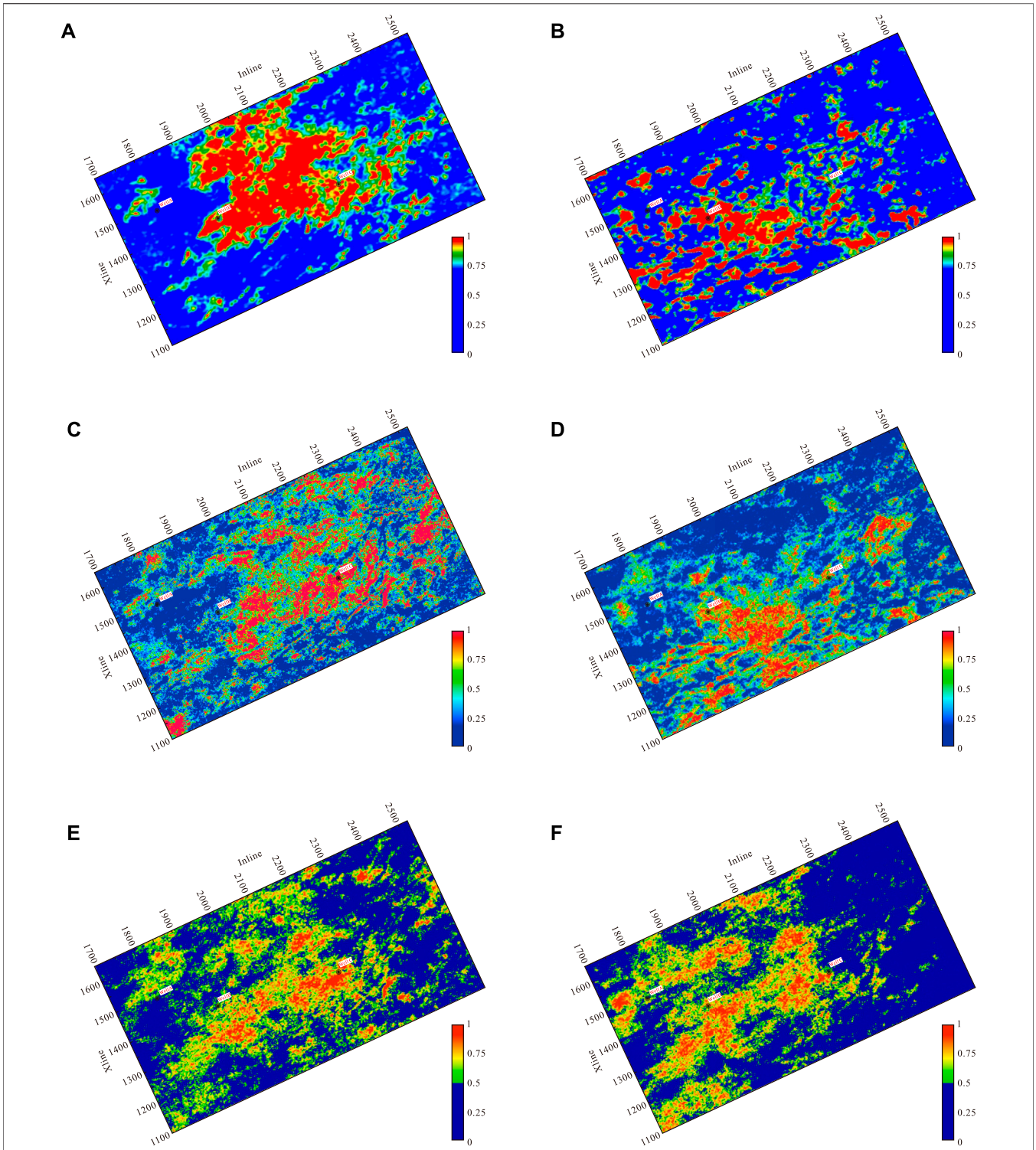

FIGURE 15 | Three dimensional result of hydrocarbon detection. **(A)** Seismic-print analysis of hydrocarbon detection results for upper member 4 of the Leikoupo Formation (T2/41). **(B)** Seismic-print analysis of hydrocarbon detection results for the lower reservoir section of the fourth member of the Leikoupo Formation (T2/43). **(C)** Prediction results of the dispersion hydrocarbon in depth domain of upper reservoir **section 4** of the Leikoupo Formation (T2/41). **(D)** Prediction results of dispersion hydrocarbon in depth domain of lower member 4 of the Leikoupo Formation (T2/43). **(E)** Prediction results of hydrocarbon in DNN of upper member 4 of the Leikoupo Formation (T2/41). **(F)** Prediction results of the hydrocarbon capacity of DNN of lower reservoir **Section 4** of the Leikoupo Formation (T2/43).

a single well is 1200. The five pre-stack gathers before and after the two wells are used as training data to form a training set of 10*1200 = 24,000 samples). The whole profile is used as a prediction sample containing 340,800 prediction samples. A deep neural network with five hidden layers is established. The activation function selects a sigmoid function, the number of neurons is 200, the loss rate of neurons is 0.6, the single training batch size of training samples is 45, and the number of iterations is 1,000. Labels 0 and 1 are the label calibrations of gas-bearing and non-gas-bearing reservoirs. The sigmoid function is used as the activation function to distribute the predicted results [0, 1]. Thus, the predicted results represent a probability closer to gas-bearing and non-gas-bearing reservoirs. When drawing, all values below 0.5 are set as non-gas-bearing, and values above 0.5 are expressed in an increasingly red color, and the profile results of hydrocarbon detection results are obtained, as shown in **Figure 14**. It can be seen from the results that the overall hydrocarbon prediction results are highly consistent with the drilling results and geological laws. The test results show that well A is a water layer in T2*l*41–T2*l*43. Well B has strong gas-bearing characteristics in the upper section of the fourth member of the Leikoupo section. The overall results are consistent with the drilling results, especially well A without network training, and the results are also consistent with the actual, indicating the effectiveness and stability of the neural network algorithm.

5.2.4 Three-Dimensional Data Analysis

Based on the two-dimensional profile calculation results, three methods are used to predict the slicing results of the upper reservoir of the Leikoupo fourth section, the lower reservoir of the Leikoupo fourth section, and the Leikoupo third section in the three main target horizons of the whole area. **Figures 15A,C, and E** are the hydrocarbon prediction results of the upper sub-member fourth of the Leikoupo Formation, and b,d, and f are the lower members, **Figures 15A,C, and E** represent the seismic-print analysis method, depth-domain dispersion, and the DNN network method, and **Figures 15B,D, and F** correspond to the meanings of a, c, and e. The upper and lower reservoir prediction results show the effectiveness and consistency of the three methods. The upper reservoir results show the characteristics of well A without gas, well B with gas, and well C with the gas–water mixture, while the lower reservoir results show the characteristics of well A without gas, well B with gas, and well C with gas. The predicted results are consistent with the actual drilling results, indicating the effectiveness of the proposed method.

5.3 Discussion

The burial depth of the carbonate strata of the Leikoupo Formation in the study area is more than 5,500 m, and the thickness of a single reservoir is several meters to 10 m. The physical properties of the gas-bearing reservoirs and water-bearing reservoirs are small, making the detection of gas-bearing reservoirs based on seismic data prone to errors. Before drilling, all the wells have been used for reservoir prediction and gas-bearing detection using the most advanced methods and technologies, including the failed well which is low in production. Even after drilling, the test results are still not completely consistent with the actual drilling results of some wells by adding the well data constraints. This shows that the existing gas detection methods cannot meet the exploration needs in deep, complex reservoir conditions. From the experimental results introduced in the previous section, the detection results of our newly developed reservoir hydrocarbon detection method are highly consistent with the actual drilling results. The seismic deep learning (SDL) method has higher accuracy, but the calculation cost is high. In comparison, the seismic-print analysis (SPA) method has higher efficiency. The depth-domain seismic dispersion analysis (DDSDA) method has more practical significance and can accurately predict the gas-bearing depth and location. This shows that the new method can better adapt to strong heterogeneity and weak seismic response of the ultra-deep ancient carbonate reservoir medium. The main advantage of the new methods is that they are data-driven and do not need to model rock physics and seismic response mechanisms, so they can naturally adapt to any complex medium. In contrast to the DHI methods such as AVO analysis, the calculation expression of evaluation parameters has made many assumptions in derivation. If the actual situation does not coincide with these assumptions, it may be wrong. At the same time, we should also see that the evaluation standard of data-driven reservoir hydrocarbon detection depends on the calibration of well data. When the available well data are few, or no well data are available at all, it is possible to make mistakes according to experience. But, we believe that with the accumulation of practical application data, the reliability of data-driven reservoir gas detection methods will be higher and higher. Data-driven reservoir gas-bearing detection results are essentially probabilistic and, in most cases, qualitative. The success of oil and gas exploration wells depends on quantity. Only when the product reaches the level of economic benefits can it be called a success. Therefore, the evaluation of reservoir hydrocarbon should develop from qualitative detection to quantitative prediction in the future, and the technology of reservoir hydrocarbon prediction should be developed. The existing drilling data reveal that the ultra-deep ancient carbonate reservoir has strong heterogeneity. At the same time, due to deep burial and other reasons, the seismic response of the reservoir is weak and complex, so that the prediction of reservoir hydrocarbon based on rock physics and seismic response analysis modeling is almost impossible. Deep network adaptive non-linear modeling based on deep learning can play a role, which may be the most potential breakthrough research.

In general, this article studies and discusses the current hydrocarbon prediction methods for deep and ultra-deep carbonate rocks. The seismic-print method is mainly for post-stack data, which can quickly and efficiently obtain weak gas-bearing information, but require a relatively high signal-to-noise ratio for post-stack data. The noise immunity is not particularly good. The depth-domain attenuation method can detect hydrocarbon from a depth perspective, making the prediction results more accurate, but the accuracy of time-depth conversion needs to be improved; the neural network hydrocarbon prediction is based on pre-stack data, which improve the

efficiency and accuracy of calculation, but the establishment of a sample database is still a problem that needs to be further studied.

6 CONCLUSION

This article describes three methods for gas reservoir identification of ultra-deep carbonate rocks in the Sichuan Basin: seismic-print analysis method, depth-domain dispersion analysis method, and seismic deep learning method. The seismic-print analysis method uses cepstrum analysis to highlight the reservoir's weak response signal and reveal the cepstrum characteristics of the gas-bearing reservoir. The first-order and second-order cepstrum coefficient anomalies are a convex mirror symmetry. The depth-domain dispersion analysis method converts the dispersion analysis usually carried out in the time domain to the real space domain, creating conditions for estimating the reservoir hydrocarbon based on dispersion. The seismic deep learning method uses the adaptive non-linear modeling ability of a complex system of the deep network to construct the deep network model that directly predicts reservoir hydrocarbon from pre-stack seismic data. These three methods can be regarded as data-driven reservoir hydrocarbon detection methods, which do not explicitly involve establishing rock physical and seismic response analysis models. Therefore, compared with the existing DHI method, the applicability of these methods to the weak seismic response of ultra-deep strong heterogeneous reservoirs is stronger. The practical application results also demonstrate that these methods are more effective. Nevertheless, it is still not a silver bullet, and there is still a situation where the prediction results are not consistent with the actual situation, and it has not been widely applied.

DATA AVAILABILITY STATEMENT

The original contributions presented in the study are included in the article/Supplementary Material; further inquiries can be directed to the corresponding author.

AUTHOR CONTRIBUTIONS

Conception and design of study: JC, XJ, YX, RT, and MC. Acquisition of data: XJ, YX, and MC. Analysis and/or interpretation of data: XJ, YX, RT, and MC. Drafting the manuscript: XJ, YX, MC, and XT. Revising the manuscript critically for important intellectual content: XJ, YX, MC, and TX. Approval of the version of the manuscript to be published: JC, XJ, YX, RT, MC, and TX.

FUNDING

This work was supported by the National Natural Science Foundation of China (Grant Nos. 42030812, 41974160, and 41430323), project of the SINOPEC Science and Technology Department (Grant No. P20055-6), and Special Project of the Local Science and Technology Development guided by the Central Government in Sichuan (2021ZYD0030).

REFERENCES

Berryman, J. G., and Wang, H. F. (2000). Elastic Wave Propagation and Attenuation in a Double-Porosity Dual-Permeability Medium. *Int. J. Rock Mech. Min. Sci.* 37, 63–78. doi:10.1016/s1365-1609(99)00092-1

Campbell, J. P. (1997). Speaker Recognition: A Tutorial. *Proc. IEEE* 85, 1437–1462. doi:10.1109/5.628714

Cao, J. (2017). Deep Learning and its Application in Deep Gas Reservoir Prediction. *Comput. Tech. Geophys. Geochem. Explor.* 39, 775–782.

Cao, J., He, X., and Wu, S. (2017). *Reservoir Detection Method Based on Deep Learning of Seismic Data*. chinese invention patent: Zl 2017 1 0115720.6.

Cao, J., Liu, S., Tian, R., Wang, X., and He, X. (2011a). Seismic Prediction of Carbonate Reservoirs in the Deep of Longmenshan Foreland Basin. *Acta Petrol. Sin.* 27, 2423–2434.

Cao, J., Tian, R., and He, X. (2011b). Seismic-print Analysis and Hydrocarbon Identification. *AGU Fall Meet. Abstr.* 2011, S33B–S01.

Cao, J., and Tian, R. (2011). *Reservoir Detection Method Based on Seismic Pattern Analysis*. chinese invention patent:zl 20111 0165615.6.

Cao, J., and Wu, S. (2017). "Deep Learning: Chance and Challenge for Deep Gas Reservoir Identification," in International Geophysical Conference, Qingdao, China, 17-20 April 2017 (Houston, Texas, USA: Society of Exploration Geophysicists and Chinese Petroleum Society), 711–712.

Cao, J., Xue, Y., Tian, R., and Shu, Y. (2019). Advances in Hydrocarbon Detection in Deep Carbonate Reservoirs. *Geophys. Prospecrting Petroleum (in Chinese)* 58, 9–16.

Cao, X. Y. J., and Tian, R. (2019). Advancesinhyg Drocarbon detectionindeepcarbonatereservoirs. *Geophysical Prospecting for Petroleum* 58, 9G–16G.

Castagna, J. P., and Backus, M. M. (1993). *Offset-dependent Reflectivity—Theory and Practice of AVO Analysis*. Houston, Texas, USA: Society of Exploration Geophysicists.

Castagna, J. P., Sun, S., and Siegfried, R. W. (2003). Instantaneous Spectral Analysis: Detection of Low-Frequency Shadows Associated with Hydrocarbons. *The leading edge* 22, 120–127. doi:10.1190/1.1559038

Cavalca, M., Fletcher, R., and Du, X. (2015). "Q-compensation through Depth Domain Inversion," in 77th EAGE Conference and Exhibition 2015 (Houten, Netherlands: European Association of Geoscientists & Engineers), 1–5. doi:10.3997/2214-4609.201413250

Chopra, S., and Castagna, J. (2014). *Avo (Investigations in Geophysics Series No. 16)*. Houston, Texas, USA: Society of exploration geophysicists.

Cui, C.-j., Gong, Y.-j., and Shen, D.-y. (2010). Application of Wave Impedance Inversion to Reservoir Prediction Research. *Progress in Geophysics* 25, 9–15.

Das, R. K., and Prasanna, S. R. M. (2018). Speaker Verification from Short Utterance Perspective: a Review. *IETE Technical Review* 35, 599–617. doi:10.1080/02564602.2017.1357507

Dilay, A., and Eastwood, J. (1995). Spectral Analysis Applied to Seismic Monitoring of Thermal Recovery. *The Leading Edge* 14, 1117–1122. doi:10.1190/1.1437081

Fawad, M., Hansen, J. A., and Mondol, N. H. (2020). Seismic-fluid Detection-A Review. *Earth-Science Reviews* 210, 103347. doi:10.1016/j.earscirev.2020.103347

Futterman, W. I. (1962). Dispersive Body Waves. *J. Geophys. Res.* 67, 5279–5291. doi:10.1029/jz067i013p05279

Gan, M., Wang, C., and Zhu, C. a. (2016). Construction of Hierarchical Diagnosis Network Based on Deep Learning and its Application in the Fault Pattern Recognition of Rolling Element Bearings. *Mechanical Systems and Signal Processing* 72-73, 92–104. doi:10.1016/j.ymssp.2015.11.014

Gao, J., Song, Z., Gui, J., and Yuan, S. (2020). Gas-bearing Prediction Using Transfer Learning and Cnns: An Application to a Deep Tight Dolomite Reservoir. *IEEE Geoscience and Remote Sensing Letters* 19.

Goodfellow, I., Bengio, Y., and Courville, A. (2016). *Deep Learning*. Cambridge, MA, USA: MIT press.

Hammond, A. L. (1974). Bright Spot: Better Seismological Indicators of Gas and Oil. *Science* 185, 515–517. doi:10.1126/science.185.4150.515

He, X., Cao, J., and X, J. (2018). *A Reservoir Gas-Bearing Evaluation Method Based on Seismic Wave Dispersion Analysis in Depth Domain*. chinese invention patent, zl 201811388697.9.

He, Z., Xiong, X., and Bian, L. (2008). Numerical Simulation of Seismic Low-Frequency Shadows and its Application. *Appl. Geophys.* 5, 301–306. doi:10.1007/s11770-008-0040-4

Helle, H. B., Pham, N. H., and Carcione, J. M. (2003). Velocity and Attenuation in Partially Saturated Rocks: Poroelastic Numerical Experiments. *Geophysical Prospecting* 51, 551–566. doi:10.1046/j.1365-2478.2003.00393.x

Jiang, X., Cao, J., Hu, J., Xiong, X., and Liu, J. (2020a). Pre-stack Gather Optimization Technology Based on an Improved Bidimensional Empirical Mode Decomposition Method. *Journal of Applied Geophysics* 177, 104026.

Jiang, X., Cao, J., Yang, J., Liu, J., and Zhou, P. (2020b). Avo Analysis Combined with Teager-Kaiser Energy Methods for Hydrocarbon Detection. *IEEE Geoscience and Remote Sensing Letters* 19, 1–5.

Jiang, X., Cao, J., Zu, S., Xu, H., and Wang, J. (2021). Detection of Hidden Reservoirs under Strong Shielding Based on Bi-dimensional Empirical Mode Decomposition and the Teager-Kaiser Operator. *Geophysical Prospecting* 69, 1086–1101. doi:10.1111/1365-2478.13073

Jin, S., Cambois, G., and Vuillermoz, C. (2000). Shear-wave Velocity and Density Estimation from PS-Wave AVO Analysis: Application to an OBS Dataset from the North Sea. *Geophysics* 65, 1446–1454. doi:10.1190/1.1444833

Kersta, L. G. (1962). Voiceprint Identification. *The Journal of the Acoustical Society of America* 34, 725. doi:10.1121/1.1937211

Li, J., and Zhang, J. (2021). "A Study of Voice Print Recognition Technology," in 2021 International Wireless Communications and Mobile Computing (IWCMC) (Harbin City, China: IEEE), 1802–1808. doi:10.1109/iwcmc51323.2021.9498681

Li, X., Guo, J., Zhang, Q., and Tong, K. (2008). Determining Method for the Lower Limit of Physical-Property Parameters in Gas Reservoirs. *Natural Gas Exploration and Development* 31, 33–38.

Liao, X., Cao, J., Hu, J., You, J., Jiang, X., and Liu, Z. (2019). First Arrival Time Identification Using Transfer Learning with Continuous Wavelet Transform Feature Images. *IEEE Geoscience and Remote Sensing Letters* 17, 2002–2006.

Liu, D., Wang, W., Chen, W., Wang, X., Zhou, Y., and Shi, Z. (2018). "Random Noise Suppression in Seismic Data: What Can Deep Learning Do?," in *SEG Technical Program Expanded Abstracts 2018* (Houston, Texas, USA: Society of Exploration Geophysicists), 2016–2020.

Mitchell, J. T., Derzhi, N., Lichman, E., and Lanning, E. N. (1996). "Energy Absorption Analysis: A Case Study," in *SEG Technical Program Expanded Abstracts 1996* (Houston, Texas, USA: Society of Exploration Geophysicists), 1785–1788. doi:10.1190/1.1826480

Pujol, J., and Smithson, S. (1991). Seismic Wave Attenuation in Volcanic Rocks from Vsp Experiments. *Geophysics* 56, 1441–1455. doi:10.1190/1.1443164

Robinson, J. C. (1979). A Technique for the Continuous Representation of Dispersion in Seismic Data. *Geophysics* 44, 1345–1351. doi:10.1190/1.1441011

Russell, B. H., Hedlin, K., Hilterman, F. J., and Lines, L. R. (2003). Fluid-property Discrimination with AVO: A Biot-Gassmann Perspective. *Geophysics* 68, 29–39. doi:10.1190/1.1543192

Singh, Y. (2012). Deterministic Inversion of Seismic Data in the Depth Domain. *The Leading Edge* 31, 538–545. doi:10.1190/tle31050538.1

Smith, G. C., and Sutherland, R. A. (1996). The Fluid Factor as an Avo Indicator. *Geophysics* 61, 1425–1428. doi:10.1190/1.1444067

Song, Z., Yuan, S., Li, Z., and Wang, S. (2022). kNN-Based Gas-Bearing Prediction Using Local Waveform Similarity Gas-Indication Attribute - an Application to a Tight Sandstone Reservoir. *Interpretation* 10, SA25–SA33. doi:10.1190/int-2021-0045.1

Veeken, P., and Silva, M. D. (2004). Seismic Inversion Methods and Some of Their Constraints. *First break* 22, 1013. doi:10.3997/1365-2397.2004011

Winkler, K. W., and Nur, A. (1982). Seismic Attenuation: Effects of Pore Fluids and Frictional-sliding. *Geophysics* 47, 1–15. doi:10.1190/1.1441276

Wu, R., Zhu, H., Lin, B., and Xue, S. (2007). "Wavelet Analysis and Convolution in Depth Domain," in 2007 SEG Annual Meeting (Richardson, TX, USA: OnePetro).

Xue, Y.-j., Cao, J.-x., and Tian, R.-f. (2013). A Comparative Study on Hydrocarbon Detection Using Three EMD-Based Time-Frequency Analysis Methods. *Journal of Applied Geophysics* 89, 108–115. doi:10.1016/j.jappgeo.2012.11.015

Xue, Y.-j., Cao, J.-x., Tian, R.-f., Du, H.-k., and Yao, Y. (2016). Wavelet-based Cepstrum Decomposition of Seismic Data and its Application in Hydrocarbon Detection. *Geophysical Prospecting* 64, 1441–1453. doi:10.1111/1365-2478.12344

Xue, Y.-j., Cao, J.-x., and Tian, R.-f. (2014). EMD and Teager-Kaiser Energy Applied to Hydrocarbon Detection in a Carbonate Reservoir. *Geophysical Journal International* 197, 277–291. doi:10.1093/gji/ggt530

Yang, F., and Ma, J. (2019). Deep-learning Inversion: A Next-Generation Seismic Velocity Model Building Method. *Geophysics* 84, R583–R599. doi:10.1190/geo2018-0249.1

Zhang, R., Zhang, K., and Alekhue, J. E. (2017). Depth-domain Seismic Reflectivity Inversion with Compressed Sensing Technique. *Interpretation* 5, T1–T9. doi:10.1190/int-2016-0005.1

Zong, Z., Yin, X., and Wu, G. (2013). Elastic Impedance Parameterization and Inversion with Young's Modulus and Poisson's Ratio. *Geophysics* 78, N35–N42. doi:10.1190/geo2012-0529.1

Conflict of Interest: The authors declare that the research was conducted in the absence of any commercial or financial relationships that could be construed as a potential conflict of interest.

The reviewer JX declared a shared affiliation with the authors, JC, XJ, RT, TX, and MC to the handling editor at the time of the review.

Publisher's Note: All claims expressed in this article are solely those of the authors and do not necessarily represent those of their affiliated organizations, or those of the publisher, the editors, and the reviewers. Any product that may be evaluated in this article, or claim that may be made by its manufacturer, is not guaranteed or endorsed by the publisher.

frontiers | Frontiers in Earth Science

ORIGINAL RESEARCH
published: 12 July 2022
doi: 10.3389/feart.2022.873541

Wave Equation Numerical Simulation and RTM With Mixed Staggered-Grid Finite-Difference Schemes

Wei Liu [1,2], Ziduo Hu [1,2], Xueshan Yong [1,2], Gengxin Peng [3], Zhonghua Xu [1,2] and Linghe Han [1,2]*

[1]Research Institute of Petroleum Exploration and Development-Northwest, PetroChina, Lanzhou, China, [2]Key Laboratory of Petroleum Resources of CNPC, Lanzhou, China, [3]Tarim Oilfield Company, PetroChina, Korla, China

For the conventional staggered-grid finite-difference scheme (C-SFD), although the spatial finite-difference (FD) operator can reach $2M^{th}$-order accuracy, the FD discrete wave equation is the only second-order accuracy, leading to low modeling accuracy and poor stability. We proposed a new mixed staggered-grid finite-difference scheme (M-SFD) by constructing the spatial FD operator using axial and off-axial grid points jointly to approximate the first-order spatial partial derivative. This scheme is suitable for modeling the stress–velocity acoustic and elastic wave equation. Then, based on the time–space domain dispersion relation and the Taylor series expansion, we derived the analytical expression of the FD coefficients. Theoretically, the FD discrete acoustic wave equation and P- or S-wave in the FD discrete elastic wave equation given by M-SFD can reach the arbitrary even-order accuracy. For acoustic wave modeling, with almost identical computational costs, M-SFD can achieve higher modeling accuracy than C-SFD. Moreover, with a larger time step used in M-SFD than that used in C-SFD, M-SFD can achieve higher computational efficiency and reach higher modeling accuracy. For elastic wave simulation, compared to C-SFD, M-SFD can obtain higher modeling accuracy with almost the same computational efficiency when the FD coefficients are calculated based on the S-wave time–space domain dispersion relation. Solving the split elastic wave equation with M-SFD can further improve the modeling accuracy but will decrease the efficiency and increase the memory usage as well. Stability analysis shows that M-SFD has better stability than C-SFD for both acoustic and elastic wave simulations. Applying M-SFD to reverse time migration (RTM), the imaging artifacts caused by the numerical dispersion are effectively eliminated, which improves the imaging accuracy and resolution of deep formation.

Keywords: mixed staggered-grid finite-difference, numerical simulation, dispersion relation, finite-difference coefficients, numerical dispersion

OPEN ACCESS

Edited by:
Jianping Huang,
China University of Petroleum, Huadong, China

Reviewed by:
Chenglong Duan,
The University of Texas at Dallas, United States
Weiting Peng,
China University of Petroleum (Huadong), China

****Correspondence:***
Wei Liu
liuwei2013@petrochina.com.cn

Specialty section:
This article was submitted to Solid Earth Geophysics, a section of the journal Frontiers in Earth Science

Received: *10 February 2022*
Accepted: *06 June 2022*
Published: *12 July 2022*

Citation:
Liu W, Hu Z, Yong X, Peng G, Xu Z and Han L (2022) Wave Equation Numerical Simulation and RTM With Mixed Staggered-Grid Finite-Difference Schemes. Front. Earth Sci. 10:873541. doi: 10.3389/feart.2022.873541

1 INTRODUCTION

Wave equation simulation is an important technique to study the characteristics of seismic waves in complex media (Carcione, 2015; Cao and Chen, 2018), and a key kernel in reverse time migration (RTM) (Virieux et al., 2011; Berkhout, 2014) and full waveform inversion (FWI) (Pratt et al., 1998; Virieux and Operto, 2009). Compared to the pseudo-spectral method (Reshef et al., 1988; Mittet, 2021) and finite-element method (Marfurt, 1984; Moczo et al., 2010; Moczo et al., 2011), the finite-

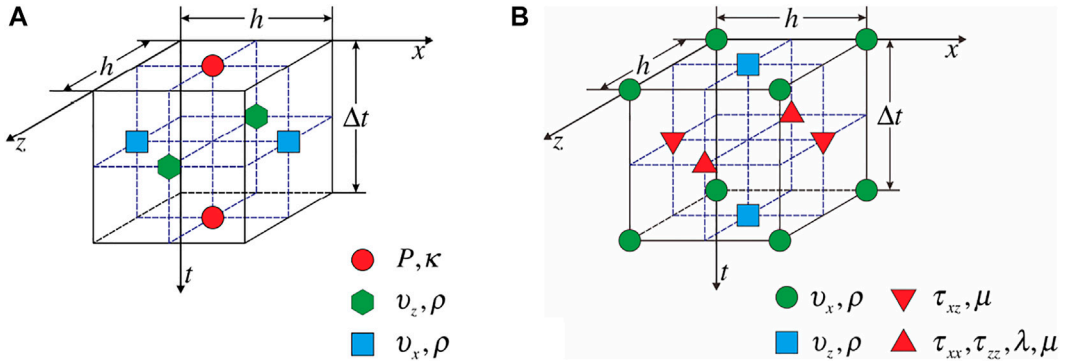

FIGURE 1 | Schematic representation of the relative position of the wave-field variables and elastic parameters in **(A)** acoustic wave and **(B)** elastic wave staggered-grid FD schemes.

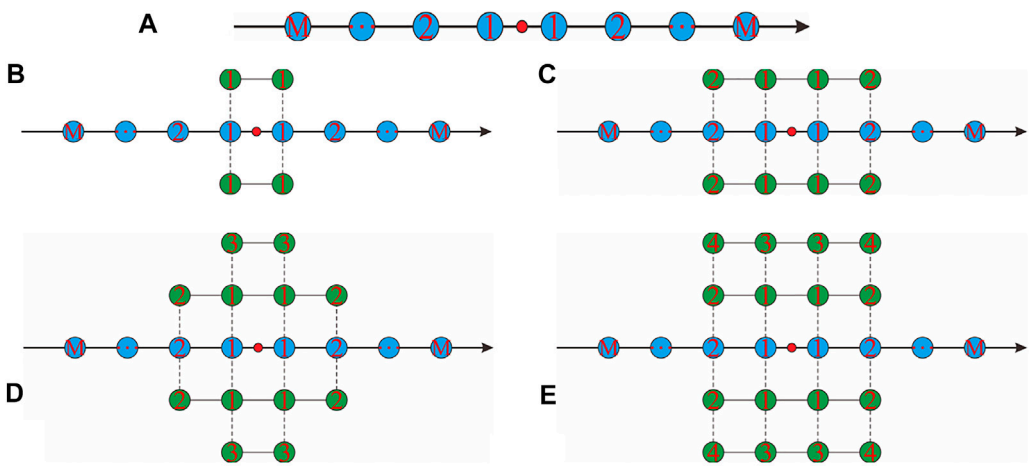

FIGURE 2 | Schematic representation of the spatial FD operators of **(A)** C-SFD and **(B–E)** M-SFD (*N*=1, 2, 3, and 4).

difference (FD) method has the advantage of high computational efficiency, small memory occupation and easy implementation (Alford et al., 1974; Mulder, 2017). Hence, the FD method has become the most widely used numerical method for wave propagation simulation (Alterman and Karal, 1968; Chen et al., 2021). However, the inherent numerical dispersion in FD methods seriously affects the modeling accuracy (Alford et al., 1974; Dablain, 1986) and leads to an adverse impact on RTM and FWI results (Ren et al., 2021). So suppressing the numerical dispersion to improve the modeling accuracy is an important issue for the FD method.

Dablain (1986) pointed out that approximating the temporal and spatial partial derivatives with high-order FD operators can reduce the numerical dispersion. Unfortunately, the temporal high-order FD operator significantly increases the amount of computation and decreases the stability. Hence, conventional FD (C-FD) and staggered-grid FD (C-SFD) commonly adopt temporal second-order and spatial $2M^{\text{th}}$-order FD operators (Fornberg, 1988). With the FD coefficients calculated based on the space domain dispersion relation and Taylor series expansion (TE), the spatial FD operators in C-FD and C-SFD can achieve $2M^{\text{th}}$-order accuracy, but the FD discrete wave equations are still only second-order accuracy (Liu and Sen, 2009). However, wave equation simulation is implemented by solving the FD discrete wave equation iteratively. So in order to improve the modeling accuracy, we should try to increase the accuracy of the FD discrete wave equation rather than improve separately the accuracy of the temporal and spatial FD operators. Liu and Sen (2009; 2011) proposed to calculate the FD coefficients of C-FD and C-SFD based on the time–space domain dispersion relation and TE, which makes the 2D and 3D FD discrete wave equations reach $2M^{\text{th}}$-order accuracy along 8 and 48 propagation directions respectively, but the accuracy is still second-order along with the rest of the directions. In addition to the aforementioned TE methods, the least squares (LS) methods are also widely adopted for computing the FD coefficients by minimizing the error of dispersion relation, phase velocity, or group velocity (Geller and Takeuchi, 1998; Chu and Stoffa, 2012). The LS methods usually

improve the accuracy of wavefield components in the medium-high frequency band but decays some accuracy of the low-frequency component. Liu (2013; 2014) found that by minimizing the relative error instead of the absolute error of space domain or time-space domain dispersion relation, the global optimal solution can be obtained without iterations.

In addition to ameliorating the method for computing the FD coefficients, constructing a more reasonable FD stencil is another important way to improve the modeling accuracy. For the 2D scalar wave equation, Liu and Sen (2013) developed a rhombus FD scheme. The FD discrete wave equation can reach $2M^{\text{th}}$-order accuracy along with all propagation directions with the FD coefficients calculated based on the time-space domain dispersion relation. However, the length of the spatial FD operator increases rapidly with M, which makes it very computationally expensive. Wang et al. (2016) proposed an FD scheme by combining the C-FD and rhombus FD schemes, which balanced the accuracy and efficiency. Motivated by the widely used mixed-grid FD scheme in the frequency domain (Jo et al., 1996; Shin and Sohn, 1998), Hu et al. (2016) proposed a mixed-grid FD scheme for 2D scalar wave equation modeling in the time–space domain. The basic idea of Hu et al. (2016) is to express the Laplace FD operator as the weighted mean of the Laplace FD operators constructed in the general and rotated Cartesian coordinate system. The resulting mixed-grid FD scheme is similar to that of Wang et al. (2016). Hu et al. (2021) derived how to construct a 3D Laplace FD operator with the off-axial grid points and further proposed a 3D mixed-grid FD scheme, which improved the accuracy and stability of 3D scalar wave equation simulation. For the stress–velocity acoustic wave equation, Tan and Huang (2014) constructed a spatial FD operator with the axial and off-axial grid points to approximate the first-order spatial partial derivatives and developed a mixed staggered-grid FD scheme (M-SFD). This M-SFD can make the FD discrete acoustic wave equation reach fourth or sixth-order accuracy. Ren and Li (2017) extended the method of Tan and Huang (2014) to elastic wave simulation, and the accuracy of P- or S-wave in the FD discrete elastic wave equation can be up to eighth-order. However, in the M-SFD of Tan and Huang (2014) and Ren and Li (2017), two sets of off-axial grid points with different distance to the center of the spatial FD operator are sometimes assigned the same FD coefficient, which is unreasonable and makes derivation of the analytic expression of the FD coefficients too difficult.

For simulation of the stress-velocity acoustic and elastic wave equation, we intended to develop a modified M-SFD by ensuring the FD coefficient assigned to the grid points varies with their distance to the center of the spatial FD operator, which will make our M-SFD more reasonable than that of Tan and Huang (2014) and Ren and Li (2017). Then we managed to derive the analytical solution for calculating the FD coefficients with the time-space domain dispersion relation and TE. We first discretized the acoustic and elastic wave equation with our M-SFD and derived the analytical solution of the FD coefficients. This is followed by analysis of difference accuracy, numerical dispersion, and stability. Then, we performed acoustic and elastic numerical simulation on a simple three-layered model and a typical complex structural model of the Tarim Basin in Western China and compared the results of M-SFD and C-SFD. In the end, we carried out acoustic RTM with M-SFD for synthetic seismic data on the complex structural model.

2 BASIC THEORY OF M-SFD

2.1 FD Discrete Acoustic and Elastic Wave Equation Given by M-SFD

The wavefield variables and elastic parameters are defined at staggered grid points in the staggered-grid FD scheme. **Figure 1** displays the relative position of the wavefield variables and elastic parameters in acoustic and elastic staggered-grid FD schemes.

C-SFD adopts temporal second-order and spatial $2M^{\text{th}}$-order FD operators. The spatial FD operator is constructed only by the axial grid points, shown in **Figure 2A**. In this spatial FD operator, M represents the number of sets of axial grid points with each set having the same distance to the center. As we know, M sets of grid points can ensure the spatial FD operator reaches $2M^{\text{th}}$-order accuracy. We can also see that the distance of these points to the center of the operator increases with M, while the contribution toward improving the modeling accuracy decreases.

In this article, we proposed a modified M-SFD by constructing the spatial FD operator using the axial and off-axial grid points while keeping the temporal second-order FD operator unchanged. In the spatial FD operators, M and N represent the number of sets of axial and off-axial grid points, respectively, and each set of grid points is equidistant from the center of the operator. The identical FD coefficient is assigned to the grid points in the same set, and different FD coefficients are assigned to different sets. **Figures 2B–E** show the four spatial FD operators of our M-SFD with N=1, 2, 3, and 4. Compared to C-SFD, M-SFD takes full use of the off-axial grid points near the center of the spatial FD operator.

The previous M-SFD (Tan and Huang, 2014; Ren and Li, 2017) inappropriately uses the symmetry of the off-axial grid points. Two different sets of off-axial grid points with unequal distance to the center are sometimes improperly regarded as one set and assigned the same FD coefficient. For example, in **Figure 2D**, the two sets of off-axial grid points labeled with ② and ③ have a different distance to the center, but the assigned FD coefficients are identical. This inappropriate assignment of the FD coefficients makes it too difficult to derive the analytical solution of the FD coefficients.

In the following, we will take M-SFD (N=1) as an example to derive the FD discrete acoustic and elastic wave equation and then derive the analytical expression of FD coefficients.

2.1.1 FD Discrete Acoustic Wave Equation

The 2D stress–velocity acoustic wave equation is given by

$$\frac{\partial P}{\partial t}+\kappa\left(\frac{\partial v_x}{\partial x}+\frac{\partial v_z}{\partial z}\right)=0,\ \frac{\partial v_x}{\partial t}+\frac{1}{\rho}\frac{\partial P}{\partial x}=0,\quad \frac{\partial v_z}{\partial t}+\frac{1}{\rho}\frac{\partial P}{\partial z}=0, \tag{1}$$

where $P=P(x,z,t)$ represents the pressure, $v_x=v_x(x,z,t)$ and $v_z=v_z(x,z,t)$ are the particle velocities, $\rho=\rho(x,z)$ represents the density, and $\kappa=\kappa(x,z)$ is the bulk modulus.

Temporal second-order FD operator to approximate $\partial P/\partial t$ is given by

$$\left.\frac{\partial P}{\partial t}\right|_{1/2,1/2}^{1/2} \approx \frac{P_{1/2,1/2}^{1} - P_{1/2,1/2}^{0}}{\Delta t}, \tag{2}$$

where $P_{m-1/2,n-1/2}^{j} = P[x + (m-1/2)h, z + (n-1/2)h, j\Delta t]$, and h and Δt represent the grid size and time step, respectively. The spatial FD operator of M-SFD (N=1) shown in **Figure 2B** to approximate $\partial v_x/\partial x$ and $\partial v_z/\partial z$ is

$$\begin{aligned}
\left.\frac{\partial v_x}{\partial x}\right|_{1/2,1/2}^{1/2} &\approx \frac{1}{h}\left\{\sum_{m=1}^{M} a_m\left[v_{x(m,1/2)}^{1/2} - v_{x(-m+1,1/2)}^{1/2}\right] + b_1\left[v_{x(1,3/2)}^{1/2} - v_{x(0,3/2)}^{1/2} + v_{x(1,-1/2)}^{1/2} - v_{x(0,-1/2)}^{1/2}\right]\right\},\\
\left.\frac{\partial v_z}{\partial z}\right|_{1/2,1/2}^{1/2} &\approx \frac{1}{h}\left\{\sum_{m=1}^{M} a_m\left[v_{z(1/2,m)}^{1/2} - v_{z(1/2,-m+1)}^{1/2}\right] + b_1\left[v_{z(3/2,1)}^{1/2} - v_{z(3/2,0)}^{1/2} + v_{z(-1/2,1)}^{1/2} - v_{z(-1/2,0)}^{1/2}\right]\right\},
\end{aligned} \tag{3}$$

where $a_1, a_2, \ldots, a_M; b_1$ are the FD coefficients, $v_{x(m,n-1/2)}^{j-1/2} = v_x[x + mh, z + (n-1/2)h, t + (j-1/2)\Delta t]$, and $v_{z(m-1/2,n)}^{j-1/2} = v_z[x + (m-1/2)h, z + nh, t + (j-1/2)\Delta t]$.

Similarly, we can get the FD expressions of $\partial v_x/\partial t, \partial P/\partial x, \partial v_z/\partial t$ and $\partial P/\partial z$. Substituting the FD expressions into **Eq. 1**, we have

$$\begin{aligned}
\frac{P_{1,2,1/2}^{1} - P_{1,2,1/2}^{0}}{\Delta t} &\approx -\frac{\kappa}{h}\left\{\sum_{m=1}^{M} a_m\left[v_{x(m,1/2)}^{1/2} - v_{x(-m+1,1/2)}^{1/2}\right] + b_1\left[v_{x(1,3/2)}^{1/2} - v_{x(0,3/2)}^{1/2} + v_{x(1,-1/2)}^{1/2} - v_{x(0,-1/2)}^{1/2}\right]\right\}\\
&\quad -\frac{\kappa}{h}\left\{\sum_{m=1}^{M} a_m\left[v_{z(1/2,m)}^{1/2} - v_{z(1/2,-m+1)}^{1/2}\right] + b_1\left[v_{z(3/2,1)}^{1/2} - v_{z(3/2,0)}^{1/2} + v_{z(-1/2,1)}^{1/2} - v_{z(-1/2,0)}^{1/2}\right]\right\},\\
\frac{v_{x(0,1/2)}^{1/2} - v_{x(0,1/2)}^{-1/2}}{\Delta t} &\approx -\frac{1}{\rho h}\left\{\sum_{m=1}^{M} a_m\left(P_{m-1/2,1/2}^{0} - P_{-m+1/2,1/2}^{0}\right) + b_1\left[P_{1/2,3/2}^{0} - P_{-1/2,3/2}^{0} + P_{1/2,-1/2}^{0} - P_{-1/2,-1/2}^{0}\right]\right\},\\
\frac{v_{z(1/2,0)}^{1/2} - v_{z(1/2,0)}^{-1/2}}{\Delta t} &\approx -\frac{1}{\rho h}\left\{\sum_{m=1}^{M} a_m\left(P_{1/2,m-1/2}^{0} - P_{1/2,-m+1/2}^{0}\right) + b_1\left[P_{3/2,1/2}^{0} - P_{3/2,-1/2}^{0} + P_{-1/2,1/2}^{0} - P_{-1/2,-1/2}^{0}\right]\right\},
\end{aligned} \tag{4}$$

Equation 4 is the FD discrete acoustic wave equation given by M-SFD (N=1). Similarly, the FD discrete acoustic wave equation given by M-SFD (N=2,3,4) can be derived.

2.1.2 FD Discrete Elastic Wave Equation

The 2D stress–velocity elastic wave equation is given by

$$\begin{aligned}
\frac{\partial v_x}{\partial t} &= \frac{1}{\rho}\left(\frac{\partial \tau_{xx}}{\partial x} + \frac{\partial \tau_{xz}}{\partial z}\right), \quad \frac{\partial v_z}{\partial t} = \frac{1}{\rho}\left(\frac{\partial \tau_{xz}}{\partial x} + \frac{\partial \tau_{zz}}{\partial z}\right),\\
\frac{\partial \tau_{xx}}{\partial t} &= (\lambda + 2\mu)\frac{\partial v_x}{\partial x} + \lambda\frac{\partial v_z}{\partial z}, \qquad \frac{\partial \tau_{zz}}{\partial t} = \lambda\frac{\partial v_x}{\partial x}\\
&\quad + (\lambda + 2\mu)\frac{\partial v_z}{\partial z}, \qquad \frac{\partial \tau_{xz}}{\partial t} = \mu\left(\frac{\partial v_x}{\partial z} + \frac{\partial v_z}{\partial x}\right),
\end{aligned} \tag{5}$$

where $v_x = v_x(x,z,t)$ and $v_z = v_z(x,z,t)$ are the particle velocities, $\tau_{xx} = \tau_{xx}(x,z,t)$, $\tau_{zz} = \tau_{zz}(x,z,t)$ and $\tau_{xz} = \tau_{xz}(x,z,t)$ are the stress components, $\lambda = \lambda(x,z)$ and $\mu = \mu(x,z)$ are the Lamé constants, and $\rho = \rho(x,z)$ is the density.

Similar to the derivation process of the FD discrete acoustic wave equation, the FD discrete elastic wave equation given by M-SFD (N=1) can be derived. Here, we only gave one of the five FD equations:

$$\begin{aligned}
\frac{v_{x(0,0)}^{1} - v_{x(0,0)}^{0}}{\Delta t} &\approx \frac{1}{\rho h}\sum_{m=1}^{M} a_m\left[\left(\tau_{xx(m-1/2,0)}^{1/2} - \tau_{xx(-m+1/2,0)}^{1/2}\right) + \left(\tau_{xz(0,m-1/2)}^{1/2} - \tau_{xz(0,-m+1/2)}^{1/2}\right)\right]\\
&\quad + \frac{b_1}{\rho h}\left[\begin{array}{l}\left(\tau_{xx(1/2,1)}^{1/2} - \tau_{xx(-1/2,1)}^{1/2}\right) + \left(\tau_{xx(1/2,-1)}^{1/2} - \tau_{xx(-1/2,-1)}^{1/2}\right) +\\ \left(\tau_{xz(1,1/2)}^{1/2} - \tau_{xz(1,-1/2)}^{1/2}\right) + \left(\tau_{xz(-1,1/2)}^{1/2} - \tau_{xz(-1,-1/2)}^{1/2}\right)\end{array}\right],
\end{aligned} \tag{6}$$

TABLE 1 | Number of the off-axial grid points required by our M-SFD and the previous M-SFD to make the FD discrete acoustic wave equation reach specified order accuracy.

FD accuracy	Number of the off-axial grid points	
	Our M-SFD	M-SFD proposed by Tan and Huang (2014) and Ren and Li (2017)
4th-order	4	4
6th-order	8	12
8th-order	16	24

where $a_1, a_2, \ldots, a_M; b_1$ are the FD coefficients.

Using the same method, the FD discrete elastic wave equation given by M-SFD (N=2,3,4) can be derived.

2.2 FD Coefficient Calculation

2.2.1 FD Coefficient Calculation for the FD Discrete Acoustic Wave Equation

In a homogeneous medium, **Eq. 1** has the following discrete plane wave solution

$$\begin{aligned}
P_{m-1/2,n-1/2}^{j} &= A_P e^{i\left[k_x(x+(m-1/2)h) + k_z(z+(n-1/2)h) - \omega\left(t+j\Delta t\right)\right]},\\
v_{x(m,n-1/2)}^{j-1/2} &= A_{v_x} e^{i\left[k_x(x+mh) + k_z(z+(n-1/2)h) - \omega\left(t+\left(j-1/2\right)\Delta t\right)\right]},\\
v_{z(m-1/2,n)}^{j-1/2} &= A_{v_z} e^{i\left[k_x(x+(m-1/2)h) + k_z(z+nh) - \omega\left(t+\left(j-1/2\right)\Delta t\right)\right]},\\
k_x &= k\cos\theta, \quad k_z = k\sin\theta,
\end{aligned} \tag{7}$$

where A_P, A_{v_x}, and A_{v_z} are the plane wave amplitude factors, k is the wavenumber, ω is the angular frequency, and θ is the propagation angle.

Substituting **Eq. 7** into **Eq. 4**, we can get

$$\begin{aligned}
\frac{A_P}{\Delta t}\sin\left(\frac{\omega\Delta t}{2}\right) &\approx -\frac{\kappa A_{v_x}}{h}\left\{\sum_{m=1}^{M} a_m \sin[(m-1/2)k_x h] + 2b_1\cos(k_z h)\sin\left(\frac{k_x h}{2}\right)\right\}\\
&\quad -\frac{\kappa A_{v_z}}{h}\left\{\sum_{m=1}^{M} a_m \sin[(m-1/2)k_z h] + 2b_1\cos(k_x h)\sin\left(\frac{k_z h}{2}\right)\right\},\\
\frac{A_{v_x}}{\Delta t}\sin\left(\frac{\omega\Delta t}{2}\right) &\approx \frac{A_P}{\rho h}\left\{\sum_{m=1}^{M} a_m \sin[(m-1/2)k_x h] + 2b_1\cos(k_z h)\sin\left(\frac{k_x h}{2}\right)\right\},\\
\frac{A_{v_z}}{\Delta t}\sin\left(\frac{\omega\Delta t}{2}\right) &\approx \frac{A_P}{\rho h}\left\{\sum_{m=1}^{M} a_m \sin[(m-1/2)k_z h] + 2b_1\cos(k_x h)\sin\left(\frac{k_z h}{2}\right)\right\}.
\end{aligned} \tag{8}$$

By eliminating A_P, A_{v_x}, and A_{v_z} and considering $\omega = vk$ and $\kappa = \rho v^2$, we obtain

$$\begin{aligned}
\frac{1}{(v\Delta t)^2}\sin\left(\frac{rkh}{2}\right) &\approx \frac{1}{h^2}\left\{\sum_{m=1}^{M} a_m \sin[(m-1/2)k_x h] + 2b_1\cos(k_z h)\sin\left(\frac{k_x h}{2}\right)\right\}^2\\
&\quad + \frac{1}{h^2}\left\{\sum_{m=1}^{M} a_m \sin[(m-1/2)k_z h] + 2b_1\cos(k_x h)\sin\left(\frac{k_z h}{2}\right)\right\}^2,
\end{aligned} \tag{9}$$

where v represents wave velocity, and $r = v\Delta t/h$ is the Courant number.

Equation 9 represents the dispersion relation of the FD discrete acoustic wave equation given by M-SFD (N=1), and it is also named as a time-space domain dispersion relation.

Taking the Taylor series expansion for cosine and sine functions in **Eq. 9**, we have

$$\left\{\sum_{j=0}^{\infty}c_j\beta_j(k_x/2)^{2j+1}h^{2j}+2b_1\left[\sum_{j=0}^{\infty}\beta_j(k_x/2)^{2j+1}h^{2j}\right]\cdot\left[\sum_{j=1}^{\infty}\gamma_j k_z^{2j}h^{2j}\right]\right\}^2$$
$$+\left\{\sum_{j=0}^{\infty}c_j\beta_j(k_z/2)^{2j+1}h^{2j}+2b_1\left[\sum_{j=0}^{\infty}\beta_j(k_z/2)^{2j+1}h^{2j}\right]\cdot\left[\sum_{j=1}^{\infty}\gamma_j k_x^{2j}h^{2j}\right]\right\}^2$$
$$\approx\left[\sum_{j=0}^{\infty}r^{2j}\beta_j(k/2)^{2j+1}h^{2j}\right]^2, \tag{10}$$

where the expressions of c_j, β_j and γ_j are

$$c_j=\sum_{m=1}^{M}(2m-1)^{2j+1}a_m+2b_1,\quad \beta_j=\frac{(-1)^j}{(2j+1)!},\quad \gamma_j=\frac{(-1)^j}{(2j)!}. \tag{11}$$

Comparing the coefficients of $k_x^2k_z^2h^2$ on both sides of **Eq. 11**, we obtain

$$c_0b_1=\frac{r^2}{24}. \tag{12}$$

Comparing the coefficients of $k_x^{2j+2}h^{2j}\,(j=0,1,2,\ldots,M-1)$ on both sides of **Eq. 11**, we obtain

$$\begin{aligned}&c_0^2=1\quad(j=0),\\ &\sum_{p=0}^{j}c_pc_{j-p}\beta_p\beta_{j-p}=\sum_{p=0}^{j}\beta_p\beta_{j-p}r^{2j}\quad(j=1,2,\cdots,M-1).\end{aligned} \tag{13}$$

Equation 13 gives $c_0=\pm1$, when c_0 changes from 1 to -1, the FD coefficients $a_1,a_2,\ldots,a_M;b_1$ will become their opposite number, which doesn't affect the final result. Therefore, we let $c_0=1$. Then, we can obtain

$$c_j=r^{2j}\quad(j=0,1,\cdots,M-1). \tag{14}$$

Substituting **Eq. 14** into **Eq. 11**, we have

$$\sum_{m=1}^{M}(2m-1)^{2j+1}a_m+2b_1=r^{2j}\quad(j=0,1,\cdots,M-1). \tag{15}$$

Rewriting **Eq. 15** into a matrix equation, we have

$$\begin{bmatrix}1&1&1&\cdots&1\\1^2&3^2&5^2&\cdots&(2M-1)^2\\1^4&3^4&5^4&\cdots&(2M-1)^4\\\vdots&\vdots&\vdots&\ddots&\vdots\\1^{2M-2}&3^{2M-2}&5^{2M-2}&\cdots&(2M-1)^{2M-2}\end{bmatrix}\begin{bmatrix}a_1+2b_1\\3a_2\\5a_3\\\vdots\\(2M-1)a_M\end{bmatrix}=\begin{bmatrix}1\\r^2\\r^4\\\vdots\\r^{2M-2}\end{bmatrix}. \tag{16}$$

Equation 16 is a type of Vandermonde matrix equation.

Combining $c_0=1$ and **Eq. 12**, we get $b_1=r^2/24$. Then, by solving **Eq. 16**, we obtain

$$b_1=\frac{r^2}{24},\quad a_1=\prod_{2\le k\le M}\left[\frac{r^2-(2k-1)^2}{1-(2k-1)^2}\right]-\frac{r^2}{12},$$
$$a_m=\frac{1}{2m-1}\prod_{1\le k\le M,k\ne m}\frac{r^2-(2k-1)^2}{(2m-1)^2-(2k-1)^2}\quad(m=2,3,\cdots,M). \tag{17}$$

Equation 17 gives the analytical expression of the FD coefficients for M-SFD (N=1). Analogously, the analytical expression for M-SFD, with N taking any positive integer value, can be derived as well. The analytical expressions of the FD coefficients for M-SFD (N=2,3,4) are given in the Appendix.

2.2.2 FD Coefficient Calculation for the FD Discrete Elastic Wave Equation

Similar to the derivation of the dispersion relation of the FD discrete acoustic wave equation, substituting the discrete plane wave solution into the FD discrete elastic wave equation and eliminating the amplitude factors, we have

$$\left[\sin^2\left(\frac{\omega\Delta t}{2}\right)-\frac{\lambda+2\mu}{\rho}\left(f_x^2+f_z^2\right)\right]\left[\sin^2\left(\frac{\omega\Delta t}{2}\right)-\frac{\mu}{\rho}\left(f_x^2+f_z^2\right)\right]=0,$$
$$f_x=\frac{\Delta t}{h}\left\{\sum_{m=1}^{M}a_m\sin[(m-1/2)k_xh]+2b_1\cos(k_zh)\sin\left(\frac{k_xh}{2}\right)\right\},$$
$$f_z=\frac{\Delta t}{h}\left\{\sum_{m=1}^{M}a_m\sin[(m-1/2)k_zh]+2b_1\cos(k_xh)\sin\left(\frac{k_zh}{2}\right)\right\}. \tag{18}$$

Equation 18 is the dispersion relation of the FD discrete elastic wave equation given by M-SFD (N=1).

From **Eq. 18**, we can get

$$\frac{1}{(v_p\Delta t)^2}\sin\left(\frac{r_pkh}{2}\right)\approx\frac{1}{h^2}\left\{\sum_{m=1}^{M}a_m\sin[(m-1/2)k_xh]+2b_1\cos(k_zh)\sin\left(\frac{k_xh}{2}\right)\right\}^2$$
$$+\frac{1}{h^2}\left\{\sum_{m=1}^{M}a_m\sin[(m-1/2)k_zh]+2b_1\cos(k_xh)\sin\left(\frac{k_zh}{2}\right)\right\}^2, \tag{19}$$

$$\frac{1}{(v_s\Delta t)^2}\sin\left(\frac{r_skh}{2}\right)\approx\frac{1}{h^2}\left\{\sum_{m=1}^{M}a_m\sin[(m-1/2)k_xh]+2b_1\cos(k_zh)\sin\left(\frac{k_xh}{2}\right)\right\}^2$$
$$+\frac{1}{h^2}\left\{\sum_{m=1}^{M}a_m\sin[(m-1/2)k_zh]+2b_1\cos(k_xh)\sin\left(\frac{k_zh}{2}\right)\right\}^2, \tag{20}$$

where $v_p=\sqrt{(\lambda+2\mu)/\rho}$ and $v_s=\sqrt{\mu/\rho}$ represent the P- and S-wave velocity, respectively, $r_p=v_p\Delta t/h$ and $r_s=v_s\Delta t/h$ are the P- and S-wave Courant numbers.

Eq. 19 and **20** are the P- and S-wave time–space domain dispersion relation. We can see that **Eq. 19** and **20** have the same format with **Eq. 9**, so the FD coefficients in the FD discrete elastic wave equation given by M-SFD (N=1) can be calculated with the same method. Equations about the FD coefficients are established via expanding the trigonometric functions in **Eq. 19** with the Taylor series. Solving the equations, we can get

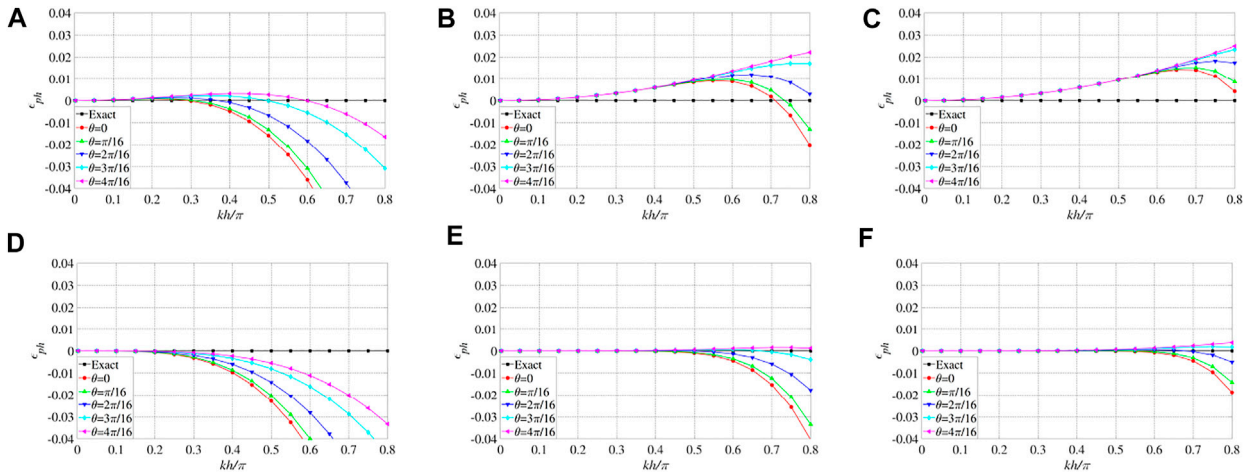

FIGURE 3 | Phase velocity dispersion curves of the acoustic staggered-grid FD schemes with r = 0.3. **(A–C)** C-SFD (M=2, 5, and 8); **(D–F)** M-SFD (M=2, 5, and 8; N=1).

$$b_1(r_p) = \frac{r_p^2}{24}, \quad a_1(r_p) = \prod_{2\le k\le M}\left[\frac{r_p^2-(2k-1)^2}{1-(2k-1)^2}\right] - \frac{r_p^2}{12},$$
$$a_m(r_p) = \frac{1}{2m-1}\prod_{1\le k\le M, k\ne m}\frac{r_p^2-(2k-1)^2}{(2m-1)^2-(2k-1)^2} \quad (m=2,3,\cdots,M). \tag{21}$$

Equation 21 is one of the analytical expressions of the FD coefficients in the FD discrete elastic wave equation given by M-SFD (N=1), and the other analytical expression can be obtained by substituting r_p with r_s, which is based on the S-wave time-space domain dispersion relation. Using the same method, the analytical solutions of the FD coefficients in the discrete elastic wave equations given by M-SFD (N=2,3,4) can be worked out. They are similar to the analytical solutions of the FD coefficients in discrete acoustic wave equation given in the Appendix, just substituting r with r_p or r_s.

For simulation of the elastic wave equation, the FD coefficients calculated based on the P-wave time-space domain dispersion relation ensure high modeling accuracy of P-wave, whereas the accuracy of S-wave is relatively low. On the contrary, the FD coefficients calculated from the S-wave time-space domain dispersion relation ensure high modeling accuracy of S-wave, but the accuracy of P-wave is relatively low.

2.3 Accuracy Analysis of the FD Discrete Wave Equation

According to **Eq. 9**, we can define the error function $E_{M-SFD(N=1)}$ of the dispersion relation as

$$E_{M-SFD(N=1)} = \frac{1}{h^2}\left\{\sum_{m=1}^{M} a_m \sin[(m-1/2)k_x h] + 2b_1\cos(k_z h)\sin\left(\frac{k_x h}{2}\right)\right\}^2 + \frac{1}{h^2}\left\{\sum_{m=1}^{M} a_m \sin[(m-1/2)k_z h] + 2b_1\cos(k_x h)\sin\left(\frac{k_z h}{2}\right)\right\}^2 - \frac{1}{(v\Delta t)^2}\sin\left(\frac{rkh}{2}\right). \tag{22}$$

Using **Eqs. 10–13**, **Eq. 22** can be rewritten as

$$E_{M-SFD(N=1)} = \sum_{j=M}^{\infty}\sum_{p=0}^{j}\left(c_p c_{j-p} - r^{2j}\right)\beta_p\beta_{j-p}\frac{1}{2^{2j+2}}\left(k_x^{2j+2}+k_z^{2j+2}\right)h^{2j} + \sum_{j=2}^{\infty}\sum_{p=0}^{j-1}\left[\frac{4b_1\gamma_{j-p}}{2^{2p+2}}\sum_{q=0}^{p}\left(c_q\beta_q\beta_{p-q}\right) + \frac{4b_1\gamma_{p+1}}{2^{2(j-p)}}\sum_{q=0}^{j-p-1}\left(c_q\beta_q\beta_{j-p-1-q}\right)\right]k_x^{2p+2}k_z^{2(j-p)}h^{2j} - \sum_{j=2}^{\infty}\sum_{p=0}^{j-1}\left[\frac{r^{2j}C_{j+1}^{p+1}}{2^{2j+2}}\sum_{q=0}^{j}\left(\beta_q\beta_{j-q}\right)\right]k_x^{2p+2}k_z^{2(j-p)}h^{2j}, \tag{23}$$

where $C_{j+1}^{p+1} = \frac{(j+1)!}{(p+1)!(j-p)!}$ is the number of combinations, and the expressions of c_j, β_j, and γ_j are given by **Eq. 11**.

Equation 23 shows that the minimum power of h in the error function $E_{M-SFD(N=1)}$ is 4, so the FD discrete acoustic wave equation given by M-SFD (N=1) can reach fourth-order accuracy. Similarly, we can demonstrate that the discrete acoustic wave equation given by M-SFD can reach sixth, sixth, and eighth-order accuracy when N takes 2, 3, and 4. Theoretically, arbitrary even-order accuracy can be reached by increasing the value of N. The FD discrete acoustic wave equations given by C-SFD has only second-order accuracy, so M-SFD can improve the modeling accuracy more effectively.

For elastic wave simulation with M-SFD (N=1,2,3,4), with the FD coefficients calculated based on the P-wave time-space domain dispersion relation, the P-wave can reach fourth, sixth, sixth, and eighth-order accuracy respectively, but the accuracy of S-wave remains second-order. On the contrary, with the FD coefficients calculated from the S-wave time–space domain dispersion relation, the S-wave can reach fourth, sixth, sixth, and eighth-order accuracy, but the accuracy of the P-wave remains second-order.

Table 1 lists the number of off-axial grid points required by our M-SFD and the previous M-SFD (Tan and Huang, 2014; Ren and Li, 2017) to make the FD discrete acoustic wave equations

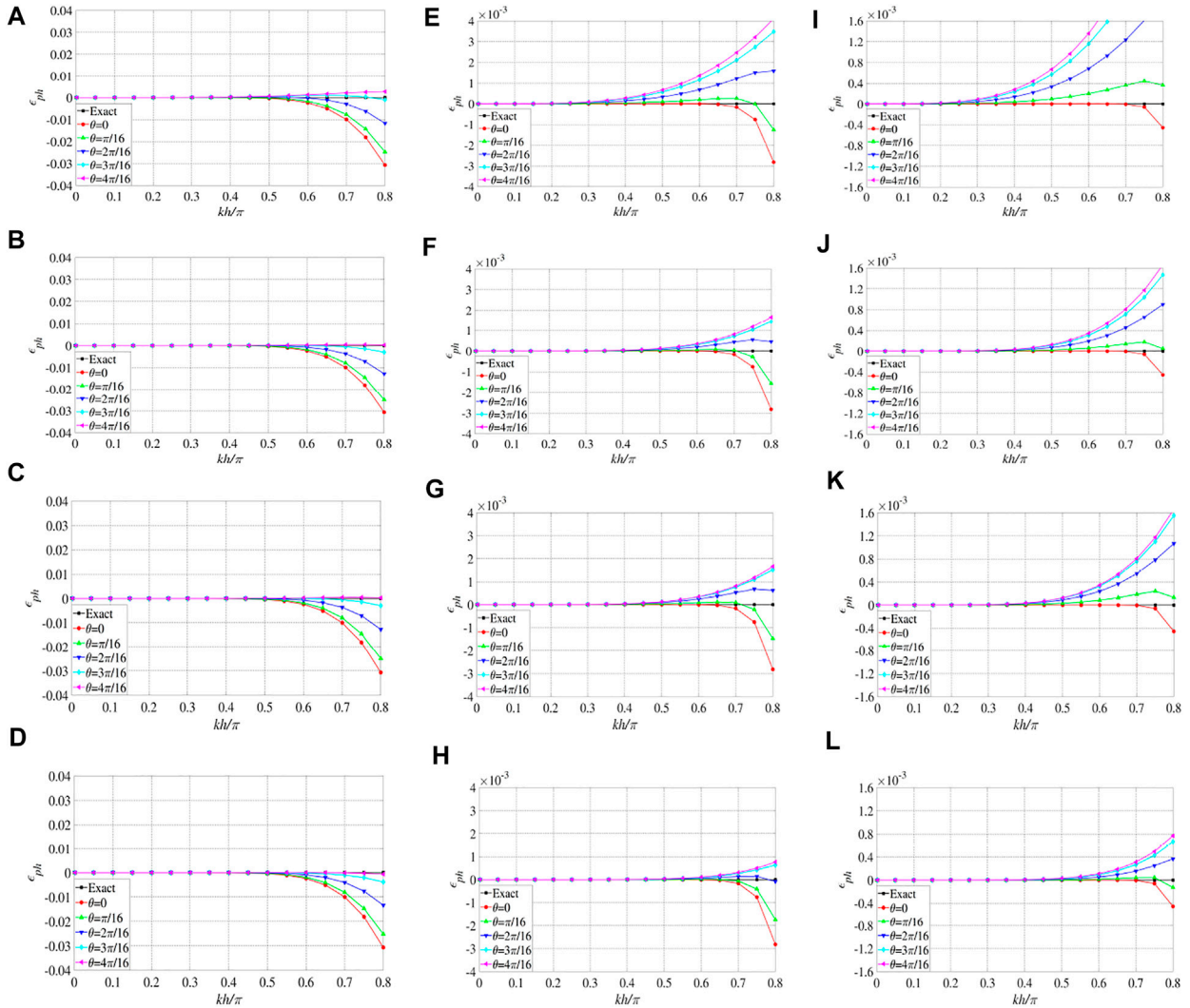

FIGURE 4 | Phase velocity dispersion curves of the acoustic staggered-grid FD schemes with r = 0.3. **(A–D)** M-SFD (M=6; N=1, 2, 3, and 4), **(E–H)** M-SFD (M=18; N=1, 2, 3, and 4), **(I–L)** M-SFD (M=30; N=1, 2, 3, and 4).

reach fourth, sixth, and eighth-order accuracy. We can find that our M-SFD usually needs fewer off-axial grid points than that of the previous M-SFD, to achieve the same order accuracy, which enables our M-SFD to be more efficient.

3 ELASTIC WAVE MODELING STRATEGY WITH HIGH ACCURACY

For elastic wave simulation with M-SFD, the FD coefficients calculated with P- or S-wave time–space domain dispersion relation can only ensure the P- or S-wave to achieve high modeling accuracy respectively. In order to improve the modeling accuracy of P- and S-wave simultaneously, the elastic wave **Equation 5** can be decomposed as (Li et al., 2007)

$$v_x = v_x^P + v_x^S, \quad v_z = v_z^P + v_z^S, \tag{24}$$

$$\frac{\partial v_x^P}{\partial t} = \frac{1}{\rho}\frac{\partial \tau_{xx}^P}{\partial x}, \quad \frac{\partial v_z^P}{\partial t} = \frac{1}{\rho}\frac{\partial \tau_{zz}^P}{\partial z},$$
$$\frac{\partial \tau_{xx}^P}{\partial t} = (\lambda + 2\mu)\left(\frac{\partial v_x}{\partial x} + \frac{\partial v_z}{\partial z}\right), \quad \frac{\partial \tau_{zz}^P}{\partial t} = (\lambda + 2\mu)\left(\frac{\partial v_x}{\partial x} + \frac{\partial v_z}{\partial z}\right), \tag{25}$$

$$\frac{\partial v_x^S}{\partial t} = \frac{1}{\rho}\left(\frac{\partial \tau_{xx}^S}{\partial x} + \frac{\partial \tau_{xz}^S}{\partial z}\right), \quad \frac{\partial v_z^S}{\partial t} = \frac{1}{\rho}\left(\frac{\partial \tau_{xz}^S}{\partial x} + \frac{\partial \tau_{zz}^S}{\partial z}\right),$$
$$\frac{\partial \tau_{xx}^S}{\partial t} = -2\mu\frac{\partial v_z}{\partial z}, \quad \frac{\partial \tau_{zz}^S}{\partial t} = -2\mu\frac{\partial v_x}{\partial x}, \quad \frac{\partial \tau_{xz}^S}{\partial t} = \mu\left(\frac{\partial v_x}{\partial z} + \frac{\partial v_z}{\partial x}\right). \tag{26}$$

The workflow to solve the decomposed elastic wave equations with M-SFD is as follows: ① the FD discrete equations for the decomposed P-wave (**equation 25**) and S-wave (**Equation 26**) with M-SFD are derived. ② The discrete P-wave equation is

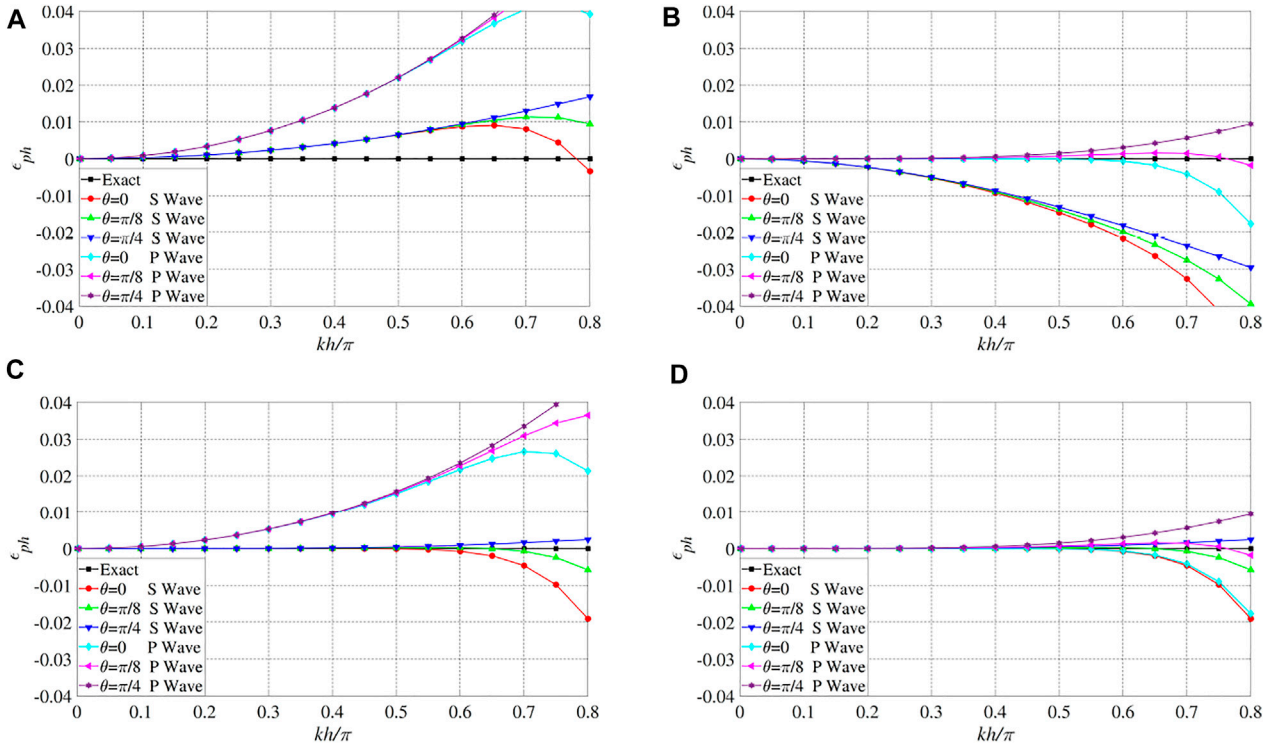

FIGURE 5 | P-wave and S-wave phase velocity dispersion curves of the elastic staggered-grid FD schemes with r_p = 0.45 and r_s = 0.25. **(A)** C-SFD (*M*=8) and **(B)** M-SFD (*M*=8; *N*=1) with the FD coefficients calculated based on the P-wave time–space domain dispersion relation. **(C)** M-SFD (*M*=8; *N*=1) with the FD coefficients calculated based on the S-wave time–space domain dispersion relation. **(D)** M-SFD (*M*=8; *N*=1), the P-wave, and S-wave phase velocity dispersion curves are plotted with the FD coefficients calculated based on the P-wave and S-wave time–space domain relation, respectively.

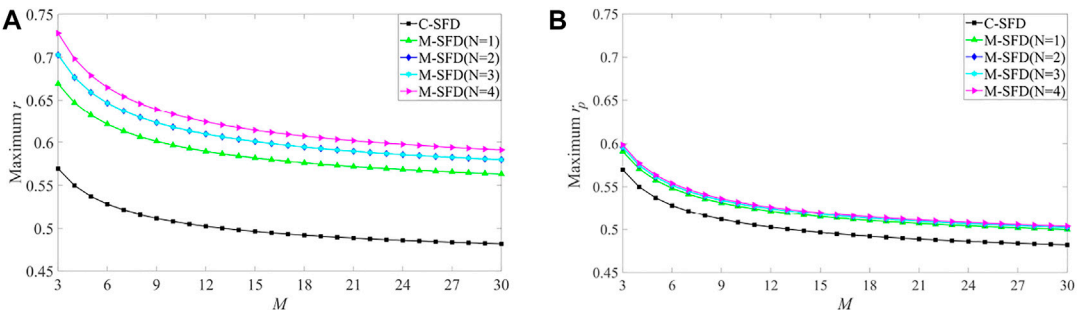

FIGURE 6 | Stability curves of the FD discrete **(A)** acoustic wave and **(B)** elastic wave equation given by C-SFD and M-SFD (*N*=1, 2, 3, and 4). In **(B)**, the FD coefficients are calculated with the S-wave time–space domain dispersion relation for M-SFD (*N*=1, 2, 3, and 4).

solved with the FD coefficients computed by the P-wave time-space domain dispersion relation. ③ The discrete S-wave equation is solved with FD coefficients computed by the S-wave time-space domain dispersion relation. ④ v_x and v_z are updated at the current moment using **Eq. 24**. ⑤ Steps ②-④ are repeated until the maximum recording time is reached.

According to the aforementioned workflow, the decomposed P- and S-wave equations are solved with the FD coefficients calculated based on the P- and S-wave time-space domain dispersion relation respectively, and then P- and S-wave can reach high modeling accuracy at the same time.

4 DISPERSION AND STABILITY ANALYSES

4.1 Dispersion Analysis

According to **Eq. 9** and the phase velocity formula $v_{ph} = \omega/k$, we define an error function $\varepsilon_{ph}(\theta)$ of normalized phase velocity to

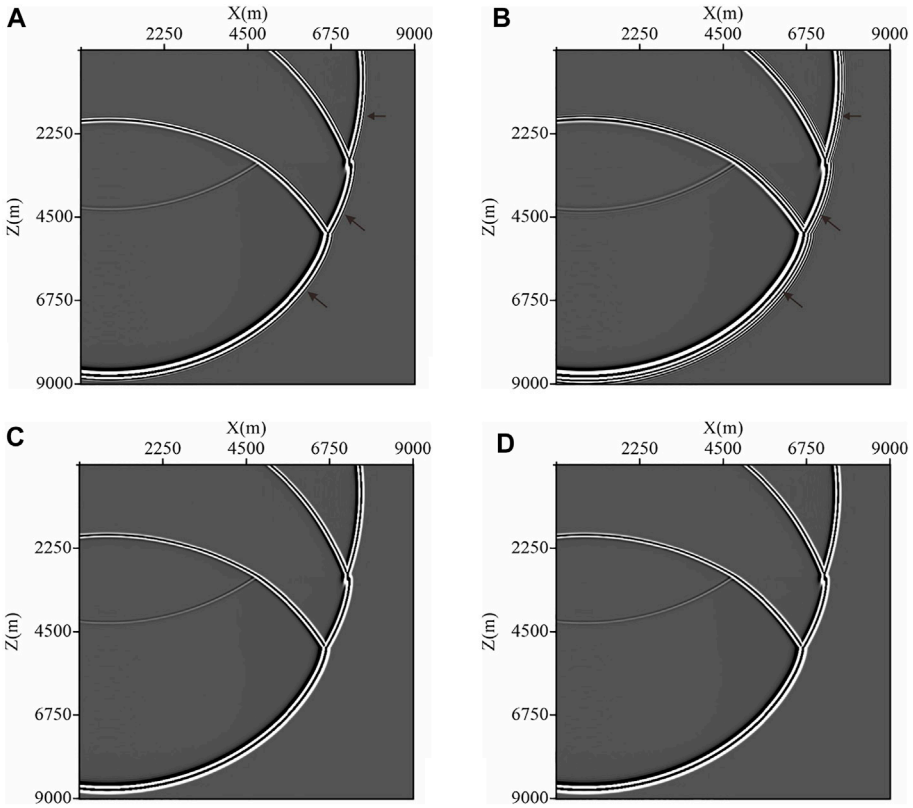

FIGURE 7 | Acoustic snapshots at 3.0s for the three-layered model. **(A,B)** C-SFD (*M*=10) with the time step Δt = 1.0ms and Δt = 1.5ms. **(C) (D)** M-SFD (*M*=8; *N*=1) with time step Δt = 1.0ms and Δt = 1.5ms.

describe numerical dispersion for M-SFD (N=1), and $\varepsilon_{ph}(\theta)$ is given by

$$\varepsilon_{ph}(\theta) = \frac{v_{ph}}{v} - 1 = \frac{2}{rkh}\sin^{-1}\left(r\sqrt{q}\right) - 1,$$

$$q = \left\{\sum_{m=1}^{M} a_m \sin\left[(m-1/2)kh\cos\theta\right] + 2b_1\cos(kh\sin\theta)\sin\left(\frac{kh\cos\theta}{2}\right)\right\}^2 + \left\{\sum_{m=1}^{M} a_m \sin\left[(m-1/2)kh\sin\theta\right] + 2b_1\cos(kh\cos\theta)\sin\left(\frac{kh\sin\theta}{2}\right)\right\}^2. \tag{27}$$

If $\varepsilon_{ph}(\theta)$ equals 1, there is no dispersion, if $\varepsilon_{ph}(\theta)$ is smaller than 1, space dispersion will occur, and if $\varepsilon_{ph}(\theta)$ is larger than 1, time dispersion will occur.

Similarly, we can derive the expressions of $\varepsilon_{ph}(\theta)$ for M-SFD (N=2, 3, and 4). Furthermore, according to the P- and S-wave time-space domain dispersion relation, the expressions of $\varepsilon_{ph}(\theta)$ for P- and S-wave can be derived.

Using the expressions of $\varepsilon_{ph}(\theta)$, we can plot the phase velocity dispersion curves of C-SFD and M-SFD (N=1, 2, 3, and 4) and then analyze the numerical dispersion characteristics.

Figure 3 gives the phase velocity dispersion curves of C-SFD (M=2, 5, 8) and M-SFD (M=2, 5, and 8; N=1) with r = 0.3 for acoustic wave simulation. This figure shows several important phenomena: i) Both C-SFD (M=2) and M-SFD (M=2; N=1) have obvious space dispersion. ii) C-SFD (M=5,8) shows obvious time dispersion, and the dispersion does not decrease as M increases from 5 to 8. iii) The dispersion curves of M-SFD (M=5,8) converge well, and the dispersion decreases further as M increasing from 5 to 8. Based on the analyses we can infer that when M is small (M is about 2), both M-SFD and C-SFD cannot suppress the numerical dispersion well, and when M is large (M is about 8) M-SFD can suppress the numerical dispersion more effectively than C-SFD, to gain higher accuracy for acoustic wave modeling.

Figure 4 gives the phase velocity dispersion curves of M-SFD (M=6, 18, 30; N=1, 2, 3, and 4) with r = 0.3. This figure involves three columns (A-D), (E-H), and (I-L); each column has its own scale on the vertical axis. From this figure, there are some points that deserve to be mentioned: i) When M is 6, the differences in the numerical dispersion of M-SFD (N=1,2,3,4) are negligible. ii) When M is 18, the dispersion curves of M-SFD are of better convergence and display lower numerical dispersion when N varies from one to two; nonetheless, the dispersion characteristics of M-SFD have a high similarity even if N has been increased to four after then. iii) When M is 30, the dispersion curves of M-SFD are of better convergence as N varies from one to two, and further increasing N up to four, the dispersion curves will exhibit much better convergence and even lower numerical dispersion.

From the aforementioned analyses, we can infer that, for acoustic wave simulation with M-SFD, the modeling accuracy

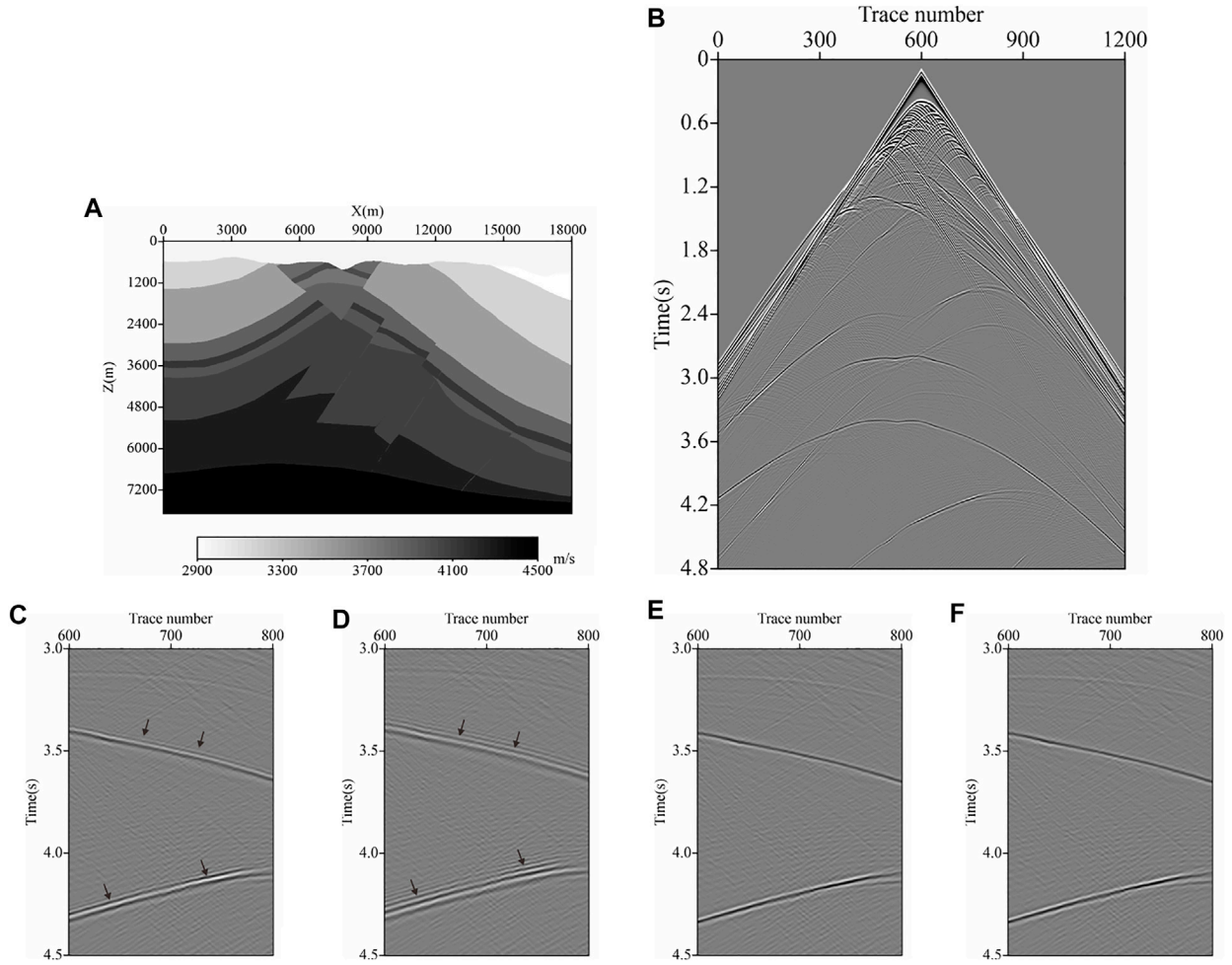

FIGURE 8 | (A) Typical complex structural model of the Tarim Basin in Western China; **(B)** acoustic record modeled by M-SFD (M=8; N=1) with time step Δt = 1.5ms; **(C) (D)** local parts of the acoustic record modeled by C-SFD (M=10) with Δt = 1.0ms and Δt = 1.5ms; **(E,F)** local parts of the acoustic record modeled by M-SFD (M=8; N=1) with Δt = 1.0ms and Δt = 1.5ms.

is relatively high for general usage with N=1 and M being about 6, and the modeling accuracy can meet extremely strict conditions with N=2 and M being about 18. The modeling accuracy further improves with N=4 and M being about 30, but it is not recommended due to very low efficiency. So wave equation modeling with M-SFD can balance modeling accuracy and efficiency by taking proper values for N and M.

We can also find in **Figure 4** that, increasing N from 2 to 3 while M is fixed, the dispersion characteristics of M-SFD are unchanged. This is due to the fact that the FD discrete acoustic wave equations given by M-SFD (N=2,3) are both sixth-order accuracy.

Figure 5 displays the P-wave and S-wave phase velocity dispersion curves of C-SFD (M=8) and M-SFD (M=8; N=1) with r_p = 0.45 and r_s = 0.25. The dispersion curves of M-SFD (M=8;N=1) are plotted with the FD coefficients calculated with different methods. From this figure, four conclusions can be deduced: i) For C-SFD (M=8), both the P-wave and S-wave have obvious time dispersion. ii) For M-SFD (M=8;N=1), with FD coefficients calculated based on P-wave time-space domain dispersion relation, P-wave shows small dispersion but S-wave shows obvious space dispersion, and with FD coefficients calculated based on S-wave time-space domain dispersion relation, S-wave shows small dispersion but P-wave shows obvious time dispersion. iii) For M-SFD (M=8;N=1), with the FD coefficients calculated based on the P- and S-wave time-space domain dispersion relation respectively, the dispersion of both P- and S-wave is small, i.e., solving the decomposed P- and S-wave equation with the FD coefficients calculated based on the P- and S-wave time-space domain dispersion relation respectively can ensure both P- and S-wave to reach high modeling accuracy. iv) Comparing **Figures 5A, C**, the numerical dispersion of both P-wave and S-wave of M-SFD (M=8;N=1) is smaller than that of C-SFD (M=8), when the FD coefficients of M-SFD (M=8;N=1) are calculated based on the S-wave time-space domain dispersion relation.

4.2 Stability Analysis

According to **Eq. 9**, we can get

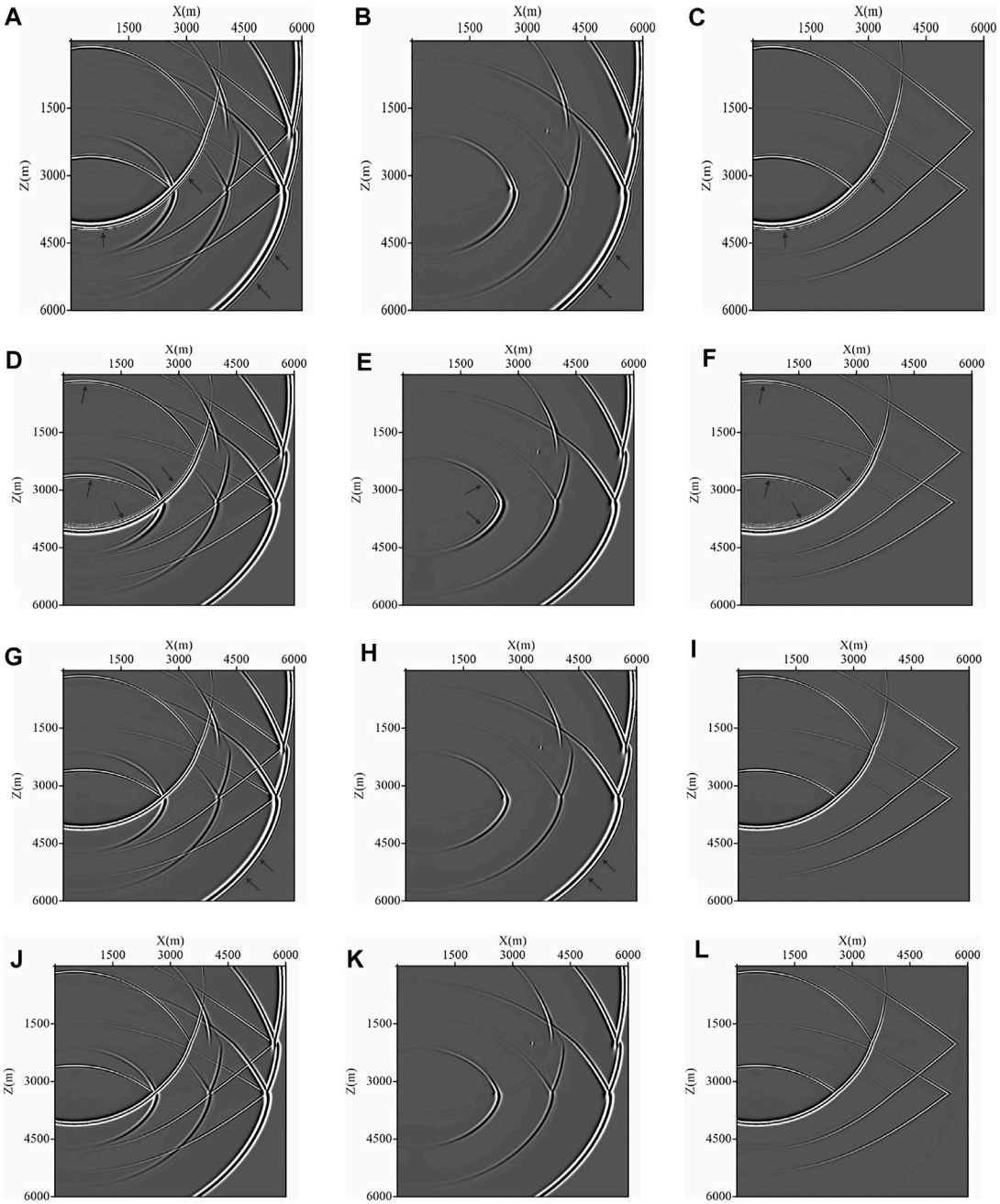

FIGURE 9 | Elastic snapshots of v_x and decomposed P- and S-wave components at 2.4 s for the three-layered model simulated with time step Δt = 1.5ms. **(A–C)** C-SFD (M=10), **(D–F),** and **(G–I)** M-SFD (M=8; N=1) with the FD coefficients calculated based on the P- and S-wave time-space domain dispersion relation, respectively. **(J–L)** M-SFD (M=8; N=1), solving the decomposed P- and S-wave equations.

$$\frac{1}{r^2}\sin\left(\frac{rkh}{2}\right) \approx \left\{\sum_{m=1}^{M} a_m \sin\left[(m-1/2)k_x h\right] + 2b_1 \cos\left(k_z h\right)\sin\left(\frac{k_x h}{2}\right)\right\}^2 + \left\{\sum_{m=1}^{M} a_m \sin\left[(m-1/2)k_z h\right] + 2b_1 \cos\left(k_x h\right)\sin\left(\frac{k_z h}{2}\right)\right\}^2. \tag{28}$$

Letting $k_x = k_z = \pi/h$ and considering $0 \le \sin^2(rkh/2) \le 1$, we have

$$r \le S = \frac{1}{\sqrt{2}\left|\sum_{m=1}^{M}(-1)^{m-1}a_m - 2b_1\right|}, \tag{29}$$

where S is the stability factor.

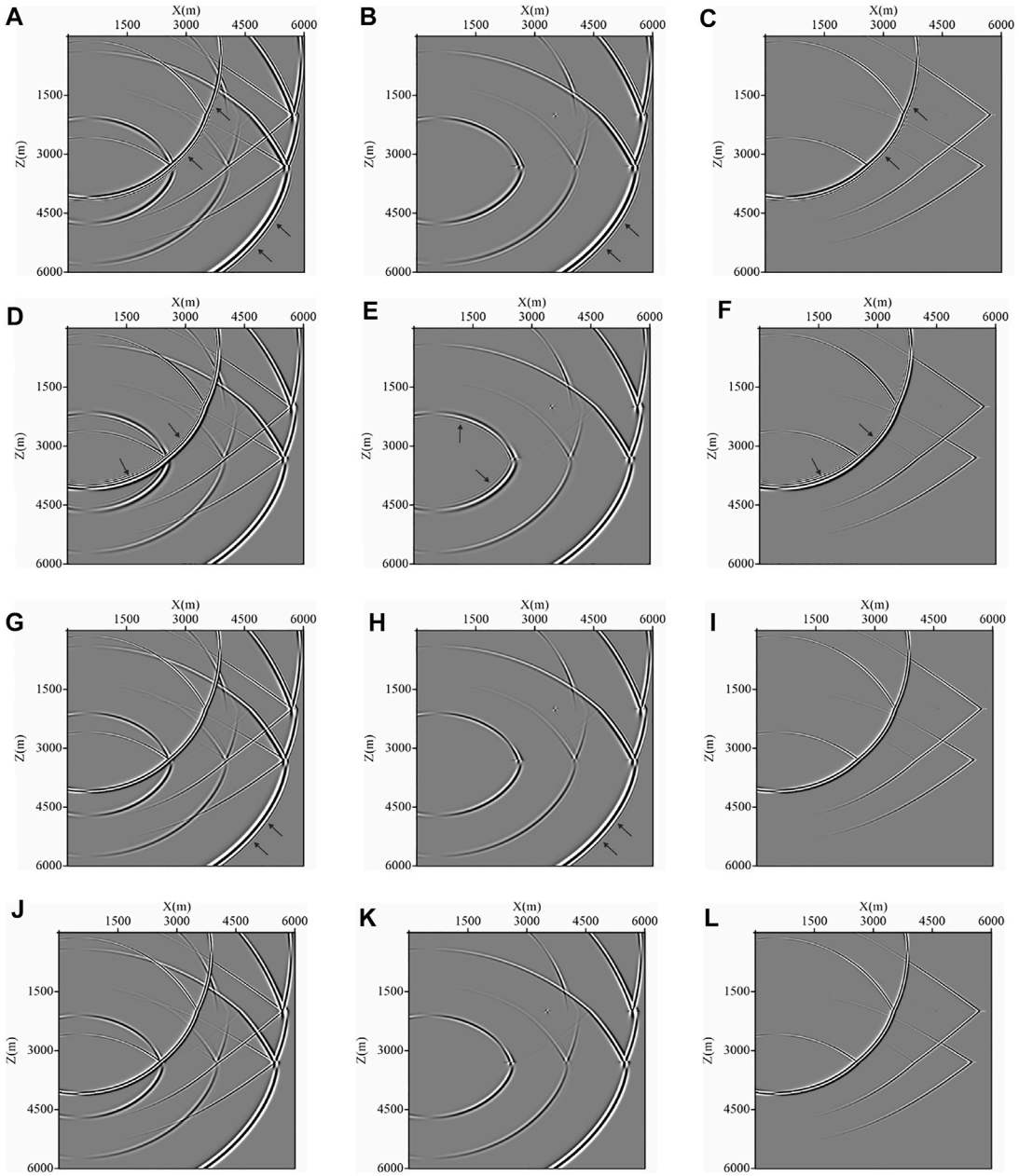

FIGURE 10 | Elastic snapshots of v_z and decomposed P- and S-wave components at 2.4 s for the three-layered model simulated with time step Δt = 1.5ms. **(A–C)** C-SFD (*M*=10), **(D–F),** and **(G–I)** M-SFD (*M*=8; *N*=1) with the FD coefficients calculated based on the P- and S-wave time-space domain dispersion relation, respectively. **(J–L)** M-SFD (*M*=8; *N*=1), solving the decomposed P- and S-wave equations.

Equation 29 represents the stability condition of the FD discrete acoustic wave equation given by M-SFD (*N*=1). Similarly, the stability condition of C-SFD and M-SFD (*N*=2,3,4) can also be derived. Furthermore, we can also derive the P-wave and S-wave stability conditions of C-SFD and M-SFD (*N*=1,2,3,4) in the same way.

Figure 6 displays the curve of maximum r limited by the stability condition with M, which is called the stability curve. **Figure 6A** shows the stability curves of the FD discrete acoustic wave equation given by C-SFD and M-SFD (*N*=1,2,3,4). In most cases $r_p > r_s$, so the stability of the FD discrete elastic wave equation is determined by the P-wave stability. If the FD coefficients are calculated based on the P-wave time-space domain dispersion relation for M-SFD (*N*=1,2,3,4), the P-wave stability curves of C-SFD and M-SFD (*N*=1,2,3,4) are identical to **Figure 6A**. With the FD coefficients calculated based on the S-wave time-space domain dispersion relation for M-SFD (*N*=1,2,3,4), the P-wave stability curves of C-SFD and M-SFD (*N*=1,2,3,4) are shown in **Figure 6B**.

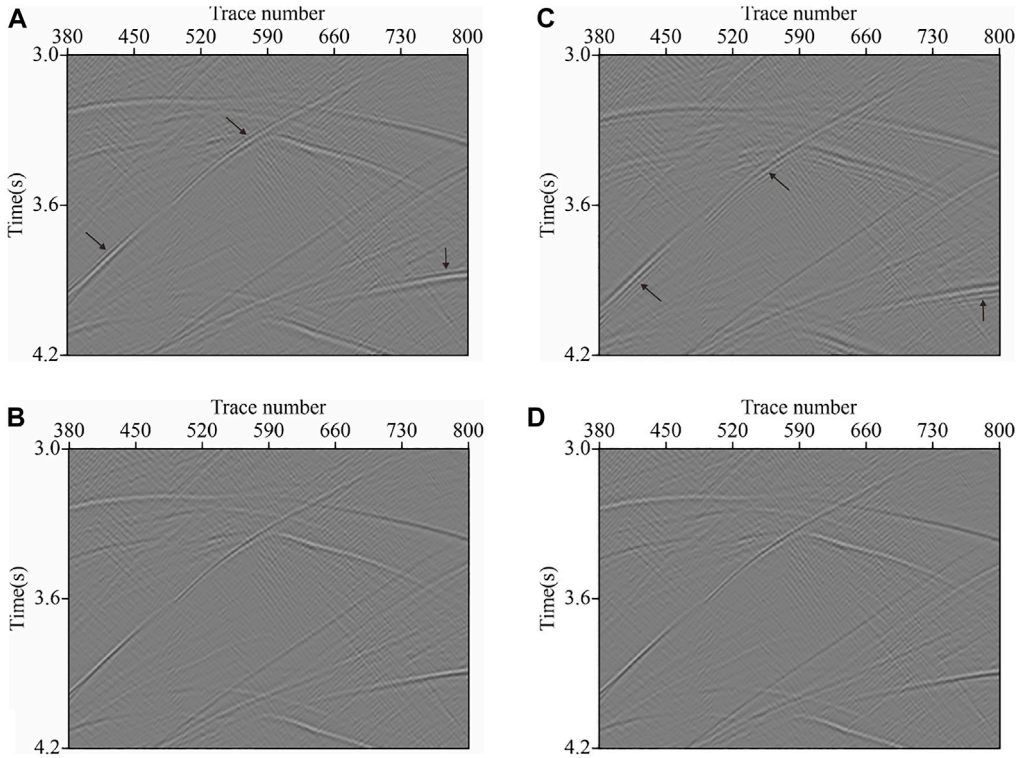

FIGURE 11 | Local parts of the elastic record of the v_z component for the complex structural model simulated with time step Δt = 1.0ms: **(A)** C-SFD (M=10); **(B,C)** M-SFD (M=8; N=1) with the FD coefficients calculated based on the P-wave and S-wave time-space domain dispersion relation, respectively; **(D)** M-SFD (M=8; N=1), solving the decomposed P-wave and S-wave equation.

Figure 6 demonstrates that for acoustic and elastic wave simulation, the stability of M-SFD (N=1,2,3,4) is better than C-SFD. In addition, the stability of M-SFD with N=2 and N=3 is identical. This can be explained by the same order accuracy of the FD discrete wave equations given by M-SFD (N=2,3).

5 NUMERICAL MODELING AND RTM

5.1 Acoustic Wave Modeling

A three-layer model is designed to test our M-SFD method. The horizontal and vertical grid numbers of the model are both 601, with grid size equaling 15 m. The depths of the two reflecting interfaces are 3000 and 4950m, respectively. The acoustic velocities of the three layers are 2400, 2700, and 3200 m/s, respectively. A Ricker wavelet source with a dominant frequency of 20 Hz is located at (750 m, 750 m). Acoustic simulations are performed with C-SFD (M=10) and M-SFD (M=8; N=1), with time step Δt = 1.0ms and Δt = 1.5ms, respectively. **Figure 7** shows the modeling snapshots at 3.0 s.

A complex structure model representative of the Tarim Basin in Western China is shown in **Figure 8A**. The horizontal and vertical grid numbers of the model are 1,201 and 526 respectively, with grid size equaling 15 m. A Ricker wavelet with a dominant frequency of 25 Hz is used as the source, located at (9000 m, 150 m). Acoustic numerical simulations are conducted with C-SFD (M=10) and M-SFD (M=8; N=1), with time step Δt = 1.0ms and Δt = 1.5ms respectively. **Figure 8B** shows a seismic record modeled by M-SFD (M=8; N=1) with Δt = 1.5ms. **Figures 8C–F** give the amplified local parts of the seismic records modeled by C-SFD (M=10) and M-SFD (M=8; N=1) with Δt = 1.0ms and Δt = 1.5ms.

The spatial FD operators of C-SFD (M=10) and M-SFD (M=8; N=1) are both composed of 20 grid points, so the computational amount of one iteration for C-SFD (M=10) and M-SFD (M=8; N=1) is almost the same. Then, C-SFD (M=10) and M-SFD (M=8; N=1) will be almost the same computational efficiency when the same time step is adopted.

Comparing the snapshots in **Figure 7** and the amplified regions of the seismic records in **Figures 8C–F**, we find that slight time dispersion exists in the results simulated by C-SFD (M=10) with time step Δt = 1.0ms. As the time step increasing to Δt = 1.5ms, the time dispersion becomes more serious. However, there is no obvious dispersion in the results modeled by M-SFD (M=8; N=1) with time step Δt = 1.0ms and Δt = 1.5ms. Therefore, M-SFD (M=8; N=1) can suppress the numerical dispersion better than C-SFD (M=10), when the same time step is adopted. That is to say, with almost the same computational efficiency, M-SFD (M=8; N=1) can reach higher modeling accuracy than C-SFD (M=10). Furthermore, we find that M-SFD (M=8; N=1) with Δt = 1.5ms can suppress the numerical dispersion better than

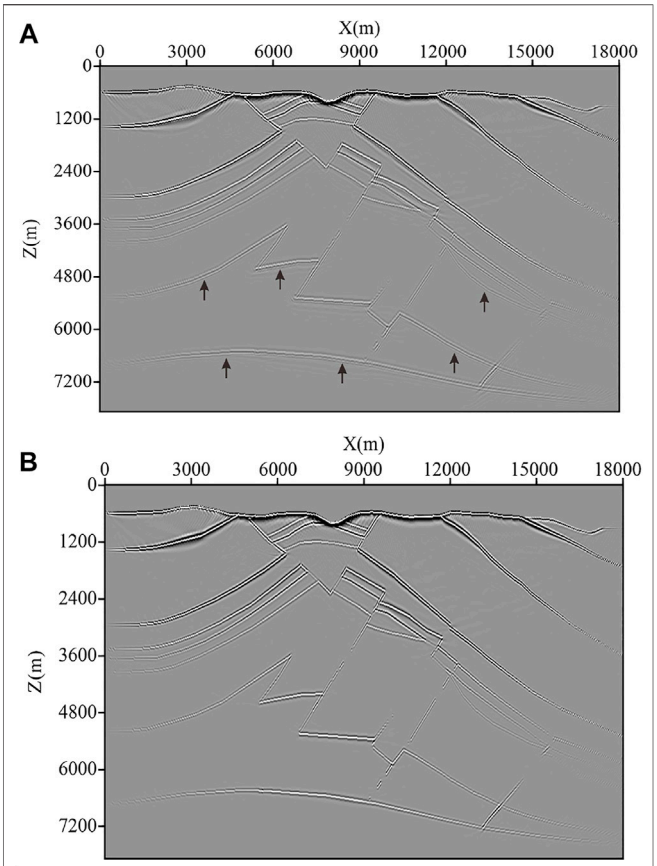

FIGURE 12 | Acoustic wave RTM results with **(A)** C-SFD (*M*=10) and **(B)** M-SFD (*M*=8; N=1) for the typical complex structural model of the Tarim Basin in Western China.

C-SFD (*M*=10) with Δt = 1.0ms, so compared to C-SFD (*M*=10), M-SFD (*M*=8; *N*=1) can take larger time step to reach higher computational efficiency and get higher modeling accuracy at the same time.

5.2 Elastic Wave Modeling

The first elastic wave modeling is carried out on a three-layered model. The horizontal and vertical grid numbers of the model are both 601, with grid size equaling 10 m. The P-wave velocities of the three layers are 2400, 2700, and 3200 m/s, and the S-wave velocities of the three layers are 1500, 1620, and 1800 m/s respectively. The depths of the two reflectors are 2000 and 3300 m. A Ricker wavelet source with a dominant frequency of 20 Hz is located at (500 m, 500 m). **Figures 9**, **10** show the snapshots of the v_x and v_z component at 2.4 s modeled by C-SFD (*M*=10) and M-SFD (*M*=8; *N*=1) with Δt = 1.5ms.

Figures 9, **10** indicate that in the result modeled by C-SFD (*M*=10), both P-wave and S-wave show obvious time dispersion. In the result modeled by M-SFD (*M*=8; *N*=1) with the FD coefficients calculated based on the P-wave time-space domain dispersion relation, P-wave has no obvious numerical dispersion, but obvious space dispersion exists in S-wave. In the result modeled by M-SFD (*M*=8; *N*=1) with the FD coefficients calculated based on the S-wave time-space domain dispersion relation, S-wave has no obvious numerical dispersion, but slight time dispersion exists in P-wave. In the result modeled by M-SFD (*M*=8; *N*=1) with the decomposed P- and S-wave equation, both P- and S-wave have no obvious numerical dispersion.

Based on the aforementioned analyses, we can infer that with almost the same computational efficiency, M-SFD (*M*=8; *N*=1), with the FD coefficients calculated based on the S-wave time-space domain dispersion relation, suppresses the numerical dispersion of both P- and S-wave more effectively to obtain higher modeling accuracy than C-SFD (*M*=10). In addition, solving the decomposed P- and S-wave equations with M-SFD (*M*=8; *N*=1) can further improve the modeling accuracy. But it will increase the amount of computation and the occupation of memory. Calculating The FD coefficients based on the P-wave time-space domain dispersion relation for M-SFD (*M*=8; *N*=1) is not recommended, which causes serious spatial dispersion for S-wave.

The typical complex structural model of the Tarim Basin of Western China is used in the following simulation. The P-wave velocity model is shown in **Figure 8A**. The S-wave velocity is generated by dividing 1.8 by the P-wave velocity. The grid size is changed to 10 m. A Ricker wavelet with a dominant frequency of 20 Hz is used as the source, located at (6000 m, 100 m). **Figure 11A–D** display the amplified regions of the seismic records of the v_z component modeled by C-SFD (*M*=10) and M-SFD (*M*=8; *N*=1) with time step Δt = 1.0ms.

By examining the zoomed region of the seismic records we can see that the seismic record modeled by C-SFD (*M*=10) shows obvious time dispersion. With the FD coefficients calculated based on the P-wave time-space domain dispersion relation, the seismic record modeled by M-SFD (*M*=8; *N*=1) shows some space dispersion. With the FD coefficients calculated based on the S-wave time-space domain dispersion relation, the seismic record modeled by M-SFD (*M*=10; *N*=1) displays no obvious dispersion. The seismic record obtained by solving the decomposed P-wave and S-wave equation with M-SFD (*M*=10; *N*=1) also has no obvious dispersion, but it is of high computational expense and memory occupation.

The aforementioned analyses demonstrate that for elastic wave simulation, with almost the same computational efficiency, M-SFD (*M*=8; *N*=1), with the FD coefficients calculated based on the S-wave time-space domain dispersion relation, can suppress the numerical dispersion more effectively to reach higher modeling accuracy than C-SFD (*M*=10).

5.3 Acoustic RTM

We further extend M-SFD to acoustic wave RTM and then perform an RTM test on the complex structure model in **Figure 8A**. The source wavelet is a Ricker wavelet with a dominant frequency of 25 Hz. And 150 shot gathers without numerical dispersion are modeled by C-SFD (*M*=15) with a very small time stepΔt = 0.1ms, which is used as the input gathers for RTM. Each shot gathered has 600 traces. The source interval is 120 m and the trace interval is 30 m.

We use C-SFD (*M*=10) and M-SFD (*M*=8; *N*=1) as the wavefield propagation operator of the RTM with the time step

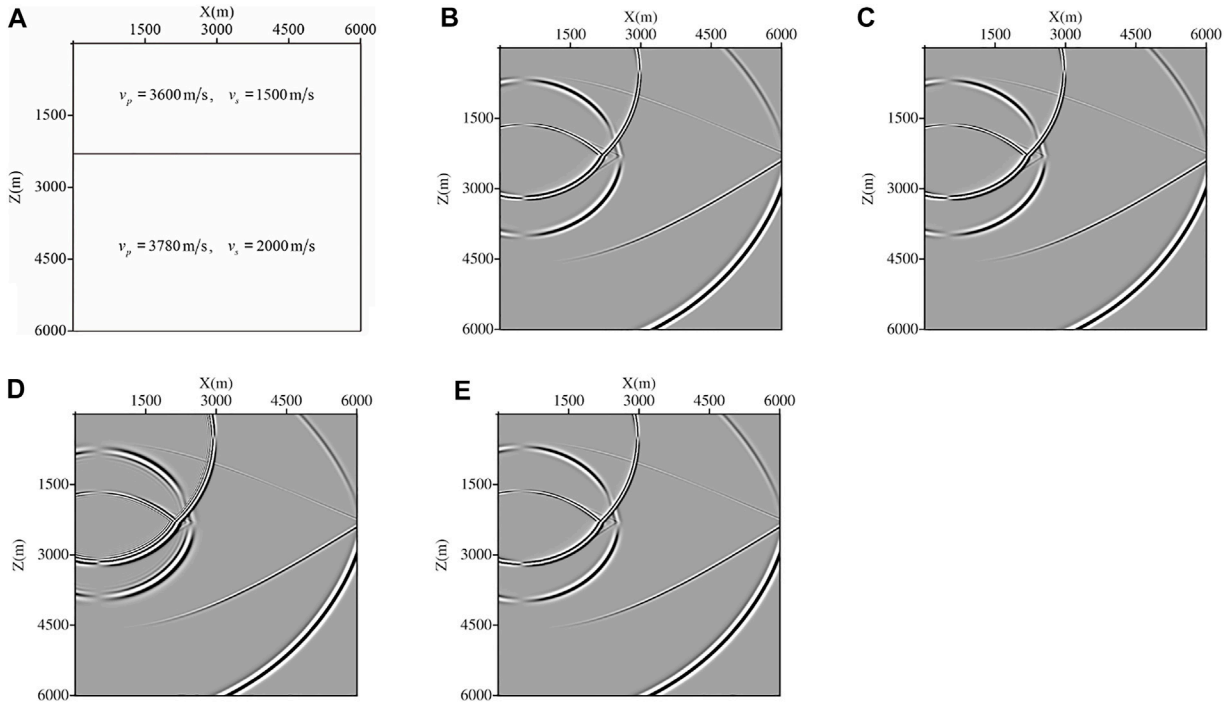

FIGURE 13 | Layered model and snapshots of the v_z component simulated by different SFD schemes. **(A)** Two-layered model. **(B)** C-SFD (M=10) with Δt = 1ms. **(C)** M-SFD (M=8; N=1) with Δt = 1ms, the FD coefficients calculated based on the P-wave time-space domain dispersion relation. **(D)** M-SFD (M=8; N=1) with Δt = 1.5ms, the FD coefficients calculated based on the S-wave time-space domain dispersion relation. **(E)** M-SFD (M=8; N=1) with Δt = 1.5ms, solving the decomposed P-wave and S-wave equations.

Δt = 1.5ms. The cross-correlation imaging condition is adopted and the Laplace filter is used to suppress the low-frequency noise that existed in the RTM results. **Figure 12** shows the final RTM result with C-SFD (M=10) and M-SFD (M=8; N=1) respectively. It exhibits that, there are serious imaging artifacts caused by the numerical dispersion in the deep portion of the RTM result with C-SFD (M=10). While the imaging artifacts are successfully suppressed in the RTM result with M-SFD (M=8; N=1). So M-SFD used as the wavefield propagation operator in RTM can improve the imaging accuracy and resolution of deep structures.

6 DISCUSSION

In this section, we discussed the stability of C-SFD and M-SFD for elastic wave simulation on a medium with a high Poisson's ratio. A two-layered model shown in **Figure 13** is adopted, with a grid size equaling 10 m. The Poisson's ratios of the layer are 0.395 and 0.306. **Figure 13**(B-E) displays the snapshots of the v_z component at 1.8 s simulated by C-SFD (M=10) and M-SFD (M=8; N=1).

Limited to the stability condition, the simulation by C-SFD (M=10), with a time step Δt equaling 1.0 ms, is stable, while Δt increasing to 1.5 ms, it becomes unstable. Similarly, with the FD coefficients calculated based on the S-wave time-space domain dispersion relation, the simulation by M-SFD (M=8; N=1) is stable with Δt = 1.0ms but unstable with Δt = 1.5ms. With the FD coefficients calculated based on the P-wave time-space domain dispersion relation, the simulation by M-SFD (M=8; N=1) is stable with Δt = 1.5ms, but obvious space dispersion exists in the modeling snapshot. Solving the decomposed P- and S-wave equations by M-SFD (M=8; N=1) with Δt = 1.5ms is also stable.

The aforementioned analyses show that both C-SFD and M-SFD are suitable for elastic wave simulation on a model with a high Poisson's ratio. However, the stability of M-SFD is better than C-SFD, when the FD coefficients are calculated based on the P-wave time-space domain dispersion for M-SFD or the simulation is implemented by solving the decomposed P- and S-wave equations with M-SFD. The better stability ensures M-SFD to adopt a larger time step.

After the comprehensive considerations of the modeling accuracy and stability, elastic wave simulation with M-SFD by solving the decomposed P- and S-wave equations could be a feasible option. Nevertheless, this scheme is at the expense of rather high computational resources, so its superiority of it should be further evaluated thoroughly.

7 CONCLUSION

In this article, by constructing the spatial FD operator with the axial and off-axial grid points jointly to approximate the first-order spatial derivatives, we developed an M-SFD for acoustic and elastic wave equation simulation. Furthermore, we

successfully derived the analytical expression of the FD coefficients based on the time-space domain dispersion relation and TE. Then, FD accuracy analysis, dispersion analysis, stability analysis, numerical simulation, and RTM tests are performed. Several conclusions can be deduced:

1) The FD discrete acoustic equation given by C-SFD can only reach the second-order accuracy, while the FD discrete acoustic equation given by M-SFD (N=1, 2, 4) can reach the fourth, sixth, or eighth-order accuracy, and theoretically, it can reach arbitrary even-order accuracy with increasing N continuously.
2) For acoustic wave simulation, compared to C-SFD, M-SFD can suppress the numerical dispersion more effectively to reach higher modeling accuracy with almost the same computational efficiency. Moreover, M-SFD can achieve higher computational efficiency by adopting a larger time step and reach higher modeling accuracy at the same time.
3) The FD coefficients calculated based on P- or S-wave time-space domain dispersion relation can ensure only the P- or S-wave in the FD discrete elastic wave equation given by M-SFD (N=1,2,4) reaches the fourth, sixth, and eighth-order accuracy respectively. Solving the decomposed P- and S-wave equation with M-SFD (N=1, 2, 4) can make P- and S-waves reach the fourth, sixth, and eighth-order accuracy at the same time.
4) For elastic wave simulation, with almost the same efficiency, M-SFD, with its FD coefficients calculated based on the S-wave time-space domain dispersion relation, can suppress both P- and S-wave dispersion more effectively to achieve higher modeling accuracy than C-SFD. By solving the decomposed P- and S-wave equation with M-SFD, the modeling accuracy can be improved further, but the computation efficiency degrades. The FD coefficients calculated based on the P-wave time-space domain dispersion relation should not be adopted for M-SFD, which causes serious spatial dispersion for the S-wave.
5) For both acoustic and elastic wave simulations, M-SFD has better stability than C-SFD.
6) Compared to C-SFD, M-SFD used as the wavefield propagation operator in RTM more effectively eliminates the imaging artifacts caused by the numerical dispersion, which successfully improves the imaging accuracy and resolution of the deep structure.

DATA AVAILABILITY STATEMENT

The raw data supporting the conclusion of this article will be made available by the authors, without undue reservation.

AUTHOR CONTRIBUTIONS

WL derived the analytical expression of the FD coefficients and performed the numerical modeling. ZH performed the numerical dispersion analysis. XY performed the stability analysis. GP conducted the RTM. ZX plotted some of the Figures. LH conducted the elastic wave modeling.

FUNDING

This research is supported by the Project of Science and Technology of CNPC under the Grant No. 2021DJ3501.

ACKNOWLEDGMENTS

We would like to thank the editor Dr. Jianping Huang and the two reviewers for their valuable comments and suggestions, which greatly improved the quality of our article. We also thank Dr. Dunshi Wu and Dr. Wei Zhu for their help in revising this English manuscript.

SUPPLEMENTARY MATERIAL

The Supplementary Material for this article can be found online at: https://www.frontiersin.org/articles/10.3389/feart.2022.873541/full#supplementary-material

REFERENCES

Alford, R. M., Kelly, K. R., and Boore, D. M. (1974). Accuracy of Finite-difference Modeling of the Acoustic Wave Equation. *Geophysics* 39 (6), 834–842. doi:10.1190/1.1440470

Alterman, Z., and Karal, F. C. (1968). Propagation of Elastic Waves in Layered Media by Finite Difference Methods. *Bull. Seismol. Soc. Am.* 58 (1), 367–398.

Berkhout, A. J. G. (2014). Review Paper: An Outlook on the Future of Seismic Imaging, Part I: Forward and Reverse Modelling. *Geophys. Prospect.* 62 (5), 911–930. doi:10.1111/1365-2478.12161

Cao, J., and Chen, J.-B. (2018). A Parameter-Modified Method for Implementing Surface Topography in Elastic-Wave Finite-Difference Modeling. *Geophysics* 83 (6), T313–T332. doi:10.1190/geo2018-0098.1

Carcione, J. M. (2015). *Wave Fields in Real Media*. Oxford: Elsevier.

Chen, J.-B., Cao, J., and Li, Z. (2021). A Comparative Study on the Stress Image and Adaptive Parameter-Modified Methods for Implementing Free Surface Boundary Conditions in Elastic Wave Numerical Modeling. *Geophysics* 86 (6), T451–T467. doi:10.1190/geo2020-0418.1

Chu, C., and Stoffa, P. L. (2012). Determination of Finite-Difference Weights Using Scaled Binomial Windows. *Geophysics* 77 (3), W17–W26. doi:10.1190/geo2011-0336.1

Dablain, M. A. (1986). The Application of High-order Differencing to the Scalar Wave Equation. *Geophysics* 51 (1), 54–66. doi:10.1190/1.1442040

Fornberg, B. (1988). Generation of Finite Difference Formulas on Arbitrarily Spaced Grids. *Math. Comp.* 51, 699–706. doi:10.1090/s0025-5718-1988-0935077-0

Geller, R. J., and Takeuchi, N. (1998). Optimally Accurate Second-Order Time-Domain Finite Difference Scheme for the Elastic Equation of Motion: One-Dimensional Case. *Geophys. J. Int.* 135 (1), 48–62. doi:10.1046/j.1365-246X.1998.00596.x

Hu, Z. D., He, Z. H., Liu, W., Wang, Y. C., Han, L. H., Wang, S. J., et al. (2016). Scalar Wave Equation Modeling Using the Mixed-Grid Finite-Difference Method in the Time-Space Domain (In Chinese). *Chin. J. Geophys* 59 (10), 3829–3846. doi:10.6038/cjg20161027

Hu, Z. D., Liu, W., Yong, X. S., Wang, X. W., Han, L. H., and Tian, Y. C. (2021). Mixed-grid Finite-Difference Method for Numerical Simulation of 3D Wave Equation in the Time-Space Domain (In Chinese). *Chin. J. Geophys* 64 (8), 2809–2828. doi:10.6038/cjg2021O0296

Jo, C. H., Shin, C., and Suh, J. H. (1996). An Optimal 9-point, Finite-difference, Frequency-space, 2-D Scalar Wave Extrapolator. *Geophysics* 61 (2), 529–537. doi:10.1190/1.1443979

Li, Z., Zhang, H., Liu, Q., and Han, W. (2007). Numerical Simulation of Elastic Wavefield Separation by Staggering Grid High-Order Finite-Difference Algorithm (In Chinese). *Oil Geophys. Prospect.* 42 (5), 510–515.

Liu, Y. (2013). Globally Optimal Finite-Difference Schemes Based on Least Squares. *Geophysics* 78 (4), T113–T132. doi:10.1190/geo2012-0480.1

Liu, Y. (2014). Optimal Staggered-Grid Finite-Difference Schemes Based on Least-Squares for Wave Equation Modelling. *Geophys. J. Int.* 197 (2), 1033–1047. doi:10.1093/gji/ggu032

Liu, Y., and Sen, M. K. (2009). A New Time-Space Domain High-Order Finite-Difference Method for the Acoustic Wave Equation. *J. Comput. Phys.* 228 (23), 8779–8806. doi:10.1016/j.jcp.2009.08.027

Liu, Y., and Sen, M. K. (2011). Scalar Wave Equation Modeling with Time-Space Domain Dispersion-Relation-Based Staggered-Grid Finite-Difference Schemes. *Bull. Seismol. Soc. Am.* 101 (1), 141–159. doi:10.1785/0120100041

Liu, Y., and Sen, M. K. (2013). Time-space Domain Dispersion-Relation-Based Finite-Difference Method with Arbitrary Even-Order Accuracy for the 2D Acoustic Wave Equation. *J. Comput. Phys.* 232 (1), 327–345. doi:10.1016/j.jcp.2012.08.025

Marfurt, K. J. (1984). Accuracy of Finite-difference and Finite-element Modeling of the Scalar and Elastic Wave Equations. *Geophysics* 49 (5), 533–549. doi:10.1190/1.1441689

Mittet, R. (2021). On the Pseudospectral Method and Spectral Accuracy. *Geophysics* 86 (3), T127–T142. doi:10.1190/geo2020-0209.1

Moczo, P., Kristek, J., Galis, M., Chaljub, E., and Etienne, V. (2011). 3-D Finite-Difference, Finite-Element, Discontinuous-Galerkin and Spectral-Element Schemes Analysed for Their Accuracy with Respect to P-Wave to S-Wave Speed Ratio. *Geophys. J. Int.* 187 (3), 1645–1667. doi:10.1111/j.1365-246X.2011.05221.x

Moczo, P., Kristek, J., Galis, M., and Pazak, P. (2010). On Accuracy of the Finite-Difference and Finite-Element Schemes with Respect to P-Wave to S-Wave Speed Ratio. *Geophys. J. Int.* 182 (1), no. doi:10.1111/j.1365-246X.2010.04639.x

Mulder, W. A. (2017). A Simple Finite-Difference Scheme for Handling Topography with the Second-Order Wave Equation. *Geophysics* 82 (3), T111–T120. doi:10.1190/geo2016-0212.1

Ren, Z., Dai, X., Bao, Q., Cai, X., and Liu, Y. (2021). Time and Space Dispersion in Finite Difference and its Influence on Reverse Time Migration and Full-Waveform Inversion (In Chinese). *Chin. J. Geophys* 64 (11), 4166–4180. doi:10.6038/cjg2021P0041

Ren, Z., and Li, Z. C. (2017). Temporal High-Order Staggered-Grid Finite-Difference Schemes for Elastic Wave Propagation. *Geophysics* 82 (5), T207–T224. doi:10.1190/geo2017-0005.1

Reshef, M., Kosloff, D., Edwards, M., and Hsiung, C. (1988). Three-dimensional Elastic Modeling by the Fourier Method. *Geophysics* 53 (9), 1184–1193. doi:10.1190/1.1442558

Pratt, R. G., Shin, C., and Hicks, G. J. (1998). Gauss-Newton and Full Newton Methods in Frequency-Space Seismic Waveform Inversion. *Geophys. J. Int.* 133 (2), 341–362. doi:10.1046/j.1365-246X.1998.00498.x

Shin, C., and Sohn, H. (1998). A Frequency-space 2-D Scalar Wave Extrapolator Using Extended 25-point Finite-difference Operator. *Geophysics* 63 (1), 289–296. doi:10.1190/1.1444323

Tan, S., and Huang, L. (2014). An Efficient Finite-Difference Method with High-Order Accuracy in Both Time and Space Domains for Modelling Scalar-Wave Propagation. *Geophys. J. Int.* 197 (2), 1250–1267. doi:10.1093/gji/ggu077

Virieux, J., Calandra, H., and Plessix, R.-É. (2011). A Review of the Spectral, Pseudo-spectral, Finite-Difference and Finite-Element Modelling Techniques for Geophysical Imaging. *Geophys. Prospect.* 59 (5), 794–813. doi:10.1111/j.1365-2478.2011.00967.x

Virieux, J., and Operto, S. (2009). An Overview of Full-Waveform Inversion in Exploration Geophysics. *Geophysics* 74 (6), WCC1–WCC26. doi:10.1190/1.3238367

Wang, E., Liu, Y., and Sen, M. K. (2016). Effective Finite-Difference Modelling Methods with 2-D Acoustic Wave Equation Using a Combination of Cross and Rhombus Stencils. *Geophys. J. Int.* 206 (3), 1933–1958. doi:10.1093/gji/ggw250

Conflict of Interest: Author GP was employed by Tarim Oilfield Company, PetroChina.

The remaining authors declare that the research was conducted in the absence of any commercial or financial relationships that could be construed as a potential conflict of interest.

Publisher's Note: All claims expressed in this article are solely those of the authors and do not necessarily represent those of their affiliated organizations, or those of the publisher, the editors, and the reviewers. Any product that may be evaluated in this article, or claim that may be made by its manufacturer, is not guaranteed or endorsed by the publisher.

frontiers | Frontiers in Earth Science

TYPE Methods
PUBLISHED 25 August 2022
DOI 10.3389/feart.2022.893445

OPEN ACCESS

EDITED BY
Jidong Yang,
China University of Petroleum,
Huadong, China

REVIEWED BY
Qingyang Li,
Zhongyuan oilfield, Sinopec, China
Yubo Yue,
Southwest Petroleum University, China
Wenlong Wang,
Harbin Institute of Technology, China

*CORRESPONDENCE
Xiugang Xu,
xxg@ouc.edu.cn

SPECIALTY SECTION
This article was submitted to Solid Earth Geophysics,
a section of the journal
Frontiers in Earth Science.

RECEIVED 10 March 2022
ACCEPTED 27 June 2022
PUBLISHED 25 August 2022

CITATION
Sun Y, Xu X and Tang L (2022), Gradient normalized least-squares reverse-time migration imaging technology.
Front. Earth Sci. 10:893445.
doi: 10.3389/feart.2022.893445

Gradient normalized least-squares reverse-time migration imaging technology

Yanfeng Sun[1], Xiugang Xu[1,2]* and Le Tang[3]

[1]College of Marine Geosciences, Ocean University of China, Qingdao, China, [2]Key Lab of Submarine Geosciences and Prospecting Techniques, College of Marine Geo Sciences, Ocean University of China Qingdao, Qingdao, China, [3]Department of Earth and Space Sciences, Southern University of Science and Technology, Shenzhen, China

Least-squares reverse-time migration (LSRTM) can overcome the problems of low resolution and unbalanced amplitude energy of deep formation imaging in reverse-time migration (RTM); hence, it can obtain a more accurate imaging profile. In the conventional conjugate gradient LSRTM, the gradient is obtained based on cross correlation without a precondition operator, and the source has a great influence on the gradient, causing the convergence rate to be slow. In the framework of conventional conjugate gradient LSRTM, a normalized cross-correlation of the source wavefield was used in this study to effectively weaken the influence of the source effect and reduce the low-frequency noise. The idea of normalized cross-correlation of the source wavefield was adopted to improve the steepest descent gradient to further accelerate the iterative convergence speed and complete the final migration imaging. Model and field data examples verify the advantages of the proposed methods over conventional methods in reducing source effects, improving convergence speed, and enhancing underground deep illumination.

KEYWORDS

reverse-time migration, least-squares reverse-time migration, conjugate gradient, normalization, cross-correlation

Introduction

Reverse-time migration (RTM) is considered the most accurate imaging technology used in complex structure imaging (Baysal et al., 1983). It employs the numerical solution of the two-way wave equation to reverse continuation seismic records, and it can process imaging of strong velocity variation and steep dip angles. Because of the conventional RTM, cross-correlation imaging is the result of migration operator transposition rather than its inverse and limited acquisition aperture, complex underground structure, and limited seismic bandwidth. RTM can only provide fuzzy structural information, and therefore, it cannot obtain accurate imaging results (Claerbout, 1992), which cannot carry out fine imaging of complex oil and gas reservoirs. Least-squares reverse-time migration (LSRTM) is a true-amplitude imaging method based on linear inversion theory, which was first introduced into seismic inversion by Bamberger et al. (1982). Later, Tarantola (1984) proposed the theoretical framework of least-squares inversion. Furthermore, many experts

and scholars have continuously improved the LSRTM and applied it to the field data. Nemeth et al. (1999) proposed the least-squares Kirchhoff migration method for irregular seismic data (such as trace missing and sampling irregular data) to eliminate the migration artifacts caused by irregular data. Although it has the above-mentioned advantage, the calculation accuracy of Kirchhoff wave field propagator is low and cannot meet the requirements of actual production. Kuehl and Sacchi (2001a, 2003) proposed the introduction of the least-squares migration into the wave field propagator, and subsequent studies mainly focused on the areas such as rapid calculation of the Hessian matrix, the improvement of imaging resolution, regularization constraints, and the improvement of computing efficiency. Yang and Zhang (2008) adopted Fourier finite-difference migration and forward operator to carry out post-stack least-squares migration, to eliminate imaging noise to a certain extent and improve resolution. Wang et al. (2009) developed a new iterative regularization model of migration inversion imaging and proposed a hybrid conjugate gradient algorithm to solve the model. Huang et al.(2013a, 2013b) achieved good inversion results by using least-squares Kirchhoff migration algorithm for model and field data testing. Furthermore, Guo et al. (2015) realized iterative LSRTM imaging by employing the research of error functional establishment, RTM data reconstruction algorithm, Hessian reverse regularization gradient calculation, and established the implementation process of LSRTM for field data. Huang et al. (2015) studied the theoretical method and the processing process of LSRTM based on static plane wave coding. The test results showed that this method could effectively suppress the low-frequency imaging noise and crosstalk noise, and compensate deep imaging energy, which was an effective amplitude-preserved imaging strategy.

Although the LSRTM has obvious advantages, there are still many problems encountered when it is applied to field data. On the one hand, the LSRTM is computationally inefficient. On the other hand, because the actual source wavelet is difficult to estimate, the conventional conjugate gradient method has a great influence on obtaining the source energy, and it is difficult to obtain the Hessian inverse, resulting in the imbalance of underground deep illumination (Zhang et al., 2013). To solve these problems, geophysicists began to construct preconditioned operators to approximate the Hessian inverse and to preprocess the gradient, including damping constraints (Tarantola, 1984), focusing or smoothness constraints of common imaging point gathers (Kuehl and Sacchi, 2001b; Prucha and Biondi, 2002), dip angle constraint condition (Prucha and Biondi, 2002), prediction operator (Wang et al., 2003), defuzzification operator (Aoki and Schuster, 2009), and sparse transform constraints, using the sparse distribution characteristics of imaging results in the wavelet or curvelet domains to constrain (Herrmann et al., 2019).

When there is no suitable precondition operator in the gradient computation of conventional conjugate gradient LSRTM, the source effect will lead to serious interference with the migration result, resulting in shallow energy concentration, insufficient illumination in deep layers, and slow convergence rate of the iterative process. Normalization can solve the source effect problem in RTM well. In this study, the source normalization was introduced into the gradient optimization process to weaken the influence of the source effect, accelerate the convergence speed of the algorithm, and obtain the final LSRTM imaging.

Methods

Born approximation

The constant density acoustic wave equation is

$$\left(\nabla^2 - \frac{1}{v^2(X)}\frac{\partial^2}{\partial^2 t}\right)p = \delta(X - X_s)\delta(t) \tag{1}$$

where p is the wave field function, $v(X)$ is the velocity at the X position, and the X_s and X are the position of the source and the geophone, respectively.

The actual velocity field can be composed of normal field and disturbance:

$$\frac{1}{v^2(X)} = \frac{1}{v_0^2(X)}(1 - \alpha(X)) \tag{2}$$

By expanding Taylor's Eq. 2 at v_0 and removing the higher order term, we obtain the following result:

$$\frac{1}{v_0^2} - \frac{2\Delta v}{v_0^3} = \frac{1}{v_0^2}(1 - \alpha) \tag{3}$$

where $\alpha = \frac{2\Delta v}{v_0}$, $\alpha(X)$ is the disturbance. After applying Eq. 2 into (1), and transforming the equation into Fourier frequency domain, we have

$$\left[\nabla^2 + \frac{\omega^2}{v_0^2}(1 - \alpha(X))\right]P(X, X_S, \omega) = \delta(X - X_S) \tag{4}$$

where $P(X, X_S, \omega) = \int_{-\infty}^{\infty} p(X, X_S, t)e^{-j\omega t}dt$.

By expanding Eq. 4,

$$\left(\nabla^2 + \frac{\omega^2}{v_0^2}\right)P(X, X_S, \omega) = \delta(X - X_S) + \frac{\omega^2}{v_0^2}\alpha(X)P(X, X_S, \omega) \tag{5}$$

The total observed wavefield is the sum of the incident field and the scattered field:

$$P(X, X_S, \omega) = P_0(X, X_S, \omega) + P_S(X, X_S, \omega) \tag{6}$$

Applying Eq. 6 into (5) and decomposing it into two formulas:

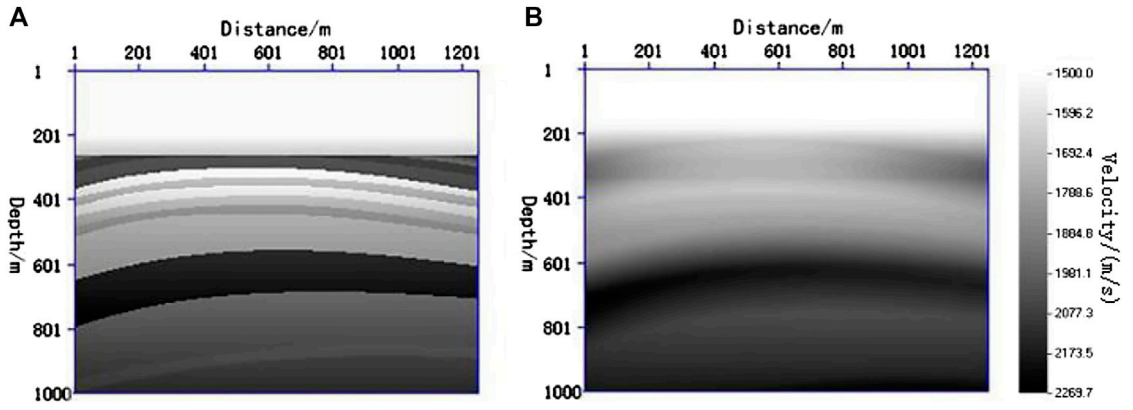

FIGURE 1
Velocity field of the simple model: **(A)** real velocity model; **(B)** Gaussian smooth velocity model.

$$\left(\nabla^2 + \frac{\omega^2}{v_0^2}\right) P_0(X, X_S, \omega) = \delta(X - X_S) \tag{7}$$

$$\left(\nabla^2 + \frac{\omega^2}{v_0^2}\right) P_S(X, X_S, \omega) = \frac{\omega^2}{v_0^2} \alpha(X) P(X, X_S, \omega) \tag{8}$$

where P_0 is the background field and P_s is the scattering disturbance field. The total wavefield can be written as

$$P(X, X_S, \omega) = P_0(X, X_S, \omega) + \iiint_V P_0(X, X', \omega) \frac{\omega^2}{v_0^2} \alpha(X) P(X, X', \omega) dX' \tag{9}$$

where V is the target region of velocity variation. Eq. 9 is the Lippmann–Schwinger integral formula. Assuming α is small, the scattering wave field under Born approximation (Liu, 2008) is expressed by:

$$P_S(X, X_S, \omega) = \iiint_V P_0(X, X', \omega) \frac{\omega^2}{v_0^2} \alpha(X) P(X, X', \omega) dX' \tag{10}$$

Defining $m(X) = \frac{2\Delta v}{v_0}$ to replace $\alpha(X)$ in Eq. 10, the wavefield in Eq. 10 can be obtained from Eqs. 11 and 12 as

$$\left(\nabla^2 + \frac{\omega^2}{v_0^2}\right) P_0(X, X_S, \omega) = \delta(X, X_S) \tag{11}$$

$$\left(\nabla^2 + \frac{\omega^2}{v_0^2}\right) P_S(X, X_S, \omega) = \omega^2 m(X) P_0(X, X_S, \omega) \tag{12}$$

The Born forward operator is represented by vector matrix:

$$d = Lm \tag{13}$$

where m is the matrix form of migration profile or reflection coefficient model, $\mathbf{d}$ is the matrix form of simulation data, and $\mathbf{L}$ is the Born approximate forward operator matrix. The calculation of scattering wavefield can be obtained by forward simulation of Eqs. 11 and 12.

Conjugate gradient least-squares reverse-time migration

Conventional RTM can be expressed as

$$m_0(x, z) = L^T D \tag{14}$$

where m_0 is the RTM profile, and L^T is the approximate migration operator. There are some errors when replacing the migration operator with the transpose of the forward modeling operator. To minimize the difference between the simulated data and the field data, the error function is defined as

$$f(m) = \frac{1}{2} \|Lm - D\|^2 \tag{15}$$

After taking partial derivative with respect to m,

$$\mathbf{g} = \frac{\partial f(m)}{\partial m} = L^T (Lm - D) \tag{16}$$

When the gradient $\mathbf{g}$ is zero, the optimal solution of the least-squares problem is obtained:

$$m = (L^T L)^{-1} L^T D \tag{17}$$

where $L^T L$ is the Hessian matrix. Because it is so large and difficult to obtain, the gradient is gradually close to zero by iteration to avoid getting the inverse of Hessian matrix.

The cross-correlation conjugate gradient method for solving Eq. 15 can be expressed as (Huang et al., 2016):

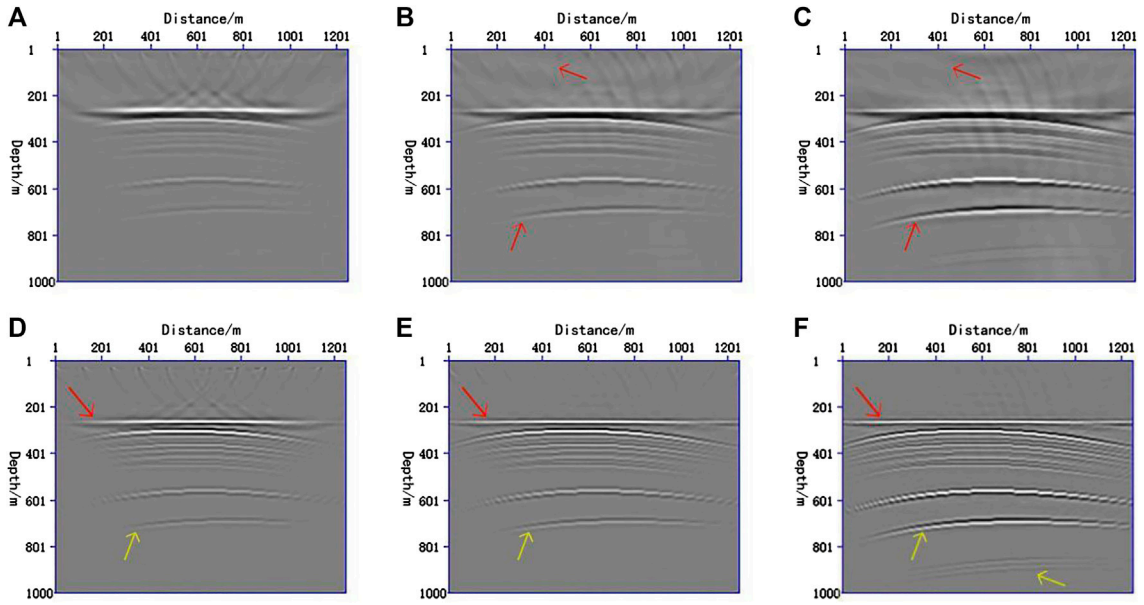

FIGURE 2
RTM and LSRTM migration profiles of a simple model. **(A)** cross-correlation RTM migration result; **(B)** result of cross-correlation conjugate gradient LSRTM with 20 iterations; **(C)** result of conjugate gradient normalized LSRTM with 20 iterations; **(D)** cross-correlation RTM following Laplace filtering; **(E)** cross-correlation conjugate gradient LSRTM following Laplace filtering; **(F)** conjugate gradient normalized LSRTM following Laplace filtering.

$$
\begin{aligned}
\boldsymbol{g}^{(k+1)} &= \boldsymbol{L}^T\left[\boldsymbol{L}\boldsymbol{m}^{(k)} - \boldsymbol{D}\right] \\
\boldsymbol{\beta} &= \frac{\boldsymbol{g}^{(k+1)}\boldsymbol{g}^{(k+1)}}{\boldsymbol{g}^{(k)}\boldsymbol{g}^{(k)}} \\
\boldsymbol{z}^{(k+1)} &= \boldsymbol{g}^{(k+1)} + \boldsymbol{\beta}\boldsymbol{z}^{(k)} \\
\boldsymbol{\alpha} &= \frac{\left[\boldsymbol{z}^{(k+1)}\right]^T\boldsymbol{g}^{(k+1)}}{\left[\boldsymbol{L}\boldsymbol{z}^{(k+1)}\right]^T\boldsymbol{L}\boldsymbol{z}^{(k+1)}} \\
\boldsymbol{m}^{(k+1)} &= \boldsymbol{m}^{(k)} - \boldsymbol{\alpha}\boldsymbol{z}^{(k+1)}
\end{aligned}
\tag{18}
$$

The gradient g expansion based on the steepest descent method can be expressed as

$$
\boldsymbol{g} = \sum_t \frac{\partial \boldsymbol{S}_s(\boldsymbol{t},\boldsymbol{x},\boldsymbol{z})}{\partial \boldsymbol{t}} \boldsymbol{R}_{res}(\boldsymbol{t},\boldsymbol{x},\boldsymbol{z}) \tag{19}
$$

where $\boldsymbol{\beta}$ is the correction factor of the conjugate gradient method, α is the update step, $\boldsymbol{z}$ is the conjugate gradient, $\boldsymbol{g}$ is the steepest descent gradient, $\boldsymbol{D}$ is the field data, S_s is the source forward wave field, and R_{res} is the backward wavefield of the residual error between Born approximate forward data and field data.

It can be seen from Eq. 18 that the difficulty of conjugate gradient LSRTM method lies in gradient calculation and Born approximate forward modeling.

$$
\boldsymbol{d}_{res} = \boldsymbol{L}\boldsymbol{m}^{(k)} - \boldsymbol{D} \tag{20}
$$

$\boldsymbol{d}_{res}$ is the residual of Born approximate forward data and field data. The calculation of the steepest descent gradient is similar to the cross-correlation of conventional RTM, except that conventional RTM is the cross-correlation of field data and forward wavefield, while the steepest descent gradient is the cross-correlation of the forward modeling wave field. In the conventional cross-correlation RTM, because of the use of an imprecise migration operator, the unbalanced wave field energy affects the imaging results. When it is close to the source and geophone with strong energy, the signal may become blurred (Yang et al., 2018). To weaken the influence of energy imbalance, the imaging conditions of source-normalized cross-correlation RTM for compensating underground illumination were proposed. Considering that the preconditioner in LSRTM of conjugate gradient method is difficult to obtain and cannot approximate the Hessian matrix well, the source effect has a great impact on the gradient. Here, the normalization is used to improve the calculation process of the steepest descent gradient and weaken the influence of the source effect.

The source-normalized cross-correlation imaging condition of the RTM source is

$$
\boldsymbol{m}_0(\boldsymbol{x},\boldsymbol{z}) = \frac{\sum_t \boldsymbol{S}_s(\boldsymbol{t},\boldsymbol{x},\boldsymbol{z})\boldsymbol{R}_s(\boldsymbol{t},\boldsymbol{x},\boldsymbol{z})}{\sum_t \left(\boldsymbol{S}_s(\boldsymbol{t},\boldsymbol{x},\boldsymbol{z})\right)^2} \tag{21}
$$

where $\boldsymbol{R}_S$ is the reverse propagation field of seismic record.

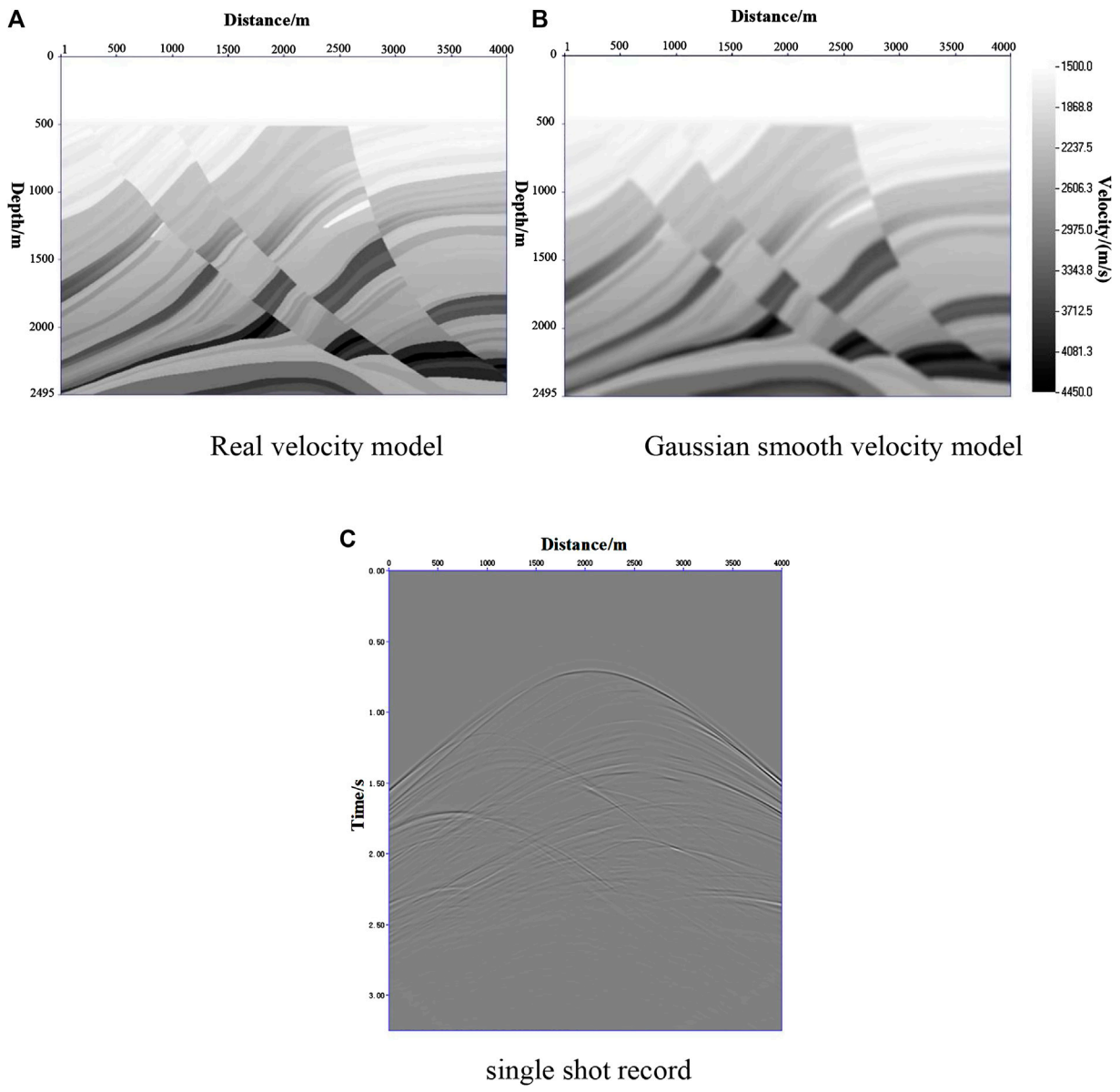

FIGURE 3
Velocity field and single-shot record of the Marmousi model. **(A)** real velocity model; **(B)** Gaussian smooth velocity model; **(C)** single-shot record.

Likewise, the source-normalized steepest descent gradient formula of LSRTM is

$$\tilde{g}^{(k+1)} = \frac{\sum_t \frac{\partial S_s(t,x,z)}{\partial t} R_{res}(t,x,z)}{\sum_t \left(\frac{\partial S_s(t,x,z)}{\partial t}\right)^2} \tag{22}$$

$\frac{\partial S_s(t,x,z)}{\partial t}$ is the first-order partial derivative of source forward propagation field, which is very important for obtaining the zero-phase imaging profile (Yao and Wu, 2015). Eq. 18 can be written as

$$\begin{aligned}
\tilde{g}^{(k+1)} &= \frac{L^T\left[Lm^{(k)} - D\right]}{\left\|L^T\left[Lm^{(k)} - D\right]\right\|_s} \\
\tilde{\beta} &= \frac{\tilde{\mathbf{g}}^{(k+1)}\tilde{\mathbf{g}}^{(k+1)}}{\tilde{\mathbf{g}}^{(k)}\tilde{\mathbf{g}}^{(k)}} \\
\tilde{z}^{(k+1)} &= \tilde{\mathbf{g}}^{(k+1)} + \tilde{\beta}\tilde{z}^{(k)} \\
\tilde{\alpha} &= \frac{\left[\tilde{z}^{(k+1)}\right]^T \tilde{\mathbf{g}}^{(k+1)}}{\left[L\tilde{z}^{(k+1)}\right]^T L\tilde{z}^{(k+1)}} \\
m^{(k+1)} &= m^{(k)} - \tilde{\alpha}\tilde{z}^{(k+1)}
\end{aligned} \tag{23}$$

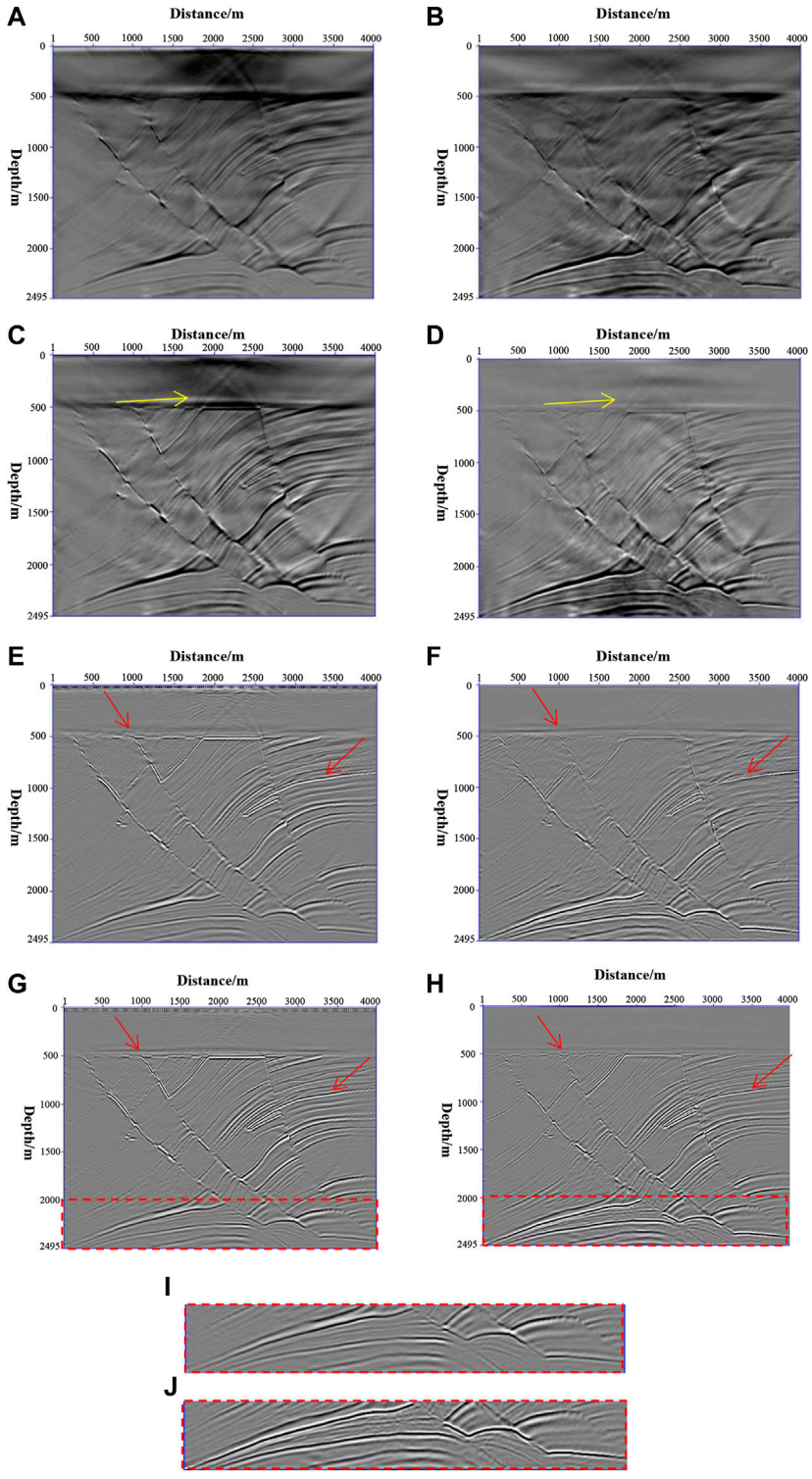

FIGURE 4
RTM and LSRTM of the Marmousi model. **(A)** RTM migration results; **(B)** normalized cross-correlation RTM migration results; **(C)** results of cross-correlation conjugate gradient LSRTM with 15 iterations; **(D)** results of conjugate gradient normalized LSRTM with 15 iterations; **(E)** Laplace filtering results of Figure 4 **(A)**; **(F)** Laplace filtering results of Figure 4 **(B)**; **(G)** Laplace filtering results of Figure 4 **(C)**; **(H)** Laplace filtering results of Figure 4 **(D)**; **(I,J)** are partial enlarged views of the red rectangular boxes in Figure 4 **(G,H)**, respectively.

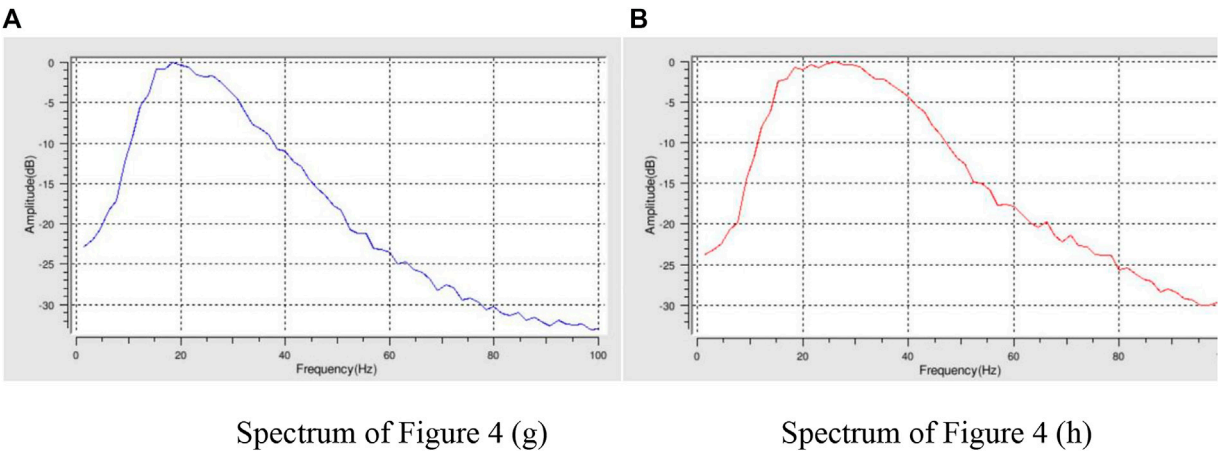

FIGURE 5
Spectrum of LSRTM. **(A)** spectrum of Figure 4 **(g)**. **(B)** spectrum of Figure 4 (h).

where $\tilde{\beta}$ is the normalized conjugate gradient correction factor, $\tilde{\alpha}$ is the update step, $\tilde{z}$ is the normalized conjugate gradient, and $\tilde{g} = \frac{L^T[Lm-D]}{\|L^T[Lm-D]\|_s}$ is the source-normalized steepest descent gradient. The LSRTM imaging is realized through the iterative calculation of the above equation.

Model trial

Simple model

The real velocity model and the Gaussian smoothed velocity model are shown in Figures 1A,B, which is used for RTM and LSRTM background velocity field. The lateral length of the model is 1,250 m and the depth is 1,000 m. It consisted of 250 traces with a trace interval of 5 m and 11 shots with a shot interval of 125 m. The receivers are fixed, and the shot point moves at equal intervals.

It can be seen that conventional cross-correlation RTM results contain low-frequency noise (Figure 2A), coupled with strong near-surface energy caused by the source effect, resulting in unbalanced wave field energy, weak deep illumination, and unclear imaging. The LSRTM can solve the problems in RTM imaging. With an increase in the number of iterations, the data of Born forward simulation are gradually approaching the field data, and the migration profile is also gradually close to the reflection coefficient profile. As can be seen from the red arrows in Figures 2B,C, after 20 iterations, the noise in the shallow part of the migration profile gradually disappears, and the energy of the profile becomes more balanced, yielding clearer deep structure imaging. Under the same iteration times, the results of LSRTM processing by conjugate gradient normalization method are better than that by the conventional conjugate gradient method.

To eliminate low-frequency noise, Laplace filtering is performed on the profiles processed by RTM, cross-correlation conjugate gradient LSRTM, and conjugate gradient normalized LSRTM. From the comparison of red arrows in Figures 2D–F, it can also be seen that the amplitude of migration profile obtained by conjugate gradient LSRTM is more balanced than that obtained by RTM, and the imaging results of deep structure are better than that processed by RTM, while the migration profile obtained by conjugate gradient normalized LSRTM is better than that processed by the cross-correlation conjugate gradient LSRTM and RTM in both amplitude equalization and deep illumination (yellow arrow).

Complex model

To verify the applicability of the conjugate gradient normalized LSRTM for complex model, imaging experiments were carried out on the Marmousi model (Figure 3). The velocity model and the Gaussian smoothed velocity model are shown in Figures 3A,B. The lateral length of the model is 4,000 m and the depth is 2,495 m. It consisted of 650 traces with a trace interval of 5 m and 14 shots with a shot interval of 250 m. The receivers were fixed, and the shot point moved at equal intervals. The seismic records were obtained using finite-difference forward modeling (Figure 3C shows the single-shot record).

The experimental work of the complex model was carried out on a workstation using the Intel(R) Xeon(R) Silver 4210R CPU @ 2.40 ghz, 128 GB memory, 64-bit operating system, and an X64-based processor. The graphics card was NVIDIA GeForce RTX3090 with 24 GB of video memory. In this computing environment, both the conventional LSRTM and conjugate

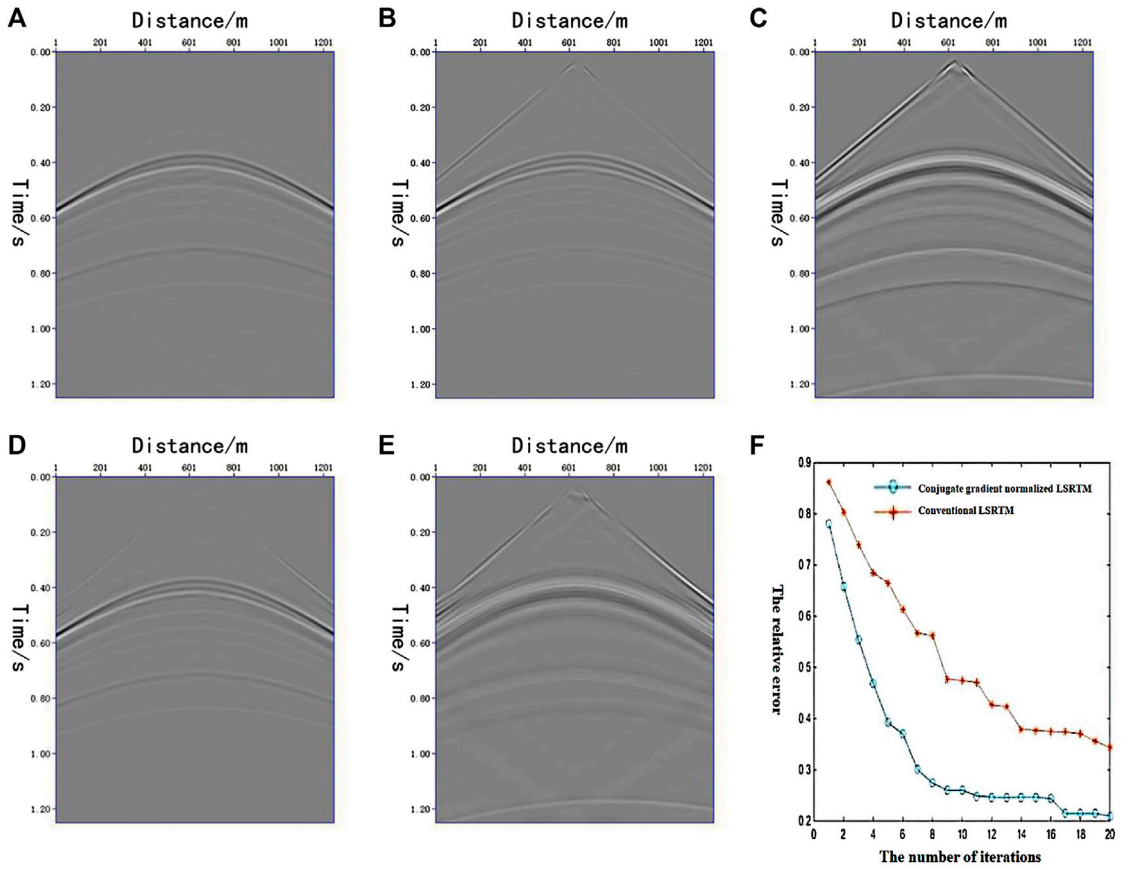

FIGURE 6
Seismic record and error curve of simple model. **(A)** the 6th observation seismic record; **(B)** the 6th simulation record of Born approximate forward modeling after 20 iterations by the conventional conjugate gradient cross-correlation LSRTM; **(C)** the difference between **(A,B)**; **(D)** the 6th simulation record of Born approximate forward modeling after 20 iterations by conjugate gradient normalized LSRTM; **(E)** the difference between **(A,D)**; **(F)** the normalized error reduction curve of the observation record and the simulation record.

gradient normalized LSRTM take approximately 3 min per iteration.

The real and Gaussian smoothed velocity field of Marmousi are shown in Figures 4A,B, which is used for the background velocity field of the RTM and LSRTM migration. From the migration results shown in Figures 4A,B, both cross-correlation RTM and normalized cross-correlation RTM will be contaminated by low-frequency noise (indicated by the yellow arrow). The low-frequency noise in the shallow part of the cross-correlation RTM is more serious. Normalized cross-correlation RTM is better in suppressing the noise in the shallow part, but there will be a small amount of low-frequency noise in the deep part. The main reason for this is that although the source-normalized imaging conditions suppress the shallow strong energy and enhance the deep illumination, they also enhance the wave field energy in the continuation process. The LSRTM can eliminate the low-frequency noise very well. It can be seen from Figures 4C,D (yellow arrow) that the low-frequency noise in the shallow part is obviously eliminated by least-squares processing, and as the number of iterations increases, the noise will continue to weaken. By comparing the low-frequency noise suppression results of the two imaging conditions, under the same number of iterations, the conjugate gradient normalized LSRTM is more significant for low-frequency suppression. In contrast, strong shallow low-frequency noise affects the imaging of underground structures by RTM. Figures 4E,F (red arrow) clearly show that reverse-time migration under different imaging conditions does not achieve accurate imaging of underground structures, some events cannot reflect accurate structure information well, and there are residual low-frequency noises in shallow parts. After the LSRTM processing, it can be seen from Figures 4G,H (red arrows) that the LSRTM can well eliminate low-frequency noise and realize accurate imaging of underground structures, and the overall amplitude of the profile is more balanced. Compare the underground illumination of the LSRTM under two

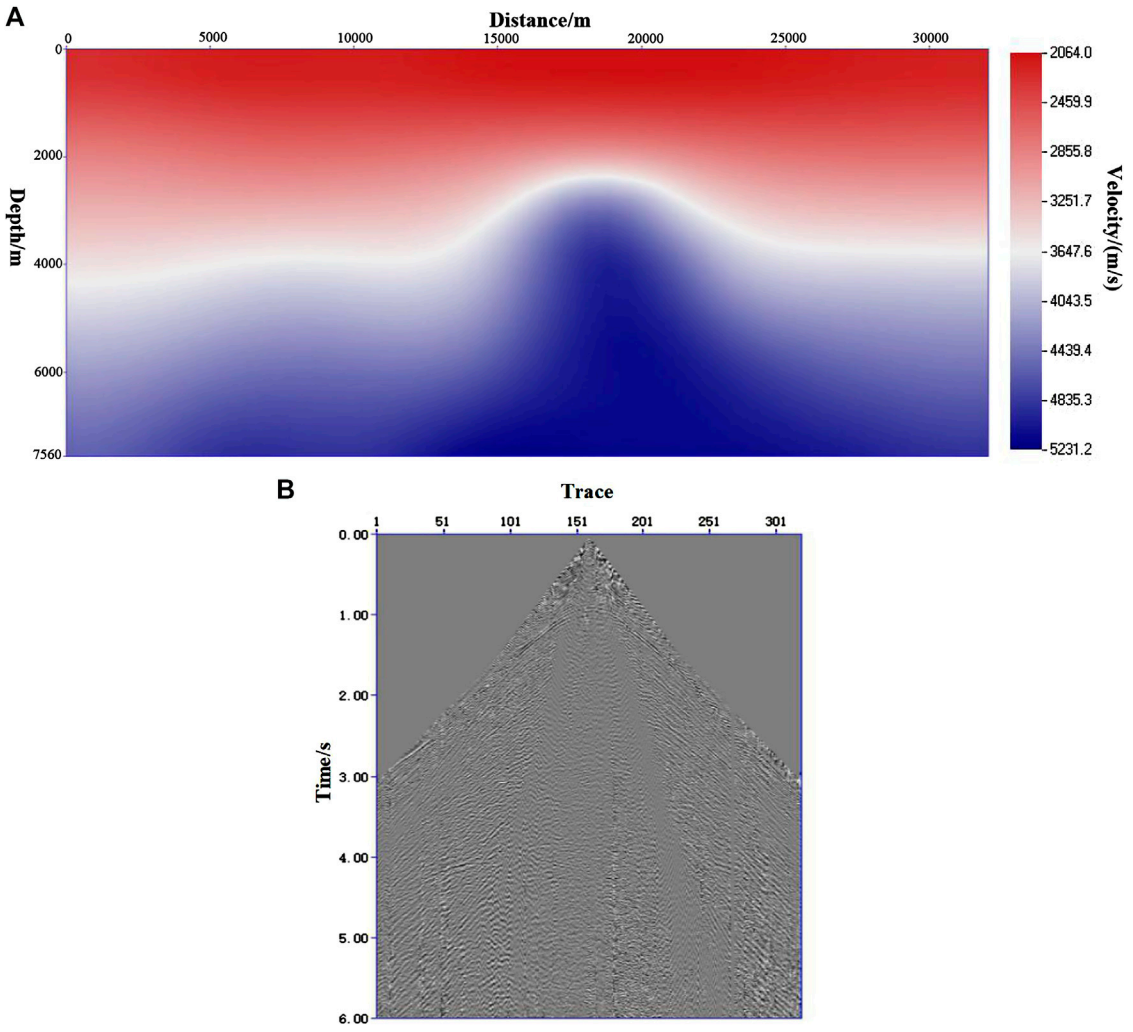

FIGURE 7
Velocity field of field seismic data and single-shot record.

different imaging conditions, it can be seen from the two enlarged images Figures 4I,J (corresponding to the two red dashed rectangular boxes in Figures 4G,H), the conjugate gradient normalized LSRTM is significantly stronger for the deep illumination than the result of the cross-correlation LSRTM. From the comparison of the whole section, we can also see that the conjugate gradient normalized LSRTM is better than the conventional LSRTM for noise suppression in the shallow part, illumination of the deep part, and imaging of the whole structure.

The spectrum of Figure 4G is shown in Figure 5A, and the spectrum of Figure 4H is shown in Figure 5B. Comparing Figures 5A,B, it can be seen that the conjugate gradient normalized LSRTM has a wider frequency band and more information. This also shows the superiority of conjugate gradient normalized LSRTM in the spectrum.

Imaging efficiency comparison

To compare the convergence speed of conjugate gradient normalized LSRTM and conventional conjugate gradient cross-correlation LSRTM, Figure 6 shows the comparison between the seismic records of Born approximate simulation and the observation records under the same number of iterations for the same shot in the simple model.

Figure 6A shows the sixth observation seismic record. The sixth shot simulation records of Born approximate forward modeling after 20 iterations of conventional conjugate gradient cross-correlation LSRTM, and conjugate gradient normalized LSRTM are shown in Figures 6B,D. We calculated the difference between the simulation record and observation record of the two LSRTM methods (Figures 6C,E). From the comparison of Figures 6C,E, it can be seen that under the same

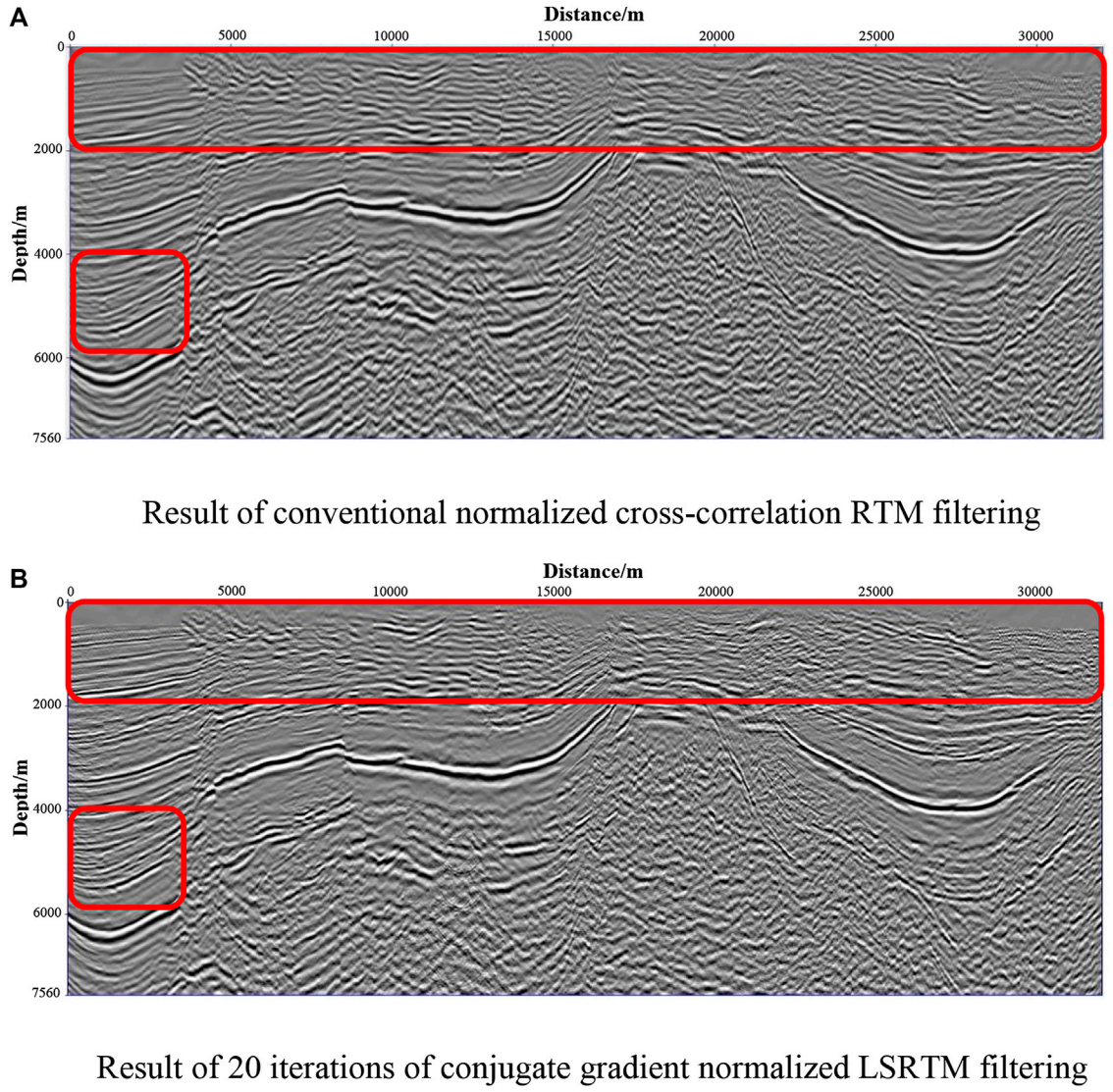

FIGURE 8
Comparison of imaging results by different methods. **(A)** results of conventional normalized cross-correlation RTM filtering; **(B)** results of 20 iterations of conjugate gradient normalized LSRTM filtering.

number of iterations, the Born approximate forward modeling record using the conjugate gradient normalized LSRTM is closer to the observation.

The normalized error reduction curve of the observation record and the simulation is shown in Figure 6F. The abscissa is the number of iterations of the two LSRTM methods, and the ordinate is the relative error. The error formula can be expressed as

$$E_r = \frac{|R_o - R_s|}{R_o}, \tag{24}$$

where E_r is the relative error, R_o denotes the observation record, and R_s denotes the simulation record. Figure 6F shows that compared to the conventional LSRTM, the conjugate gradient normalized LSRTM converges faster, and the residual error will eventually converge to a lower level. Therefore, it can be seen from the above results that the conjugate gradient normalized LSRTM converges faster than the conventional LSRTM, and its residual error is smaller after 20 iterations.

Trial processing of field data

To test the adaptability of the method to the field data, two-dimensional land-based real data were imaged using the conjugate gradient normalized LSRTM. The velocity model of the field data and

single-shot record are presented in Figures 7A,B. The velocity field of these data has a horizontal length of 32,050 m and a depth of 7,560 m. The data consisted of 328 shots with the shot interval of 100 m. The time sampling was 6 s with the sampling rate at 4 ms. Figure 8A shows the result of conventional normalized cross-correlation RTM filtering of field data, and Figure 8B shows the result of 20 iterations of conjugate gradient normalized LSRTM filtering. The conjugate gradient normalized LSRTM is superior to the conventional normalized cross-correlation RTM method, in both the suppression of shallow low-frequency noise and the illumination of deep structures. The energy of the shallow and deep layers of the method in this study is more balanced, and the profile imaging is better, especially for the middle and shallow imaging (as shown in the red box). Thus, it is better than the conventional normalized cross-correlation RTM method.

Conclusion and discussion

This study proposed an effective LSRTM method using the source-normalized steepest descent gradient. Examples of the model and field data were carried out, and the main conclusions are as follows:

1) Compared with the conventional conjugate gradient LSRTM, the normalized LSRTM can help to reduce shallow low-frequency noise, enhance underground deep illumination, and weaken the source effect, which thus improves the imaging quality of underground structures.
2) Under the same number of iterations, the Born approximation forward record of the gradient normalized LSRTM method is closer to the observation record than the conventional LSRTM method. The convergence speed of the gradient normalized LSRTM is faster, and its residual error eventually converges to a lower level.
3) In the present work, only P-waves were considered. The application of converted waves will be studied in the future (Nemeth et al., 1999; Kuehl and Scachi, 2001b; Huang et al., 2013b; Yang et al., 2018).

Data availability statement

The raw data supporting the conclusions of this article will be made available by the authors, without undue reservation.

Author contributions

All authors contributed to design of the study. YS and LT debugged the programs of RTM conventional LSRTM and conjugate gradient normalized LSRTM. XX analyzed the characteristics of the simulation data and field data. YS and XX wrote the first draft of the manuscript. All authors contributed to manuscript revision, read, and approved the submitted version.

Funding

The study is supported by the National Key R&D Program of the Ministry of Science and Technology of China (Intergovernmental Cooperation on Scientific and Technological Innovation, 2021YFE0108800) and the Open Fund Project of National Engineering Laboratory for Offshore Oil Exploration (CCL2020RCPS0419RQN).

Acknowledgments

The authors would like to thank the Shengli Geophysical Research Institute of Sinopec for providing the field data. They also thank the reviewers for their constructive comments and suggestions, which significantly improved the quality of this article.

Conflict of interest

The authors declare that the research was conducted in the absence of any commercial or financial relationships that could be construed as a potential conflict of interest.

Publisher's note

References

Bamberger, A., Chavent, G., Hemon, C., and Lailly, P. (1982). Inversion of normal incidence seismograms. *Geophysics* 47 (5), 757–770. doi:10.1190/1.1441345

Aoki, N., and Schuster, G. T. (2009). Fast least-squares migration with a deblurring filter. *Geophysics* 74 (6), WCA83–WCA93. doi:10.1190/1.3155162

Baysal, E., Kosloff, D. D., and Sherwood, J. W. C. (1983). Reverse time migration. *Geophysics* 48 (11), 1514–1524. doi:10.1190/1.1441434

Claerbout, J. F. (1992). *Earth soundings analysis: Processing versus inversion*. Boston: Blackwell Scientific Publications.

Guo, S. J., Ma, F. Z., Duan, X. B., and Wang, L. (2015). Research of least-squares reverse-time migration migration imaging method and its application. *Geophys. Prospect. Petroleum* 54 (3), 301–308. doi:10.3969/j.issn.1000-1441.2015.03.008

Herrmann, F. J., Brown, C. R., Erlangga, Y. A., and Moghaddam, P. P. (2009). Curvelet-based migration preconditioning and scaling. *Geophysics* 74 (4), A41–A46. doi:10.1190/1.3124753

Huang, J. P., Li, Z. C., Liu, Y. J., Kong, X., Cao, X., and Xue, Z. (2013a). The least square pre-stack depth migration on complex media. *Prog. Geophys* 28 (06), 2977–2983. doi:10.6038/pg20130619

Huang, J. P., Li, Z. C., Kong, X., Liu, Y., Cao, X. L., and Xue, Z. (2013b). A study on least-squares migration imaging method for fractured-type carbonate reservoir. *Chin. J. Geophys* 56 (5), 1716–1725. doi:10.6038/cjg20130529

Huang, J. P., Li, C., Li, Q. Y., Guo, S. J., Duan, X. B., Li, J. G., et al. (2015). Least-squares reverse time migration with static plane-wave encoding. *Chin. J. Geophys* 58 (06), 2046–2056. doi:10.6038/cjg20150619

Huang, J. P., Li, C., and Li, Q. Y. (2016). *Theory and method of least squares migration imaging*. Beijing: Science Press.

Kuehl, H., and Scachi, M. D. (2001a). "Split step WKBJ least squares migration/ inversion of incomplete," in *Expanded abstracts of 5th SEGJ international symposium imaging technology*, 200–204.

Kuehl, H., and Sacchi, M. D. (2001b). Generalized least-squares DSR migration using a common angle imaging condition. *Seg. Tech. Program Expand. Abstr.* 20 (1), 1025. doi:10.1190/1.1816254

Kuehl, H., and Sacchi, M. D. (2003). Least-squares wave-equation migration for AVP/AVA inversion. *Geophysics* 68 (1), 262–273. doi:10.1190/1.1543212

Liu, X. W. (2008). *Fundamentals of elastic wave field theory*. Qingdao: Ocean University of China, 147–150.

Nemeth, T., Wu, C., and Schuster, G. T. (1999). Least-squares migration of incomplete reflection data. *Geophysics* 64 (1), 208–221. doi:10.1190/1.1444517

Prucha, M. L., and Biondi, B. L. (2002). Subsalt event regularization with steering filters. in *SEG technical program expanded abstracts 2002* (Society of Exploration Geophysicists), 1–17.

Tarantola, A. (1984). Inversion of seismic reflection data in the acoustic approximation. *Geophysics* 49, 1259–1266. doi:10.1190/1.1441754

Wang, J., Kuehl, H., and Sacchi, M. D. (2003). Least-squares wave-equation AVP imaging of 3D common azimuth data. *Seg. Tech. Program Expand. Abstr.* 22 (1), 1039. doi:10.1190/1.1817449

Wang, Y. F., Yang, C. C., and Duan, Q. L. (2009). On iterative regularization methods for migration deconvolution and inversion in seismic imaging. *Chin. J. Geophys* 52 (06), 1615–1624. (in Chinese). doi:10.1002/cjg2.1392

Yang, H., Liu, W., Xu, F., and Wang, F. (2018). "Reverse time migration with combined source-receiver illumination," in *SEG technical program expanded abstracts*, 4448–4452. doi:10.1190/segam2018-2997690.1

Yang, Q. Q., and Zhang, S. L. (2008). Least-squares Fourier finite-difference migration. *Prog. Geophys.* 23 (02), 433–437.

Yao, G., and Wu, D. (2015). Least-squares reverse-time migration for reflectivity imaging. *Sci. China Earth Sci.* 58, 1982–1992. doi:10.1007/s11430-015-5143-1

Zhang, Y., Duan, L., and Xie, Y. (2015). A stable and practical implementation of least-squares reverse time migration. *Geophysics* 80, V23–V31. doi:10.1190/geo2013-0461.1

Advantages of publishing in Frontiers

OPEN ACCESS
Articles are free to read for greatest visibility and readership

FAST PUBLICATION
Around 90 days from submission to decision

HIGH QUALITY PEER-REVIEW
Rigorous, collaborative, and constructive peer-review

TRANSPARENT PEER-REVIEW
Editors and reviewers acknowledged by name on published articles

Frontiers
Avenue du Tribunal-Fédéral 34
1005 Lausanne | Switzerland

Visit us: www.frontiersin.org
Contact us: frontiersin.org/about/contact

REPRODUCIBILITY OF RESEARCH
Support open data and methods to enhance research reproducibility

DIGITAL PUBLISHING
Articles designed for optimal readership across devices

FOLLOW US
@frontiersin

IMPACT METRICS
Advanced article metrics track visibility across digital media

EXTENSIVE PROMOTION
Marketing and promotion of impactful research

LOOP RESEARCH NETWORK
Our network increases your article's readership